ADVANCED TECHNIQUES FOR MULTIPACTOR TESTING

Òscar Monerris Belda

Thesis advisor: Dr. Vicente E. Boria Esbert
Thesis co-advisor: Dr. Benito Gimeno Martínez

PhD Thesis presented at Universitat Politècnica de València

Valencia, January 2023

A Elena, qui m'ha donat a Elsa i Héctor
i junts hem format una magnífica família.
Als meus pares, Julià i Fina,
que sempre m'han animat a perseguir els meus somnis.
A Sandra, la meua germana,
qui és un gran referent per a mi.

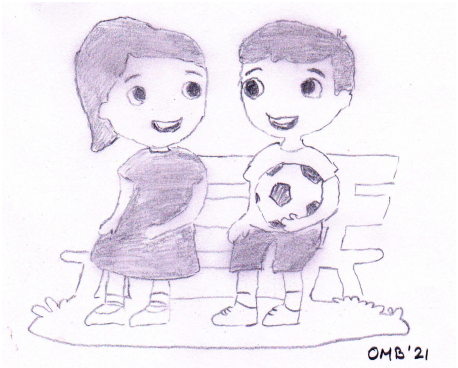

– Did you noticed that the number of worldwide granted doctorates follows an exponential trend?
– So did other bubbles in the past, didn't they?

Acknowledgments

The author would like to thank the following institutions, which have contributed, in one way or another, to this work:

- The European High Power RF Laboratory of the Val Space Consortium (VSC), València, Spain, where the author has pursued his PhD degree.
- The European Space Research and Technology Centre (ESTEC), European Space Agency (ESA), The Netherlands, where the author has always found support.
- The Universitat Politècnica de València (UPV), València, Spain, where the author has found key personnel willing to cooperate in these challenging research topics.

Special thanks go to the following great engineers and physicists who, in one way or another, have improved this thesis with their comments, suggestions and support: Daniel González Iglesias, David Argilés Ortiz, David Raboso García-Baquero, Carlos Alcaide Guillén, Alessandra Monerris Belda, Elena Díaz Caballero, Joaquín Vague Cardona, Raúl Cervera Marín, Miguel Rodríguez Jodar, John Petit, Javier Ossorio García, Vladislav Vorotynskyy Formagey and Vladimir E. Semenov. And I also dedicate it to all those with whom I have worked side by side during all these years.

Resum

En els darrers anys han proliferat els nous sistemes de satèl·lits, sobretot les grans constel·lacions a les òrbites terrestres baixes. Gairebé tots els satèl·lits transmetten dades digitals amb diverses modulacions i nivells de potència. I no només això, el model de negoci exigeix un ràpid desplegament dels satèl·lits, cosa que imposa enormes restriccions als proveïdors de càrrega útil de microones. Una àrea de risc clau per a aquests equips continua sent la descarrega de multipactor sota nivells de potència de moderats a alts. A causa de l'aleatorietat inherent al fenomen multipactor, els clients tendeixen a afegir marges de disseny addicionals per als components de microones d'alta potència. Això es tradueix en costos més elevats, dispositius més voluminosos i més temps per a les proves.

A partir de l'experiència personal realitzant assajos de multipactor, la motivació principal del treball descrit a la tesi ha estat emprendre una revisió exhaustiva d'aquest fenomen i desenvolupar capacitats d'assaig multipactor d'avantguarda. Proporcionar mitjans per a la prova ràpida de multipactors sota una varietat de senyals modulats de banda ampla.

La tesi demostra que les modulacions analògiques i digitals tenen un impacte significatiu al llindar multipactor. També s'analitzen els règims multipactor a curt i llarg termini, règims que, en alguns casos, presenten llindars multipactor molt diferents per al buit crític mateix.

La necessitat de reduir el pes de la càrrega útil de microones fa de la transmissií multiportadora en una excel·lent opció per als dissenyadors. Encaminant diverses senyals a través del mateix dispositiu, el pes de la càrrega útil es redueix dràsticament. Les solucions comercials per a proves multicarrier no són adequades a causa dels alts nivells de potència requerits. Es presenten diverses estratègies per implementar bancs de proves multiportadora amb paràmetres controlables. Els resultats demostren que el senyal amb què s'alimenta el dispositiu sotmès a proves és precís i estable en el temps.

Finalment, es proposa un nou sistema de detecció de multipactors per fer front a la detecció de multipactors quan s'utilitzen senyals modulats i multiportadors de qualsevol amplada de banda. Aquest mètode té la mateixa sensibilitat que el conegut anul·lador de microones per a senyals d'ona contínua i la supera per a senyals modulats. El processament digital de senyals utilitzat per detectar els patrons multiactor proporciona un mètode de detecció totalment autònom.

Resumen

En los últimos años han proliferado los nuevos sistemas de satélites, sobre todo las grandes constelaciones en las órbitas terrestres bajas. Casi todos los satélites transmiten señales digitales con diversas modulaciones y niveles de potencia. Y no sólo eso, el modelo de negocio exige un rápido despliegue de los satélites, lo que impone enormes restricciones a los proveedores de equipos de carga útil de microondas. Un área de riesgo clave para estos equipos sigue siendo la avería del multipactor bajo niveles de potencia de moderados a altos. Debido a la aleatoriedad inherente al fenómeno multipactor, los clientes tienden a añadir márgenes de diseño adicionales para los componentes de microondas de alta potencia. Esto se traduce en costes más elevados, dispositivos más voluminosos y más tiempo para las pruebas.

A partir de la experiencia personal realizando ensayos de multipactor, la principal motivación del trabajo descrito en la tesis ha sido emprender una revisión exhaustiva de este fenómeno y desarrollar capacidades de ensayo multipactor de vanguardia. Proporcionar medios para la prueba rápida de multipactores bajo una variedad de señales moduladas de banda ancha.

La tesis demuestra que las modulaciones analógicas y digitales tienen un impacto significativo en el umbral multipactor. También se analizan los regímenes multipactor a corto y largo plazo, regímenes que, en algunos casos, presentan umbrales multipactor muy diferentes para el mismo hueco crítico.

La necesidad de reducir el peso de la carga útil de microondas convierte a la multiportadora en una excelente opción para los diseñadores. Al encaminar varias señales a través del mismo dispositivo, el peso de la carga útil se reduce drásticamente. Las soluciones comerciales para pruebas multicarrier no son adecuadas debido a los altos niveles de potencia requeridos. Se presentan varias estrategias para implementar bancos de pruebas multiportadora con parámetros controlables. Los resultados demuestran que la señal generada es precisa y estable en el tiempo.

Por último, se propone un novedoso sistema de detección de multipactores para hacer frente a la detección de multipactores cuando se utilizan señales moduladas y multiportadora de cualquier ancho de banda. Este método tiene la misma sensibilidad que el conocido anulador de microondas para señales de onda continua y la supera para señales moduladas. El procesamiento digital de señales utilizado para detectar los patrones multipactor proporciona un método de detección totalmente autónomo.

Abstract

In the recent past, there has been a proliferation of new satellite systems, especially the large constellations in the Low Earth Orbits (LEOs). Nearly all satellites now carry digital traffic with a variety of modulations and power levels. Not only that, the business model requires rapid deployment of satellites, putting enormous constraints for the suppliers of microwave payload hardware. A key risk area for such equipment remains the multipactor breakdown under moderate to high power levels. Owing to the inherent randomness of the multipactor phenomenon, customers tend to add extra design margins for the high power microwave components. This results in higher costs, bulkier devices and longer time for testing.

Based on personal experience in multipactor testing, the prime motivator for the work described in the thesis has been to undertake a comprehensive review of this phenomenon and develop cutting edge multipactor test capabilities, providing means for the rapid multipactor testing under a variety of wide-band modulated signals.

The thesis dissertation shows that analog and digital modulations have a significant impact in the multipactor threshold. The short and long-term multipactor regimes are also analyzed, regimes that, in some cases, have very different multipactor thresholds for the same critical gap.

The need to reduce the microwave payload weight by using multicarriers in a single transponder provides an excellent option for designers. By routing several signals through the same device, the payload weight is dramatically reduced. Commercial solutions for multicarrier testing are not suitable because of the high power levels required. Several strategies to implement multipactor test benches with controllable parameters are presented. Results prove that the signal being fed to the device under tests is accurate and stable over time.

Finally, a novel multipactor detection system is proposed to cope with multipactor detection when modulated and multicarrier signals of any bandwidth are used. This method has the same sensitivity as the well known microwave nulling for continuous wave signals and surpasses it for modulated signals. The digital signal processing used to detect the multipactor patterns provides a full autonomous detection method.

Contents

Chapter 1

Introduction

1.1 Motivation

Microwave devices for space applications might suffer from radio frequency (RF) breakdown discharges, which only happen under reduced pressure or high vacuum conditions. Ensuring that these devices will not suffer from these effects is crucial. Once in orbit, the only option to mitigate such effects is to reduce the transmitted power, thus leading to a data throughput reduction, if not to a total mission failure.

The Multipactor RF breakdown, the main thesis topic, has been known for a long time. It is, in most cases, an undesired effect. The earliest references to the multipactor discharge date back to the 1930's [1, 2, 3]. By that time useful applications for this RF breakdown effect were explored. A few decades passed and by the 1950's and 1960's papers and technical reports on multipactor discharge happening in space systems started to be produced [4, 5, 6, 7]. Since that period then the multipactor RF breakdown has been identified as an undesired and potentially hazardous effect in spaceborne systems.

In current internal standards, conventional multipactor analysis and testing makes use of continuous wave (CW) or pulsed CW signals [8, 9]. For simple systems, this testing approach is representative of the actual component operation conditions, but nowadays the large number of concurrent carriers or the modulation bandwidth makes the CW or pulsed testing a non-representative scenario.

However, along the last decades, the electromagnetic spectrum saturation in space communications [10] has led to the use of higher RF transmission power levels, tighter multiplexing networks and larger bandwidths [11], and multi-level digital modulations [12]. Increasing the complexity in any of those parameters typically leads to a substantial change in the multipactor RF breakdown buildup behavior.

Concurrently to those new requirements, the improvements achieved in the computer science has brought the electromagnetic and particle-in-cell (PIC) simulators to a new paradigm. Nowadays, it is feasible to perform multipactor simulations considering an arbitrary number of RF inputs, excitation signals and geometry details. Parameters that had to simplified in

the past can be considered now.

Consequently, requests for the multipactor qualification of devices have increased in complexity, following the same progress experienced in the computer based simulations. All this together has turned into a research increment in the field of multipactor, which now include modulated signals, advanced materials of any kind, multiple carriers and broader temperature variations.

The typical multipactor specifications include a high margin owing to the uncertainty inherent in assessing the breakdown level due to this phenomena. The basic requirements to perform a CW or pulsed CW qualification in a device which is operated with modulated signals are known by the designers: frequency, average output power, signal modulation scheme, complimentary cumulative distribution function, etc.

However, uncertainty due to the multipactor breakdown nature (secondary emission change over time, electron seeding during testing, etc) and the random nature of the data to be transmitted in the satellite, which directly impacts the RF power signal make necessary the use of larger power margins on top of the average RF power level. Over testing has been, so far, the safest approach, although space industry and part of the scientific community have claimed that the test procedures and methods should be updated with more representative test cases.

New multipactor testing approaches with non-constant RF envelope signals require improved or new detection methods. In some cases, these are just upgraded versions of the existing methods. For instance, the fast electron monitoring, based on high gain and low noise current amplifiers, replaces the reliable electrometers for the electron current monitoring [13]. This fast detection method can track electron population changes at rates of 100 MHz or higher.

However, in other cases such as the microwave nulling system (see Fig. 1.1), the existing detection methods are not suitable and an alternative is proposed in this thesis.

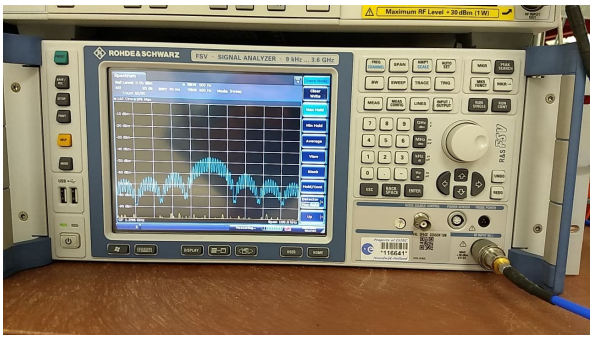

Figure 1.1: Microwave nulling system, only suitable for CW signals.

Signal generation, which is no longer limited to CW or pulsed CW signals, must be enhanced and optimized for the multipactor testing procedure and requirements [8]. Thus including analog and digitally modulated signals. To cite a few, it is common to use bursts of short pulses which may last thousands of ns each, linear frequency sweep chirp or digitally

modulated signals with up to three energy levels. In these cases, their relative bandwidth might reach 10%, which implies that only a few thousand of RF cycles will have a similar amplitude.

In general terms the complexity of digital modulations found in space communications is not comparable to those used in terrestrial applications. This is due to the lower signal-to-noise ratio available in space. However, the use modulations have grown in complexity, from simple binary or quadrature phase-shift keying (PSK), to multi-level schemes such as the 32 amplitude phase shift keying (32APSK) or the 16 quadrature amplitude modulation (16QAM). These signals are complex to generate and amplify, and so it is the detection of multipactor discharges within them.

Demand for multicarrier signals has significantly increased in recent years. Figure 1.2 shows the ten Ku-band channel multicarrier facility available in the European High Power RF Space Laboratory. The RF fields found in those systems, which are the product of different single carrier sources, present a few particularities that make them of interest from a multipactor physics perspective. The first reason is that, as they are created from the combination of different amplifiers, their maximum power level is very large. The second reason is their typically large bandwidth, often in the order of 1 GHz, which leads to very short peak voltages of high amplitude. Techniques to generate high power multipactor signals with adjustable frequency, amplitude, and relative phase of the different carriers were not found in the literature at the time of writing this document.

Figure 1.2: Ten channel and 2.4 kW CW Ku-band multicarrier facility. Photo credits: European High Power RF Space Laboratory, València, Spain.

Under non-constant envelope signals, multipactor can happen in two forms: short-term (nanoseconds) or long-term (microseconds or longer). In the first case, once the discharge starts to grow, there are no periods of net electron loss. In the second case, there are periods during which net electrons increment and net electron loss co-exist.

Operational temperature range is also a relevant topic in space hardware [14]. Even more now that missions to the moon, with broad temperature variations between day and

night, plan to be resumed. Current vector network analyzer techniques, as shown in Fig. 1.3 provide excellent calibration results at room conditions [15]. However, when temperature changes, these calibration techniques do not provide correct data.

Being able to correctly determine the group delay and its maximum positions is essential for multipactor testing, since typically the lowest multipactor threshold value is found at those frequencies.

The lack of commercial solutions to accurately characterize devices at very low or very high temperatures, has led to the development of a new temperature calibration procedure in this PhD thesis. The novel measurement technique, although requiring up to several days to be completed, provides accurate calibrated scattering parameters data. This method performs an independent calibration at each temperature level. It is carried out measuring all the calibration kit standards and the device under test along the thermal profile. Finally, once all the data is collected, a mathematical algorithm suitable for the used calibration kit removes the different error contributions for each temperature.

(a) Climatic chamber

(b) Vector Network Analyzer

(c) Coaxial calibration kit

Figure 1.3: Equipment required to perform scattering parameters measurements over temperature profiles on microwave devices: (a) climatic chamber, (b) vector network analyzer and (c) calibration standard.

To conclude this section, it is worth mentioning that the work conducted during this PhD thesis was motivated by the European space market's need of having a cutting-edge multipactor testing capabilities. All these new advances are available to entities from the European Space Agency's (ESA) member states at the European High Power RF Space Laboratory, a joint initiative of ESA and Val Space Consortium (VSC).

1.2 State of the art

In this section, the state-of-the-art in the field of RF multipactor breakdown discharge and, in particular, the effect of non-constant RF signals on its onset is reviewed.

Devices for space applications might suffer from radio frequency (RF) multipactor breakdown discharge under low pressure or high vacuum conditions [1, 4, 16]. Ensuring that the RF and microwave devices do not suffer from these effects is crucial since, once in orbit, the only option to mitigate them is to reduce the transmitted power, thus leading to a data throughput reduction, or even total mission failure.

A significant effort has been devoted to the research in the field of multipactor breakdown since 1930's. This widespread research activity, mainly based in North America, Russia, Europe and, more recently, China, has produced novel simulation techniques for space components, many technological solutions for multipactor testing, as well as advanced methods for secondary emission yield (SEY), or X-ray spectroscopy measurement and multipactor threshold increment by means of surface treatments.

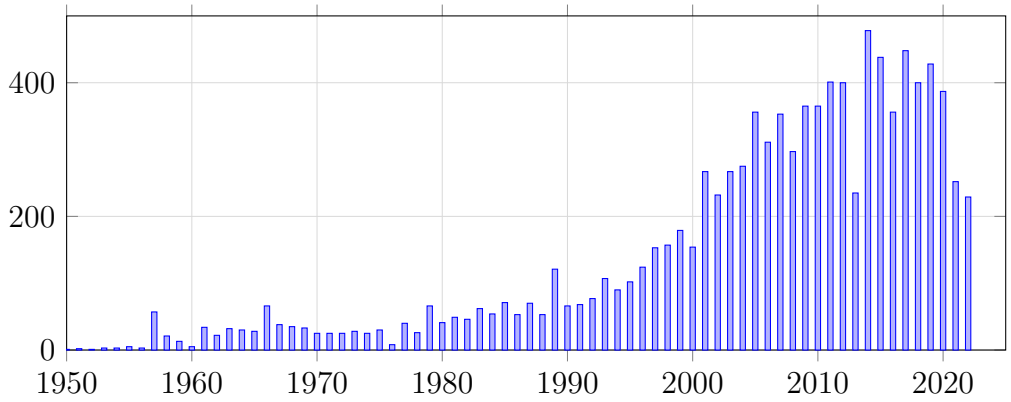

Figure 1.4: Total amount of indexed papers and book chapters devoted to the multipactor effect since 1950. Source: https://scholar.google.es/, visited on 15-Oct-2022.

The increasing number of scientific publications on multipactor RF breakdown phenomena,as shown in Fig. 1.4, confirms the growing interest of the scientific community . The first publication dates back to the 1930's [1], when the multipactor effect was discovered and valuable applications of this effect were investigated.

In the 1950's – 1970's, several space programs [4, 6], and the military equipment developed during the Cold War found multipactor breakdown to be an undesired effect happening in RF components. The period from 1970's to 1980's saw a decrease in armament development as peace attempts were made worldwide, leading to a decrease in the number of publications [17].

Finally, the Russian invasion of Afghanistan in the 1980's lead to an increment in spending within the context of the so-called second cold war. Consequently, so did the number of publications in the field of multipactor. After the end of the cold war, researchers from

Europe and China have contributed in a great deal to the knowledge generation in the field of multipactor, proved by the widespread increment of publications since 1990 [18, 19, 20], not only in terms of number of publications but also in terms of their country of origin. Contributions from Russian research in the cold war framework, which should have gone through similar issues to the ones faced by the United States of America (USA), are not easily accessible online. It is only since the 1990's when excellent contributions from Russian researchers can be found.

By the end of the 1960's, the more relevant multipactor discharge concepts were already known and fully understood: *1*) frequency-distance dependence; *2*) analytical equations for the parallel plate scenario; *3*) secondary emission yield dependence; *4*) susceptibility charts; *5*) multipactor order; *6*) harmonic noise increment; and *7*) single surface multipactor discharge. The experiments used to validate those concepts were carried out in the VHF and UHF frequency bands, with RF power levels up to several hundreds of Watts [6].

There are several different areas of scientific research in the field of multipactor: *1*) materials: dielectrics, ferrites, *2*) modeling: integration with computer assisted design (CAD) tools, fringing fields, space charge, arbitrary geometries or multiple materials; *3*) mitigation: surface finishing or superimpose of electric or magnetic and/or DC or AC fields; *4*) excitation signals: multicarrier or modulated single carrier; *5*) modulated multicarrier signal; and *6*) testing: detection methods, working frequencies and required RF power levels or excitation signals.

From the point of view materials, multipactor analysis and testing has progressed from simple parallel metal plate structures [6] to current standard materials used in space applications, such as dielectrics [21, 22, 23, 24, 25, 26] and ferrites [27, 28, 29, 30].

The multipactor analysis and testing of devices with complex geometries has become a standard nowadays [31, 11, 32, 33, 34, 35, 36]. By increasing the understanding of the actual RF multipactor breakdown behavior within special geometries, such as the ones producing fringing fields [37, 38, 31], the ability to produce accurate simulations has reached a level at which simulation matches testing even in those non-canonical scenarios.

Multipactor mitigation or even total suppression has concerned researchers since the 1960's [6]. From the very beginning, techniques of superimposing additional DC or AC fields, which affect the multipactor RF breakdown build up, have been proposed. Nevertheless, recent research has explored that area in more detail [39, 25, 40].

A different mechanism to increase the multipactor threshold, or even to totally suppress it, comes from materials science. Several surface coatings have been proposed for that purpose [34, 41, 42].

When it comes on the excitation signal used for analysis and testing, there have been major advances: from the standard CW signals used in the past to the nowadays commonly used multicarrier signals [43, 44, 45], analog modulated signals [46] and digitally modulated signals [47].

Testing techniques are also trying to cope with the characteristics of the new devices and signals being used. Some innovations in the field of detection methods have been recently

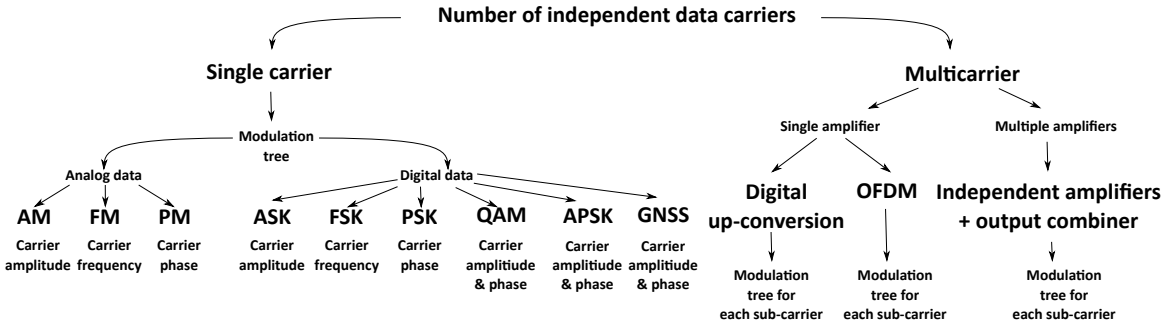

Figure 1.5: Tree for the most common analog and digital modulations, including the available mechanisms to obtain multiple carrier scenarios.

published [48, 49, 50, 51], however they still need to be improved for dealing with wideband modulated signals.

The most relevant analog and digital modulations for space applications and, thus, from the multipactor point of view, are summarized in Fig. 1.5. This tree considers the single carrier and multicarrier cases, being possible for the latter case that each sub-carrier may (or may not) have its own single carrier modulation.

To conclude it is worth mentioning that both, ESA and the National Aeronautics and Space Administration (NASA), have issued international multipactor standards ([8] and [9], respectively). Both agencies suggest a set a basic qualification routes for RF components which, given the constant improvements on that front in recent years, have been frequently updated.

1.3 Organization of the PhD thesis

This PhD thesis has been organized in parts and chapters as follows:

Chapter 1 introduces the main objective, motivation, and context in which this work has been developed.

Chapter 2 introduces the RF multipactor breakdown concepts and covers its physics, simulation, and testing.

Part 1 develops the findings on the effect of analog and digital modulations in the RF multipactor discharge build-up and threshold levels.

- **Chapter 3** presents the research and experimental results obtained in the field of multipactor testing with analog modulated signals.
- **Chapter 4** presents the research and experimental results obtained in the field of multipactor testing with digitally modulated signals.

Parts 2 introduces two novel approaches for generating RF high power multicarrier signals. Through one or another technique, it is possible to create phase-controlled multicarrier signals using either state-of-the-art or the already existing RF equipment.

- **Chapter 5** describes a multicarrier generation method using one signal generator per carrier. This method has been designed to re-purpose RF equipment already available in test laboratories and minimize the implementation cost.
- **Chapter 6** describes a multicarrier generation method using a reduced number of wideband vector signal generators. This approach generates the multicarrier signal with higher precision, less RF equipment and enhanced phase stability.

Part 3 presents the research findings of this PhD thesis, and describes two advanced testing techniques in the field of RF multipactor breakdown.

- **Chapter 7** details an advanced multipactor detection technique capable of dealing with RF modulated signals of any kind. The method is based on the statistical analysis of the system noise.
- **Chapter 8** proposes a novel calibration procedure to obtain accurate scattering parameters of RF space components when the test environment is subject to any given pressure and temperature.

Chapter 9 summarizes the main conclusions, and lists set of future research lines.

Appendices do contain the technical annexes, list of projects, list of publications and acronyms.

Appendix A presents a novel multipactor testing approach that reduces the conditioning of the material in a multipactor test, thus allowing more tests on the same device to be carried out without breaking the vacuum environment.

Appendix B proposes a minimal test bed that implements the previously presented advanced multipactor testing techniques.

Appendix C shows a pulse distortion method that increases the accuracy of the multipactor test results.

Appendix D enumerates the projects and contracts related to the development of this PhD thesis.

Appendix E lists the scientific publications outcomes from this work, including journal papers and conference contributions.

Appendix F lists the acronyms used throughout this PhD thesis.

Chapter 2

Multipactor RF breakdown

2.1 Introduction

The RF multipactor breakdown is a phenomena which requires from this factors to be present in order to develop: *1*) vacuum, *2*) free electrons, *3*) RF power, and *4*) gap.

Several factors modify the way it develops. To cite a few: *1*) cleanliness, *2*) frequency, *3*) secondary emission, or *4*) geometry.

This chapter introduces the RF multipactor breakdown physics, simulation, and testing. The most relevant concepts summarized in this chapter are the foundation stones of the research carried out in this PhD thesis.

2.2 Multipactor physics

The RF multipactor breakdown is a discharge phenomenon in which a given number of initial low energy free electrons (charged particles) interact with the RF field. These electrons, due to the Lorentz force (see eq. (2.1)), have their kinetic energy increased.

The fundamental equation describing the non-relativistic interaction between a charged particles and the electromagnetic field is

$$\vec{\mathbf{F}} = q(\vec{\mathbf{E}} + \vec{v} \times \vec{\mathbf{B}}) \tag{2.1}$$

where q is the particle charge , $\vec{v}$ is the particle velocity, $\vec{\mathbf{E}}$ is the RF electric field and $\vec{\mathbf{B}}$ the RF magnetic field.

Because of the vacuum environment, the mean free path for a charged particle, known as mean free path, is obtained from eq. (2.2). When this dimensions is larger than the device size the charged particles travel from one device side to the other without colliding with any other particle. Eventually, the charged particle will collide with the one of the device's inner walls releasing, in some cases, secondary electrons. Without the freedom of movement that the vacuum environment provides to the charged particles, multipactor cannot happen.

When pressure is higher another type of RF breakdown may happen, this other one is known as Corona RF breakdown.

The mean free path, in meters, can be computed from

$$\ell = \frac{k_{\mathrm{B}} T}{\sqrt{2}\pi d^2 p} \tag{2.2}$$

being k_B the Boltzmann constant, p the gas pressure, T the absolute temperature in Kelvin, and πd^2 the effective cross-section area for spherical particles of diameter d.

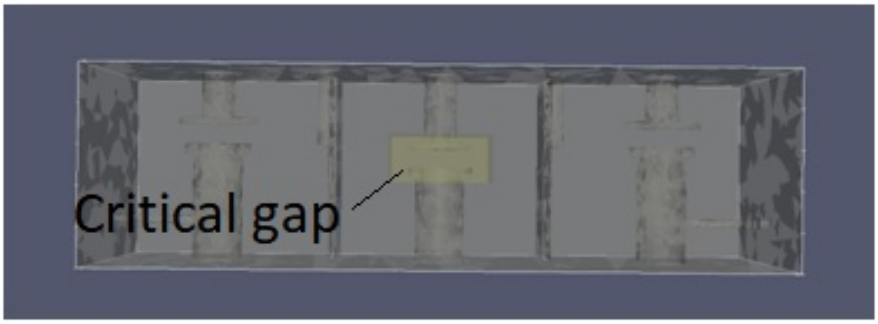

Figure 2.1: Three poles combline RF filter with the area where multipactor happens with the weakest RF fields (critical gap) highlighted in yellow.

Multipactor may happen in several parts of a device, being the critical gap the one in which the weakest RF fields initiates the multipactor breakdown, see Fig 2.1.

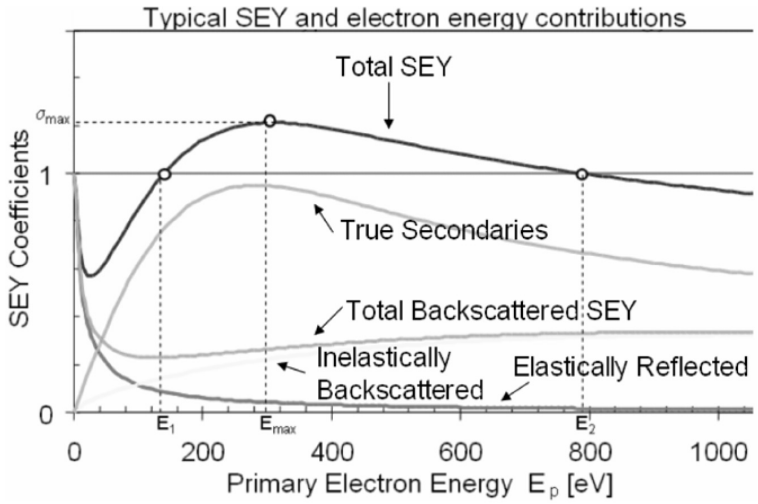

Figure 2.2: Different contributions to the secondary emission yield for copper as a function of the impact energy (normal incidence) from [52].

The Secondary Emission Yield (SEY) curve [53, 54, 55, 56] models the physics of the electron-surface collision. An example curve can be found in Fig. 2.2, which shows the average number of electrons released for each impact energy. Its main parameters are:

E_0 energy level at which the SEY curve achieves its minimum value.

E_1 energy level for SEY coefficients equal to one.

E_m energy level for the maximum SEY coefficient.

σ_{max} maximum SEY coefficient. It is always found at energies above E_1.

E_2 energy level larger than E_1 at which the SEY curve equal to one. It is typically larger than 500 eV.

It is worth mentioning that for each impact angle a different SEY curve shall be produced. Typically SEY curves are given for normal incidence, although the SEY values increase for other angles [57].

When an electron collides with a surface, three types of interactions are feasible: inelastically back-scattered, absorbed, and elastically back-scattered:

Elastically back-scattered departs with the same energy and angle to those at the instant of impact.

Inelastically back-scattered departs with the same colliding angle, but there is a loss in the output energy regarding the incident one.

Absorbed penetrates the material and does not return to the void. Depending on the impact energy, it may release secondary electrons with random initial velocities given by a Maxwellian distribution with a typical mean energy of 3 eV.

For the multipactor discharge to happen, four main parameters must be taken into account:

1. the distance between the surfaces playing a role in the discharge,
2. the RF field frequency, which together with the previous parameter determine the frequency-distance product,
3. the electron impact energy (E_i), which must be most of the time within the range defined by E_1 and E_2,
4. and the time length in which there is a net increment of electrons (impact energy $E_1 < E_i < E_2$). For a CW signal, this period is always long enough for the discharge to be completely develop completely.

Depending on the electron motion, the multipactor order or number of RF half periods required by the electron to cross the gap may change. It is always an odd value ($N = 1, 3, 5, \ldots$) for two surfaces multipactor. In some scenarios, a single surface multipactor may happen, with multipactor order being in all cases an even number ($N = 2, 4, 6, \ldots$).

For a given geometry, what is known as susceptibility charts can be produced. These charts represent the areas in which multipactor can happen, with power represented in the y-axis and the frequency-distance product in the x-axis. An example of susceptibility chart for parallel plates, from [58], can be found in Fig. 2.3.

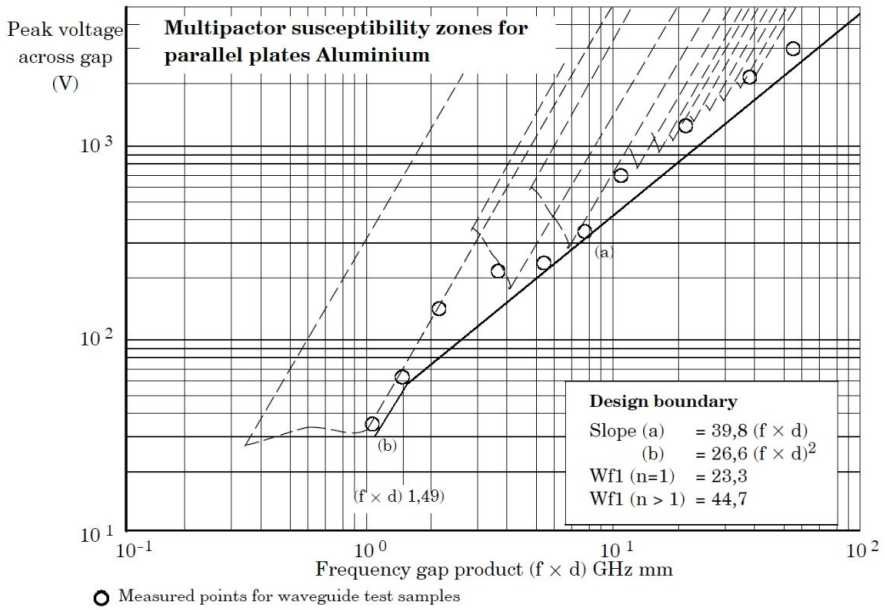

Figure 2.3: Multipactor susceptibility zones for an RF field distribution between parallel plates manufactured in aluminum [58]. The dashed lines isolate the different multipactor orders. The solid line represents the lower boundary of the multipactor threshold given a frequency-distance product.

Finally, it must be remarked that at least one free electron is required to initiate the RF breakdown. During space operation free electrons produced by the sun constantly hits the spacecraft. Some of these electrons may arrive with too low or too large energy. However, a narrow portion of them will eventually reach the device multipactor critical gap. In contrast, the earth magnetosphere and athmosphere provides protection from free electrons. As consequence, multipactor testing of RF devices in a laboratory requires from a free electron source. There are several sources of free electrons being the radioactive elements (strontium or cesium), the electron guns and the ultra violent lamps the more commons [58].

For this initial electron to develop into a large electron cloud the resonance conditions must be met. That requires the right initial velocity and location for the electron, so the minimum RF power is required to start the RF multipactor breakdown

2.3 Multipactor simulation

This section summarizes the most relevant simulation techniques used to evaluate the multipactor discharge behavior in RF devices. In general terms, the simulations techniques can be classified in two categories: particle tracing and approximate models.

Particle tracing These methods track a subset of the charge particles present in the electron cloud. The difference between the two methods in this category lies in the approach used to obtain the trajectory of given particle.

- **Analytical** In some canonical structures, the electron trajectory can be determined by solving the differential equations for the electron motion. Which is much faster than any numerical method.
- **Numerical** These simulators use numerical methods to solve the differential equations which determine the electron trajectories and velocities. They may solve the full 3D electromagnetic model or approximated equivalent circuits.

Approximate method: Coarse method Does not track the particles trajectories to obtain the electron cloud evolution. The coarse multipactor method assumes that the electron cloud evolution follows an exponential growth and decay which depends on the current RF amplitude and a set of pre-computed electron cloud growth and decay factor.

Regardless of the simulation kind, the randomness and unpredictability of some aspects involved in the RF multipactor discharge make it impossible to obtain results without error. This implies that any rigorous multipactor simulator has a non-zero residual error.

2.3.1 Particle tracing

Particle tracing multipactor simulator, also known as particle-in-cell (PIC) simulators, track the trajectory of the charged particles inside the RF device to determine when, where and how they impact with the device walls. As already mention, the only difference between the analytical and numerical simulators lies in the way they determine where and at which speed the charge particles are moving inside the device.

Given that the electron position and velocity can be precisely determined, a PIC routine can track as many electrons as required. This particle tracking must first detect the electron collisions with the surface, which is done using the position equations. Then, the velocity is computed considering the exact impact time, and finally the impact energy is obtained. From the impact energy and the SEY coefficient, the number of secondaries is computed. Finally, electron tracking is resumed with the new set of secondary electrons.

As the particles move at non-relativistic velocities, the computation of the trajectories is not a major source of error, being the computational cost the only difference between the analytic and numeric approaches. The typical execution flow in a multipactor simulator is

1. Spawn the initial electrons at random locations and with random phase.
2. Track each electron till it collides with any surface.
3. Compute the outcome of this electron-surface interaction.
4. Append the newly create electron to the electron list and suppress those absorbed during the interaction.
5. Determine if the number of electron is large enough to consider that the RF multipactor breakdown has taken place. If so, stop the simulation. If not, return to step 2.

Major uncertainty sources in the result provided by a multipactor simulator are due to the initial electron seeding and the electron–surface interaction. The random variables play a role in the multipactor simulation results are:

1. Number of initial electrons,
2. Position and velocity
3. Spawn time in which the initial electrons start the interaction with the RF electric field (known as phase of the electrons),
4. Impact angle (as surfaces are never flat at the scale of an electron),
5. Secondaries energy velocity and/or angle.

Therefore, even if the electron position and the impact energy are precisely known, the multipactor simulation result is, to some extent, random [59]. For that reason, having a large number of initial electrons is critical in order to obtain converging results.

As the number of electrons created during the multipactor buildup grows exponentially the memory limits found in current computers are rapidly reached. For this reasons workarounds have been proposed.

In general terms, particles can be tracked one by one or in the so-called macro-particle approach. Being the macro-particles elements only existing in the simulator with the charge and mass of any number of electrons, even fractions of it. These elements are used to reduce the total number of particles being tracked, while properly accounting for the total charge of the secondary electrons.

These macro-particles are a workaround needed to reduce the computational requirements of multipactor simulation, since the enormous amount of electrons found in a fully developed multipactor discharge would make simulation in current state-of-the-art workstations not feasible.

Next sections describe the analytical and numerical approaches used to determine the electrons position and velocity. Making special emphasis in highlighting the benefit and drawback of each approach.

Analytical electron motion simulation

Multipactor analytical simulation can be carried out in those cases in which the electromagnetic fields can be analytically solved. Hence, the electron position and velocity can be precisely computed by solving the equations of motion for the electrons. Such analytical routines can track as many electrons as required with a reduced computational cost.

The drawback of this approach is that it is constrained to those geometries in which the electric fields can be analytically represented. In [52] an analytic approach is used to simulate the multipactor discharge in a parallel plate scenario. The equations to determine the position and velocity of an electron in that case are shown next.

Let us consider the scenario of parallel plate geometry with a separation between plates d, and a sinusoidal RF excitation applied between them.

The first step is to relate the Lorenz force with the electron acceleration as

$$\vec{F} = m\vec{a} = -e\vec{E}_{RF} = -e\frac{V_{RF}}{d}\hat{x} \tag{2.3}$$

being m the electron mass, e the electron charge, V_{RF} the RF voltage difference between the plates, and d the distance between the plates.

From now on, the vector notation is no longer used as x, and v are in the $\hat{x}$ direction. For this case, the differential equation to be solved is

$$\ddot{x} = -\frac{eV}{md}cos(wt) \tag{2.4}$$

which considering the following boundary conditions,

$$\alpha = w \cdot t_\alpha \tag{2.5}$$
$$\dot{x} = v_0 \tag{2.6}$$
$$x = x_0 \tag{2.7}$$

where α is the electron phase, i.e., the time (t_α) in which the electrons starts to interact with the RF field.

By solving the differential equation in (2.4), the following set of equations describing the electron position and velocity over time are obtained:

$$v(t) = v_0 + \frac{eV}{mwd}\left(sin(\alpha) - sin(wt)\right) \tag{2.8}$$
$$x(t) = x_0 + \frac{v_0}{w}(wt - \alpha) + \frac{eV}{mw^2d}(cos(w) - cos(\alpha) + (wt - \alpha)sin(\alpha)) \tag{2.9}$$

where V is the electric field, e the electron charge, w the RF field angular frequency and v_0, and x_0 the initial velocity and location, respectively.

The electron position is computed from (2.9). The collision with the walls happens when $x(t_i) = 0$ or $x(t_i) = d$. Then, the electron velocity shown in (2.8) gives the impact energy, which determines the average number of released secondary electrons.

Numerical electron motion simulation

In general terms, multipactor simulations are done using particle-in-cell (PIC) routines, which numerically solve the differential equations for the electron motion. As input, they may accept the geometry and materials, and then solve the electric field or import the electric and magnetic fields for a 1D, 2D, or 3D mesh.

Although there have been published multipactor analysis codes for specific geometries such as rectangular waveguide [60], circular waveguide [60], elliptical waveguide [61] or coaxial [60, 52, 38, 39, 62], commercial tools tend to be generic and to allow random geometries, multiple materials or different models for the secondary emission physics. From the signal excitation point of view, they may allow multicarrier or modulated signals and, in some cases, they also take into account the electron-to-electron interaction [63].

The tools in which the RF field is computed using their own solvers may work in the frequency or time domain [63]. Other multipactor simulators import the electric field from third tools [64], which is convenient as only the definition of the materials SEY curves are required, with no need to build the RF model again in the multipactor simulator tool.

The required computational power for these simulators lays between 1 and 100 GB of RAM at the time of writing, being 100 GB a reasonable high limit for current workstations. In very complex geometries, a single multipactor simulation may take hours to complete when CW excitation is used and, several days when modulated signals are analyzed. In general terms, numeric electron simulators do not track more than 1 million particles, although each particle may contain the charge and mass of more than one electron. This work-around has been employed for a long time and these particles are referred to as macro-particles [65, 66].

2.3.2 Approximate models: Coarse method

The coarse multipactor simulation is an approximation of the electron population behavior. The electron population is assumed to have an exponential growth and decay [67]. Thus, the number of electrons (N_e) is obtained using the following equation

$$N_e(t) = n_0 \exp\left(\int_{t_0}^{t_1} \alpha(t)dt\right) \tag{2.10}$$

being t_0 and t_1 the signal interval in which the electron evolution is to be obtained, n_0 the initial number of electrons at t_0 and $\alpha(t)$ the instantaneous growth, which is dependent on the signal shape.

The detection criteria can be either a specified electron gain or a given number of electrons. In the first case the criteria can be written as $\int_{t_0}^{t_1} \alpha(t)dt > a_{th}$. In the second case the detection criteria would be $N_e(t_{th}) > Ne_{th}$. Both magnitudes are related as $a_{th} = \ln N_e(t_{th})/n_0$.

The accuracy of this method relies on the quality of $\alpha(t)$ data which, in turn, depends on an independent PIC simulator. For each RF power level, the α value is obtained from

the simulated electron population over time for a CW by fitting $N_e(t) = n_0 \exp^{(} \alpha t)$ and optimizing α with a least squares regression.

Finally, it must be stressed out that the coarse multipactor threshold estimation is a topic of great interest when the analysis of long modulated sequences is required.

2.3.3 The electron cloud

Once the RF breakdown conditions are met, and there is a net increment in the electron population inside the critical gap, it is time to define the limits to the electron population growth.

The electron population growth happens whilst the Coulomb repulsion force (F_C) among the electrons is weaker than Lorentz force (F_L): $F_C << F_L$. Nevertheless, as the population increases, the Lorentz force is counteracted by the electron Coulomb repulsion. As a consequence, some electrons are diverted, losing their resonance. This repulsion deviates the trajectory in some electrons, which are pushed away from the critical gap and cannot return, as they rapidly lose kinetic energy and they are absorbed by device walls. This effect of reaching a maximum number of electrons is known as multipactor saturation [68, 69]. Figure 2.4 shows the exponential growth before reaching the saturation point, and the stabilization phase for a coaxial transmission line.

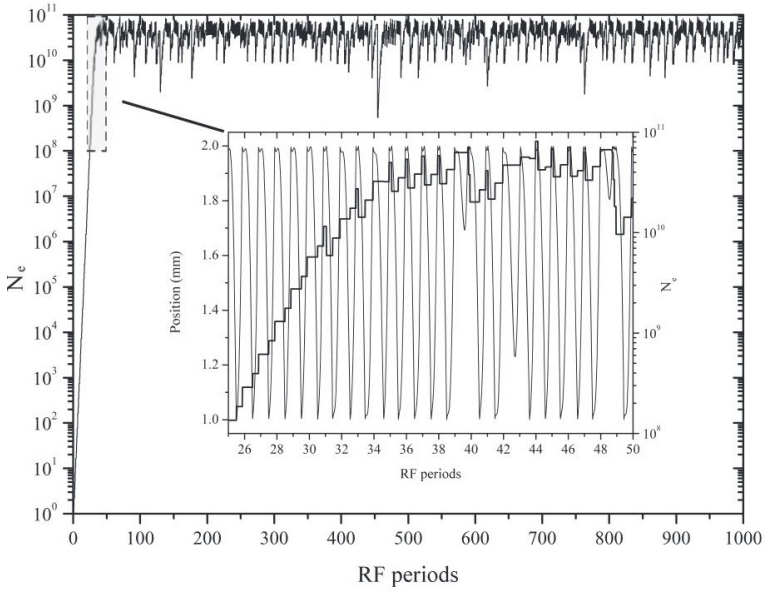

Figure 2.4: Multipactor avalanche evolution versus time for a coaxial waveguide. Chart from [69].

Another important aspect related to multipactor physics is the actual shape and behavior of the electrons in the critical gap. Some works call *electron cloud* [16, 70] to the group of electrons that have reached resonance, although it would be more precise to call it electron sheet [71, 72]. This is because the actual shape of the group of electrons is closer to a thin

sheet than to a thick cloud. The position of the electron sheet is orthogonal to the velocity vector.

With regards to the energy exchange between the electrons and the RF field, it is important to note that they also store energy, which is then released in all directions as a superimposing electric field [73, 74]. This energy release is the reason why RF noise increments isotropically when the multipactor discharge fully develops.

2.4 Long and short term multipactor discharge

To conclude this introduction to the RF multipactor discharge, and to understand some of the findings of this Ph.D. thesis, the concept of multipactor with modulations will be introduced using simple, illustrative examples. In these examples, it is assumed that the electron population follows an exponential behavior until the saturation level is reached (arbitrarily set to 10^{12} electrons). It is also assumed that the electron population cannot be less than one free electron.

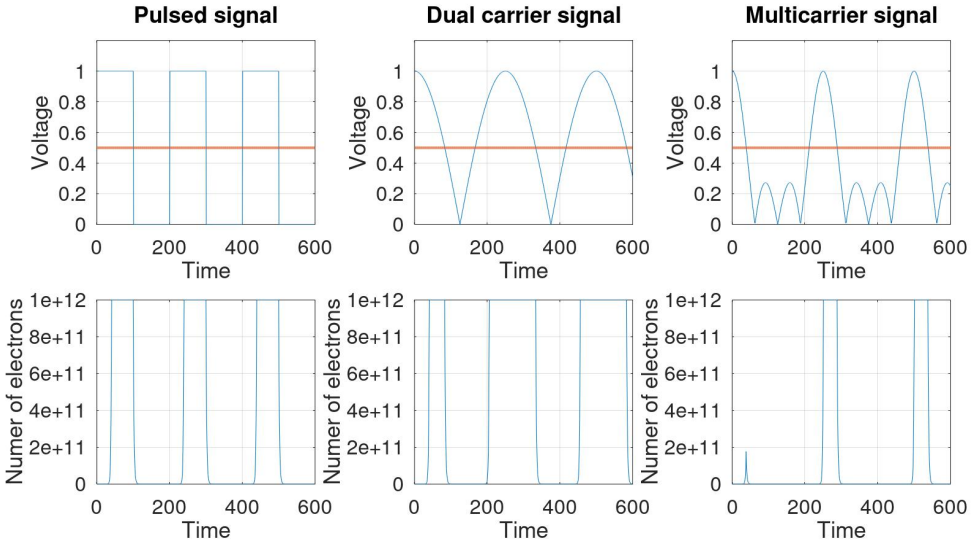

Figure 2.5: Simplified model for the electron population evolution for three signals: pulsed CW (left), dual carrier of 0.5 V_{pk} each (center), and four carriers of $0.25V_{pk}$ (right). In all cases short-term multipactor discharges are observed. Electron saturation has been set to 10^{12} electrons, and the multipactor threshold is 0.5 V.

In Fig. 2.5 the electron growth for three different modulated signals is shown. For all cases, the multipactor threshold is arbitrarily set at 0.5 Volts, which implies that there is only a net electron population increase when the voltage is above this value.

- The first case, on the left-hand side, is a pulsed CW signal with 50% duty cycle. For every RF pulse, the electron population reaches the saturation level.

- The second example is a dual carrier scenario. This case also reaches saturation every time the signal exceeds the multipactor threshold.
- The third example, on the right-hand side, is a multicarrier signal. In this example, saturation is not reached for the initial signal portion, but saturation is reached in all the other peaks.

Although all the previous examples show the typical behavior of a short-term multipactor discharge, when dealing with non-constant envelope signals, another scenario is possible. It is the so-called long-term multipactor discharge.

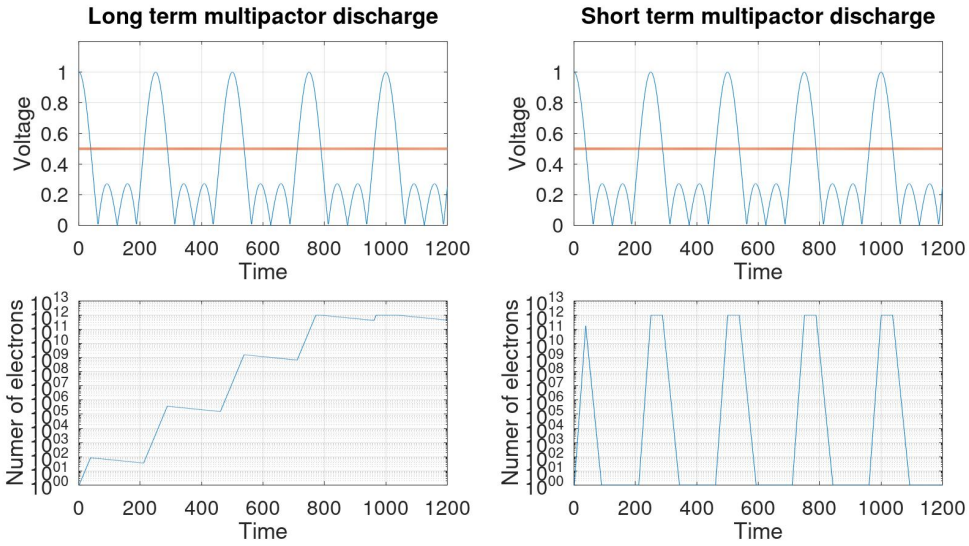

Figure 2.6: Simplified model for the electron population growth. Two scenarios are considered: long-term multipactor (left) and short-term multipactor (right). The RF signal is the same in both examples, with different α grow parameters. Electron saturation has been set to 10^{12} electrons, and the multipactor threshold is 0.5 V

In Fig. 2.6 the same RF signal is represented showing a long-term multipactor (left) and a short-term multipactor (right). As the signal is the same in both cases, the electron growth parameters have been adjusted to obtain these two behaviors. Different α growth factors for the same electric field and critical region can be obtained by using different materials.

2.5 Electron seeding

Multipactor testing requires from low energy free electrons in the range of 1 to 100 eV. For that reason electron seeding for multipactor testing is typically done by one of these methods:*1*) radoactive sources, *2*) ultraviolet light and, *3*) regulated electron guns. All these three methods have shown [58, 75] to provide converging results in laboratory results.

One of the most common mechanism of producing free electrons are the radioactive sources. These are typically made of beta emitting materials such as strontium-90, cesium-137, yttrium-90 or zirconium-90. They produce a continuous spectrum of emitted particles up to the MeV range. One of their strongest value is that these sources are very useful when the multipactor critical gap is out of line-of-sight, as they can penetrated several millimeters of metals or dielectrics while still providing a sufficiently high flux of free electrons. Their main disadvantage is related to their storage and handling precautions as well, as bureaucracy related to the owning of radioactive material.

Another popular means of producing these free electrons is the ultraviolet light lamps. This seeding method is based in the photoelectric effect, which is capable of release low energy electrons from the device metal walls. Its strongest point is its simplicity of operation and low cost.

Finally, the regulated electron gun is capable of generating a controlled flux of free electrons. Its main benefit comes from the fact that the energy of these electrons is, within a range, adjustable.

Ton conclude this section, it is worth mentioning that another practical benefit of the ultraviolet and regulated electron gun is that they can be switched off. This allows the test operator to verify whether the perturbation being detected is multipactor or not. As, when the RF set at the threshold and the electron seeding is switched off, the detection methods should return to nominal response.

2.6 Definition of RF power

Accurately measuring the RF power going into a microwave device is crucial in multipactor testing, as the RF field drives the discharge physics. In general terms, it can be defined as

$$P(t) = V(t) \cdot I(t) \tag{2.11}$$

being $P(t)$ the instantaneous RF power, $V(t)$ the instantaneous voltage and $I(t)$ the instantaneous current.

When dealing with modulated signals, there are different RF power definitions [76]. When giving test results, using one or another will depend on the RF sensor being used. In general terms:

$$P_{RMS} = \frac{1}{T \cdot Z_L} \int_0^T V_{RMS}^2(t) dt \tag{2.12}$$

being $V_{RMS}(t) = V(t)/\sqrt{2}$, Z_L the impedance and T the integration time.

Power can also be defined in terms of the I and Q components of a modulation using:

$$P_{RMS} = \frac{I^2 + Q^2}{Z_L} \tag{2.13}$$

From a practical point of view in the field of multipactor testing, there are four different RF power magnitudes of interest:

$P_I(t)$ Instantaneous RF power, whose value changes at the RF rate.

$P_e(t)$ Power averaged over the period of a carrier.

P_{pk} Maximum of $P_e(t)$. It is what would be measured by a peak power meter.

P_{avg} Average level of $P_e(t)$ over the modulation period. It is what would be measured by a thermal power meter.

These magnitudes are shown in Fig. 2.7.

Depending on the kind of RF power sensor being used either $P_e(t)$, P_{pk}, or P_{avg} can be measured. The only mechanism to estimate $P_I(t)$ is to sample the RF signal using an oscilloscope and apply $P_I(t) = V^2(t)/Z_0$, being Z_0 the oscilloscope impedance. However, using this approach $P_I(t)$ has low accuracy, due to the poor vertical resolution obtained with a high-frequency oscilloscope measurement.

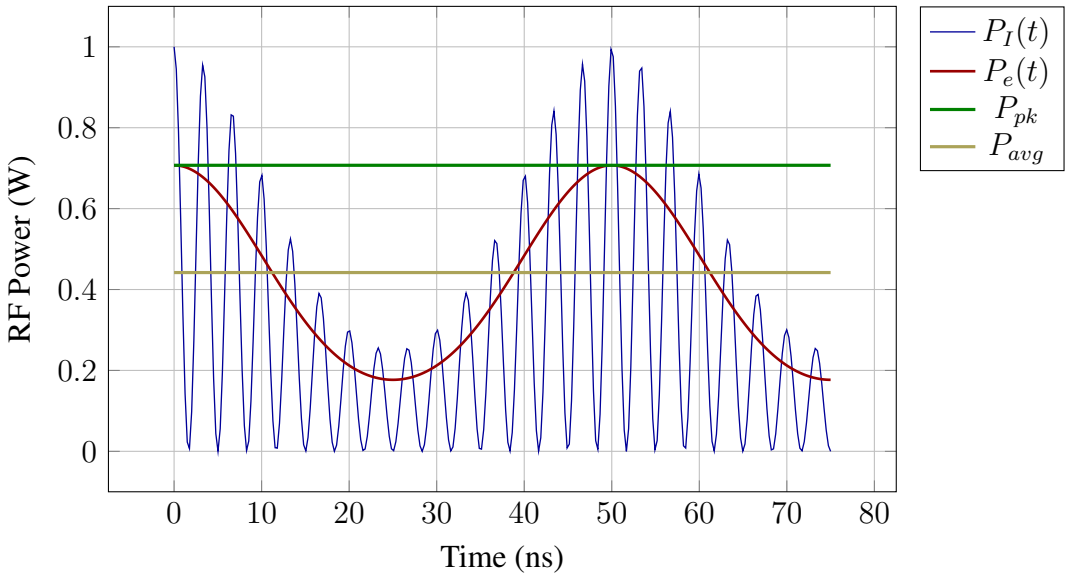

Figure 2.7: RF power measurements.

2.7 Multipactor detection methods

The multipactor detection methods can be classified either to their detection range –local and global methods [50, 51]– or to the type of measured physical parameter –RF signal magnitude at fundamental or harmonic frequencies, the quantity of free electrons (electron current), emitted ultra-violet light and pressure in the test environment–.

The local detection methods can detect the RF breakdown in the vicinity of the critical area and indicate the critical gap location. Electron current or emitted light monitoring

[8] are examples of local detection methods. However, global detection systems cannot determine wherein the test system multipactor has happened. Some of these methods are: microwave nulling, harmonic detection, close to carrier noise, and electron monitoring in the inner coaxial conductor [77].

The sensitivity of the previous methods is not related to the detection being global or local, as shown in Table 2.1. It can be noted that some of them are very sensitive, thus detecting discharges that only change their output parameters by a factor of 3 dB, while others require a change of 6 dB or more [58, 49, 8]. On top of that, these values may be different depending on the specific set-up, as the background noise standard deviation might change. It is worth noting that the high sensitivity of the microwave nulling technique is only achieved when adequately tuned and only for CW frequency, with its sensitivity rapidly decaying when de-tuned or for modulated signals.

Detection system	Background noise	Minimum change
Microwave Nulling	20 to 40 dBc	3 dB
Harmonic detection	< 90 dBc	6 dB
Electron monitoring	$< 10^{-11}$ A	6 dB
Light monitoring	< 0.1 V	3 dB
Pressure	$< 10^{-5}$ mbar	3 dB

Table 2.1: Typical background noise and minimum change of output parameters for reliable multipactor detection systems.

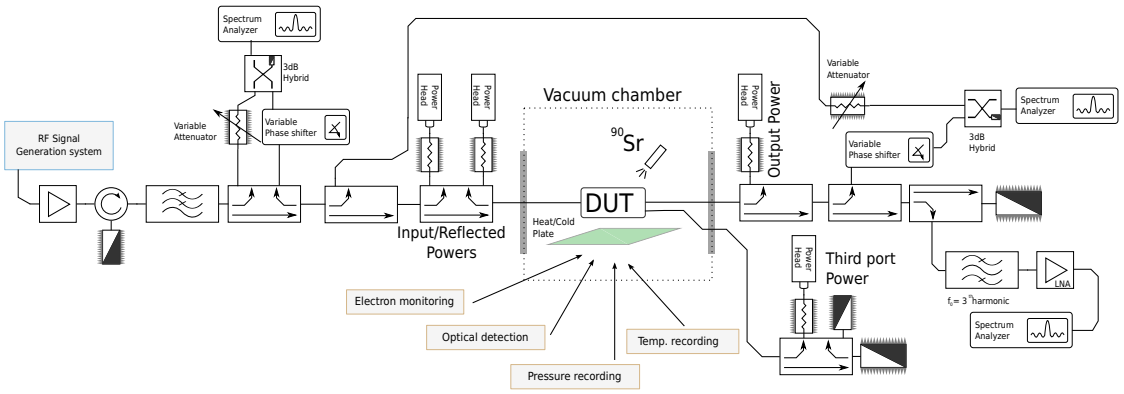

Figure 2.8: Standard multipactor test bed used for a device with three ports. Notice the different detection methods: microwave nulling (two), harmonic detection, pressure, electron and light monitoring.

The standard multipactor test bed is shown in Fig. 2.8. The schematic shows the location of the different detection methods for a device under test (DUT) with three ports. The device

is assumed to have a good matching ($Z_{\mathrm{DUT}} \approx Z_0$). For the global detection methods, the nulling systems are configured in forward-reverse and forward-output modes, the harmonic detection is placed at the device output, and the pressure sensor has a frequency response faster than 5 Hz. Concerning the local detection methods, the following ones are used: light and electron monitoring. These must be placed with line of sight to the critical gap.

2.7.1 Microwave nulling

The microwave nulling is a global detection method [8], and was designed to convert phase and amplitude variations into a scalar magnitude. Not many years ago, vector signal analyzers were not standard, so the signal phase information could not be directly measured. RF breakdown produces more phase than amplitude changes, so a physical mechanism to translate phase and amplitude imbalance into large-amplitude changes was required.

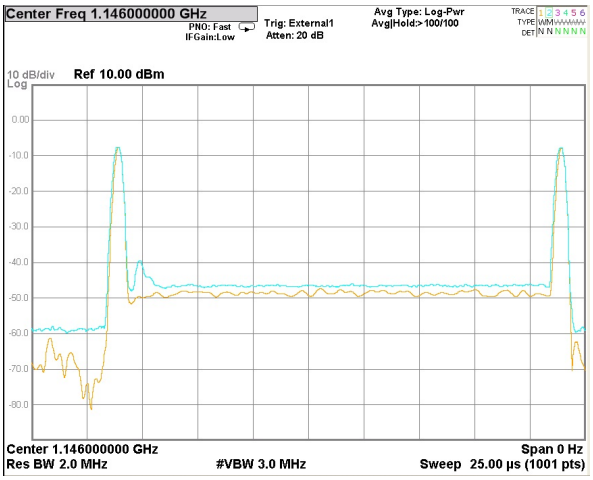

Figure 2.9: Microwave nulling response in the time domain. The leading and trailing edges can be observed.

This detection system is based on the out-of-phase addition of the equalized amplitudes of the forward and reverse signals. In an ideal signal case, the output of this addition should be zero, and only the signal analyzer noise level would be measured. Since non-ideal signals are being used, this sum has a low level instead of zero. The maximum accuracy that can be obtained in an actual microwave nulling system depends on the precision of the phase shifter and of the variable attenuator used to perform the counter-phase addition, as well as on the inherent noise of the signal source and power amplifier used for the signal generation and power amplification [58].

A few advantages of this method are its high sensitivity and ease in its set up. However, its main drawbacks are the need to be often re-tuned, its narrowband nature, the human intervention for discharge detection, and the cost of the required RF passive equipment (if used

exclusively for such tests). This detection method, which is still widely used in RF breakdown tests for CW and standard pulsed CW signals [8, 58], is not suitable for modulated, multicarrier or extremely short pulsed CW signals, that will be explained below.

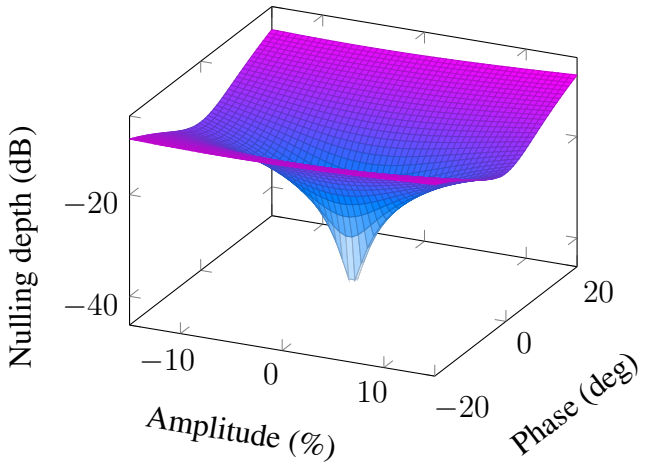

Figure 2.10: Nulling depth in dB depending on the amplitude imbalance (%) and phase imbalance in degrees, clearly showing that small changes in amplitude, and specially in phase, will change the nulling detector output.

When dealing with signals of certain bandwidth, Fig. 2.10 shows the effect of the phase and amplitude imbalance in the nulling depth. The plot shows that small phase changes cause the detector output (nulling depth) to vary substantially. As the phase shifter (see Fig. 2.11)is implemented with a transmission line of a variable length, this nulling depth is only achieved at a single frequency. Only frequencies around the center one will have a sufficiently good nulling depth for modulated signals. This is why this detection method is not well suited for modulated or multicarrier signals. Another limit of the standard microwave nulling applies to very short pulsed CW signals, where the resolution bandwidth of the spectrum analyzer being used will filter out the nulling signal when pulses in the order of nanoseconds are used for testing.

Focusing now in the nulling response stability during test, temperature changes in the DUT, or amplifier gain effect on the amplitude modulation (AM) and phase modulation (PM) [78], creates an imbalance which becomes larger over time, thus making it necessary to adjust the nulling system periodically to maintain it tuned for better sensitivity.

2.7.2 Harmonic monitoring

This global detection method is based on the monitoring of the harmonic level of the RF high power signal. This parameter substantially increases when the multipactor is occurring.

The signal can be monitored either at the input or at the output, the latter one being the most common configuration. In order to use this detection method, it must be verified that

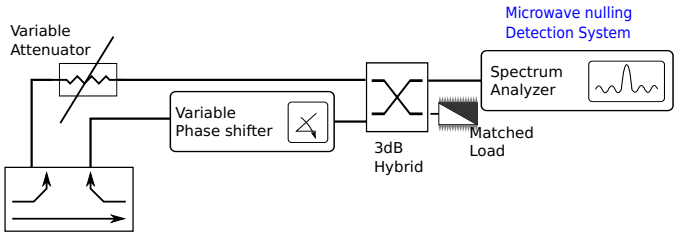

Figure 2.11: Typical microwave nulling implementation.

the device does not filter the harmonic frequencies.

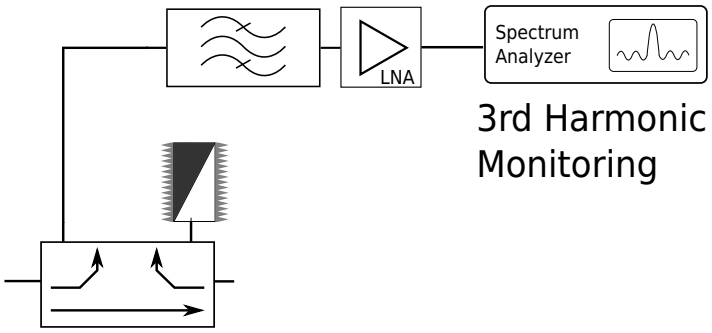

Figure 2.12: Sketch of the harmonic detection implementation.

Because it is easier to filter the fundamental signal, the third harmonic $f_{3^{rd}} = 3 \times f_0$ is typically used. However, second or fourth harmonics can be used as well.

Its operation principle is simple. When a multipactor discharge occurs, a fraction of the energy is shifted from the fundamental frequency toward the harmonics. During regular operation, the levels of the harmonics are typically low and constant. However, when the discharge is initiated, this level increases abruptly.

The harmonic levels are often very low to be measured by a spectrum analyzer, even when the discharge occurs. Thus, a high gain (> 30 dB) low noise amplifier (LNA) shall be used used, as can be seen in Fig. 2.12 (see its typical configuration in Fig. 2.13).

2.7.3 Electron monitoring

The electron monitoring (see Figs. 2.14 and 2.15) is a local detection method. It measures the electron cloud which is generated during a multipactor discharge. The electron population increases up to levels which can be measured by a pico-ammeter.

To set up this detection system, a metal wire is placed close to the critical gap. Then a fixed $+20$ to $+40$ Volts DC potential is applied to bias the wire and capture more electrons. Finally, the other wire end is connected to the pico-ammeter.

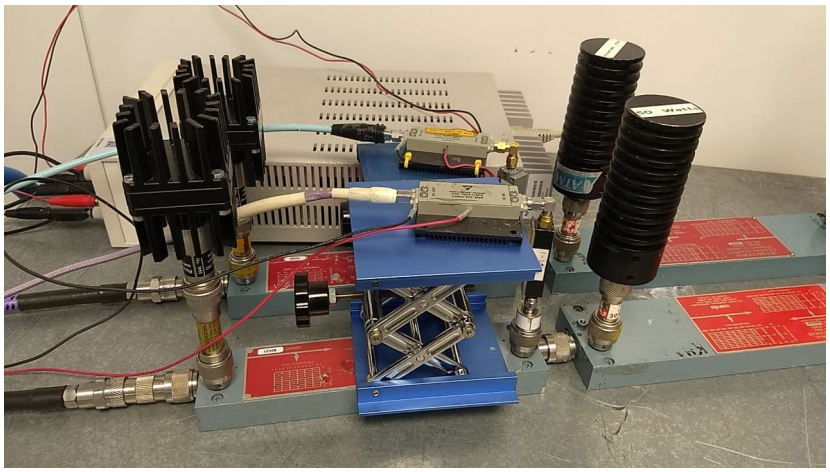

Figure 2.13: Harmonic monitoring in a device with two outputs.

During the multipactor discharge, an increment in the recorded current is noticed. Changes of one order of magnitude from nominal reading can be considered a possible indication of an RF discharge.

Proper system grounding is crucial to avoid interference with other equipment or human operation. Incorrect system set-up may render it unreliable due to large noise events being continuously captured. When several electrometers are being used, it is recommended not to share any component to avoid coupling the detected signals. Figure 2.16 shows the expected response during the discharge.

2.7.4 Ultra-violet light monitoring

During the multipactor discharge, very feeble ultraviolet light is emitted. The measurement of this light can be used as a *local* detection system. This emitted light comes from two sources: the photoelectric effect in the metal walls when the electron cloud collides with them, and the ionization of the residual molecules still present inside the device.

Proper amplification by means of a photomultiplier tube (see Fig. 2.14) is required in order to condition this light response into a measurable voltage. Signal conditioning is carried out using photomultipliers. These devices converts the input light into output current Ampers. In Fig. 2.17 the typical spectrum responsivity is shown for am being the gain $> 10^5$ A/W.

Figure 2.18 shows the expected response during the discharge, which is similar in shape to that measured by the electrometers but with the opposite sign.

The light power generated by the discharge is, typically, extremely low. From the peak value in Fig. 2.18 it is possible to estimate the light power at the photomultiplier input. Assuming a typical input impedance for a data acquisition unit of $1M\Omega$, and taking the peak voltage measurement of 7 V, the photomultiplier output current can be estimated as

Figure 2.14: Two electrometer systems including their +30V bias boxes and a photomultiplier (right).

$I_{mp} \approx 7 \cdot 10^{-6}$ Amperes. Then, the light at the photomultiplier input could be estimated to be $\approx 70 \cdot 10^{-11}$ W, when the responsivity values from Fig. 2.17 are considered.

2.7.5 Pressure

When the multipactor discharge happens, an increase in temperature will typically be observed due to the energy exchange between the electron cloud and the DUT surface. Although this increment cannot be directly measured, it might cause nearby materials to release gas. Modern pressure gauges can be used as global detection systems. Their sensitivity and response time is sufficient to detect the discharge.

The typical graph for these events (see Fig. 2.19) is a pressure increment followed by a slow exponential decay, due to the vacuum pumps removing those molecules from the thermal vacuum chamber (TVAC).

In some cases, this pressure increment may produce a multipactor-induced corona discharge [6, 79]. This induced corona is common in improperly vented devices. Although the number of released particles has a low impact on the overall TVAC pressure, if these

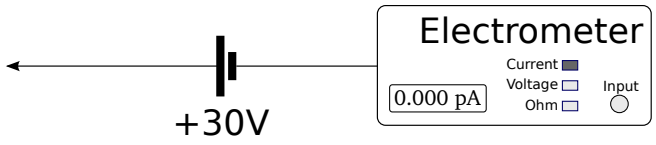

Figure 2.15: Typical electrometer setup including the bias voltage required to capture the electrons.

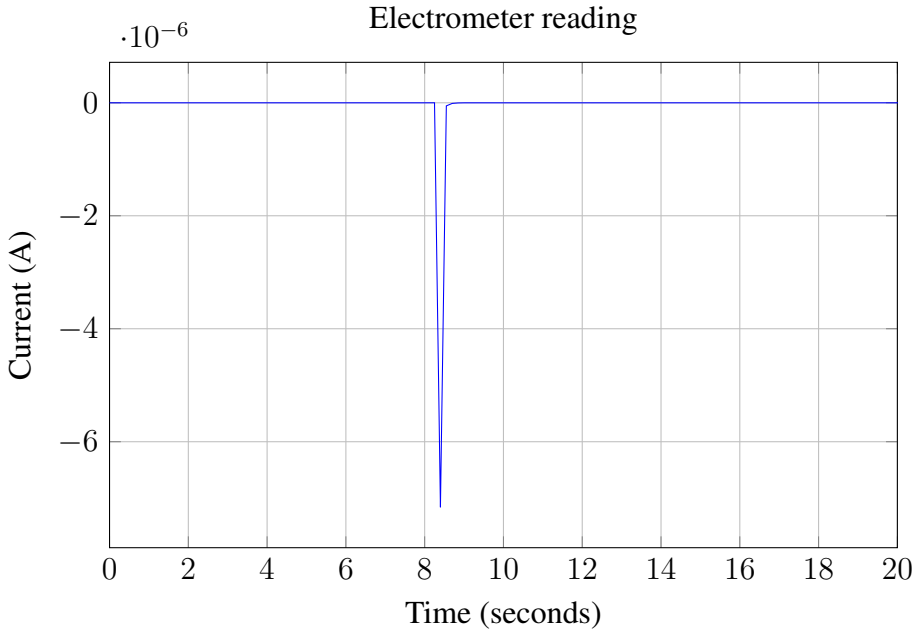

Figure 2.16: Electrometer response during a multipactor discharge.

molecules (of an order of magnitude smaller in volume than the TVAC) are not quickly removed from the critical gap, they may change the local pressure to levels in which corona discharge can ignite.

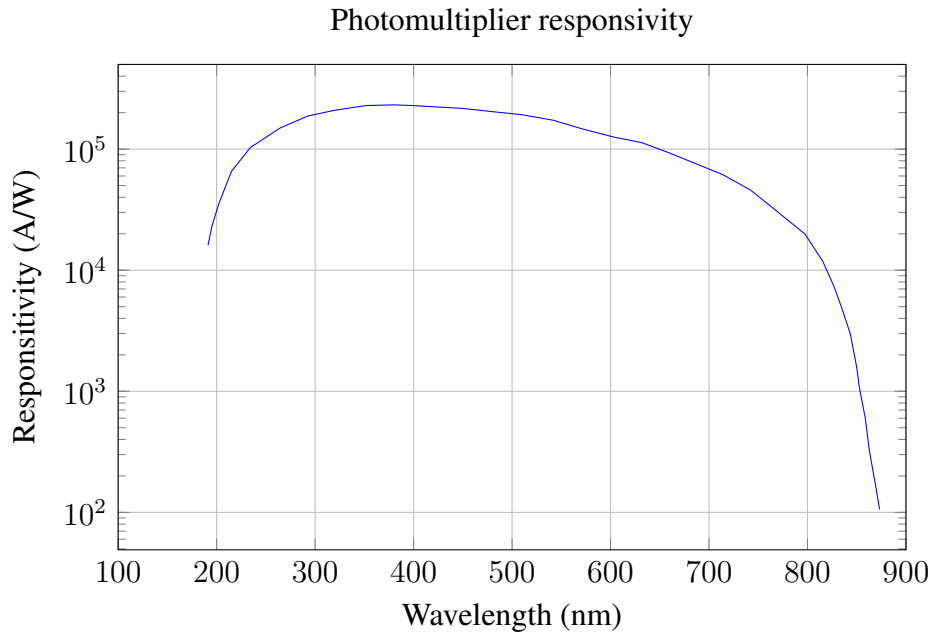

Figure 2.17: Newport Oriel 77341 photomultiplier typical responsivity curve.

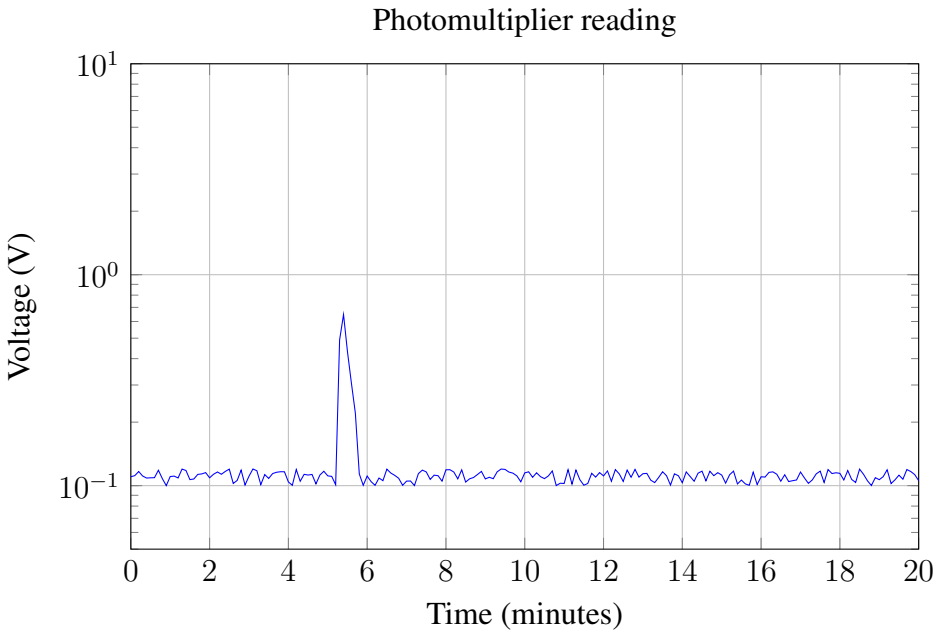

Figure 2.18: Ultra-violet light response during a multipactor discharge.

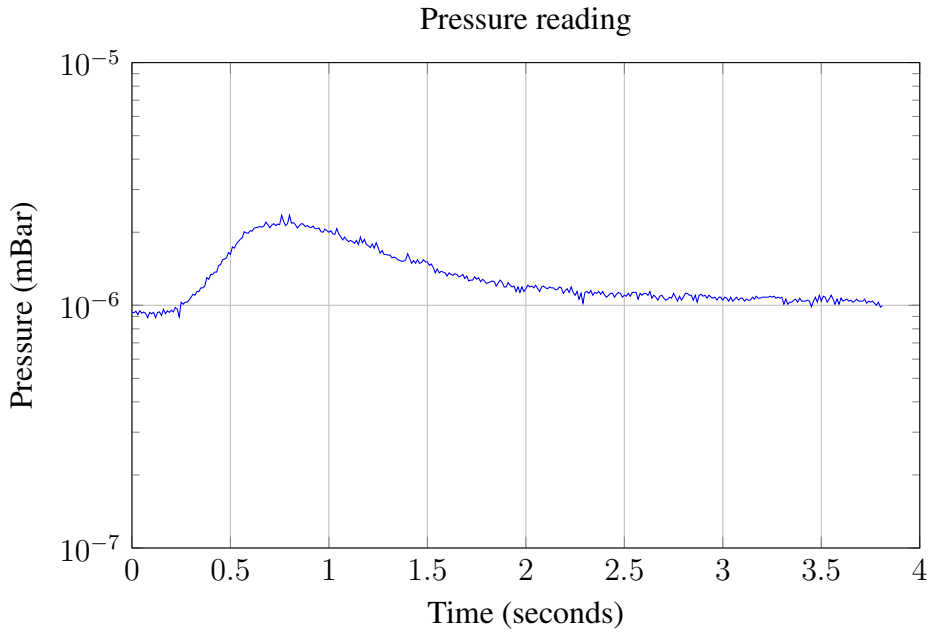

Figure 2.19: Pressure gauge response during a multipactor discharge.

Part I

Multipactor with modulated signals

Research scope

Multipactor RF breakdown has traditionally been studied for RF sources producing continuous waves. This approach is the most convenient to determine the impact of several parameters, other than the RF signal itself, into the multipactor threshold level.

As discussed in previous sections, pulse CW testing is an alternative to continuous wave testing which, in the presence of sufficient electron seeding a for pulse widths larger than 20 microseconds, leads to the same multipactor threshold values [58, 8, 9].

Except in cases like some satellite CW beacons [80], the satellite RF transmission systems change the signal characteristics to transmit useful information. In the past, that signal suffered changes at such a slow rate that the multipactor buildup was not affected and, hence, the results obtained for pulsed CW were applicable for nominal operation conditions.

Nowadays, requirements for larger satellite data throughput force the use of wider transmission bandwidths and multi-level modulations. Consequently, the multipactor threshold might be different from that of pulsed CW. This difference, which may be small or large, positive or negative, is the scope of this part of the Thesis. In all the cases studied, only one RF carrier is considered.

This part consists of two chapters: chapter 3 covers analog modulations, and chapter 4 take cares of digital modulations commonly used for satellite-to-earth communications.

Chapter 3

Multipactor testing with analog modulated signals

3.1 Summary

Information transmission is the most basic requirement that a satellite has. Either communication satellites, earth monitoring missions or positioning system all of them transmit back to earth information by means of RF signals. In early days simple data encoding schemes such as amplitude shift keying or basic radar signals where used. These signals had a low bandwidth i.e., the signal characteristics: amplitude, frequency or phase remain at similar levels for many RF cycles [4, 5, 6, 7].

As time went by, more than one information channel was transmitted using shared RF components, changing from single carrier scenarios to multiple carrier scenarios. For those cases, as given that RF power levels were still low, over-testing was still an option and the peak power level of the multicarrier signal could be handled by the RF designs.

However, new satellite generations [11] use such high power levels that testing scenarios must be adjust to the actual requirements.

Available literature in the field of multipactor discharge with short pulses is limited to theoretical models with no experimental results [81]. This chapter extends previous work and does not only limit to simulation but also provides experimental results. Then, in the field of multicarrier testing, several works are available including simulation and testing are available in literature [82, 43, 45]. However, the research carried out in this thesis focuses in the dual carrier scenario. This simplified case is an excellent framework to study the long and short-term multipactor regimes.

This section aims to study the multipactor effect when analog modulations are employed. In particular, a very simple analysis of the effect of short pulses is done in section 3.2. Next, section 3.3 considers the dual carrier scenario, in which two non-modulated with varying frequency spacing and amplitudes affect the multipactor threshold.

3.2 Narrow pulses

3.2.1 Introduction

This section covers the effect of the pulse length in the multipactor breakdown discharge development. When the RF signal is active and beyond the multipactor threshold level, the electron population in the critical gap increases. Since the active time interval shortens, it might not be feasible for the discharge to be fully developed with the same RF field strength as in the CW case. However, it may happen that higher RF fields are sufficient for the discharge to develop fully within a shorter time span.

Shorter times with active RF field imply that the colliding electrons' average impact energy must shift from values slightly higher than E_1 to values closer to the maximum SEY value E_m for the discharge to be fully developed. This extra energy is required in order to reach the multipactor saturation, which would be reached with a CW excitation in fewer RF cycles. For that reason, larger RF powers are required.

This investigation considers that the time interval in which the RF field is not active is long enough to assume each repetition is an uncorrelated experiment. Hence, the electron population at the beginning of each RF pulse is only provided by the electron seeding, with no residual electrons remaining from the previous RF pulses. These long intervals between pulses imply that only short-term discharges can happen.

3.2.2 Device under test

The coaxial dimensions used for multipactor simulations and testing are $a = 1.238$ mm and $b = 2.850$ mm for the inner and outer conductor radii, respectively. The center frequency for running multipactor simulations and experiments is $f = 1.145$ GHz. This geometry has a critical gap of $d = b - a = 1.612$ mm. Copper is the building material of both conductors.

The data for this material is extracted from [83]. The fitting parameters for the Furman and Pivi SEY true secondaries [84, 85] contribution in the model are $\sigma_m = 1.77$ $E_m = 277$ eV, and $s = 1.539$. Being

$$\delta(E_p) = \delta_m \frac{s\frac{E_p}{E_m}}{s - 1 + \left(\frac{E_p}{E_m}\right)^s} \tag{3.1}$$

the equation modeling the contribution of the true secondaries. In this equation E_p is the energy of the primary electron, δ_m is the maximum value for the experimental SEY curve of the considered material, W_m the energy at which δ_m is found and, finally, s is an adjustable parameter > 1 to fit the experimental data. The different SEY contributions (elastic, inelastic, and true secondaries) are shown in Fig. 3.1.

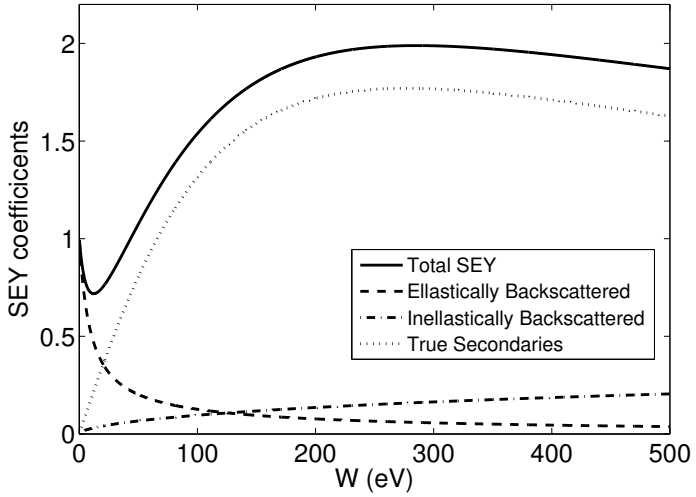

Figure 3.1: Different contributions to the secondary emission yield for copper as a function of the impact energy (normal incidence) from [86].

3.2.3 Testing technique

experimental test campaign was carried out. The set-up (see Fig 3.2) is the standard one commonly used in multipactor measurements. A detailed description can be found in [8]. Three detection methods were used: microwave nulling, third-harmonic monitoring, and electron current monitoring. Following the multipactor testing procedure from [8], the experimental threshold levels were effectively considered when two detection systems were triggered simultaneously.

A metrology-grade performance Keysight PSG signal generator, with optional hardware to generate the short pulse modulations, was used to produce the ultra-short pulses. This optional hardware provides the capability of generating RF pulses with a rise/fall time of 6 to 10 ns.

3.2.4 Simulation results

The analysis of the multipactor discharge in coaxial guides has been run using a custom simulation tool [86, 38, 28]. This code performs an individual tracking of a set of electrons in a 3D structure. The motion for the charged particles is governed by the RF electric and magnetic fields, corresponding to the coaxial transverse electromagnetic (TEM) fundamental mode. The equation is numerically solved using the Velocity-Verlet algorithm [87]. When an electron-wall collision happens, the impacting electron can be either absorbed, in-elastically backscattered, or elastically backscattered.

In inelastic collisions, true secondaries can be produced. Each of these possible interactions are modeled by means of the function described in [88, 83]. For this research, the SEY

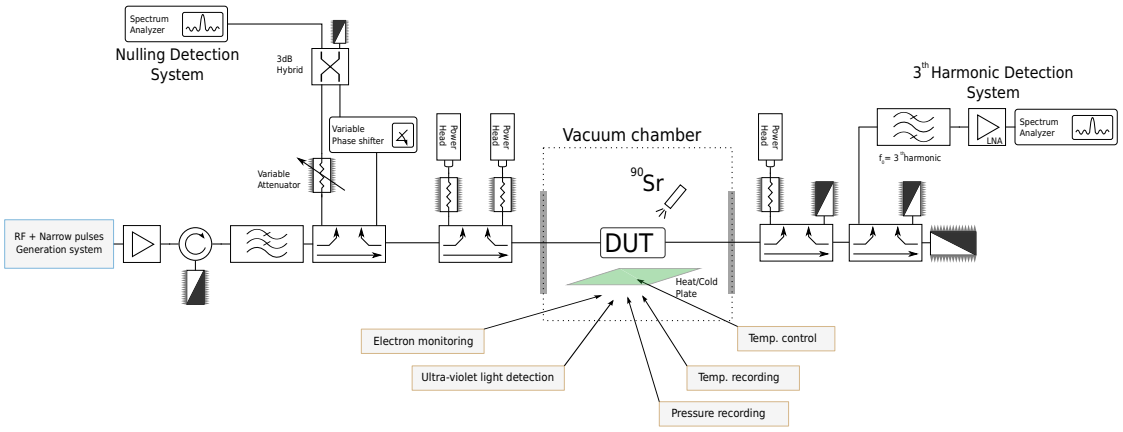

Figure 3.2: Diagram of the multipactor test beds used for the experimental validation. The analog signal generator has the build-in hardware capable of generating pulses down to 30 ns.

model and equations from [52] are used. After the collision, if the electron is not absorbed, it is launched back to the void from the colliding spot.

The multipactor analysis considers that the elastically backscattered electrons depart with the same energy and angle as those at the impact. Inelastically backscattered electrons depart with the same colliding angle, but there is a loss in the output energy regarding incident one.

Finally, true secondary electrons are released with random initial velocity given by a Maxwellian distribution with a mean average energy of 3 eV [89]. The velocity launching angle is obtained from the cosine law [90].

The multipactor threshold determination is based on detecting a large electron population to ensure that the discharge effects are noticeable from an experimental point of view. According to the literature, the electron population is expected to grow up until a steady-state (multipactor saturation) is reached [66]. At this stage, the electron population is maximum (with oscillations around this value), and its effects are supposed to be measurable.

Numerical simulations presented in [91, 69] show that the saturation level happens in the range of 10^9–10^{12} electrons. Although this value depends on the critical gap geometry, SEY and/or RF voltage. In this PhD thesis, a value of 10^{12} electrons has been selected as the multipactor onset population threshold. However, to the author knowledge, literature has not studied in detail the dependence of the threshold value with the critical gap geometry and the upper value found in literature has been selected.

For the simulations, the number of initial seeding electrons has been set to $N_i = 500$. In all cases, the simulation stopped when the number of electrons has reached a maximum of $N_e = 10000$. As stated in the previous paragraph, the level for the onset of the discharge has been chosen at the most conservative value given in [91, 69] ($N_{sat} = 10^{12}$). However, due to computational limitations, a standard workstation cannot track so many electrons in a reasonable amount of time (a few hours).

The simplification followed in this work to limit the maximum number of particles being

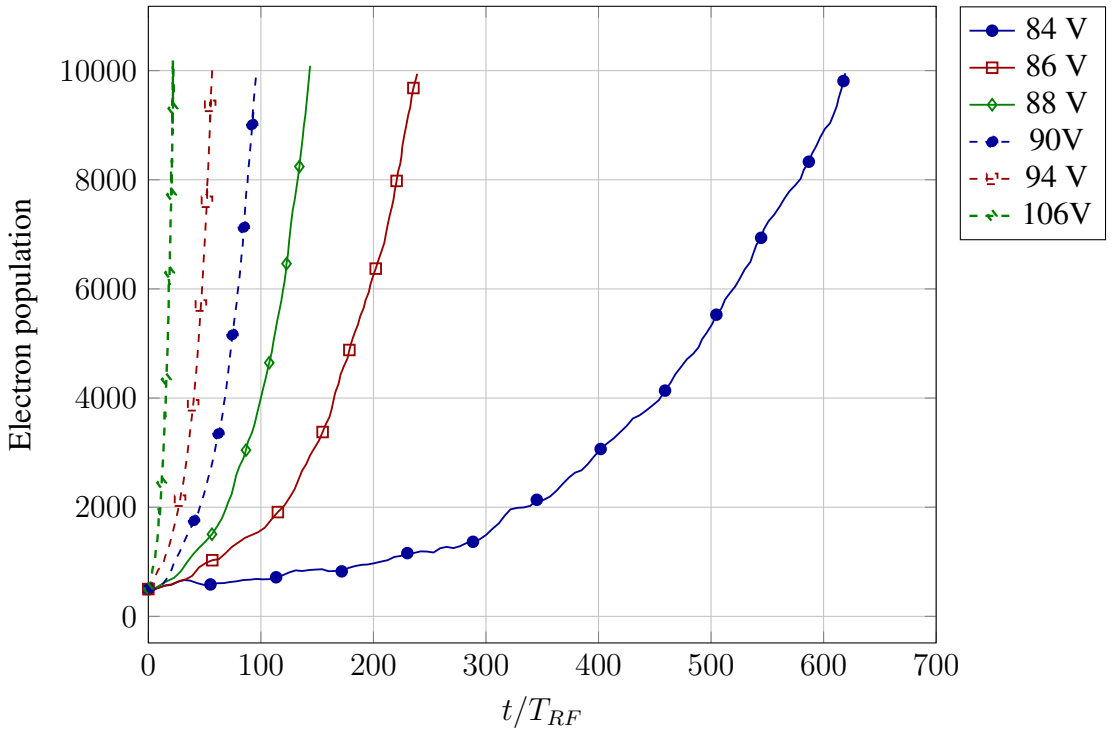

Figure 3.3: Time evolution of the electron population in the critical gap excited by a continuous wave (CW) signal as a function of the time (normalized to the RF period – T_{RF}) for different RF voltages.

tracked consists in fitting the trend of the electron population to an exponential function (see Fig. 3.3). For a CW signal, this exponential trend in the electron population leads to the inevitability of ensuring that multipactor saturation will eventually be reached. However, this is not always true when dealing with pulsed signals in which RF signal is active during t_{on} for a few RF cycles.

This trend is extrapolated to predict the time lapse required for the initial electron population to reach the saturation level. This approach allows estimating the multipactor RF for pulsed signals of any length. As expected, the higher the RF voltage, the larger the electron increment rate.

3.2.5 Experimental results

From the experimental point of view, it was observed that all the detection systems triggered together for pulses longer than 1μs. However, it was observed that only the electrometer and the harmonic system were able to detect the discharges for shorter pulses.

Figure 3.4 shows the good agreement between experimental and theoretical results. It is evident that as the pulse width becomes shorter, the RF multipactor threshold increases. In Fig. 3.3 it was already noticed that higher RF voltage produced a larger electron growth

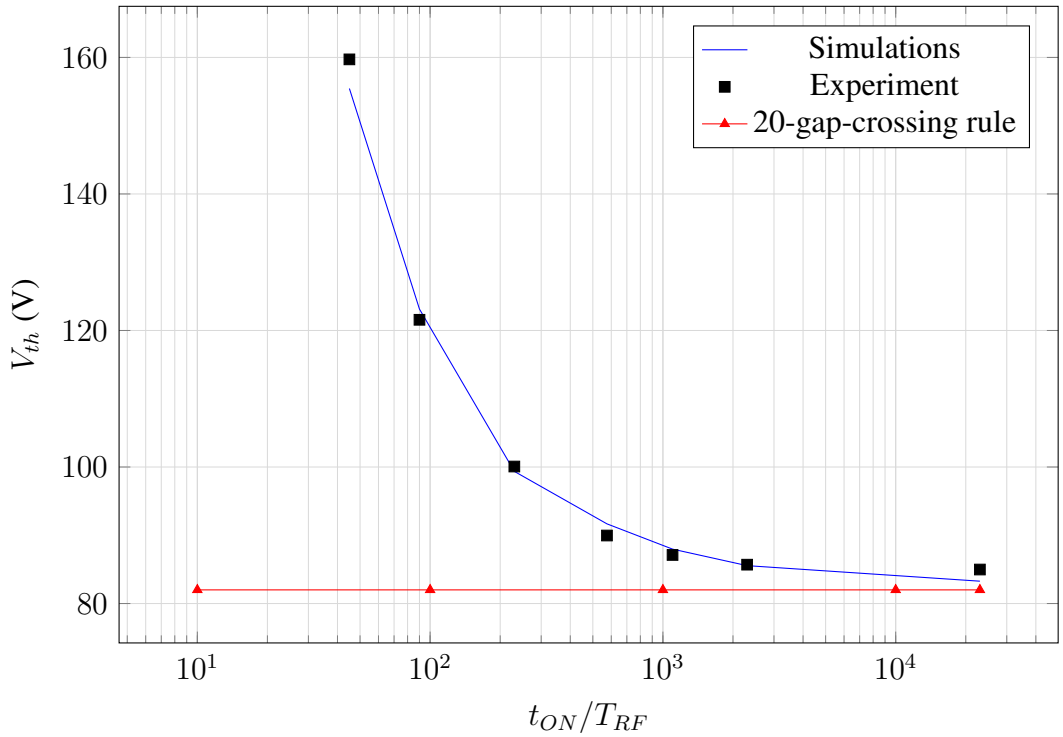

Figure 3.4: Multipactor RF voltage threshold for several RF pulse lengths normalized to the RF period of the carrier signal. Experimental and theoretical results, as well as the "20-gap crossing rule" (10 T_{RF}) predictions, are shown.

rate. Consequently, when the pulse length shortens, a larger electron growth rate is required to reach the same saturation level within the pulse active time.

It is worth mentioning that ultra-short pulses with $t_{on}/T_{RF} = 22.9$ and $t_{on}/T_{RF} = 11.45$ (where $T_{RF} = 1/f = 1/1.145{\cdot}10^9$) were measured but no multipactor discharges were found up to 199 V, which was the maximum RF voltage of the amplifier. Multipactor simulations for the two aforementioned pulses also predict no multipactor discharge up to the tested level.

Measuring multipactor in pulses shorter than $t_{on}/T_{RF} = 11.45$ was not possible since considerable distortion of the RF pulse envelope was observed due to limitations in the RF power amplifier performance.

3.3 Dual carrier signals

3.3.1 Introduction

In this section, the analysis and experimental verification of the effect of dual-carrier signals in the multipactor threshold is carried out.

The dual carrier context provides a good approach to observe what is known as long-term [26, 43] and short-term [48, 45] multipactor discharges.

For the experiments, a set of multicarrier signals has been defined. In all cases, one carrier frequency has been kept constant while increasing the other carrier frequency. This increasing frequency spacing progressively reduces the peak voltage length.

Small spacing leads to a long voltage peak. In these cases, short term multipactor discharge should be expected to happen at the lowest threshold. In contrast, large frequency spacing leads to shorter envelop periods, in which long-term multipactor is more likely to happen.

The following equation represents a dual carrier signal

$$\begin{aligned} s(t) &= a_1 \exp(j(2\pi f_1 t)) + a_2 \exp\left(j(2\pi f_2 t)\right) \\ &= a_1(\exp(j(2\pi f_1 t)) + r \exp j(2\pi(f_1 + df)t) \\ &= a_1(1 + r\exp(j2\pi df t)) \exp(j2\pi f_1) = a_1 m(t) \exp(j2\pi f_1) \end{aligned} \tag{3.2}$$

being a_1, f_1 and a_2, f_2 the amplitude and frequency for carrier 1 and 2, respectively, $r = a_2/a_1$, df is the frequency spacing that relates both carriers $f_2 = f_1 + df$, and $m(t) = 1 + r\exp(j2\pi df t)$ is the modulation produced by the combination of both carriers.

The previous equation mathematically shows that in a dual carrier scenario, there is an RF carrier $\exp(j2\pi f_1)$ which is modulated by the term $1 + r\exp(j2\pi df t)$ as shown in Figs. 3.5 and 3.6.

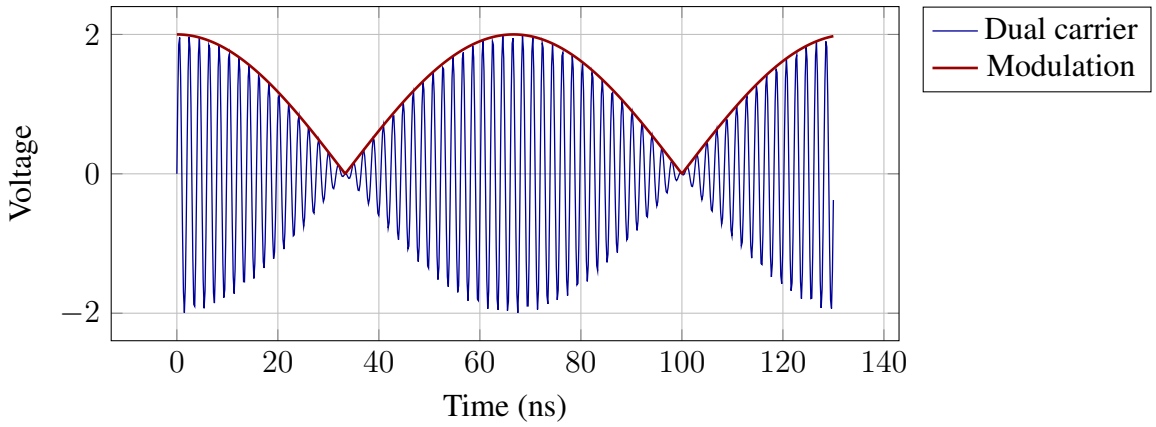

Figure 3.5: Dual carrier signal of $a_1 = a_2 = 1$, $f_1 = 500$ MHz and $f_2 = 530$ MHz, and its envelope signal ($m(t)$).

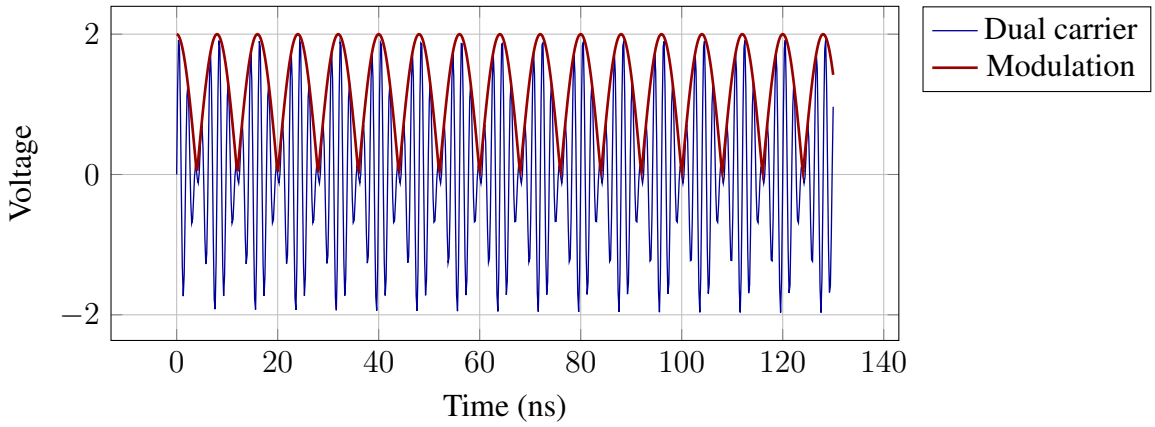

Figure 3.6: Dual carrier signal of $a_1 = a_2 = 1$, $f_1 = 500$ MHz and $f_2 = 750$ MHz, and its envelope signal ($m(t)$).

3.3.2 Devices under test

Two multipactor samples, one broad-band and the other narrow-band, have been analyzed and tested under the same set of dual-carrier signals.

LS4 wide-band coaxial (50 Ω) stripline reference sample. The internal structure of this sample has a quasi parallel-plate geometry, thus providing a very consistent and predictable multipactor breakdown behavior.

LD3 narrow-band coaxial 3-pole combline filter reference sample. The tuner-resonator structure of this sample has a geometry that produces a much higher multipactor threshold than an equivalent parallel-plate gap size due to the combined effect of fringing fields and electron loss in the resonator "well". The tuner-resonator geometry is similar to the high-power GNSS L-band filters.

3.3.3 Testing technique

For these tests, the advanced testing technique described in Appendix A has been used. The schematic of the testbed is shown in Fig. A.1, and one ^{90}Sr radioactive β^- source is used to simulate the free electrons present in space. Pictures from the test bed are shown in Figs. 3.8 and 3.9, where the parameters used for both experiments are included in Table 3.1 and 3.2. The test bed verification and validation follow the procedure defined in [8].

After >24 hours in high vacuum and +80 °C bake-out, the DUT is brought to ambient temperature, and the multipactor tests take place.

The specifications used to define the RF parameters of dual-carrier signals are the next:

- Their frequency spacing must be compatible with the available hardware, whose limit is this parameters to 160 MHz.

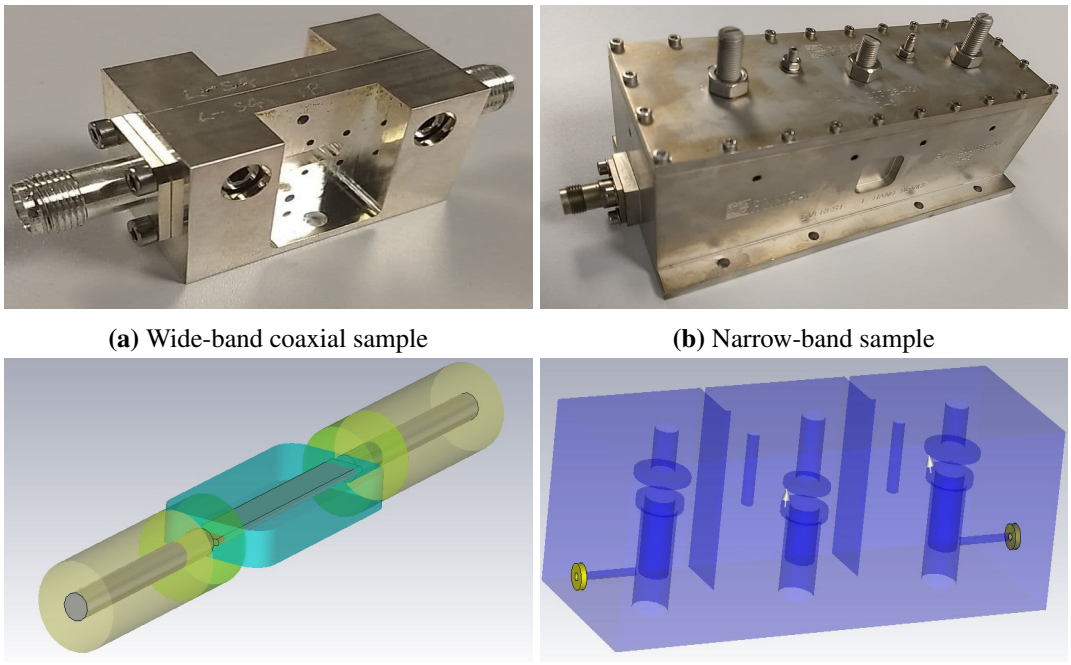

(a) Wide-band coaxial sample

(b) Narrow-band sample

(c) Wide-band coaxial sample (CST model)

(d) Narrow-band sample (CST model)

Figure 3.7: Devices under test for the dual carrier experiments. **(a)** shows a quasi-parallel plate sample and **(c)** its CST model in which the quasi-parallel plate geometry can be seen. **(b)** shows the narrow band combline filter, being the critical gap the center resonator. **(d)** shows the narrow-band sample CST model in which the empty resonators are shown.

- For the LD3 filter at least one case shall have one of the carriers in the device out-of-band region.
- Power ratio between the carriers must be changed.
- The transition from short-term to long-term multipactor must be clearly covered.

In all cases f_1 was set to a constant value and f_2 was defined using a delta frequency Δf so $f_2 = f_1 + \Delta f$. The following delta frequencies were chosen: 1, 3, 5, 10 and 30 MHz. The power relation in linear units were defined as $P_1 = P_2$, $2 \cdot P_1 = P_2$ and $P_1 = 2 \cdot P_2$, being P_1 and P_2 the RF power in Watts for the first and second carrier, respectively.

3.3.4 Simulations results

Two different analysis approaches were used during the simulations. The first set of results was obtained using a commercial PIC simulator included in CST Studio Suite (PIC solver), while the second set of results was obtained using a coarse method simulator, based on the exponential growth for the electron population as detailed in eq. (2.10) [67].

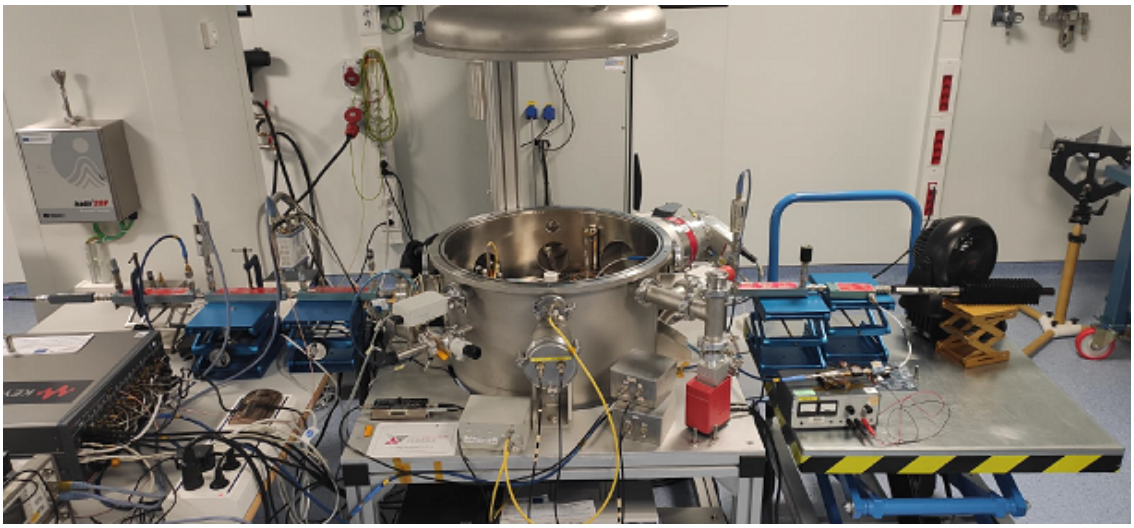

Figure 3.8: Test bed for LS4, general view.

Parameter		Value
Pressure	$<$	$1.5 \cdot 10^{-5}$ mbar
Baking temperature	$=$	+80 °C during 24 h
Test Temperature	$=$	+22 °C
Frequency	$=$	1384 MHz
PRF	$=$	250 Hz
Pulse width	$=$	100 μs
Max. RF power	$=$	450 W_{pk}

Table 3.1: Test parameters used for LS4 experiments

The α factors of the coarse method (see section 2.3.2) have been obtained, for each RF power level, using the same commercial PIC simulator. Following the same procedure, the curves shown in Figs. 3.10 and 3.11 have been obtained for the LS4 and LD3 samples. The electromagnetic model is simulated with a CW excitation at different RF power levels in each case. The commercial simulator gives as output the number of electrons versus time ($N_e(t)$), and from $N_e(t)$, $\alpha(W)$ is obtained by fitting the data to an exponential function (see section 2.3.2).

For the coarse multipactor simulations, which works at one single frequency, the instantaneous frequency [92] of the dual carrier signal is computed using:

$$IF = \frac{P_1 f_1 + P_2 f_2}{P_1 + P_2} \tag{3.3}$$

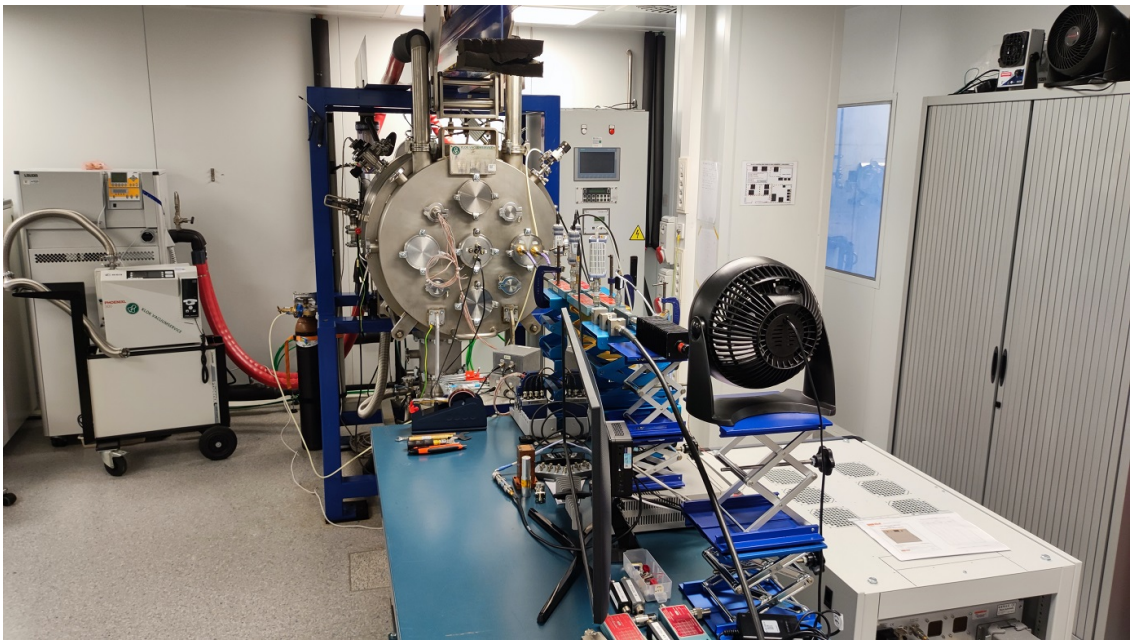

Figure 3.9: Test bed for LD3, general view.

being P_i and f_i the RF power (in Watts) and the frequency (in Hz) for the $i-th$ carrier, respectively.

Simulation results for LS4

Tables 3.3 - 3.5 summarize the simulation results comparing those obtained with the commercial PIC simulator and the coarse multipactor simulation method. The tables also state if the prediction indicates a short-term (ST) or long-term (LT) multipactor discharge.

From the results it is clear that, in general terms, the coarse method is an excellent multipactor threshold predictor for simple structures such as LS4. The threshold difference for all the short-term cases is smaller (or slightly larger) than the RF power measurement uncertainty in an actual experimental validation (typically 0.1 dB). The long-term cases also shows a good agreement, which confirms that this kind of structures with monotonically increasing alpha values (see Fig. 3.10) are good candidates for applying the coarse method.

The increasing multipactor threshold for the short-term results as the bandiwdth increases, is justified from the results obtained in the previous section, see Fig. 3.4. Shorter signal peaks require from larger RF power to reach the saturation level. However, the transition from short-term to long-term discharge shows a decrement in the threshold, as the pulse-to-pulse repetition period is reduced sufficiently for the existing electrons in the critical gap, thus not allowing them to completely disappear. This enables the breakdown buildup at lower RF power than that simulated for the last short-term case (10 MHz).

Parameter		Value
Pressure	$<$	$1.5 \cdot 10^{-5}$ mbar
Baking temperature	$=$	+80 °C during 24 h
Test Temperature	$=$	+22 °C
Frequency	$=$	1574 MHz
PRF	$=$	250 Hz
Pulse width	$=$	100 μs
Max. RF power	$=$	450 W_{pk}

Table 3.2: Test parameters used for LD3 experiments

Δf	IF MHz	f_2 MHz	W_{th} CST	W_{th} Coarse	dB Delta	Long/Short term
1	1400.5	1401	37.81	39.28	-0.17	ST
3	1401.5	1403	40.31	42.86	-0.27	ST
5	1402.5	1405	43.44	45.75	-0.23	ST
10	1405.0	1410	49.69	51.72	-0.17	ST
30	1415.0	1430	52.81	48.08	-0.41	LT

Table 3.3: Summary of the multipactor simulation results for LS4 when ($P_{f_1} = P_{f_2}$) using the CST multicarrier module and the coarse method.

Simulation results for LD3

Tables 3.6 - 3.8 summarize the simulation results comparing those obtained with the commercial PIC simulator CST and the coarse multipactor simulation method. The tables also state if the prediction indicates a short-term or long-term multipactor discharge.

This device shows a particular behavior in the α graph which produces interesting results (see Fig. 3.11). Multipactor threshold for short-term cases (1 to 3 MHz) show similar results for both analysis methods. Although matching is not excellent as in LS4, they are still reasonably good considering the complexity in LD3 geometry. For the long-term case (30 MHz) results are still within 1 dB of difference, which is acceptable.

Multipactor threshold change considerably from short-term to long-term cases. The reason behind this can be found in the graph for the α, values which now have a negative area from 50 W to 140 W. This effect is due to the device geometry which, by having empty resonators (similar to a well), do show a net secondary electrons suppression in this RF power range. When the RF power is within this large range, it is difficult for the electron cloud to fully develop. As a consequence, the short-term threshold is found in the 20-30 W, right from the moment the α values turn positive. However, in this device RF power must go up to 150 W to reach a long-term discharge.

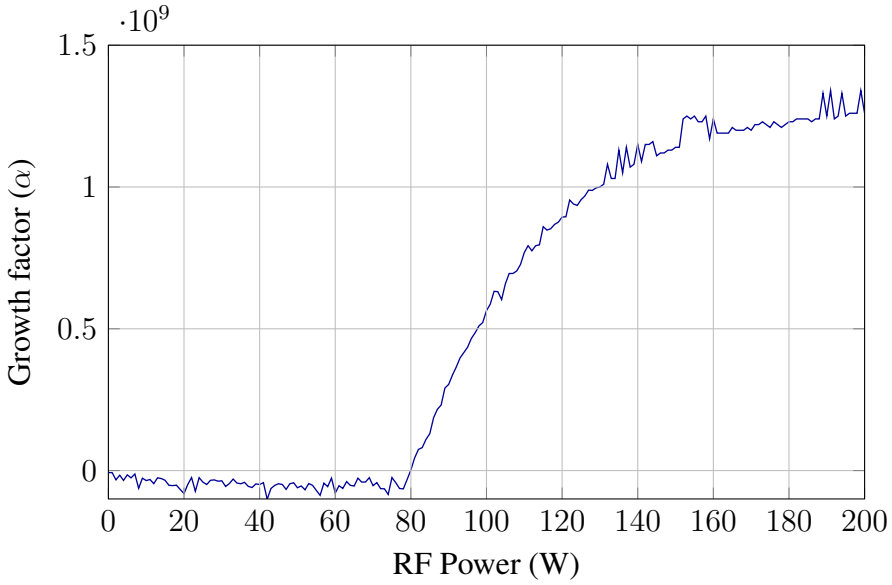

Figure 3.10: Alpha growth factor for the LS4 sample. Obtained using the commercial multipactor PIC from CST. Notice that it follows an almost monotonic increment trend once the first positive value is recorded.

Some other geometries showing a valley for the α such as the one in Fig. 3.11, cold show a long-term discharge which do not require from reaching the other end of the valley (i.e., in this case a value of 145 W). However, for this particular structure, simulations show that reaching these RF power levels is the only way to record a long-term multipactor discharge.

The results for this structure also show that both simulation methods do not record the transition from short-term to long-term multipactor for the same frequency spacing. As a consequence, the result divergence is very large in such cases.

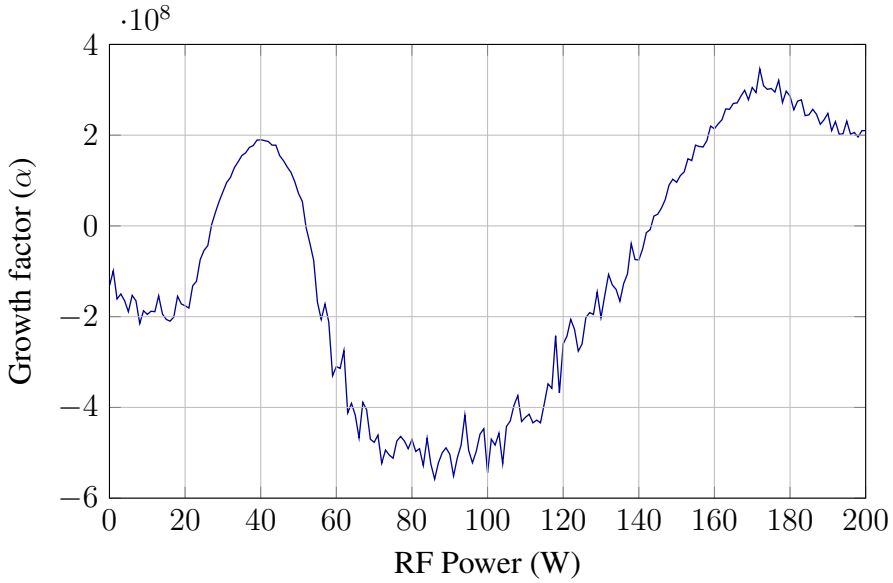

Figure 3.11: Alpha growth factor for the LD3 sample. Obtained using the commercial CST simulator for a sweep of CW signals. Notice the band-gap with negative α values from 50 to 145 W.

Δf	IF MHz	f_2 MHz	W_{th} CST	W_{th} Coarse	dB Delta	Long/Short term
1	1400.58	1401	37.81	38.75	+0.11	ST
3	1401.76	1403	41.51	41.36	-0.02	ST
5	1402.92	1405	44.69	43.20	+0.15	ST
10	1405.85	1410	49.69	47.78	-0.17	ST
30	1417.57	1430	54.37	50.17	-0.35	LT

Table 3.4: Summary of the multipactor simulation results for LS4 when ($P_{f_1}/P_{f_2} = -3\ dB$) using the CST multicarrier module and the coarse method.

Δf	IF MHz	f_2 MHz	W_{th} CST	W_{th} Coarse	dB Delta	Long/Short term
1	1400.41	1401	37.81	38.75	+0.11	ST
3	1401.24	1403	40.94	41.16	+0.2	ST
5	1402.07	1405	44.06	43.23	-0.09	ST
10	1404..14	1410	49.69	47.87	-0.16	ST
30	1412.42	1430	53.44	49.50	-0.33	LT

Table 3.5: Summary of the multipactor simulation results for LS4 when ($P_{f_1}/P_{f_2} = +3\ dB$) using the CST multicarrier module and the coarse method.

Δf	IF MHz	f_2 MHz	W_{th} CST	W_{th} Coarse	dB Delta	Long/Short term
1	1400.5	1401	22.26	22.32	-0.54	ST
3	1401.5	1403	27.42	24.35	0.90	ST
5	1402.5	1405	147.17	27.32	7.3	LT/ST
10	1405.0	1410	154.68	–	–	LT/–
30	1415.0	1430	181.85	143	0.93	LT

Table 3.6: Summary of the multipactor simulation results for LD3 when ($P_1 = P_2$) using the CST multicarrier module and the coarse method.

Δf	IF MHz	f_2 MHz	W_{th} CST	W_{th} Coarse	dB Delta	Long/Short term
1	1400.58	1401	22.73	20.45	-0.46	ST
3	1401.76	1403	27.42	23.06	-0.75	ST
5	1402.92	1405	141.56	27.43	-7 to -13	LT/ST
10	1405.85	1410	150.93	500.7	5.20	LT
30	1417.57	1430	185.62	146.6	-1.02	LT

Table 3.7: Summary of the multipactor simulation results for LD3 when ($P_1/P_2 = -3\ dB$) using the CST multicarrier module and the coarse method.

Δf	IF MHz	f_2 MHz	W_{th} CST	W_{th} Coarse	dB Delta	Long/Short term
1	1400.41	1401	22.73	20.56	-0.44	ST
3	1401.24	1403	27.42	23.06	-0.80	ST
5	1402.07	1405	149.06	27.32	-7 to -37	LT/ST
10	1404..14	1410	152.81	3413	13.49	LT
30	1412.42	1430	178.12	146.9	-0.84	LT

Table 3.8: Summary of the multipactor simulation results for LD3 when ($P_1/P_2 = +3\ dB$) using the CST multicarrier module and the coarse method.

3.3.5 Experimental results

This section shows the experimental results obtained to validate the simulations carried out in dual-carrier scenarios. The test sequence for each device is the same and comprises the following steps:

1. Set the relative RF power per carrier
2. Initial Control test using a pulsed CW at f_1
3. Dual carrier tests for Δf = 1, 3 and 5 MHz
4. Intermediate control test using a pulsed CW at f_1
5. Dual carrier tests for Δf = 10, 30 and 34 MHz
6. Final control test using a pulsed CW at f_1

For each power ratio three control tests were conducted. The purpose of these tests was to verify that the SEY properties did not change along the test sequence because of surface conditioning. This verification allowed the execution of all the tests without breaking breaking the vacuum between tests. The pass criteria for this assumption was that the initial, intermediate and final control tests recorded the very similar multipactor threshold values.

Table 3.9 summarizes all the results and thresholds values obtained for all the different cases of the LS4 sample, including comparison between simulated and experimental data. Moreover, Table 3.10 summarizes all the results and threshold values obtained for all the different cases of the LD3 sample.

Experimental results for LS4

Results for the wide-band LS4 device have shown a divergence between simulation and experiments absolute threshold levels, although the threshold trend with Δf is similar.

The control tests using pulsed CW confirmed that for each scenario: $P_1 = P_2$, $P_1 > P_2$ and $P_1 < P_2$, the sample did not showed signs for material conditioning. However, *1*) a significant error difference between the simulated and testing thresholds has been recorded and, *2*) a progressive decrement in the pulsed CW threshold as the number of tests carried out without breaking the vacuum increased.

The first point is to explain the large thresholds difference between simulation and testing as, for such a simple structure, the error between simulation and testing should not be small.

From the simulation side, the project file was verified to detect potential configuration errors. With no error being found. Then, from the experimental side, a different multipactor sample showed that the measurement error was within the standard tolerance for the multipactor test bed (< 0.2 dB). For these reasons, the error source was assumed to be an incorrect SEY data.

For this activity the device SEY was characterized in Val Space Consortium Space Materials Laboratory. The actual device was used for this purpose as no SEY sample had been manufactured. However, the technician in charge of the measurements warned that the surfaces were smaller than the electron gun spot, which is not optimal as characterizing the SEY from small surface may produce unreliable SEY data.

Next point to tackle is the daily drop in the threshold for the first control pulse CW test. This test recorded a reduction in the threshold from day to day. This is an atypical behavior, as a longer time in vacuum and a larger number of accumulated multipactor discharges should produce none or a net increment in the multipactor threshold. Lack of funding for this activity prevent further investigations in this respect.

However, since the daily results for the pulsed CW test was good, the general trend in the multipactor threshold can be considered correct. For each RF power ratio, the experimental results show a monotonic increment in the multipactor threshold, what is in line with the simulations results.

Focusing now in the change between short and long-term discharge modes, this samples showed not to be a good device for this purpose. When using the simulator it is possible to view the electron population trend at a nano-scale ratio. This allows to verify if the multipactor happens in the short-term or now. However, detection systems used are not able to give this granularity and short-term discharges may be either continue and be confused with long-term or, if they stop, not be detected.

Additionally, from the simulation results shown in tables 3.3 to 3.5, predictions indicated small threshold increments when switching from short to long-term multipactor modes. So, it is not technically feasible to stated if the discharges were from short-term origin or not.

Experimental results for LD3

Experimental results for LD3 show good agreement with simulation for long-term results, but short-term results were either not happening or not detected.

The control tests using pulsed CW confirmed that for each scenario: $P_1 = P_2$, $P_1 > P_2$ and $P_1 < P_2$, the sample did not showed signs for material conditioning. However, a constant difference between simulation and testing was found.

In this case, the area of interest for the SEY measurement was larger in one of the surfaces, so SEY characterization was more accurate, thus leading to an very good agreement in all the long-term cases.

This device did provide in simulation a good set of results to validate by testing the presence of the short and long-term multipactor discharges. Short-term results, including the control tests with pulsed CW, showed a very low threshold. Whereas long-term results were found to have much larger threshold levels.

In general terms, testing failed to match the short-term multipactor threshold. This is clearly shown in table 3.10, as in no case a threshold close to 20 W was recorded. Even the control pulsed CW cases diverge between simulation and testing. However, long-term discharges have shown excellent agreement for all the available cases.

Test nr.	Δf MHz	$P_1 = P_2$ **Exp.**	$P_1 = P_2$ **Sim.**	$P_1 > P_2$ **Exp.**	$P_1 > P_2$ **Sim.**	$P_1 < P_2$ **Exp.**	$P_1 < P_2$ **Sim.**
1	CW	104	73.1	96	73.1	89	73.1
2	1	115	37.8	134	37.8	99	37.8
3	3	114	40.3	132	40.9	104	41.5
4	5	123	43.4	131	44.1	104	44.7
5	CW	103	73.1	93	73.1	80	73.1
6	10	130	49.7	130	49.7	110	49.7
7	30	131	52.8	132	53.4	111	54.4
8	34	137	53.4	154	53.4	119	54.4
9	CW	100	73.1	93	73.1	90	73.1

Table 3.9: Comparison of the experimental and simulated multipactor thresholds in Watts for LS4. Control tests 1, 5 and 9 are done with a single carrier CW to verify that the SEY conditioning is not playing a major role in the threshold variations. Results record a large absolute error between simulation and testing, although threshold trend is similar. From the experimental detection systems it was not possible to state if the discharge was short or long-term discharge.

Without considering the CW cases, it would be a valid assumption that the current state-of-the-art multipactor test bed is not capable of recording short-term discharge. However, divergences in CW cases imply that the simulators are not considering some physical effect actually happening in the device. Due to the lack of funding and particularities of this device which are not typically found in combline filters (resonators with void inside) the reasons for this very low short-term multipactor threshold are not known.

Test nr.	Δf MHz	$P_1 = P_2$ Exp.	$P_1 = P_2$ Sim.		$P_1 > P_2$ Exp.	$P_1 > P_2$ Sim.		$P_1 < P_2$ Exp.	$P_1 < P_2$ Sim.	
1	CW	90	39.6	ST	90	39.6	ST	90	39.6	ST
2	1	140	22.3	ST	120-130	22.7	ST	120-130	22.7	ST
3	3	140	27.4	ST	130	27.4	ST	140	22.4	ST
4	5	140-150	147.2	LT	130	149.1	LT	150	149.1	LT
5	CW	100	39.6	ST	90	39.6	LT	90	39.6	ST
6	10	140-160	154.7	LT	150-160	152.8	LT	160	150.9	LT
7	30	180-190	181.9	LT	160-170	178.1	LT	NA	185.6	LT
8	34	200-210	200.6	LT	180	193.1	LT	200-220	189.37	LT
9	CW	100	39.6	ST	90	39.6	ST	90	39.6	ST

Table 3.10: Comparison of the experimental and simulated multipactor thresholds in Watts for LD3. Control tests 1, 5 and 9 are done with a single carrier CW to verify that the SEY conditioning is not playing a major role in the threshold variations. Short-term (ST) and long-term (LT) marks apply for the simulation results. From the experimental detection systems it was not possible to state if the discharge was ST or LT. Experimental thresholds suggest that all results were in the power range of LT discharges.

3.4 Conclusions

This chapter has firstly discussed the impact of short pulses in the multipactor threshold values. It was found that multipactor RF breakdown is a phenomenon which actually builds up in the time range of tens of thousands of nanoseconds. Consequently, when the RF field is active only for such periods, the multipactor threshold for these signals changes.

Experimental results for the short-pulsed signals have shown excellent correlation with simulations, with errors in the multipactor threshold no larger than 3%. As expected, a shorter time with the RF field active ($t_{on}/T_{RF} = 45$) requires larger growth rates to achieve the saturation level, which experimentally implies that the detection systems show signs of multipactor. In contrast, for longer times with the RF field active, e.g. results from $t_{on}/T_{RF} = 1100$, they converge to the CW results with a difference smaller than 3%. These results have proven that the basic concept behind the coarse multipactor simulation, the exponential growth approximation, is valid and can be extended to other scenarios. This has been achieved not only with simple CW simulations bu by considering envelope changing schemes such as de dual carrier cases shown in section 3.3.

Regarding the dual-carrier signal research, it has provided an excellent framework for the validation of the coarse simulation method and the new testing techniques. This method, which approximates the multipactor simulation by a growing and decaying exponential, has provided reliable simulation results. The main benefit ot his method is that, once the α value for a particular device are obtained, the multipactor threshold for any signal of any length can be found in a few seconds.

For the simple sample (LS4) simulation results do not differ by more than 0.35 dB when comparing a commercial simulator with this method. For the complex sample (LD3), in which the α values do not show a monotonical increment, results are within 1 dB of error for short-term and fully developed long-term multipactor events. However, transition form short-term to long-term is not correctly predicted by the coarse method, and errors in this transition regions are very large (> 7 dB).

The source of this large error comes for two aspects: the fact that LS4 showed a very large threshold difference between short and long-term multipactor modes and, the used frequency spacing. These Δf had a granularity that, for $P_1/P_2 = -3dB$ considered cases very close to the mode transition which was located between 5 and 10 MHz, whereas in the other cases the transition happened from 10 to 30 MHz, giving more margin both simulators to converge to closer results.

When focusing in the experimental verification activity, results differ by sample. For LS4 sample, the obtained thresholds for dual-tone cases follow a similar increasing trend, despite the discrepancy on the absolute power value. However, the high threshold obtained for CW signals has been consistent along the campaign, although it differs considerably from the analysis results. A clear reason for this behavior has not been identified.

For LD3 sample the situation is different. This sample has been tested after measuring the SEY values, and the threshold for the long-term multipactor discharges do match the predicted values. However, short-term results do not match prediction results, as it seems that

either they cannot be measured by the implemented detection methods or they do not happen during the experiment. Results for short-term cases show a similar multipactor threshold as the ones predicted for the long-term discharges.

In general terms, during the dual carrier signals investigations, the set up has proved excellent to reduce the device conditioning, thus providing consistent threshold values along the test succession. The novel testing capabilities allow running all the tests for a single device in less than 5 hours, in contrast to the three, or even more days, required using the standardized test procedure as stated in [8]. These benefits come without loss of accuracy in the estimation of the multipactor threshold results.

Finally, this chapter has also shown that the "20-gap crossing rule" is not always a good predictor for the multipactor threshold. It would be wise to think about the coarse simulation method as a replacement of such rule when quick threshold estimations are required and the signals being considered has a change rate get close to this 20-gap crossing period.

3.5 List of own publications and projects

The techniques presented in this Chapter have been published in several peer-review journals and conferences. A list of publications and projects related to this research is shown below.

3.5.1 Journal papers

- D. González, **O. Monerris**, M.E. Díaz, B. Gimeno, V.E. Boria and D. Raboso, "Experimental analysis of the multipactor effect with RF pulsed signals", in IEEE Electron Device Letters, vol. 36, no. 10, pp. 1085-1087, Oct. 2015, doi: 10.1109/LED.2015.2468068.

- **O. Monerris**, R. Cervera, M. Rodríguez, E. Diaz, C. Alcaide, J. Petit, V.E. Boria, B. Gimeno and D. Raboso, "High power RF discharge detection rechnique based on the in-phase and quadrature signals", in IEEE Transactions on Microwave Theory and Techniques, vol. 69, no. 12, pp. 5429-5438, Dec. 2021, doi: 10.1109/TMTT.2021.3120657.

- P. González, C. Alcaide, R. Cervera, M. Rodríguez, **O. Monerris**, J. Petit, A. Rodríguez, A. Vidal, J. Vague, J.V. Morro and P. Soto, "Multipactor threshold estimation techniques based on circuit models, electromagnetic fields, and particle simulators", in IEEE Journal of Microwaves, vol. 2, no. 1, pp. 57-77, Jan. 2022, doi: 10.1109/JMW.2021.3132284.

3.5.2 Conference papers

- **O. Monerris**, D. Argilés, V.E. Boria, B. Gimeno, D. Raboso and P. Angeletti, "Multipactor testing and emerging qualification protocols", in 46th European Microwave Conference (EuMC), Madrid, Spain, September 2016, pp. 222-225, doi: 10.1109/EuMC.2016.7824318.

- V.E. Boria, L. Nuño, **O. Monerris**, D. Smacchia, D. Argilés and D. Raboso, "Experimental measurements and diagnosis of radio-frequency space high power and electromagnetic compatibility effects", in ESA Workshop on Aerospace EMC (Aerospace EMC), Valencia, Spain, May 2016, pp. 1-6, doi: 10.1109/AeroEMC.2016.7504600.

- D. Gonzalez, A. M. Pérez, **O. Monerris**, S. Anza, J. Vague, B. Gimeno, V.E. Boria, Á. Gomez, A. Vegas, E. Díaz, D. Raboso and A. Coves, "Recent advances of the multipactor RF breakdown in RF satellite microwave passive devices", Progress In Electromagnetic Research Symposium (PIERS), Shanghai, China, August 2016

- **O. Monerris**, D. Raboso, V.E. Boria, B. Gimeno and David Argilés, "Nuevos métdos de ensayo del efecto multipactor", In XXXI Simposium de la Unión Científica Internacional de Radio (URSI), Madrid, Spain, September 2016.

- D. González, **O. Monerris**, B. Gimeno, V.E. Boria and D. Raboso "Estudio del efecto multipactor en líneas de transmisión coaxial con señales pulsadas", In XXXI Simposium de la Unión Científica Internacional de Radio (URSI), Madrid, Spain, September 2016.

- D. González, **O. Monerris**, M.E. Díaz, B. Gimeno, V.E. Boria, D. Raboso and Á. Coves, "Analysis of the multipactor effect with RF pulsed signals", In XII Iberian Meeting on Computational Electromagnetics (EIEC), Coimbra, Portugal, May 2018

3.5.3 Projects

- **Title** Development and validation of an enhanced multipactor prediction method with multicarrier digital modulated signals

  Reference VSC2017/ESA/RFQ1300042382

  Holder Val Space Consortium

  Number of members in the research team 3

  Issuer European Space Agency

Chapter 4

Multipactor testing of digital modulations

4.1 Summary

This chapter covers the investigations carried out in the field of the RF multipactor breakdown with digitally modulated signals. Several digital modulation schemes used in satellite communications have been considered with increasing modulation complexity, understanding complexity as the number of symbols and energy levels.

Because the amount of data to transmit from satellites has dramatically increased in recent years, and due to the saturation of the electromagnetic spectrum. Higher peak power levels and more complex modulations are used in order to squeeze as much data as possible in each Hz [11, 10]. These modulations use several energy levels and very large bandwidths.

Previous works in the field of multipactor with modulated signals are scarce and with a limited scope. Either they constrain to analysis and simulation only [47, 93] or consider very little experimental cases [94]. In this thesis, the effect of digitally modulated signals in the multipactor threshold is considered both, in simulation and testing, covering all the modulations currently used in satellite communications.

When considering basic digital modulation the Amplitude Shift Keying (ASK) is studied from an analog point of view in section 3.2. This modulation scheme uses a train of RF pulses to transmit the information and, for that reason, it is better understood from the analogical perspective. For that reason, it is not considered in this chapter.

This chapter investigates in detail the most commonly used modulations schemes: BPSK, QPSK, 16-QAM, 16-ASK and 32-ASK.

The different activities carried out in this chapter have focused on assessing how the following parameters contribute to modifying the multipactor threshold: *1*) number of energy levels, *2*) modulation order (M), and *3*) transmitted symbol sequence.

The chapter contents are structured as follows:

Section 4.2 contains an introduction to the key concepts in the field of digital communica-

tions. These concepts are not common in the field of RF multipactor breakdown, but they are required to understand the reasons behind the investigations described in the following sections.

Section 4.3.1 describes the multipactor samples used for these investigations.

Section 4.3.2 presents the multipactor test beds and testing techniques that have been used in order to obtain the experimental results.

Section 4.4.1 studies the effect of the binary phase-shift keying (BPSK) modulation in the multipactor threshold level. The results include a detailed analysis of the discharge behavior using ideal rectangular shaping filters.

Section 4.4.2 focuses on the quadrature phase-shift keying (QPSK), as the first step to increase the constellation complexity, that is achieved by increasing the number of symbols with the same energy.

Section 4.4.3 completes the research in this field by considering all the modulations found in the second standard for digital video broadcasting by satellite (DVB-S2) [95], which are: 8 symbols amplitude phase-shift keying (8-APSK), quadrature amplitude of 16 symbols (16-QAM), and 32 symbols amplitude and phase-shift keying (32-APSK).

Section 4.5 discusses about the so-called "20-gap crossing rule". Its predictions are compared to the ones obtained using other analysis tools for the digital modulations considered in this chapter.

4.2 Introduction to digital communication systems

Digital communications are a de-facto standard in almost all data transmissions systems, either wired or wireless. From optical fiber links to satellite data transmissions, they all use one or another kind of digital modulation scheme.

In general terms, the objective of new data transmissions methods pursues improving transmission efficiency, which is achieved by:

- Reducing service cost with minimum energy per bit.
- Enabling a faster data transfer rate than its predecessors.
- Decreasing the bit error rate (BER) due to simple decoder implementation.
- Increasing the spectral density.

The data efficiency measured in bits per Hertz must be maximized in all communication system, even more in wireless transmissions. For this purpose, two techniques are employed

[96]: increment of the bits/Hz rate, and use of multi-beam or orthogonal transmission in order to re-use the same spectrum band as many times as possible.

An increment in the spectral efficiency (bits/Hz) can be achieved by using high-order modulations. However, there is a hard limit that is not possible to exceed. The following eq. (4.1), known as Shannon law determines the maximum capacity of a given channel for a given signal to noise ratio and bandwidth.

$$C = B + \log_2\left(1 + \frac{S}{N}\right) \tag{4.1}$$

being C the channel capacity measured in bits per second, B the bandwidth in Hertz, and the signal S to noise N ratio (SNR) represented in linear units.

Other techniques to achieve capacities closer to the ones determined by (4.1), such as the orthogonal frequency division multiplexing [97], are not used in satellite communications due to the high peak to average power ratio (PAPR). These modulation schemes require from extremely linear amplifiers which are either very inefficient in terms of power consumption or which lack the RF power output level required in space applications.

In Fig. 4.1, all the digital modulation schemes used in satellite communications and considered in this thesis are shown. The red dots represent the symbol position within the constellation, and the black circles indicate the different symbol energy.

Given an M-APSK modulation, although circular ones are the most common (see Fig. 4.1), several constellation shapes can implement each modulation order [98]. In general terms, for any multilevel modulation, increasing the number of energy levels (rings) decreases the bit error rate at the expenses of having a higher PAPR.

In long-distance communications, in particular satellite communications [99], high order modulations are not feasible. This limitation is due to their lower SNR compared to short-range systems. Recent digital communication satellites implement adaptative coding and modulation (ACM). This mechanism dynamically changes the data coding (redundancy bits) or the modulation type depending on the receiver SNR. This technique is known as modulation and coding (MODCON) and maximizes the data throughput while ensuring the required link availability.

For extreme cases, such as deep space research, signal-to-noise ratios are even lower [100, 101]. Even using large phase arrays antenna, signal-to-noise ratios are typically close to, or even less than 0 dB. In these cases, simple modulations are used, and high redundancy coding, is also required.

The most common modulations, and some examples of their applications in space communications, can be found below [102, 12]:

BPSK Telemetry and control, deep space missions (Voyager 2, Mars exploration), ISDB-S3.

QPSK Telemetry and control, telephone services (Iridium), DVB-S2, ISDB-S3, One Web, SpaceX, or Telesat.

8-PSK Data transmission: DVB-S2, ISDB-S3, Iridium, One Web, SpaceX, Telesat

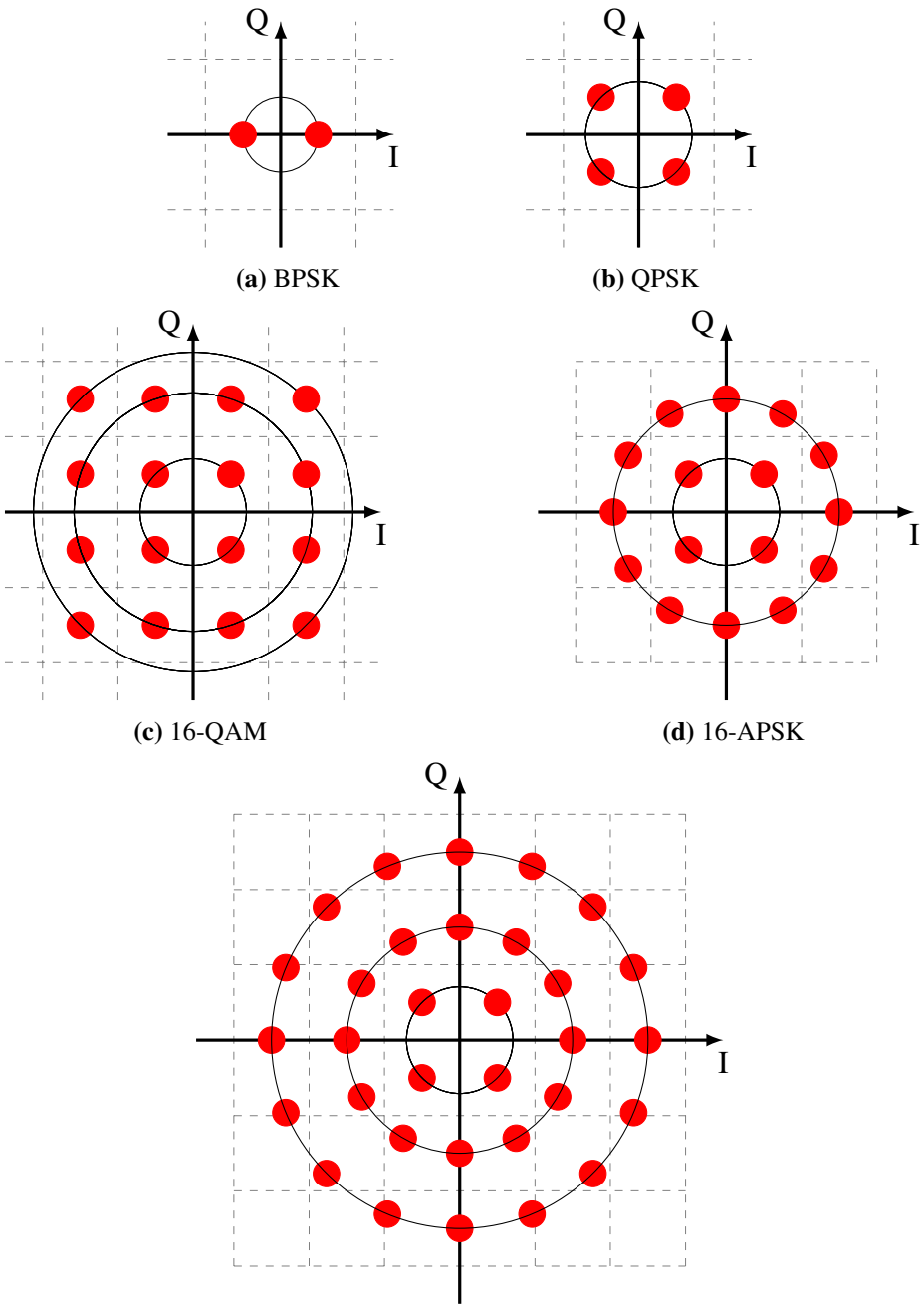

(a) BPSK **(b)** QPSK

(c) 16-QAM **(d)** 16-APSK

(e) 32-APSK

Figure 4.1: Constellation for the digital modulation schemes considered in this work: BPSK, QPSK, 16-QAM, 16-APSK and 32-APSK.

16-APSK Data transmission: DVB-S2, ISDB-S3, Iridium, One Web, SpaceX, Telesat

32-APSK Data transmission: DVB-S2, ISDB-S3, Iridium, One Web, SpaceX, Telesat

64/128/256-APSK Data transmission: DVB-S2X

16-QAM Data transmission (experimental): DVB-S2, SpaceX

32-QAM and 64-QAM Data transmission (experimental): SpaceX

The basic digital transmission chain is described in [103] and a simplified block diagram for a single channel digital communication system is shown in Fig. 4.2. From a multipactor perspective, the modulator and the pulse shaping filter are the most relevant parts, as they are fundamental elements that impact the RF field shape. Other blocks, such as the arbitrary baseband generator (ARB), the up-conversion, and amplification, also impact the signal shape. However, their contribution comes from the fact that they are tangible elements that present non-linearity and, consequently, change the RF field shape.

In general terms, from the RF multipactor breakdown point of view, the data source and encoding are not relevant, as they do not determine the symbol position. For that reason, the results are always referred to the symbols being used and not the bits.

The next element which impacts the electric field is the pulse shaping filter. Although there are several options, the square root raised cosine (SRRC) filter is the most common, and provides a mechanism to reduce the PAPR requirements in the transmitter. It also provides a good inter-symbol interference (ISI) performance [103] when combined with another SRRC pulse shaping in the receiver.

when the transmission channel can be measured, the receiver may estimate the frequency response by applying such filtering, so that the composition of the transmission filter ($h_{tx} = h_{SRRC}$), plus the combination of the channel frequency response (h_{ch}) and receiver (h_{rx}) one, is such of the cosine filter.

$$h_t(t) = h_{tx}(t) * h_{ch}(t) * h_{rx}(t) = h_{RC}(t) \tag{4.2}$$

To conclude this section, the equation for the impulse response of an SRRC filter is given next.

$$h_{SRRC}(t) = \begin{cases} \dfrac{1}{T_s}\left(1+\beta(\dfrac{4}{\pi}-1)\right), & t=0 \\ \dfrac{\beta}{T_s\sqrt{2}}\left[\left(1+\dfrac{2}{\pi}\right)\sin\left(\dfrac{\pi}{4\beta}\right)+\left(1-\dfrac{2}{\pi}\right)\cos\left(\dfrac{\pi}{4\beta}\right)\right], & t=\pm\dfrac{T_s}{4\beta} \\ \dfrac{1}{T_s}\dfrac{\sin\left[\pi\dfrac{t}{T_s}(1-\beta)\right]+4\beta\dfrac{t}{T_s}\cos\left[\pi\dfrac{t}{T_s}(1+\beta)\right]}{\pi\dfrac{t}{T_s}\left[1-\left(4\beta\dfrac{t}{T_s}\right)^2\right]}, & \text{otherwise} \end{cases} \tag{4.3}$$

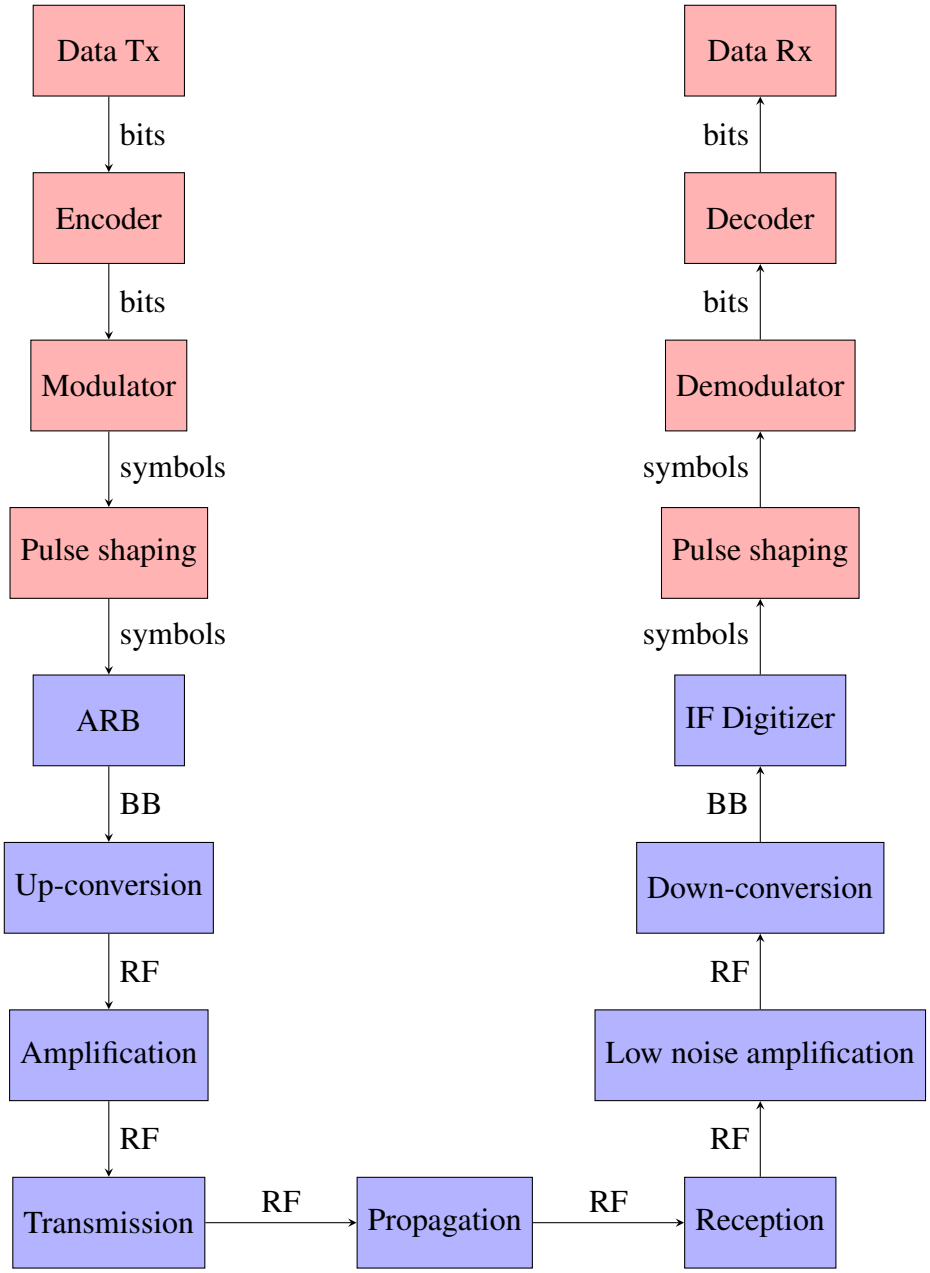

Figure 4.2: End to end block diagram for a digital communication system. The transition between the virtual domain (bits, symbols) to the physical domain (electric field) is carried out in the arbitrary baseband generator (ARB) module. The real signal is converted back into the virtual domain in the IF digitizer, at the receiver end.

being T_s the symbol duration and β the roll-off factor, a number from 0 to 1 that controls the sharpness of the raise and fall. For a value of 0 a brick filter (time domain) is obtained.

4.3 Multipactor samples and testing technique

4.3.1 Multipactor samples

For this experiments a pure coaxial samples have been used. The reason for this selection comes from the constraints imposed by the custom made multipactor simulator, which for this activity is the one developed in [39]. The employed test samples operate in P- and L-bands. Both have coaxial connectors, and are manufactured with a constant outer radius and changing inner radius, as shown in Fig. 4.3. Their frequency response is broadband, with a group delay identical to that of a coaxial transmission line at all frequencies.

Figure 4.3: Example of a multipactor sample used for the multipactor analysis and experiments with digital modulated signals.

BPSK For the BPSK multipactor investigations, a coaxial sample with a critical gap in which the inner and outer radius of $a = 1.515$ mm and $b = 3.490$ mm, respectively, has been employed. Both conductors are made of copper, and the critical gap is $d = b - a = 1.975$ mm. Input and output connectors are TNC (male).

QPSK and high order modulations For these experiments, a coaxial sample with a critical gap in which the inner and outer radius of $a = 1.238$ mm and $b = 2.850$ mm, respectively, has been employed. Both conductors are made of copper, and the critical gap is $d = b - a = 1.612$ mm. Input and output connectors are TNC (female).

4.3.2 Testing technique

Two test beds have been prepared for the experimental verification of the predicted multipactor threshold values. These test beds share the same layout, shown in Fig. 4.4. The signal generation has been carried out using one Keysight PSG E8267D, combined with a M9330A, a wideband ARB manufactured by Keysight. This device can generate in-phase and quadrature (IQ) signals at a rate of 1.25 GSps (Giga-Samples per second).

Concerning the multipactor detection, the standard methods were employed since, at the time these experiments were run, the novel detection technique detailed in chapter 7 was not yet available.

The pulse by pulse testing method, like the one used in section 3.3, had not been developed at the time either. Consequently, the measurement campaigns took much longer than they would have with the new testing technique. This extra test time is due to surface conditioning, which forced the vacuum to be broken after two or three tests.

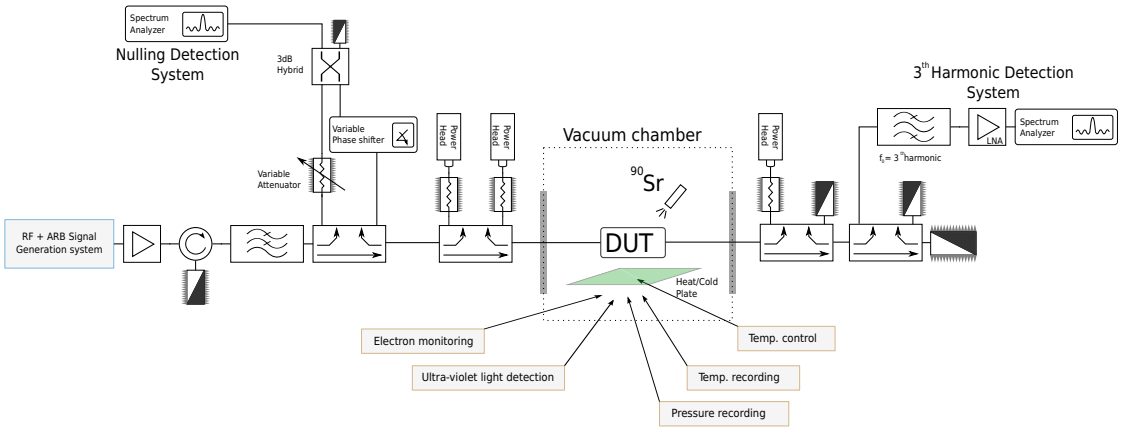

Figure 4.4: Diagram of the multipactor test beds used for the experimental validations with digital modulated signals.

4.4 Simulation and experimental results

4.4.1 Binary phase-shift keying

This section presents the impact of a simple digital modulation in the multipactor effect build-up and, consequently, with the corresponding threshold level. For that reason, the binary phase-shift keying (BPSK) modulation scheme (see Fig. 4.1a) has been considered.

This research focuses on the impact of the phase changes in the multipactor electron avalanche growth, due to the perturbation of the resonant electron trajectories. Out of all the possible cases, this initial research focused on the worst case for the BPSK modulation: a transmission sequence –101010 . . .–, implying a phase jump of 180° in each symbol transition.

A key parameter to analyze the change of the multipactor threshold voltage compared to the non-modulated case is the ratio between the symbol duration T_{sym} and the RF carrier period $T = 1/f$, which is defined as

$$\xi = \frac{T_{sym}}{T_{RF}} \tag{4.4}$$

Results shown in Fig. 4.5 point out that the symbol alternation does produce a variation in the multipactor threshold value. The change is less than the one observed for the short pulses even for low t_{ON}/T_{RF} values as, in this case, the RF never goes to zero. The results also show good agreement between the analysis and the experiment.

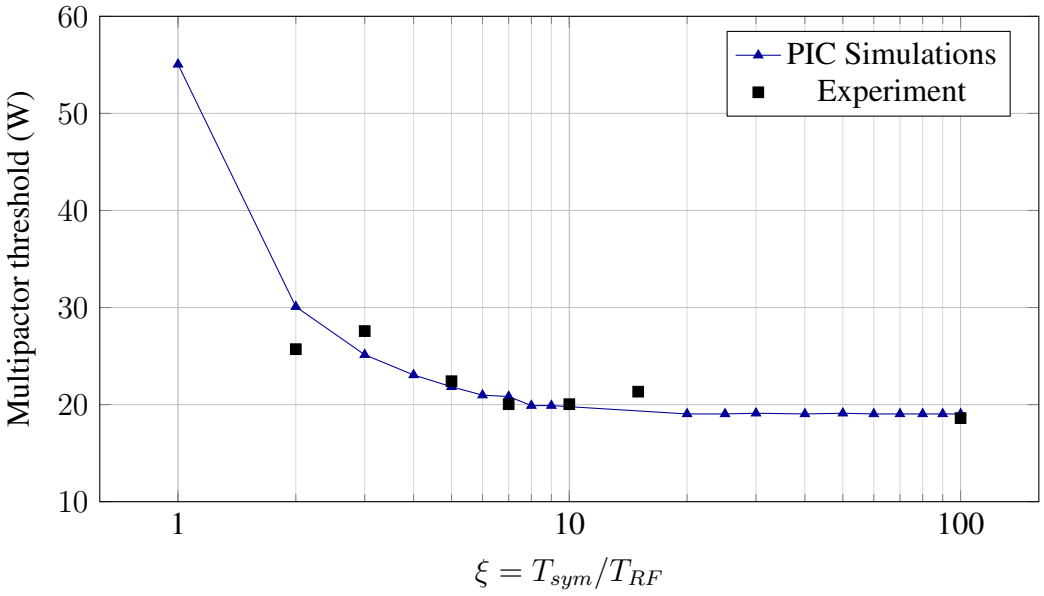

Figure 4.5: Simulation and experimental results for the multipactor threshold power as a function of the ξ parameter at $f = 435$ MHz. Signal modulated with a BPSK using rectangular filter and the sequence $101010\ldots$.

4.4.2 Quadrature phase-shift keying

For the QPSK modulation scheme (see Fig. 4.1b), two different sequences of two symbols have been selected as shown in Fig. 4.6. These are: *1*) the consecutive transition between symbols with only a $\pi/2$ phase change (sequence Q), and; *2*) the transition from opposite symbols with continuous π radians phase change (sequence X).

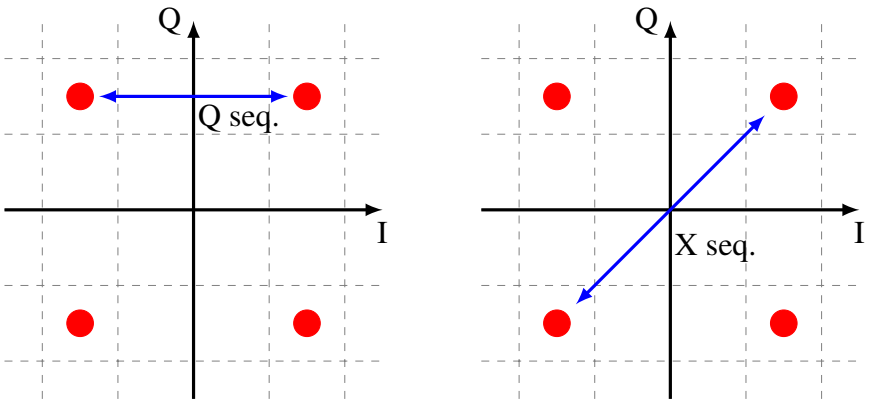

Figure 4.6: QPSK: Experimental test sequences Q and X.

The results are shown in Fig. 4.8 where several ratios for $\xi = T_{sym}/T_{RF}$ have been considered. The multipactor threshold voltage of a digitally modulated signal compared to the CW threshold is expressed as

$$\bar{V}_{th}(dB) = 20\log\left(\frac{V_{th}}{V_{th,CW}}\right) \tag{4.5}$$

being V_{th} is the multipactor threshold voltage for the modulated signal, and $V_{th,CW}$ is the multipactor threshold voltage for the non-modulated case at the RF carrier center frequency.

When comparing simulations (Fig. 4.7) and experimental (Fig. 4.8) results, it is clear that for the Q sequence a constant threshold for different ξ values should be expected. Experimental results do not totally confirm this assumption, as there is convergence between experimental and simulated data as ξ gets smaller. The discrepancy between $\xi = 400$ and $\xi = 20$ is about 17%.

The X sequence simulations accounted for an slight threshold increment as ξ decreases, which is also confirmed by experimental data for $\xi = 400, 40$. However, the experimental results for $\xi = 20$ shows an unjustified decrement.

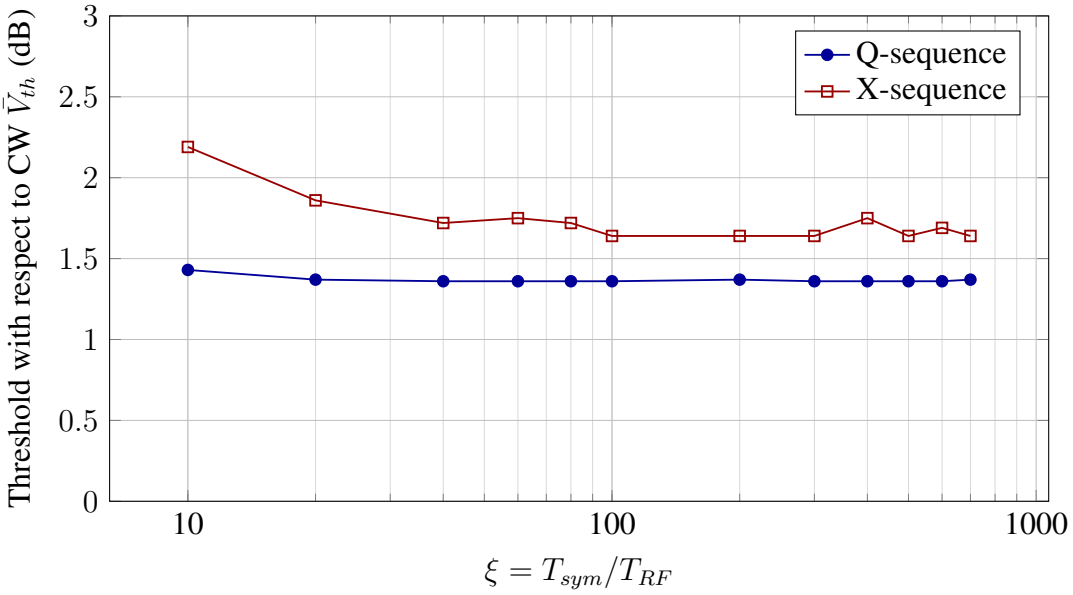

Figure 4.7: QPSK: Simulation results for X and Q sequences.

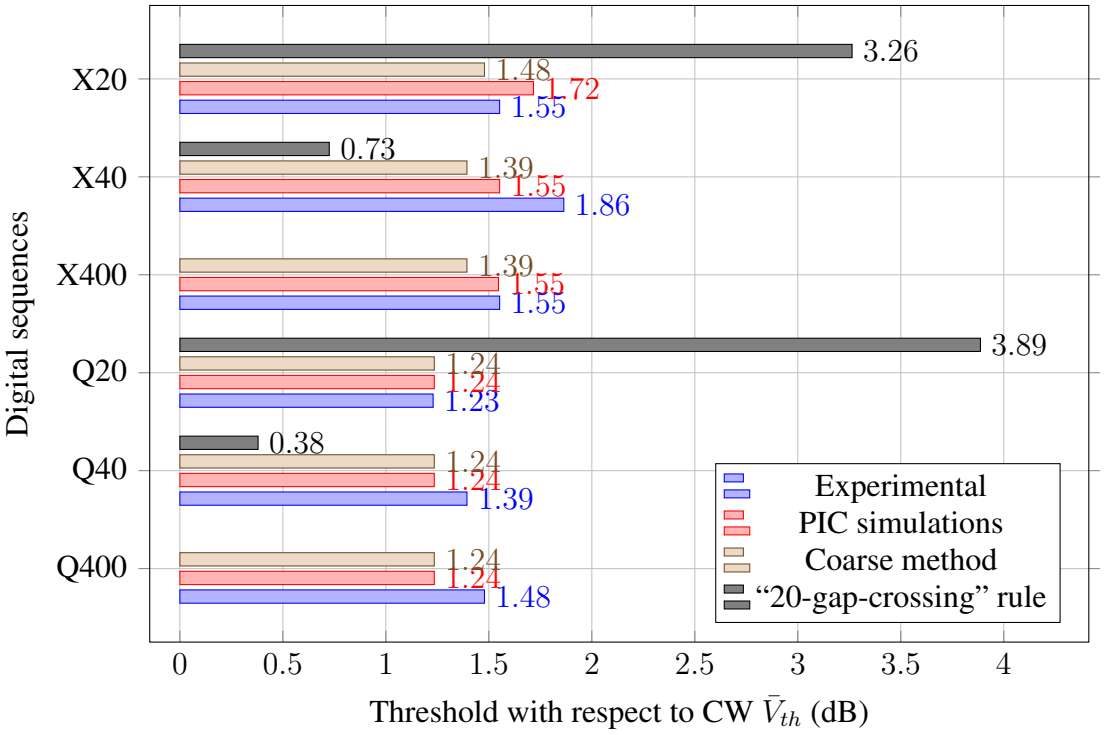

Figure 4.8: QPSK: Experimental results for Xξ and Qξ sequences, for $\xi = 20, 40, 400$.

4.4.3 High order modulations

Figures 4.1b to 4.1e show the set of high order modulations considered in this thesis. Instead of repetitive sequences, a random sequence has been used in each case.

The first result obtained from simulations is the transition from long-term to short-term multipactor discharge (see Fig. 4.9). Depending on the modulation scheme, this transition is smoother or sharper, but in all cases, the transition happens in the range $\xi \in [40, 100]$.

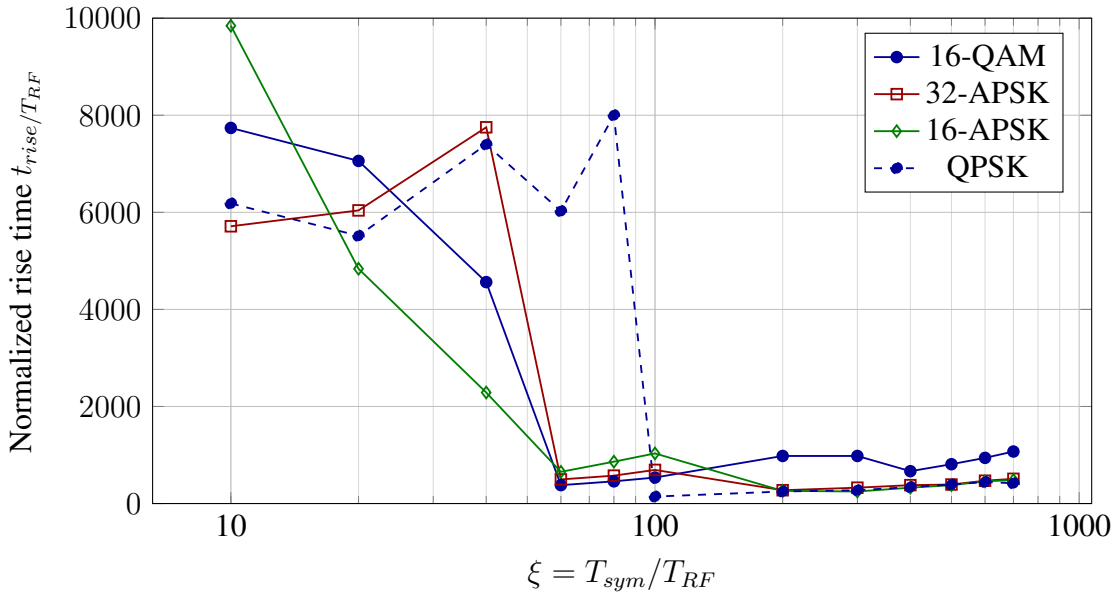

Figure 4.9: Simulation results showing the multipactor rise time in terms of the symbol rate (ξ). Transition from long-term to short-term is noticeable for ξ between 60 and 100.

From the theoretical results shown in 4.10 it can be observed that there is a major threshold change between in which $\xi < 40$ and thos in which $\xi > 300$. For that reason the experiments have been carried out using symbol rates such that $\xi = 40$ and $\xi = 400$.

High order modulation results show an excellent agreement between simulation and testing, with a deviation(between measured and PIC-code simulated data) of less than 0.55 dB in the worst case (see Fig. 4.11). The threshold change (larger than 2 dB) predicted in the simulations (see Fig. 4.11) is confirmed by testing. However, the threshold for large ξ values do not converge, as expected from the simulation results.

Finally, it is worth noting that three energy level modulation 16-QAM has shown the largest $\xi = 400$ to $\xi = 40$ threshold change. When comparing the APSK modulations the three energy levels 32-APSK has recorded a lower threshold ratio for both scenarios ($\xi = 40, 400$ cases) when compared to the 16-APSK.

The reason why the threshold change is larger for the 16-QAM might be due to the fact that it has only scheme with 4 high energy symbols. So, if an equal number of symbols of each energy is transmitted, this leads to a higher PAPR when compared to the 32-APSK

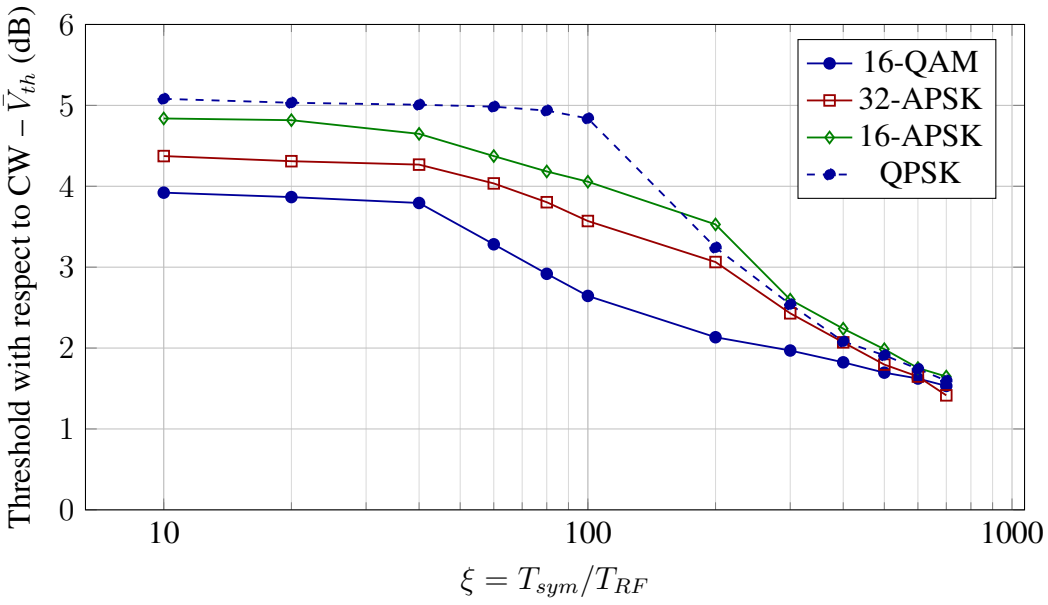

Figure 4.10: Simulation results obtained with the PIC method for several ξ values, random sequences.

or the 16-APSK. Additionally, lower number of high energy symbols leads to shorter peak power intervals, since the chances of changing from high energy symbol to another high energy symbol are reduced.

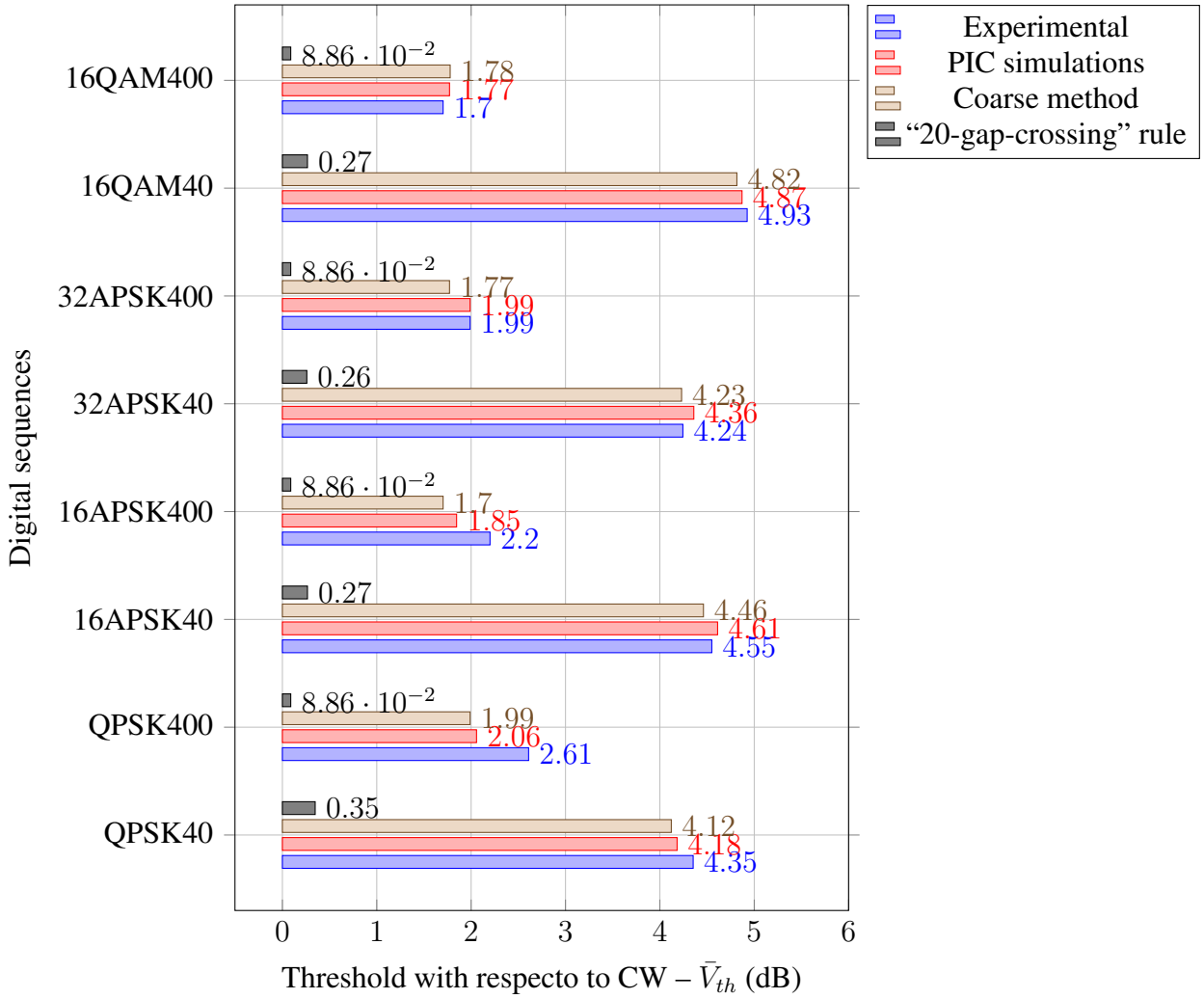

Figure 4.11: Experimental results for high order modulations with random sequences.

4.5 Accuracy of the 20-gap crossing rule as multipactor predictor

The multipactor threshold for several signal types is analyzed and experimentally verified in this thesis. In some cases, the prediction made using the "20-gap crossing rule" , suggested in [8], has been included.

This rule states that in any signal with non-constant envelope, RF multipactor breakdown will happen if the signal remains above the multipactor threshold for a certain time length. This time length is defined from the electron transit time between the two surfaces involved in the multipactor discharge. The threshold level is such of the CW case for any length larger than this time length.

Results shown in chapters 3 and 4 prove that the "20-gap crossing rule" is inaccurate. Other works in which the applicability of this rule is refuted can be found in [81, 75, 104].

The first results where the rule fails to provide accurate threshold levels are shown in section 3.2. In those examples, multipactor of order one is expected and, consequently, the time required for an electron to perform 20 crossings in the critical gap is 10 RF periods. According to the "20-gap crossing rule", the RF multipactor threshold shall be a constant value (see Fig. 3.4), at the level of the CW threshold value, for pulses longer than 10 RF periods. However, accurate simulations and experimental results refute the "20-gap crossing rule" prediction by showing that the threshold level does increase as the pulse length narrows.

The second set of results where this rule fails to predict the multipactor threshold correctly is found in sections 4.4.2 and 4.4.3. Its prediction is far from the results given by two different multipactor analysis methods and the experimental data. Errors up to 4.5 dB between experimental results and prediction from this rule have been recorded. Indeed, this rule has provided the worst prediction results in all the considered cases compared to the commercial tools or custom PIC codes.

Changes on the "20-gap crossing rule" to improve its accuracy are not feasible unless a major change in the rule itself is done. Since only the time length is a degree of freedom for this predictor, and the impact of RF power in the threshold is not considered, the author considers that moving to a simplified coarse method would be a better option.

The coarse method, as used in the thesis, uses accurate multipactor simulations in order to obtain the α values. However, a simplified method could be implemented by using 1 dimension analytic multipactor simulators to obtain those alphas in very short time (seconds). Obtaining the α values analytically would turn the coarse method into a stand alone applications that could be bundled in the ECSS multipactor tool [8, 105]. The accuracy of this method would be closer to that of the coarse with accurate α values than those provided by the "20-gap crossing rule".

4.6 Conclusions

This chapter has considered most of the digital modulations used in space applications: BPSK, QPSK, 16-QAM, 16-APSK and 32-APSK. In a similar fashion as in the short pulses investigation, results have been expressed in terms of $\xi = T_{sym}/T_{RF}$, which relates the symbol length with the RF carrier period. The coarse method has been used as well and its predictions are presented in this chapter. In al cases it has proved that its predictions are accurate even when digital modulations are employed.

In general terms, results show that there is a noticeable multipactor threshold increment when the signal change rate gets closer to the RF carrier frequency.

Firstly, the BPSK modulation, the alternating 10101... sequence pretends to observe the effect of a 180°phase change in the multipactor threshold. For that reason a triangular filter is employed after the modulator. Experimental results show a good agreement with the custom made PIC simulations and a clear threshold increment as the ξ gets closer to one.

Secondly, the QPSK modulation is used to compare a 180°and a 90 °phase changes. For that purpose the so-called X and Q periodic sequences are created (see Fig. 4.6).

Simulation and experimental results show that the X sequence, which has a zero crossing, leads to a larger difference compared to the non-modulated scenario. For the Q sequence, which does not have a zero crossing, the results indicate a higher threshold level than in CW. However, its dependency with ξ is low.

Finally, the high order modulations experiments have been carried out with random sequences to ensure that all the symbols are transmitted. Two ξ values have been used: 40 and 400. Out of this investigation two conclusions should be highlighted. In first place the transition between short-term to long-term multipactor, which is found to happen when the ξ takes values between 60 and 100, has been determined. In second place, it has been found that the multipactor threshold increases with the number of energy levels in the constellation and with a reduction of the ξ parameter.

4.7 List of own publications and projects

The techniques presented in this Chapter have been published in several peer-review journals and conferences. A list of publications and projects related to this research is shown below.

4.7.1 Journal papers

- D. González, **Ó. Monerris**, B. Gimeno, M.E. Díaz, V.E. Boria and P. Martín, "Multipactor RF breakdown in coaxial transmission lines with digitally modulated signals", in IEEE Transactions on Electron Devices, vol. 63, no. 10, pp. 4096-4103, Oct. 2016, doi: 10.1109/TED.2016.2596801.

- D. González, M.P. Belloch, **Ò. Monerris**, B. Gimeno, V.E. Boria and D. Raboso, "Analysis of multipactor effect using a Phase-Shift Keying single-carrier digital modulated signal", in IEEE Transactions on Electron Devices, vol. 60, no. 8, pp. 2664-2670, Aug. 2013, doi: 10.1109/TED.2013.2266275.

- P. González, C. Alcaide, R. Cervera, M. Rodríguez, **O. Monerris**, J. Petit, A. Rodríguez, A. Vidal, J. Vague, J.V. Morro and P. Soto, "Multipactor threshold estimation techniques based on circuit models, electromagnetic fields, and particle simulators", in IEEE Journal of Microwaves, vol. 2, no. 1, pp. 57-77, Jan. 2022, doi: 10.1109/JMW.2021.3132284.

4.7.2 Conference papers

- D. González, **O. Monerris**, B. Gimeno, V.E. Boria, D. Raboso and V. Semenov, "Análisis del efecto multipactor en señales moduladas con Phase-Shift Keying," in XIX Simposium de la Unión Científica Internacional de Radio (URSI). Valencia, Spain, September 2014

- **O. Monerris**, D. Argilés, V.E. Boria, B. Gimeno, D. Raboso and P. Angeletti, "Multipactor testing and emerging qualification protocols", in 46th European Microwave Conference (EuMC), Madrid, Spain, September 2016, pp. 222-225, doi: 10.1109/EuMC.2016.7824318.

- V.E. Boria, L. Nuño, **O. Monerris**, D. Smacchia, D. Argilés and D. Raboso, "Experimental measurements and diagnosis of radio-frequency space high power and electromagnetic compatibility effects", in ESA Workshop on Aerospace EMC (Aerospace EMC), Valencia, Spain, May 2016, pp. 1-6, doi: 10.1109/AeroEMC.2016.7504600.

- D. Gonzalez, A.M. Pérez, **O. Monerris**, S. Anza, J. Vague, B. Gimeno, V. E. Boria, Á. Gomez, A. Vegas, E. Díaz, D. Raboso and A. Coves, "Recent advances of the multipactor RF breakdown in RF satellite microwave passive devices", Progress In Electromagnetic Research Symposium (PIERS), Shanghai, China, August 2016.

- **O. Monerris Belda**, D. Raboso, V.E. Boria, B. Gimeno and David Argilés, "Nuevos métdos de ensayo del efecto multipactor", In XXXI Simposium de la Unión Científica Internacional de Radio (URSI), Madrid, Spain, September 2016.
- D. González-Iglesias, **O. Monerris**, B. Gimeno, M.E. Díaz, V.E. Boria and P. Martín, "Analysis of the multipactor effect in a coaxial transmission line under the excitation of digitally modulated signals", in XI Iberian Meeting on Computations Electromagnetics (EIEC), Oviedo, Spain, November 2016.
- **O. Monerris**, D. Gonzalez, V.E. Boria, B. Gimeno and D. Raboso, "Impact of the multipactor discharge on the digital signal integrity", in International workshop on Multipactor, Corona and Passive Intermodulation (MULCOPIM), ESTEC, The Netherlands, April 2017.

4.7.3 Projects

- **Title** H2020-ESA-007 Multipactor Prediction Techniques for GNSS Signals

  Reference 4000126048/18/NL/AS

  Holder Val Space Consortium

  Number of members in the research team 8

  Issuer European Space Agency

- **Title** Development and validation of an enhanced multipactor prediction method with multicarrier digital modulated signals (Part I)

  Reference VSC2017/ESA/RFQ1300042382

  Holder Val Space Consortium

  Number of members in the research team 3

  Issuer European Space Agency

- **Title** Development and validation of an enhanced multipactor prediction method with multicarrier digital modulated signals (Part II)

  Reference VSC2017/ESA/RFQ1300042381_v2

  Holder Val Space Consortium

  Number of members in the research team 5

  Issuer European Space Agency

Part II

Multicarrier generation

Research scope

The multipactor analysis and testing using multicarrier signals is a novel field for the microwave research community. These signals provide the shortest peak power transients that any space component may deal with.

Although there are peak to average power ratio (PAPR) reduction techniques, used to prevent short peak power transients [106, 107], these techniques are designed to avoid operating a single power amplifier close to its non-linear region. However, typical requirements for multipactor testing using multicarrier signals generally require the use of a multi-amplifier setup, in which the phase cannot be controlled beforehand to minimize the PAPR. Moreover, under actual satellite operation conditions, the random nature of the information transmitted by each channel renders these techniques too complicated or even impossible to apply.

The radio frequency (RF) components in a satellite typically subject to these signals are: RF connectors, output multiplexers, filters, orthomodes and antennas [11].

When dealing with RF high power multicarrier tests, the available degrees of freedom per carrier are: RF power level, frequency and phase. The specific satellite requirements determine the frequency and power parameters, but the phase for each carrier is a random variable. Due to randomness in the data to be transmitted in each channel, all phase combinations will exist during the satellite operational life.

In order to run a laboratory test in a reasonable amount of time, the phase scheme leading to the lowest RF breakdown threshold level must be analytically found and verified by testing. It has been proved that the in-phase signal, which has the largest peak-to-average value for all the phase combinations, does not necessarily lead to a reasonable estimation for the lowest RF breakdown threshold value [44, 43].

To simulate a satellite system, and because of the RF high power level required for testing –usually above 200 W CW per carrier–, it is not typically feasible to amplify the multicarrier signal in one single RF high power amplifier (HPA). It is common to amplify each carrier separately, and then combine all of them with an output multiplexer (OMUX), [11, 108, 109, 110].

Assuming that the specific phases to be tested are known, phase drift in the signal generators and distortion from the RF high power amplifiers [78] degrade the multicarrier signal behavior over time. This degradation must be continuously compensated in order to run a multipactor test with a multicarrier signal.

The multicarrier signal bandwidth is the frequency difference between the lowest and

highest frequency values. This parameter directly depends on the number of carriers and the carrier frequency spacing. In satellite communications, this parameter varies from a few MHz in narrowband components to GHz or even more for multi-band devices [11, 111]. The number of channels depends on each application, reaching up to 20 or more in some communication satellites [112].

Many works devoted to the generation of narrowband multicarrier signals, such as Orthogonal Frequency-Division Multiplexing (OFDM) [97] or its practical implementations –e.g. Digital Video Broadcasting (DVB) [113] or Long-Term Evolution (LTE) [114]– can be found in literature. Nevertheless, the average RF power of such signals is in the 10 W CW range. Being its bandwidth lower than 80 MHz and having RF frequencies below 5 GHz. These multicarrier signals are generated in one single signal generator and amplified in one RF high power amplifier. Since only one local oscillator is used, phase drift among the carriers does not occur. Moreover, the total RF power is not very high, so one single amplifier can cope with the required output power levels.

Several commercial solutions offer one single RF equipment capable of generating a wide-band low power multicarrier. These solutions are typically based on employing an arbitrary waveform generator (AWG) [115], such as the Keysight M8196A [116]. The use of these AWGs has some disadvantages in comparison with the use of a set of signal generators, since AWGs need an input multiplexer (IMUX) plus an output multiplexer (OMUX) in order to split the carriers before the high power amplifiers (HPAs) and combine them back. In addition, the AWG reconfiguration, and output settle times after changing the sequence, are not as smooth as the performance offered by a signal generator. The implementation of high power multicarrier systems with these devices is considered in chapter 6.

Other commercial solutions provide the means to create phase-coherent signals at the same frequency in several signal generators [117]. This approach is used in an alternative for the generation of a multicarrier signal, which has also been considered in this thesis work.

The strategies shown in this part solve the problem of obtaining and maintaining a wide-band RF high power multicarrier signal for long periods. In chapter 5, a low cost solution is proposed, so it is based on hardware commonly existing in test laboratories, thus being preferred to solutions using new equipment. Then, in chapter 6, a compact and more phase stable solution based in the use of wide-band vector signal generators is shown.

Currently, no commercial solution is available to generate flexible high power multicarrier signals with smooth adjustment in terms of phase and amplitude. Having phase control is very important, since testing devices for high vacuum RF breakdown effects use some detection methods that could be tricked by non-smooth amplitude or phase changes.

Chapter 5

Multicarrier generation using one signal generator per carrier

5.1 Summary

Multicarrier operation is an standard nowadays in satellite communications [11, 10]. Many RF components in the transmission change handle more than one carrier which, in turn, transmit random information using similar or different modulations schemes and bandwidths. Performing a multipactor verification in those devices is, even nowadays, challenging.

Many efforts have been carried out in the simulation and experimental sides in order to properly consider these cases [44, 104, 82]. Finding the worst phase scheme from the multipactor discharge perspective is still challenging.

However, literature does not contain works devoted to the automatic generation of multicarrier signals. All the experiments carried ot so far perform the phase adjustment manually and, for that reason, the total number of carrier being use is reduced (less than 10).

This chapter presents a low cost method for the generation of such signals using one signal generator per carrier. The method aims to re-purpose analog or narrow band digital signal generators, which are typically already available on the RF high power laboratories.

The chapter is structured as follows. In section 5.2, the theory to obtain the absolute amplitude and phase error of the generated multicarrier signal is described. Then, sections 5.2.1 and 5.2.2 show, respectively, two new phase minimization methods and the proposed amplitude correction technique. In section 5.2.3, the algorithm is extended to work in the intermediate frequency domain. Section 5.3 shows the complete algorithm flow-chart. Some numerical results are included in section 5.4, and a set of experimental results are shown in section 5.5, including RF high power measurements. Finally, in section 5.6, the most relevant conclusions are highlighted.

5.2 Theory

A multicarrier signal, without sub-modulated carriers, is a wave formed by the superposition of M sinusoidal tones, each one with its corresponding amplitude, frequency, and initial phase. This type of signal can be mathematically represented as

$$mcs(t) = \sum_{i=1}^{M} v_i \cos(2\pi f_i t + \varphi_i) \tag{5.1}$$

where M is the number of carriers and v_i, f_i and φ_i are the amplitude (V), the frequency (Hz) and initial phase (rad) of the i-th carrier, respectively.

The RF bandwidth of the signal defined in (5.1) is

$$BW = max(f_i) - min(f_i), \quad \forall i. \tag{5.2}$$

In some cases this signal repeats over time with period

$$T_{env} = 1/gcd(f_i) \tag{5.3}$$

gcd being the greatest common divisor.

Accepting any delayed version of the multicarrier signal defined in (5.1) as valid, the following equations define a set of signals in the time and frequency domains, respectively,

$$smcs(t, \tau_d) = mcs(t - \tau_d) \tag{5.4}$$
$$SMCS(f, \tau_d) = e^{-i2\pi f \tau_d} MCS(f) \tag{5.5}$$

where $\tau_d \in [0, T_{env}[$ is defined as the delayed time. Any signal satisfying the above equations is accepted as a valid output of the algorithm [118]. A time shift does represent, in the frequency domain (5.5), the same spectrum with a frequency dependent phase shift. In the time domain, this translates into

$$smcs(t, \tau_d) = \sum_{i=1}^{M} v_i \cos(2\pi f_i (t - \tau_d) + \varphi_i)$$
$$smcs(t, \tau_d) = \sum_{i=1}^{M} v_i \cos(2\pi f_i t + \varphi_i') \tag{5.6}$$
$$\varphi_i' = \varphi_i - 2\pi f_i \tau_d \tag{5.7}$$

where (5.6) shows that the time-delayed signal is the same signal with another set of initial phases.

Having defined the signal to be recovered, the hardware needed to generate and correct the RF high power multicarrier signal is shown in Fig. 5.1. One signal generator and one power amplifier are used for each RF channel. There are some cases where one RF high

power amplifier might handle several carriers, but this would come at the expense of creating inter-modulation tones. If more than one amplifier is used, an output multiplexer combines all the channels. Finally, the oscilloscope is used to measure the signal in the time domain, which is required to correct the potential amplitude and phase shifts.

The reference plane, where the desired multicarrier signal shall exist, is labeled as A in Fig. 5.1. This reference plane is where the DUT interfaces with the corresponding test bed.

Because of the high voltage RF fields in the reference plane A, the signal cannot be measured at that point. For that reason, a second reference plane C is defined. The signal is measured in C and compared with a filtered version of the ideal signal. The transfer functions between $B \Rightarrow A$ and $B \Rightarrow C$ determine the frequency domain response to filter the ideal multicarrier signal.

Given the desired –or ideal– multicarrier signal in the reference plane A, the first algorithm step transfers the ideal multicarrier signal from A to C. The transfer function between these two planes, $H_T(f)$, can be measured using a Vector Network Analyzer (VNA) (see Fig. 5.2). The translation from A to C can be done in two steps, the first one being filtering from $B \Rightarrow A$ and the second one filtering $B \Rightarrow C$, where $H_{ab}(f)$ and $H_{cb}(f)$ are the corresponding transfer functions. It can be mathematically represented as

$$\begin{aligned} MCS_C(f) &= MCS(f) \cdot H_T(f) \\ &= MCS(f) \cdot H_{cb}(f) \cdot H_{ab}^{-1}(f) \end{aligned} \tag{5.8}$$

where $MCS(f)$ is the ideal multicarrier signal. The frequency dependent functions $H_{ab}(f)$ and $H_{cb}(f)$ are obtained from the measurement of the S_{21} scattering parameter from B to A and from B to C of the RF network shown in Fig. 5.2, respectively. This is a good approximation as long as $S_{11} < 20$ dB.

The periodically measured multicarrier signal $s_c(t)$ is converted to the frequency domain. The Fast Fourier Transform (FFT) is the most widely used technique to perform this transformation. Nevertheless, out of all the frequency domain data, only a few complex values (S_{Ci}), corresponding to M carrier frequencies, are needed.

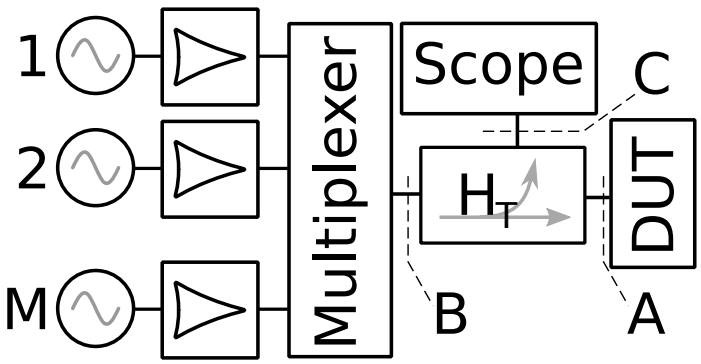

Figure 5.1: Block diagram of the RF high power multicarrier generation system, where the signal sampling network used to monitor the multicarrier signal is represented by H_T.

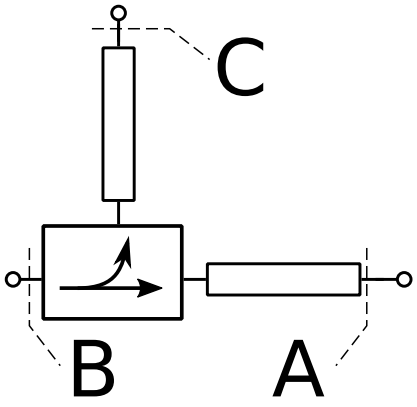

Figure 5.2: Block diagram of the multicarrier signal sampling network (H_T) in the RF domain, –i.e. passive network–. Three reference planes are highlighted: DUT input port A, input of the coupling element B and oscilloscope input port C.

Once the M complex values MCS_{Ci} and S_{Ci} are available, the coarse amplitude and phase errors are obtained from

$$\Delta\varphi_i = \angle\Big(\frac{MCS_{Ci}}{S_{Ci}}\Big) \quad i = 1 \ldots M \tag{5.9}$$

$$\Delta v_{bi} = \Big|\frac{MCS_{Ci}}{S_{Ci}}\Big| \quad i = 1 \ldots M \tag{5.10}$$

where MCS_{Ci} and S_{Ci} are the i-th carrier frequency terms for the target signal and the measured signal at C, respectively. By applying these values to the M signal generators, the correct multicarrier signal is obtained at the reference plane A. However, the phase shift can be optimized in several ways in order to minimize the applied phase shift.

The proposed algorithm adjusts the amplitude and phase on the signal generators, so that the multicarrier signal in the reference plane C matches $MCS_C(f)$. Nevertheless, since any delayed version of $mcs(t)$ is accepted according to (5.5), the algorithm finds the phase shift that minimizes the required phase change set to each signal generator.

Minimizing the phase shift (5.9) is of crucial importance in a multipactor test, because the most reliable detection method is based on the measurement of the carrier amplitude and phase (nulling system) [118] or IQ detection (chapter 7). Thus, if these two parameters are externally changed, the detection system may return a wrong output. This issue is discussed in next subsections 5.2.1 and 5.2.2.

5.2.1 Phase shift correction

In the previous parts of section 5.2, the phase and amplitude errors were obtained according to eqs. (5.9) and (5.10). Here, two methodologies are presented to optimize the phase shift

by finding an optimal time shift for the measured data. Both of them produce a multicarrier signal which simultaneously satisfies (5.5) and minimizes the phase shift.

Two different optimization approaches are proposed: a) minimum global phase shift and b) minimum $(M-1)$-phases shift (carrier tracking).

In the first approach, once the absolute phase error (5.9) is obtained, the minimum phase shift is found. The first step consists in minimizing the the error function defined next as,

$$Err(\tau) = \sum_{i=1}^{M} \Big(mod\big(\Delta\varphi_i + 2\pi f_i \tau + \pi, 2\pi\big) - \pi \Big)^2 \tag{5.11}$$

where τ is the delay to be optimized. Although an unconstrained optimization can be used, the output τ_{opt} can be wrapped in the $[0, T_{env}[$ interval.

The second approach –carrier tracking– is a constrained version of the first one defined by:

$$\tau_{opt} = min\left(\frac{-\Delta\varphi_i}{2\pi f_i} + \frac{n}{2f_i} \right) \tag{5.12}$$

where $i \in [1, \ldots, M]$ is the index of the carrier being tracked and $n = 0, \ldots, \lceil 2 f_i T_{env} \rceil$ and integer number which is used to shift the τ_{opt} by a certain amount of half-cycles for the carrier being tracked. This n values preserved the conditions that no phase shift is required for the carried being tracked.

Once τ_{opt} is obtained, the final phase shift is given as indicated next,

$$\Delta\varphi_i' = mod\big(\Delta\varphi_i + 2\pi f_i \tau_{opt} + \pi, 2\pi\big) - \pi \tag{5.13}$$

for $i = [1, \ldots, M]$.

5.2.2 Amplitude correction

The amplitude correction defined in (5.10) shall be applied in order to recover the ideal signal properly. Due to the need for accuracy in the RF power measurement, it is convenient to obtain a redundant RF power measurement through a powerhead or spectrum analyzer. So the amplitude measurement from the oscilloscope is not used.

The best practice is to obtain the RF power level using a powerhead configured with the correct frequency and offset –measured from the powerhead location to reference plane A–. Three options are proposed: *1*) to measure the RF power of each carrier using a set of M powerheads, each in one RF channel before the OMUX; *2*) to measure the absolute RF power in one carrier (with one CW powerhead) and combine this information with relative power measurement on the oscilloscope measured signal; or, *3*) to measure the RF power of the multicarrier signal using a thermal powerhead and combine with the oscilloscope data.

Out of the three options $1)$ is the most recommended and accurate way to precisely measure the RF power. Nevertheless, options $2)$ and $3)$ can provide good differential RF power measurements if the oscilloscope is able to measure a large number of of multicarrier envelopes (n_{env}), e.g. $n_{env} > 500$.

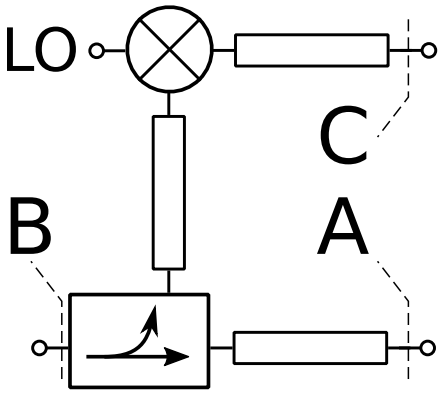

Figure 5.3: Block diagram of the multicarrier signal sampling network (H_T) in the RF/IF domains, –i.e. including frequency down-conversion–. Three reference planes are highlighted: DUT input port A (RF domain), input of the coupling element B (RF domain), and oscilloscope input port C (IF domain).

5.2.3 Frequency downconversion

The multicarrier generation algorithm shown in section 5.2 can be extended to work also in the intermediate frequency (IF) domain [119], [120], [121]. This is especially useful when very high-frequency multicarrier signals are generated (typically higher than 6 GHz). For this purpose, a frequency mixer is placed in the path from B to C (see Fig. 5.3). A practical implementation may require additional filtering after the mixer in order to remove the undesired signals generated in the down-conversion process.

This configuration allows the use of an oscilloscope with enough bandwidth to cope with the multicarrier total frequency span according to (5.2), but which is not capable of measuring the multicarrier signal at RF level. So the signal recovery is performed in the IF domain, and then mapped back to the RF domain.

In order to convert the ideal signal, the frequency must be converted from the RF into the IF domain, taking into account that now, $H_{cb}(f)$ not only changes the amplitude and phase but also the carrier frequencies as follows:

$$f_i' = f_i - f_{LO}. \tag{5.14}$$

where f_{LO} is de local oscillator frequency.

Then, the algorithm runs in the same way as explained in the previous sections but in the IF domain. Once the optimized signal delay is found in the IF domain (τ_{IFopt}) using (5.12), the phase shift in the RF domain is found as

$$\Delta\varphi_i' = mod\big(\Delta\varphi_i + 2\pi f_i \tau_{IFopt} + \pi, 2\pi\big) - \pi \tag{5.15}$$

for $i = [1, \ldots, M]$.

The amplitude correction to be applied is the one obtained in (5.10).

5.2.4 Multicarrier generation with digitally modulated carriers

High vacuum breakdown phenomena, such as corona and multipactor, are usually tested using non-modulated CW signals. Switching to multicarrier signals is a big step forward towards getting closer to the real scenario of the actual DUT operation. The proposed approach does not pretend to be used as a general method for multicarrier signal pre-distortion, but to provide the means to phase lock a set of M signal generators even if they are transmitting modulated signals. Multipactor and corona testing do not have a hard requirement in terms of the data transmission throughput.

In contrast to the solution proposed in chapter 4, in this case, there is one narrow band digital signal generator creating the modulation for each carrier. This approach is useful when the signal generator cannot create all the modulated carriers at once, either because their maximum modulation bandwidth is not large enough, or because the output power is not enough to drive the amplifier/es.

The nature of multipactor or corona tests allows the use of custom digital sequences easily. One relevant issue in data transmission is the recovery of the carrier frequency. Several digital signal processing techniques have been developed for that purpose [122, 123]. However, multipactor and corona tests do allow the use of CW segments at the carrier frequency which are used as phase calibration beacons.

Two approaches are proposed in Fig 5.4. The first option uses a custom digital sequence carrying the carrier information, which is periodically transmitted. The second option appends the carrier information at the beginning or end of each data sequence.

Assuming that the digital memory on the signal generators is a vector of P complex values containing the IQ samples, the carrier recovery sequence would be a set of values such that

$$IQ(i) = \frac{Vd_{rms}}{\sqrt{10}} \quad i = 1, 2, \ldots, P \tag{5.16}$$

where Vd_{rms} is the RMS voltage of the digital sequence to be transmitted. The amplitude factor of $\sqrt{10}$ is arbitrarily chosen to avoid triggering the breakdown while the RF carrier information is being transmitted. Although other values would also be acceptable.

Finally, the number of elements in the sequence (P) must be long enough for the algorithm to operate (see more details in section 5.4). Thus, it depends on the IQ sample rate configured in each generator.

Independent carrier information sequence

The first approach consists on using two different sequences in each signal generator. The first sequence is the digital signal with the pattern of the symbols to be transmitted. The data sequence might be different in each channel, but should be of equal time length. The second sequence is such that it produces an RF signal of constant amplitude and phase. This second

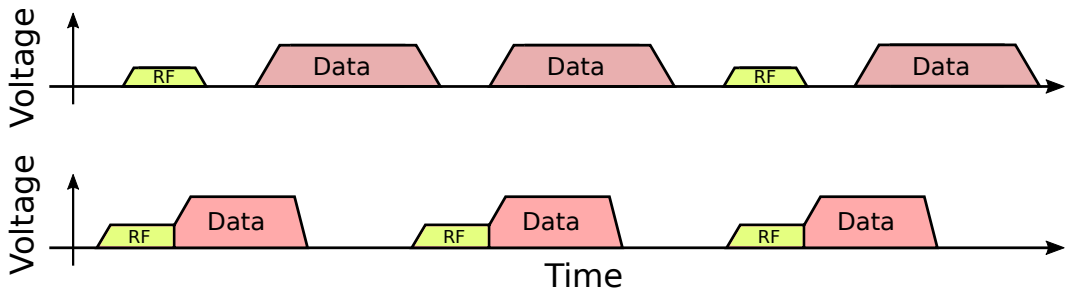

Figure 5.4: Scheme for the carrier recovery when using digital modulations. In both cases, the RF carrier is transmitted with 10 dB back-off with respect to the RMS power of the digital sequence. Independent RF carrier sequence (above), where the RF carrier is transmitted every few seconds. Embedded RF carrier sequence (below), the RF carrier is transmitted at the beginning of each sequence.

sequence must be transmitted simultaneously by all the generators. A TTL marker shall be sent to the oscilloscope for trigger purposes.

Embedded carrier information sequence

The second approach is less efficient from the data throughput point of view, but it is acceptable for the RF high power tests being considered in this work. In this case, the carrier recovery sequence is embedded before or after the digitally modulated sequence. In each repetition, the RF carrier information can be easily measured using the oscilloscope, which trims the acquired waveform to keep the desired part and discard the rest.

5.3 Multicarrier generation algorithm

The multicarrier generation algorithm (see Fig. 5.5) uses the developed theory in order to create the desired signal from a known initial state. The algorithm execution is divided into a static part, which is run only once, and a dynamic part periodically executed while the test is running.

The static part comprises: *1*) initialization of the connection with the RF equipment and filtering the ideal signal according to $H_T(f)$; *2*) acquisition of the RF/IF signal, transformation employing the FFT, and location of the exact frequencies of the carriers (which may be slightly different to the ideal frequencies).

The dynamic part consists of: *1*) acquisition of the RF/IF signal and conversion to the frequency domain with the DFT or FFT methods; *2*) phase and amplitude optimization to obtain the minimum phase shift and amplitude error; *3*) adjustment of the signal generators if any error is greater than the specified threshold.

Finally, although in the following numerical and experimental examples the phase and

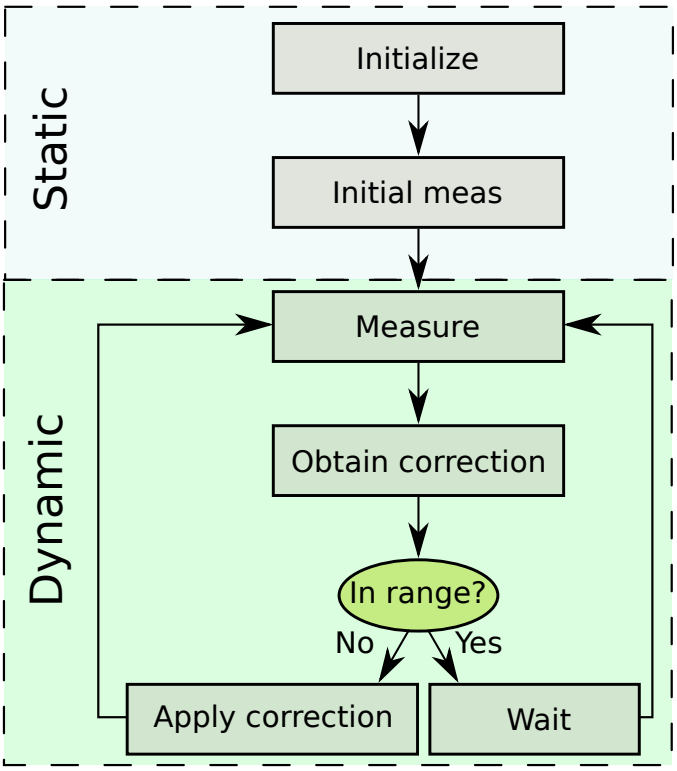

Figure 5.5: Simplified flow chart of the multicarrier generation algorithm when used in a real RF high power test. The static part is run only once, and the dynamic part is periodically run.

amplitude corrections are applied in just one step, note that, in a real test, it is recommended to apply the correction in small steps no larger than 1° per second for the phase, and of 0.01 dB per second for the amplitude. These small steps guarantee that changes will not trigger the multipactor detection systems.

5.4 Numerical results

The above-presented theory has been extensively tested using GNU Octave [124]. In order to evaluate the theoretical results, two figures of merit have been defined. Both are independent of the time offset between the ideal and recovered signals.

The first one has been chosen for its simplicity, and better measurement of the high amplitude intervals of the signal. It is defined by means of the cross-correlation as:

$$F(s_I, s_O) = \frac{max(\rho_{s_I s_O}(\tau))}{max(\rho_{s_I s_I}(\tau))} \tag{5.17}$$

where $\rho_{s_I s_O}(\tau)$ is the cross-correlation, being s_I the target signal (ideal), and s_O the recovered signal. The closer to 1 the function value is, the better behavior of the proposed

multicarrier generation algorithm is proved.

The second figure of merit uses the complementary cumulative distribution function (CCDF). This function is defined as

$$G(s_I, s_O) = \sum \left(ccdf(s_I) - ccdf(s_O)\right)^2 \tag{5.18}$$

where $ccdf$ is a vector of n elements in which each value represents the percentage of time –with respect to the total length– that the signal is below V_i, being V_i a set of n values in the $[min(s(t)), max(s(t))]$ range. The nature of this function makes it optimal for evaluating the low amplitude intervals of the given multicarrier signal. In this case, the closer to 0 the value of this function is, the better, validation of the proposed algorithm is obtained.

The first numerical example shows the recovery of a four-carriers signal. The chosen frequencies are 1.0 GHz, 1.1 GHz, 1.2 GHz, and 1.3 GHz with an in-phase scheme. The algorithm is fed with a random amplitude and phase signal in order to simulate a strong HPA distortion. The FFT oversampling factor (OS_{FFT}) is set to 32, and the FFT windows function is flat-top. Without loss of generality $H_{bc}(f) = 1$ has been assumed.

The result of the algorithm is shown in Fig. 5.6, where the ideal and corrected envelopes are shown. The error function values, according to eqs. (5.17) and (5.18), are $F = 0.9995$ and $G = 0.0185$, showing that both signals are very similar.

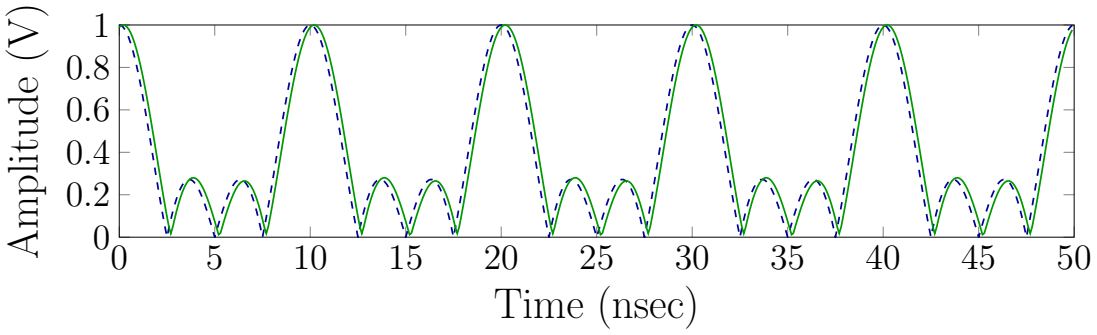

Figure 5.6: Comparison of the initial 50 ns of the ideal (solid) and the recovered (dashed) four-carriers signals using a flattop window, a 10 μs sequence and $F_s = 10$ Gsps.

In this case, the multicarrier generation algorithm has been executed with the carrier tracking method, taking the lowest carrier as a reference. The phase shift error as a function of the time delay τ_d (5.11) is shown in Fig. 5.7. The solid line represents all the possible solutions that would be considered in the full optimization mode, and the square marks show the right solutions for the phase tracking method.

In the second part of this numerical evaluation, the algorithm has been tested in all its degrees of freedom. Some are costly from the economic point of view, such as higher sampling frequency or the number of measured points, whereas others are only related to the computation time: FFT window function and FFT oversampling. This work has analyzed

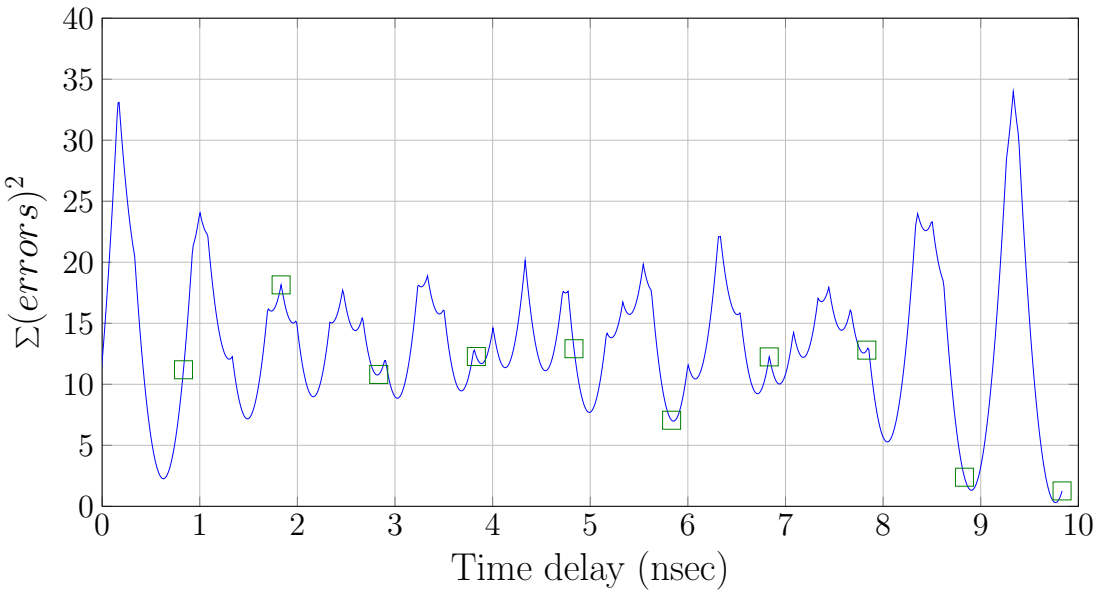

Figure 5.7: Summation, for all carriers, of the squares of the phase shift versus the time delay used in the phase shift optimization of (5.11). The minimum error for all the delays (solid line) is found with the optimization method, whereas the carrier tracking method is constrained to find the minimum among a reduced set of values (square marks).

the impact of the different parameters in the output results, in order to explore their effects and achieve the optimal trade-off.

The set of simulations comprises a varying number of captured multicarrier envelopes (n_{env}), number of FFT oversampling (n_{FFT}), and several FFT windows. A parametric sweep over these parameters ($n_{env} = [1, \ldots, 100]$, $n_{FFT} = [1, \ldots, 64]$ and FFT windows: Hamming, Blackman, flat-top, and no windowing) has been applied. The sampling frequency has also been adjusted to 5 Giga samples per second (GSa/s) and 10 GSa/s, respectively.

Five thousand random "measured signals" have been fed as input to the algorithm for each configuration. Then, the algorithm has recovered the ideal signal from these random signals.

The following conclusions can be drawn from this numerical study: *1*) the algorithm fails to recover the signal when $n_{env} < 5$; *2*) the FFT oversampling with values greater than 32 reduced $G(s_I, s_O)$ value by one order of magnitude for $n_{env} < 40$; *3*) for $n_{env} > 100$, the FFT oversampling does not have a clear impact on the results; and, *4*) the flattop window gives slightly better results.

The above results have been obtained considering constant carrier amplitudes in all the periods. However, the experimental results show that the measured waveform is far from constant over time, since a residual amplitude modulation usually exists. This residual amplitude modulation is only noticeable when using high-power amplifiers.

5.5 Experimental verification

In order to validate the proposed algorithm, a set of three low-power and one high-power experimental measurements have been carried out.

The following hardware has been used. We can find *1*) signal generation: three Keysight PSG (two E8257D, and one E8267D) units, and one Rohde & Schwarz SMBV100A equipment; *2*) data acquisition systems: one Keysight MSO9404A with a sampling rate of 20 GSa/s, and 4 GHz RF bandwidth; *3*) frequency downconversion: Keysight PXA N9030B up to 50 GHz.

The RF devices are synchronized with a 10 MHz signal, with the E8267D being the frequency master. In addition, the equipment has been warmed up for 30 minutes to achieve a stable temperature in the oven control crystal oscillators (OCXOs). As remarked in [117], phase drift would be reduced if the reference frequency was 1 GHz instead of 10 MHz. However, the signal generators do not have the required hardware to share a 1 GHz reference signal.

5.5.1 Low power multicarrier examples

Three scenarios have been chosen for this study: four closely spaced carriers in L-band; four widely spaced carriers in the L- and S-bands; and, finally, the last example uses three closely spaced carriers in the Ku-band, requiring from a down-converter in order to sample them using the available oscilloscope.

The RF passive network used for power combining is implemented with three 10 dB couplers, all of them operating from 1 GHz to 18 GHz (low-power RF devices). Even though this combination scheme is not optimal, the authors believe that it is adequate for a first validation of the proposed algorithm.

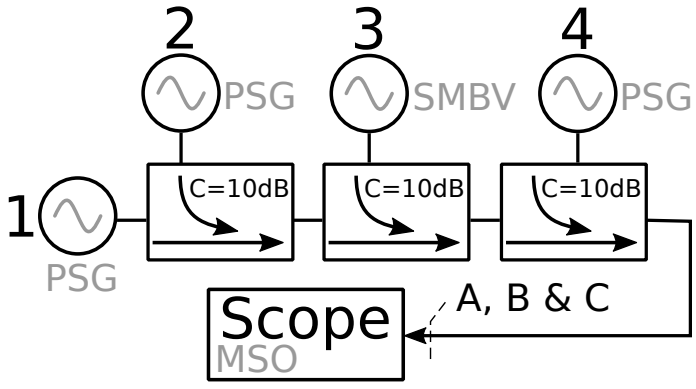

Figure 5.8: Experimental set-up used for validation in the RF domain. The signal generators, RF power combining network and oscilloscope are shown. Given that $H_T(f) = 1$, all the reference planes are located at the oscilloscope input. Being the PSG Keysight RF generators and the SMBV a R&S generator.

For simplicity, but without loss of generality, the transfer function between the DUT port and the oscilloscope port has been considered $H_T(f) = 1$. The test bed schematic in Fig. 5.8 shows the reference planes corresponding to the DUT position A, the output of the combining network B, and the oscilloscope input port C. Because of the assumption mentioned before, the three reference planes are located at the same point of the RF network.

Given the outstanding quality of the signal generators (OCXOs), and the absence of the HPAs, the phase drift is much lower than it would be in a RF high power scenario. That implies that, once the desired signal has been recovered, it remains with the correct phase and amplitude longer than it would if the HPAs were used. Nevertheless, because the algorithm execution time (< 2 seconds) is much faster than the phase drift of the HPA (< 0.01 radians per second [125]), the algorithm would be able to recover the ideal multicarrier signal as often as needed.

For all the examples, the initial random signal (whose phases are unknown) is further randomized by applying an additional random phase shift, $\Delta\varphi_i \in [0 \dots 2\pi]\_\forall i$. The initial amplitude in all the carriers is set to -10 dBm.

Because the multicarrier signal is composed of non-modulated CW tones, its envelope can be obtained using the Hilbert transform ($\mathcal{H}$) [126], [127] as follows

$$S_{env}(t) = \sqrt{(s(t)^2 + j\mathcal{H}[s(t)]^2)} \tag{5.19}$$

where $s(t)$ is the measured signal in the oscilloscope. This transform has been used to ease the task of visually comparing the multicarrier signals.

The first example uses four carriers whose frequencies are: 1.0 GHz, 1.1 GHz, 1.2 GHz, and 1.3 GHz. Excellent results are obtained in only three iterations, as can be seen in Fig. 5.9 and Table 5.1. The sampling frequency has been set to 10 GSa/s, and the number of acquired points is $100k$.

Iter.	Channel 1		Channel 2		Channel 3		Channel 4	
	ΔdB	Δrad	ΔdB	Δrad	ΔdB	Δrad	ΔdB	Δrad
1	-3.16	0.0	6.30	-0.865	5.22	5.132	5.54	0.593
2	-0.04	0.0	-0.04	-0.019	-0.04	-0.294	-0.05	-0.340
3	0.00	0.0	-0.02	0.008	-0.01	-0.060	0.02	0.014

Table 5.1: Corrections applied to the closely spaced L-band example

The second example uses four frequencies: 1.0 GHz, 2.0 GHz, 3.0 GHz and 4.0 GHz. Excellent results are also obtained in only three iterations, as can be observed in Fig. 5.10 and Table 5.2. The sampling frequency has been set to 20 GSa/s, with 100k acquired points.

The third example uses three carriers whose frequencies are: 17.1 GHz, 17.2 GHz, and 17.3 GHz. A Keysight PXA has been used as a down-converter using its IF output. The down-conversion device has been characterized using the manufacturer specifications. Given that a phase error of $< \pm 5$ degrees and an amplitude flatness of $< \pm 0.2$ dB can be expected

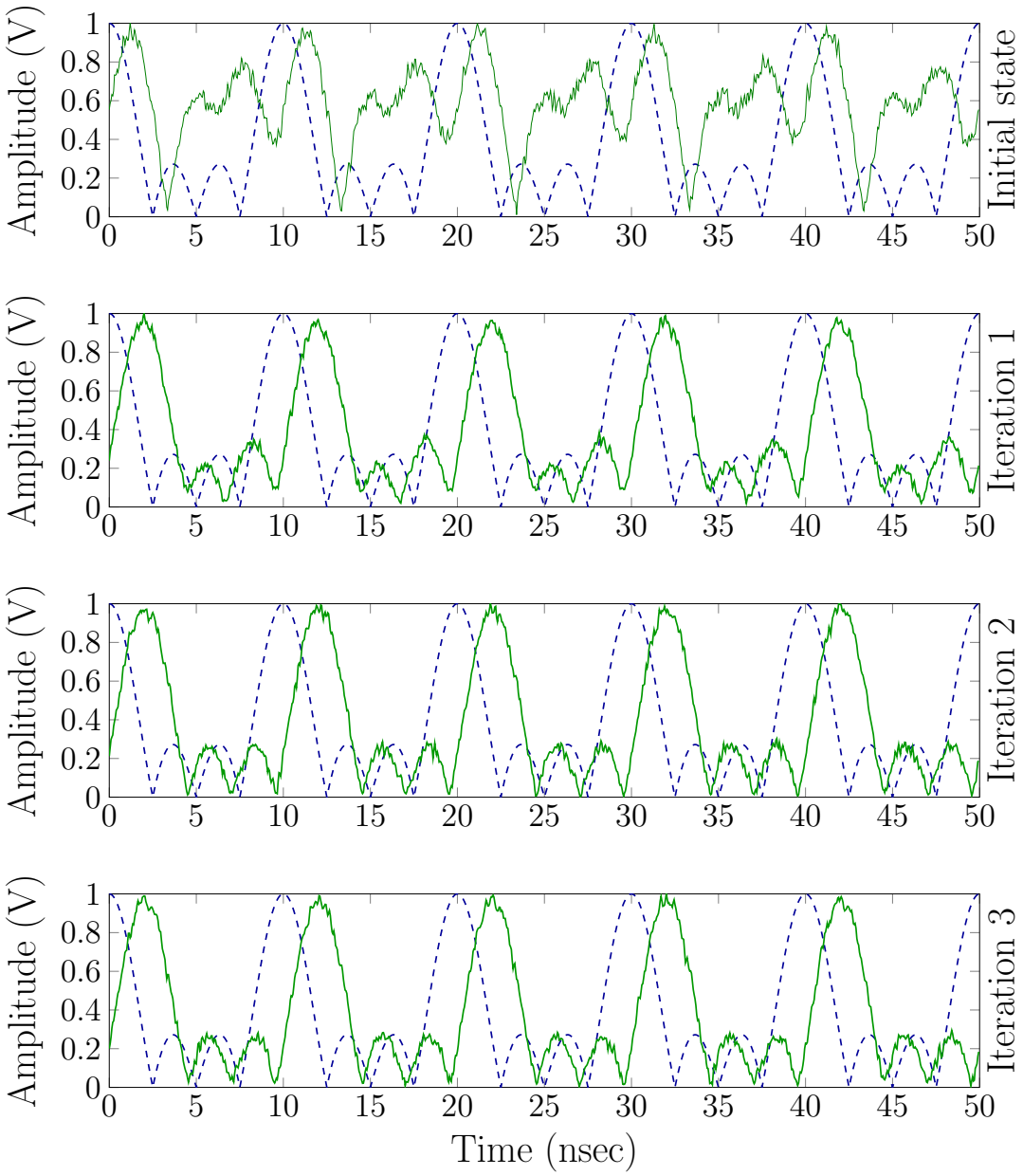

Figure 5.9: Evolution of the measured multicarrier signal (solid line) in each iteration compared to the ideal multicarrier signal (dashed line) for the closely spaced L-band carriers example.

in the down-conversion stage, the following approximation has been assumed $H_{cb}(f) = H_{Mixer}(f) \approx 1$. For this reason, the total transfer function is given by $H_T(f) = H_{ab}^{-1}(f) \cdot H_{cb}(f) \approx 1$, as $H_{ab}(f) = 1$. The test bed schematic in Fig. 5.11 shows the reference planes corresponding to the DUT position A, the output of the combining network B, and

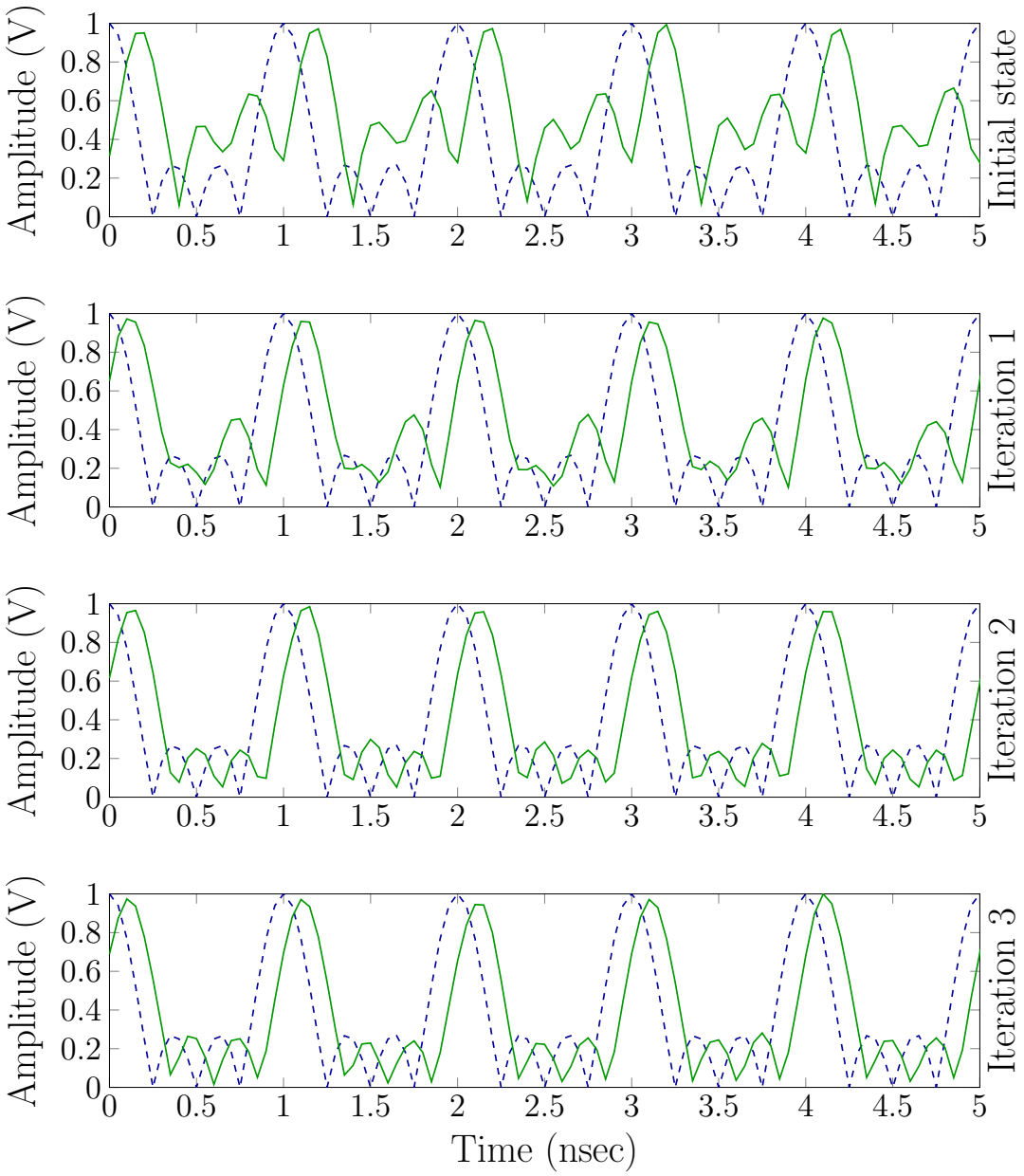

Figure 5.10: Evolution of the measured multicarrier signal (solid line) in each iteration compared to the ideal multicarrier signal (dashed line) for the widely spaced L- and S-bands carriers example.

the oscilloscope input port C.

The mentioned approximation and the high frequency impact the recovered signal, which, in this case, is not as accurate as in the previous two examples. The results from the first

Iter.	Channel 1		Channel 2		Channel 3		Channel 4	
	ΔdB	Δrad	ΔdB	Δrad	ΔdB	Δrad	ΔdB	Δrad
1	-3.14	0.0	0.287	6.664	-1.641	5.13	1.717	3.552
2	-0.10	0.0	-0.189	-0.118	0.425	-0.29	-0.648	-0.189
3	-0.08	0.0	-0.003	-0.068	0.038	-0.06	0.019	0.146

Table 5.2: Corrections applied to the Widely spaced L- and S-bands example

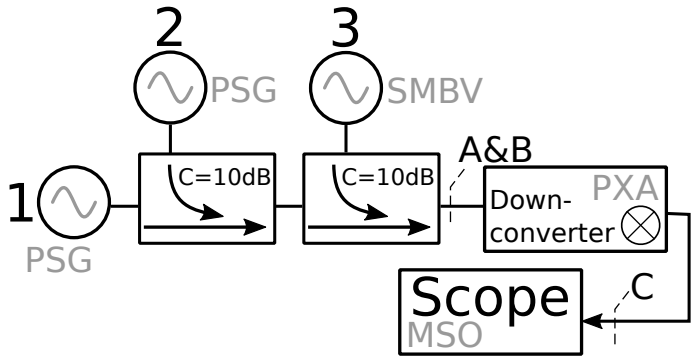

Figure 5.11: Experimental set-up used for validation in the RF/IF domain. The signal generators, the RF power combining network, the down-converter and the oscilloscope are shown. Given that $H_T(f) \approx 1$, the signal at reference plane A is equal to the one at C (excepting the frequency shift between IF and RF carriers).

three iterations can be seen in Fig. 5.12 and Table 5.3, where increasing the number of iterations has not been shown to improve the results. The IF multicarrier tones are located at 222.5 MHz, 322.5 MHz, and 422.5 MHz.

Iter.	Channel 1		Channel 2		Channel 3	
	ΔdB	Δrad	ΔdB	Δrad	ΔdB	Δrad
1	-2.22	0.791	5.75	0	3.06	0.092
2	-0.02	1.243	0.07	0	-0.02	-0.147
3	-0.02	0.084	0.03	0	0.02	-0.091

Table 5.3: Corrections applied to the closely spaced Ku-band example

From the obtained RF low power results, it can be observed that an amplitude change in the signal generator output also changes the phase. For that reason, the initial algorithm step does not fully recover the target signal. Only after the amplitudes have been set close to their final values, the phase adjust correctly shapes the multicarrier signal into its desired form. The algorithm has also provided excellent results for phase schemes other than the in-phase one.

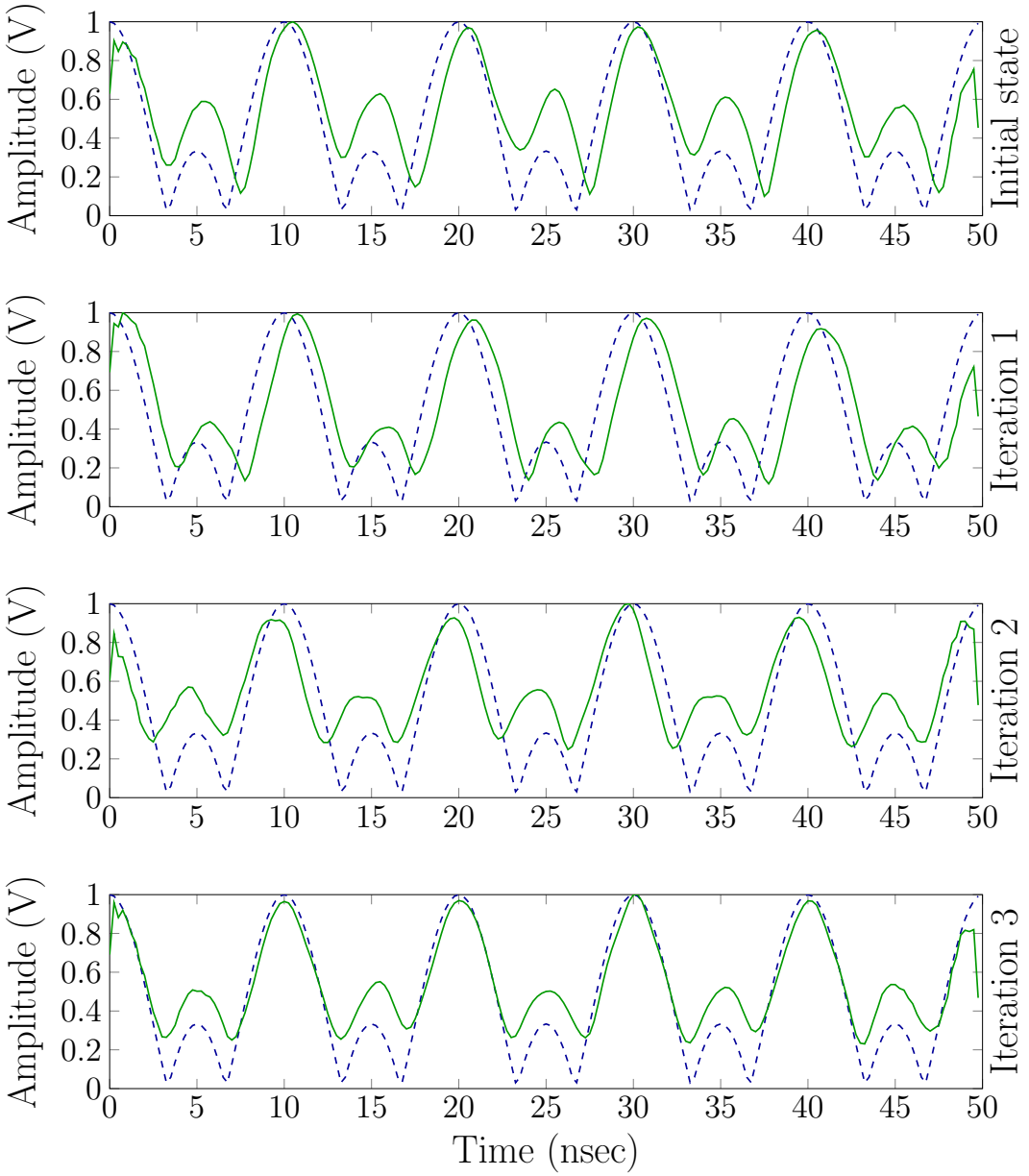

Figure 5.12: Evolution of the measured IF multicarrier signal (solid line) in each iteration compared to the ideal multicarrier signal (dashed line) for the closely spaced Ku-band carriers example.

From the RF low power measurement, the following conclusions can be drawn: *1*) the number of measured points has been changed in all the configurations, and the results stand valid for values as low as 1k samples (for the used sampling rate it is equivalent to $n_{env} \approx 5$); *2*) the results are acceptable in all this range although the recommended minimum value

would fall in the 200 to 1000 multicarrier envelopes; *3*) the window function has been changed as well, obtaining similar performance for Hanning, Hamming, Flattop and Blackman window functions for the 1000 envelopes case; and, *4*) the sampling frequency has been decreased to $F_s = 3.0 \cdot f_{max}$ with good results as well for just three or four iterations.

5.5.2 High power multicarrier measurements

The last example has been performed using RF high power in S-band. Three solid-state amplifiers (SSPAs) and one high power OMUX have been used (see the experimental set up in Fig. 5.13) to amplify and combine three CW carriers. The SSPAs are two 360 W CW units and one 1000 W CW unit from Milmega UK. The OMUX is an S-band triplexer with TNC connectors. The circuit is ended with a RF high power load connected to the DUT reference plane. The frequencies, which are constrained by the OMUX channels, are: $f_1 = 2.030$ GHz, $f_2 = 2.180$ GHz and $f_3 = 2.330$ GHz, being the frequency spacing $\Delta f = 150$ MHz. The oscilloscope sampling frequency has been set to 10 GSa/s, with 10M acquired samples.

Since the European High Power RF Space Laboratory has granted permission to apply up to 50 W CW per carrier at the triplexer inputs, the RF target level has been set to 30 W per carrier. The highest frequency carrier has been set as phase reference.

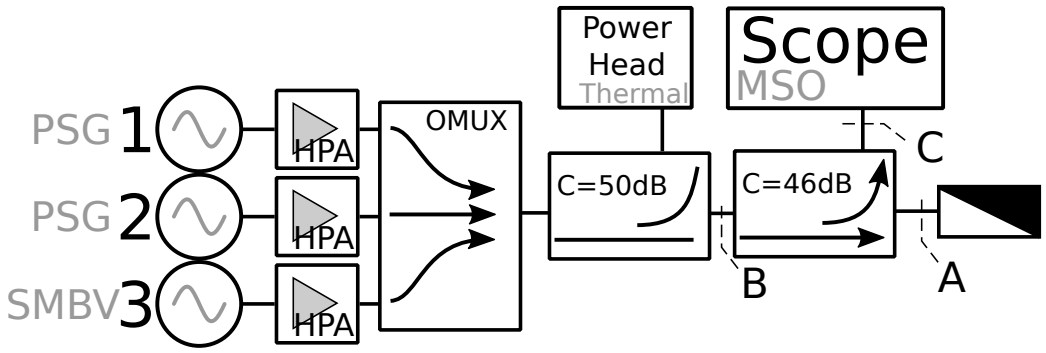

Figure 5.13: Experimental set up used for validation using RF high power in S-band. The signal generators, RF power combining network and oscilloscope are shown.

Iter.	Channel 1		Channel 2		Channel 3	
	ΔdB	Δrad	ΔdB	Δrad	ΔdB	Δrad
1	+7.30	0.20	+5.39	-0.04	+2.10	0.00
2	-0.27	0.48	+0.01	-0.49	+0.14	0.00
3	-0.24	0.37	-0.02	0.04	-0.08	0.00
4	-0.02	0.11	-0.00	0.10	-0.02	0.00

Table 5.4: Corrections applied to S-band the high power example

From the data shown in Fig. 5.14 and Table 5.4, it is clear that the algorithm has converged from iteration two onward. The large amplitude error recorded in channels 1 and 2 in iteration one are due to the cold start initialization. These errors are produce because of different amplifiers models and interface cables being used for each channel, which leads to

a very different RF power per channel at the output of the OMUX when the signal generators are initialized to the same output RF power. Iteration three is just a time-shifted version of the ideal signal, which happens because the software triggers the oscilloscope asynchronously, and a time shift can occur in some iterations.

This final example shows how the algorithm is able to quickly recover the desired multicarrier envelope in only three iterations, even with the presence of high power amplifiers. These results prove that it is able to cope with the phase drift of the signal generators and high power amplifiers simultaneously.

5.6 Conclusions

In this work, the theory for the generation of RF high power multicarrier signals has been described. These signals can have an arbitrary number of carriers, any phase scheme, and unequal RF power level per carrier.

The presented algorithm is focused on creating and adjusting the desired multicarrier signal used in RF high power tests over long periods. Since it considers wideband and high power RF signals, it is suitable for use in multipactor discharge or corona breakdown testing. The algorithm flexibility has been proven through a wide range of simulations where, using random input signals, the algorithm has been able to obtain the desired output signal in one single step.

The main advantage of multicarrier signal comes from the fact that they provide a repetitive pattern of a succession of high and low amplitude values. In contrast to modulated signals, which comes from one source, the generation of multicarrier signals can be split into several generators and amplifiers, thus providing high output RF power and higher spectral purity.

This periodic pattern of high and low amplitude intervals is extremely useful in the filed of RF multipactor breakdown, as the short and long-term multipactor discharges can be better identified in these simple scenarios. On top of that, the maximum RF power achievable in a multicarrier signals will always be larger than that obtained in a system transmitting a digital signal of similar bandwidth.

Optimal approaches to find the worst phase configuration leading to the lowest multipactor threshold is a topic of great interest. This is a very complex tasks as the number of cases to be considered increase to the power of the number of carriers. Nevertheless, this thesis has not focused in this ultimate goal. however, the proposed method is able to conduct Montecarlo testing of changing phase schemes or any other sequential approach.

Experimental low power measurements have shown that the theory can be applied to actual RF generation in several frequency ranges (L, S, and Ku bands) and bandwidths (300 MHz and 3000 MHz). The third experimental example has shown that the algorithm can recover the desired RF multicarrier signal from an IF measurement.

Finally, the fourth experimental test shows a high power multicarrier signal generation. After an initial iteration in which large amplitude unbalance are recorded, convergence is

fast and smooth. This initial unbalance is due to unequal amplifier gain and different cable lengths being used in the setup before the output multiplexer.

To conclude this chapter, it is worth mentioning that all these examples prove the excellent applicability of the theory for the generation of fully customizable high power multicarrier signals.

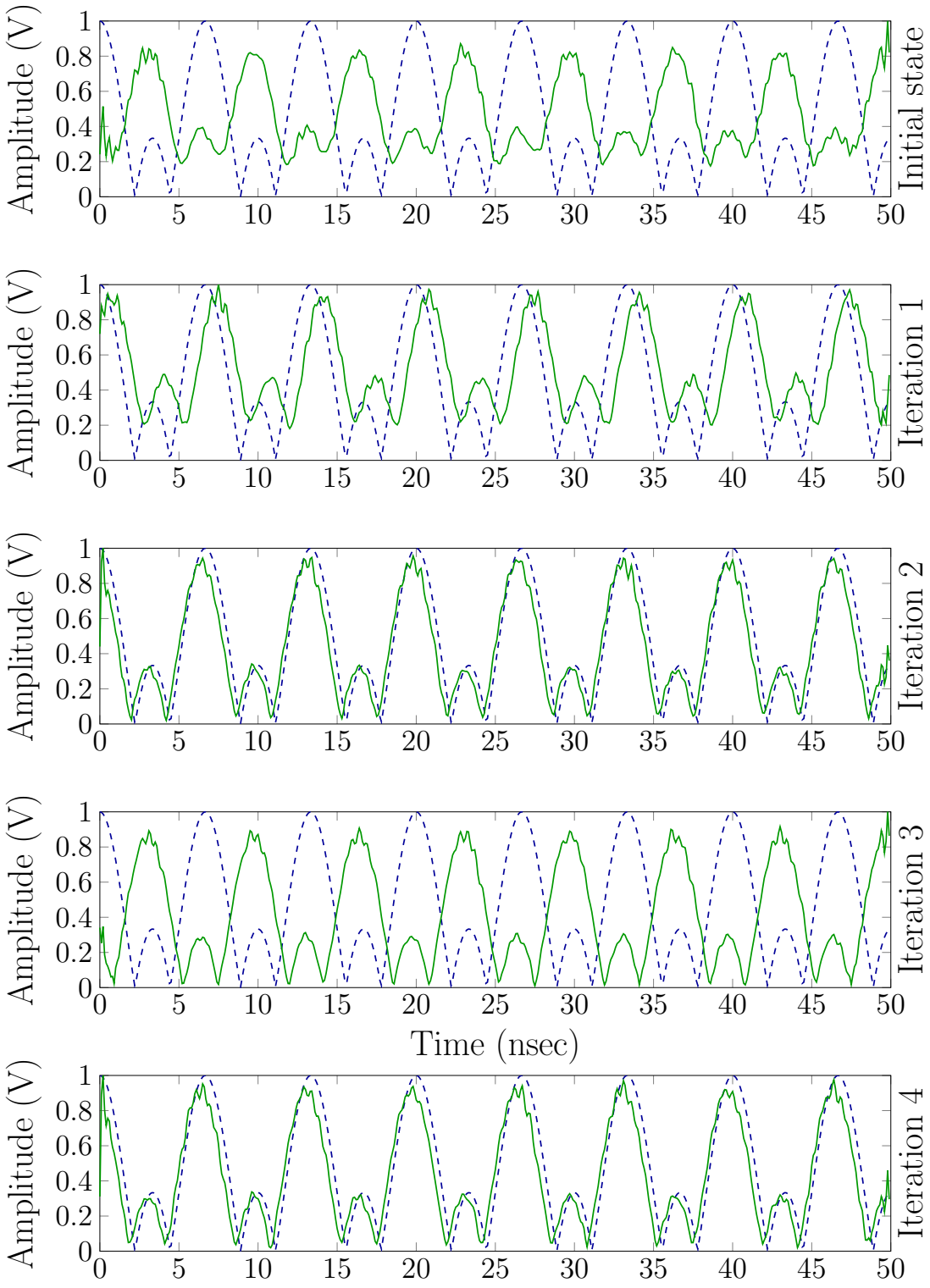

Figure 5.14: Evolution of the measured multicarrier signal (solid line) in each iteration compared to the ideal multicarrier signal (dashed line) for the RF high power S-band carriers example.

5.7 List of own publications and projects

The multicarrier generation techniques presented in this chapter have been subject to peer review, and have been accepted in several international journals and conferences. This section lists all the author's publications related to this topic.

5.7.1 Journal papers

- **Ò. Monerris**, E. Díaz, V.E. Boria and B. Gimeno, "High-power multicarrier generation for RF breakdown testing", in IEEE Transactions on Electron Devices, vol. 64, no. 2, pp. 556-563, Feb. 2017, doi: 10.1109/TED.2016.2641243.

5.7.2 Conference papers

- **Ò. Monerris**, E. Díaz , V.E. Boria and B. Gimeno, "Generación de señales multiportadora en la zona crítica del componented de RF", in XXXII Simposium de la Unión Científica Internacional de Radio (URSI). Cartagena, Spain, September 2017.

Chapter 6

Multicarrier generation using wideband vector signal generators

6.1 Summary

In this chapter several strategies for the generation of high power multicarrier signals using wideband digital vector generators are presented. The benefit of using wideband digital generators lies in the fact that their phase stability over time exceed the performance that can be obtained from non phase-coherent analog generators. However, the strategies presented in this chapter do not aim to re-purpose already existing hardware. So the improved performance comes at the cost of requiring new RF equipment [117].

The benefits of using the generation techniques shown in this chapter are:

- Minimal RF equipment phase drift.
- Less RF equipment required.
- Enhanced phase stability when using modulated carriers.
- Better suited for long tests (> 2h) with a constant phase scheme.

The basic equations required to create low power multicarrier signals using digital generators are widely known, and can be found in literature [128, 129]. However, this chapter does not only create these low power signals, but investigates several approaches to implement a high power multicarrier system. Besides creating the signal, it is needed that some requirements applicable to multipactor testing [8] are met in the final signal.

The chapter is structured as follows. In section 6.2, the theory to generate multicarrier signal in the digital domain is presented. Next, section 6.3 covers four strategies used to create RF high power signals. The signal tuning equations are similar to the ones used in chapter 5. However, the differences found when used with digital signal generators are analyzed in section 6.4. In contrast to the previous chapter, where each generator handles one carrier,

multicarrier signal generation using wideband digital signal generators introduces larger signal distortion. In order to improve the distortion before amplifying the low power signals, different options to reduce the distortion are shown in section 6.5. To experimentally validate the most complex strategy for the multicarrier generation, out of the four presented, some experimental measurements are shown in section 6.6. To conclude this chapter, section 6.7 highlights the most relevant conclusions.

6.2 Theory

The high power multicarrier signal generation begins with the determination of a mathematical expression which creates a complex signal with the desired parameters. This expression is widely known and can be found in [128, 129] for non-modulated carriers. The equation of interest is:

$$mc(t) = \sum_{i=0}^{N} a_i \exp\left(j(2\pi \cdot f_i \cdot t + \varphi_i)\right) \tag{6.1}$$

where N is the number of carriers, t the time and f_i, φ_i and a_i are, respectively, the carrier frequency (in Hz), initial phase (in radians) and the amplitude (in Volts) for the $i-$th carrier.

This signal can be transformed in its baseband equivalent by shifting the carriers frequencies to their baseband domain. The equation to be applied is:

$$f_{BB_i} = f_i - f_c \tag{6.2}$$

being f_i the RF frequency for the $i - th$ carrier (in Hz) and f_c the frequency shift to be applied (in Hz), or in practical terms, the signal generator center frequency.

When the frequency shift is such that,

$$f_c = \sum_{i=0}^{N} \frac{f_i}{N} \tag{6.3}$$

then, the multicarrier signal

$$mc(t) = \sum_{i=0}^{N} a_i \exp\left(j(2\pi \cdot f_{BB_i} \cdot t + \varphi_i)\right) \tag{6.4}$$

is a basedband signal centered at 0 Hz.

This signal is still a mathematical representation of the desired multicarrier signal. However, if an adequate sampling rate is used, a vector of complex number can be obtained. This succession of complex numbers can be loaded in a wideband signal generator configured at a center frequency of f_c, which will produce a physical electrical signal with the desired multicarrier signal form. In section 6.2.2, the correct approach to sample the multicarrier signal is presented.

Following in the mathematical realm, in addition to the non-modulated case considered in (6.4), it is possible to have modulated carriers adding a few terms to the same mathematical expression. These terms are the complex representation of the modulated signal found in each carrier $s_i(t)$, using $s_i(t) = 1$ for those carriers which are non-modulated.

$$mc(t) = \sum_{i=1}^{N} s_i(t) \cdot a_i \exp\left(j(2\pi \cdot f_{BB_i} \cdot t + \varphi_i)\right) \tag{6.5}$$

being $s_i(t)$ the normalized complex baseband modulated waveform for the $i-$ th carrier.

6.2.1 Baseband representation of modulated signals

In this section, as means of example, the equations to determine the $s(t) = I + jQ$ expression of a digitally modulated BPSK signal, and an analog modulated chirp, are shown; being I the in-phase and Q the quadrature components.

For a BPSK signal without pulse shaping, the equations to determine I and Q are:

$$I = \begin{cases} 1 & \text{if } bit = 1 \\ -1 & \text{if } bit = 0 \end{cases} \tag{6.6}$$

$$Q = 0 \tag{6.7}$$

being bit the digital bit to be transmitted.

For an analog modulated chirp signal, the equations to obtain the complex basedbad signal are:

$$a = \pi(f_1 - f_0)/t_1 \tag{6.8}$$

$$b = 2\pi f_0 \tag{6.9}$$

$$s(t) = \exp\left(j(a \cdot t^2 + b \cdot t + \varphi)\right) \tag{6.10}$$

where f_0 and f_1 are initial and final baseband chirp signal frequencies in Hz, respectively, φ is the chirp initial phase in radians, and $t \in [0, t_1]$ is the current time in seconds. From $s(t)$ it can be obtained that $I(t) = \Re(s(t))$ and $Q(t) = \Im(s(t))$.

6.2.2 Discrete representation of the complex multicarrier signal

In the discrete domain (6.5) is written as

$$mc[n] = \sum_{i=1}^{N} s_i[n] a_i \exp\left(j(2\pi \cdot f_{BB_i} \cdot t[n] + \varphi_i)\right) \text{ for } n = 0, .., N \tag{6.11}$$

being N the total number of samples, and $t[n]$ the time vector.

The time vector is defined as $t[n] = n/f_s$ for $n \in \mathbb{N}$, being f_s the sampling frequency being used. In order to properly generate the complex signal, whilst minimizing the total number of samples, the sampling frequency must meet the Nyquist criteria for the complex signals which, in practice, implies that the signal bandwidth (BW) satisfies $BW < 0.8 \cdot f_s$. Applying this constraint to the multicarrier signal generation defined in (equation 6.11) results in

$$BW = (max(f_{BB_i}) - min(f_{BB_j})) < 0.8 \cdot f_s, \quad \forall i, j \in 1, \ldots, N \quad i \neq j. \tag{6.12}$$

where f_{BB_i} and f_{BB_j} are the baseband frequencies for the $i-th$ and $j-th$ carrier, respectively.

Next question to be solved is how to create a continuous multicarrier signal (infinite length) using a memory constrained device. The solution to this problem is to create a finite length vector which, when repeated, creates a continuous periodic multicarrier signal. However, it is not possible to create this continuity effect in all the scenarios, and several constraints must be met in order to produce a periodic signal from (6.11). These constraints can be divided as strong and weak. Whereas the strong constraints must be met, the weak constraints should be met in order to obtain the most accurate performance possible.

Strong The non-modulated multicarrier signal must be periodic (T_{env}).

Strong The sub-carrier modulation must have a finite length which fits in the generator memory sampled at f_s.

Strong The length of all the sub-carrier modulations must be any integer number of T_{env}.

Weak The sampling frequency is related with the carrier frequencies by a rational number to obtain better control of the peak values.

Weak The number of samples N is a hardware-dependent power of 2. This value is not fixed and varies for different RF equipment. By using the correct number of samples, the automatic zero padding produced by some devices is prevented.

Once all the strong constraints are met, and T_{max} is known, the time vector is defined as:

$$t[n] = n/f_s \quad 0, \ldots, T_{max} \cdot f_s. \tag{6.13}$$

Finally, once the time vector is known, the final determination of the complex basedband signal is obtained using (6.11).

6.3 Strategies for multicarrier generation

In the previous section, the equations to create multicarrier signals in the digital domain have been presented. These signals can have or not modulated carriers, however, in any case they

share the same strategies in order to be translated into de desired high power signals used for multipactor testing. Next, this section presents four strategies to implement a high power multicarrier system using one or more wideband digital signal generators.

As signal distortion and mis-alignments may happen in several parts of the RF path from the vector signal generator to the device under test, all the strategies have a feedback loop which is used to adjust the different signal parameters such as amplitude, frequency and phase. This is necessary because the splitting, amplification or combining stages are not equalized, thus producing an undesired imbalance which may change with time. This feedback loop is implemented by sampling the high power signal using either a vector signal analyzer or an oscilloscope.

When more than one high power amplifier is used to create the signal, an output multiplexer is required [109, 110, 130] to combine the outputs of the RF high power amplifiers. On top of that, some of the strategies may also require from input multiplexers, which can be implemented in a similar technology but with reduced power requirements. However, these microwave devices are not always required, as can be found in the following sections.

6.3.1 Strategy 1: one generator – one amplifier – without IMUX

The first strategy is the most basic one. In this case a digital vector signal generator (VSA) creates all the tones. Then, one single high power amplifier increases the signal power level to the desired value. Finally, the multicarrier signal, ready to be used for multipactor testing, is found in the multicarrier signal (MCS) node. A feedback loop is implemented by means of a vector signal analyzer (VSA) or an oscilloscope to compensate for amplitude and/or phase distortion happening in the amplifier. The block diagram of this strategy is shown in Fig. 6.1.

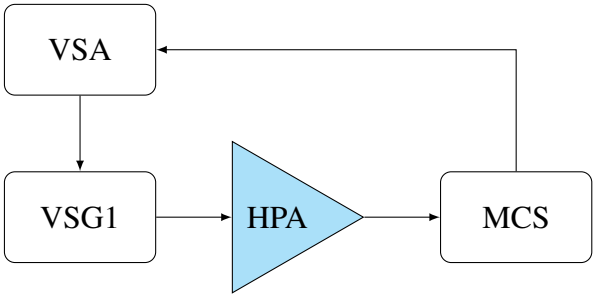

Figure 6.1: Basic multicarrier generation diagram by means of one VSG and one HPA.

6.3.2 Strategy 2: one generator – M amplifiers – with IMUX

The second strategy uses one digital signal generator and several amplifiers. In this strategy, each amplifier can handle one or several carriers. Being the case in which one carrier is amplified per each amplifier the most complex one (see Fig. 6.2). This approach has the benefit

of providing a better spectral purity and a larger peak power. The enhanced spectral purity is due to the lower number of carriers in each power amplifier: for the best performance only one per amplifier.

By reducing the number of carrier handled in each amplifier, inter-modulation products are reduced. Additionally, the amplifier back-off that is required in Fig. 6.1 due to the presence of several tones, is no longer required in the case of having a lower number of carriers, or even just one. This allows to drive the amplifiers to saturation when only one unmodulated carrier is feed to each unit.

The significant drawbacks of this approach is: the need for an input multiplexer (IMUX) and an output multiplexer (OMUX), which must be designed for a specific set of frequencies.

The design complexity of the input multiplexer depends on the value for the maximum losses acceptable between the RF generator and the RF power amplifiers. Its design can be as simple as a power divider in combination with a bank of bandpass filters, or advanced structures such as a waveguide manifold-based multiplexer [109].

In this strategy a feedback loop is implemented in a similar way as to strategy 1.

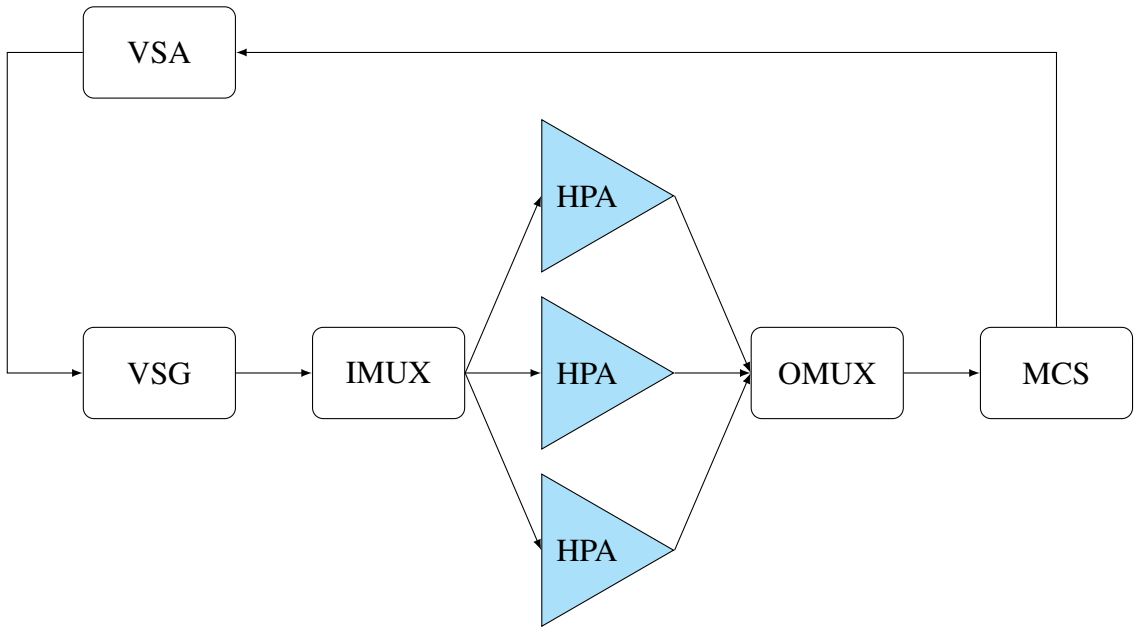

Figure 6.2: Multicarrier generation diagram employing one VSG and three HPAs. Note the need of an input multiplexer in order to feed only one carrier to each amplifier.

6.3.3 Strategy 3: N generators – N amplifiers – without IMUX

The third approach uses not one but two (or more) phase-coherent digital signal generators (see Fig. 6.3). Each generator is connected to one high power amplifier. In this scenario, each generator may create one or several tones. However, input multiplexers are not used.

As a consequence of having several RF signal generators, it is more likely that it will be possible to drive each amplifier without requiring pre-amplification.

In this strategy a feedback loop is implemented in a similar way as to strategy 1.

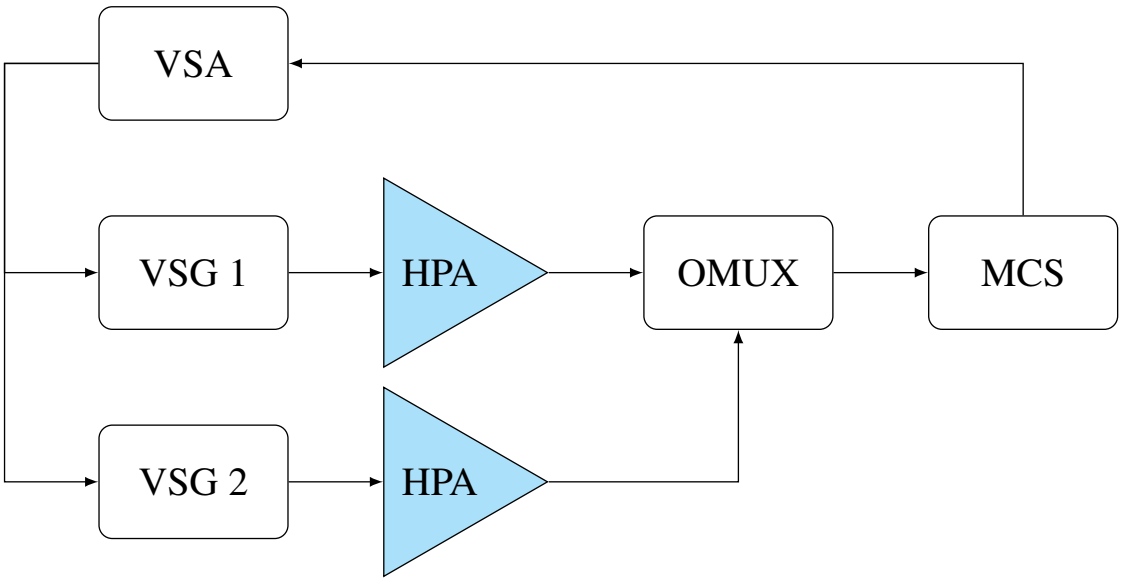

Figure 6.3: Multicarrier generation diagram employing two VSGs and two HPAs. In this case only an output multiplexer is required to combine the signals from the amplifiers.

6.3.4 Strategy 4: N generators – M amplifiers – with IMUX

The last strategy (see Fig. 6.4) consists of a multi-vector signal generator driving several high power amplifiers. In contrast to strategy 3, now each amplifier strictly handles only one carrier.

This approach presents several advantages: it improves the high power signal spectrum by reducing the active inter-modulation produced in the high power amplifiers; and it reduces the back-off used to drive each amplifier, increasing the maximum RF peak power.

The number of signal generators is selected to avoid the use of pre-amplifiers. This is achieved by ensuring that the losses from the generator outputs to the amplifier inputs are low enough, so that the RF amplitude at the HPA input is large enough to drive it to saturation. Typically, RF high power amplifiers reach saturation when 0 dBm are applied to the input port. It is important to remark that this requirement shall be met for the most demanding phase scheme, which is an in-phase multicarrier scenario.

One major drawback of this implementation is that one or more IMUXes are also required. This reduces the system reconfigurabilty as the IMUX are designed for a given set of center frequencies and bandwidths. However, as the IMUXes do have more relaxed specification than the OMUX in terms of power handling, so they are cheaper and easier to design and manufacture.

To conclude this part, it is worth mentioning that this strategy has been proposed to implement an upgrade on the well known European Space Agency multicarrier facility available in Val Space Consortium [131].

European Space Agency (ESA) multicarrier system

This section describers a proposed upgrade fo the 10 Ku-bad channel facility available in the European High Power RF Space Laboratory. In this facility the multicarrier signal achieves a maximum output power of 2.4 kW CW at the input port of the device under test. Each amplifier handles only one carrier and is placed in two rack columns, one for the odd carriers and another for the even ones.

For the practical implementation of this facility, we have followed the strategy 4. So that it handles the odd carriers in one RF generator, and the even in the other unit (see Fig. 6.4). This approach simplifies the IMUX design, as channel spacing is twice that of the OMUX.

However, in order to obtain improved phase coherency, both signal generators share the local oscillator and trigger lines to provide phase-coherent signal generation in both outputs. Additionally, having two vector signal generators also allows driving the amplifiers without pre-amplification.

Finally, one single vector signal analyzer or an oscilloscope is used to implement the feedback loop and then adjust the amplitude and phase of the generated signal.

6.3.5 Summary of the digital multicarrier generation strategies

Once all the strategies have been presented, Table 6.1 contains a review of the key parameters for each one. This table must be read considering that $\uparrow\uparrow$ represents the best option among the four and $\downarrow\downarrow$ the worst one. However, being the worst strategy in one particular aspect does not imply that it might be more suitable under certain scenarios.

For instance, strategy 1 could be the most suitable one when a 100 carrier test is required in a component at a peak power level that, let us say, keeps a peak power level below 20 dB of the amplifier back-off one.. Whereas strategy 4 might be the most convenient one when the required output power is almost the sum of the saturation power of the M amplifiers being used, and M is large enough so only one signal generator cannot drive all the amplifiers simultaneously.

Strategy	Number of carriers	Output power	Signal fidelity	Reconfigurability	Solution size
1	⇓	⇓	⇓	⇑	⇑
2	↓	↑	↑	↓	⇓
3	↑	↓	↓	↑	↑
4	⇑	⇑	↑	⇓	⇓
Legend	⇑: excellent ↓: bad		↑: good ⇓: worst		

Table 6.1: Summary of the four multicarrier generation strategies, and their strong and weak points when setting up a multipactor test system.

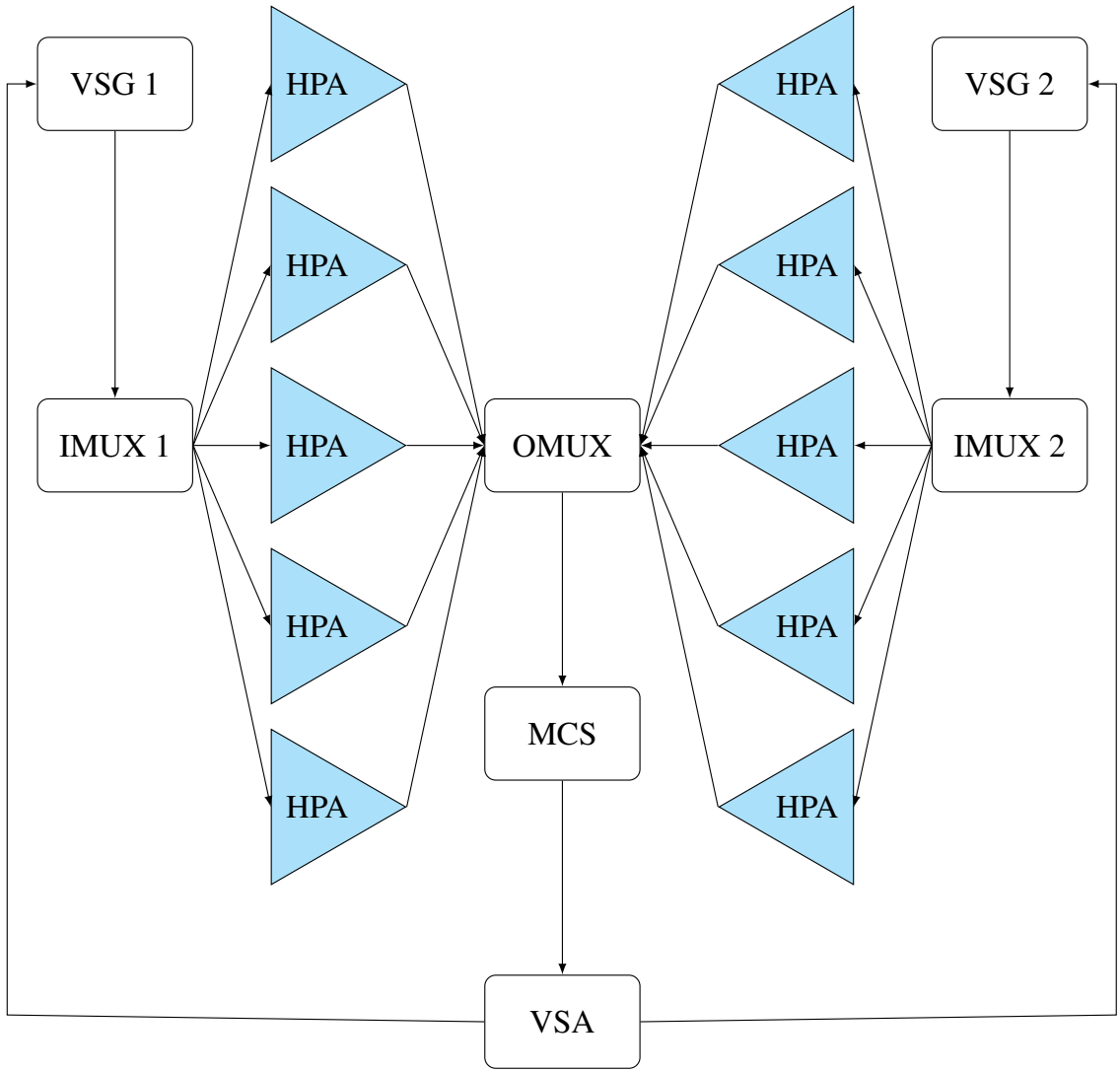

Figure 6.4: Ten channel multicarrier generation diagram by means of two VSGs and ten HPAs. A couple of low power input multiplexer are required to divide each of the two input signals.

6.4 Multicarrier signal adjustment

Although the RF low power signal found at the vector signal generator output is very accurate, the different stages required to obtain the RF high power signals are not equalized, and the amplitude or phase may drift over time. Different insertion losses, gain or phase change over time are factors to be taken into account in real time to have and maintain the desired multicarrier signal.

Out of the three set of parameters to be adjusted in a multicarrier signal: amplitude, frequency and phase, only the frequency remains invariant and requires no adjustment. Several method used to recover the required amplitude and phase levels are introduced in this section.

This section is the core of the high power multicarrier generation algorithm, and has many parts in common with the methods used in chapter 5. Without these adjustments, the high power signal would be far different from the desired one.

Signal adjustment must be done periodically in multipactor testing, in order to ensure that any drift is corrected. The recommended adjustment sequence is:

1. Verify carrier frequencies.
2. Adjust amplitude.
3. Adjust phase.
4. Adjust amplitude.
5. Repeat from 2.

Firstly, different methods to recover the RF power level in each carrier is presented. Secondly, the way to verify the location of the carrier frequency is mentioned. Finally, the method to recover the phase is shown.

6.4.1 RF power level recovery

To recover the RF power level of each channel, two approaches can be used:

1. integrate the spectral power density within the channel band; or,
2. use calibrated power sensors at the output of each HPA.

To recover the amplitude from the spectral power density, the signal sampled with the vector signal analyzer or the oscilloscope must be converted to the frequency domain. This can be done with a simple discrete Fourier transform. By integrating the signal in the different channels bandwidths, the uncalibrated RF power can be obtained.

Alternatively, to recover the RF power level from the power heads is straightforward, as a direct reading of the power sensor will provide the current value.

Considering that both approaches have been properly calibrated with the actual offset, the first option has an approximate accuracy below 0.5 dB. Whereas by using one independent power sensor for each channel, an accuracy of 0.1 dB can be easily obtained.

To obtain a calibrated RF power measurement, the calibration factor for each channel must be obtained. This can be done beforehand and, as long as the high power section is not changed, the obtained values remain invariant.

Once the RF power per carrier is known, and if there are differences with regard to the target levels, corrections must be applied. To proceed, two kind of scenarios are possible: each generator creates only one carrier (some cases of strategy 3), or each generator handles more than one carrier (strategies 1,2, 3 and 4).

When only one carrier is created in the signal generator, RF power adjustment is straightforward. By changing its output level accordingly to the difference, the high power carrier will be fine tuned to the target RF power level.

Scenarios in which more than one carrier is created in each signal generator are slightly more complicated. In this cases, the next steps are required:

1. Convert the RF power levels into voltages for the target and measured values.
2. Normalize the voltages, so that the largest one is equal to 1.
3. Obtain the difference between the target and measured values for every carrier.
4. Apply these offsets to the current amplitude values.
5. Obtain the RMS value for the multicarrier signal with the updated previous settings.
6. Obtain the RMS value for the multicarrier signal with updated settings.
7. From the RMS values, obtain the RF power difference in dB between the previous and new low power multicarrier signals.
8. Update the vector signal generator waveform with the new multicarrier signal.
9. Update the vector signal generator output level with the RF power difference obtained in step 7.

6.4.2 Frequency recovery

Major errors in the center frequencies are not common. However, it is convenient to check these values by looking to the discrete Fourier transform. Center frequencies will be close to the Fourier transform point with the highest peak value within each channel bandiwdth.

If and error is detected, the frequency offset will be, most likely, due to lack of reference frequency sharing between the vector signal generator/s and the acquisition device: vector signal analyzer or oscilloscope.

6.4.3 Phase recovery

Phase recovery is the most demanding operation in terms of computing power. Whereas for the amplitude recovery from the spectral domain requires not many frequency points, phase recovery needs a very large number of points ($> 2^{24}$) in the frequency domain data.

With respect to the algorithm, the one shown in previous chapter 5 handles this operation properly. However, as mention in the power recovery section, changing the phase of any of the carriers affects the amplitude in the other carriers created in the same vector signal generator. Correcting the generator output level by means of the RMS power delta between the previous and the updated multicarrier waveforms is good step towards minimizing the amplitude error due to a phase adjustment.

Computing the RMS value for the previous and the new low power multicarrier signals may help to keep the same RF power level after phase adjustment. Once the power offset between the waveform with and without the phase adjustment is known, the output level in the signal generator can be changed accordingly to keep the power in each carrier as settle as possible.

Finally, phase recovery is not recommended when the RF power levels are not properly adjusted. Any RF power level error will produce wrong phase corrections.

6.5 Signal conditioning

This section describes the impact of the different signal filtering stages in the high power multicarrier signal fidelity.

Except for strategy 3, where each vector signal generator handles one carrier, all the strategies produce in a stronger or weaker extend active intermodulation and harmonics at the output of the generator/s. Even the best RF equipment working in its most linear region do create this undesired effect. For the state-of-the-art arbitrary waveform generator inter-modulation is about -50 dBc and harmonics -30 dBc [132, 133]. If not filtered, these undesired tones will be further amplified alongside the actual carriers and, eventually, will create more noise due to the non-linearities of the high power amplifiers.

The typical microwave component chain for a multicarrier signal is shown in Fig. 6.5. From left to right, the RF signals progresses from the signal generator to the device under test. Once the signal is created in the generator, it goes through a succession of elements which propagates it to the device under test, amplifies it into the desired RF power level and filters undesired spectral components.

Input stage: low power RF path

Typically, the generator output is connected using coaxial cables to the next element, which can be either the multiplexer or the amplifier. This connection does not filter the signal, unless filters in coaxial technology are implemented.

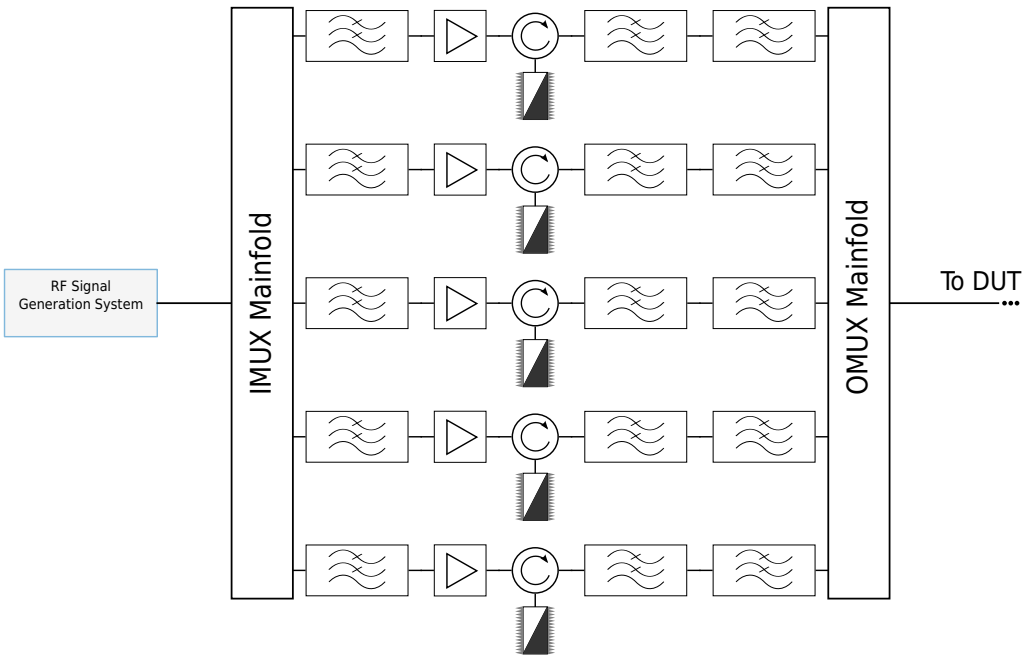

Figure 6.5: Typical signal conditioning hardware required for a multicarrier system implementation using vector signal generators.

When multiplexers are used, there is an inherent channel filtering. The key parameters to be taken into account for its design are:

- Low loss (typically <1 dB).
- Flat frequency response (typically <0.5 dB).
- Larger channel bandwidth than the output multiplexer filters (typ. +10%).
- Maximum attenuation for the local oscillator leakage (typ. >20 dB).
- Adjacent channel rejection (typ. >20 dB).

Because the output level of the signal generator limits, it is important to reduce as much as possible the input stage losses. When selecting the different elements, the objective is to keep each carrier level at the input of each amplifier at a level of 0 dBm.

Local oscillator leakage is also an important source of distortion. When using vector signal generator at its maximum bandwidth setting, it is typical to observe what is known as generator local oscillator leakage [134]. Filtering out this undesired tone is critical in this stage, as it is the strongest noise component being produced by the digital signal generator. The tone is located at the RF equipment center frequency. The noise level produced by the local oscillator leakage depends only on the signal generator output power level setting.

In case the signal generator has a very large bandwidth, it is recommended to set the local oscillator above or below the furthest multicarrier frequency, where it is easier to remove. However, if the generator bandwidth is limited, this tone will typically be located close to the mean frequency of the multicarrier band. In that case the input multiplexer should be designed to filter this frequency out as much as possible (> 20 dB).

It is highly recommended to digitally shift the multicarrier signal if the local oscillator overlaps with any channel. In case the the multicarrier signal mean frequency overlaps with a channel, typical when an odd number of carriers are used, digital down-conversion must be applied to shift the local oscillator outside any channel bandwidth. This is achieved by selecting a different center frequency in (6.3), so f_c is located between two adjacent channels.

Output stage: high power RF path

In the high power section there are four major contributors to the signal conditioning:

- Transmission line type.
- High power amplifier.
- Circulator and harmonic filtering.
- Output multiplexer.

The transmission line type may contribute to remove many of the undesired tones. If rectangular waveguide is used, its cut-off frequency will completely attenuate all the low frequency components by acting as a high pass filter.

Then, for the high frequencies, the high power amplifier bandwidth will ensure that harmonics are not amplified, although it will create more active inter-modulation by it-self. Additionally the circulators, and harmonic filters at the output of the high power amplifier will attenuate these tones even further.

Finally, the output multiplexer combines the different channels and filters any undesired spectral component within the band of interest (frequency band comprised between the lowest and highest multicarrier frequencies). The channel bandwidth shall be reduced to the minimum one, which for communication satellites goes typically from 36 to 72 MHz [135].

6.6 Experimental results

This section presents a set of experimental results which show the generation of a real multicarrier signal. The results have been obtained in order to implement a multicarrier signal following strategy 4.

All the measurements have been made using two National Instrument PXIe-5820 Vector Signal Transcivers (VST). Both units are installed in the same PXI chassis and share the

local oscillator and the trigger lines. For signal acquisition a 40 GSps Lecroy oscilloscope and a Rhode & Schwarz FSPU 26.5 GHz spectrum analyzer have been used.

The experimental validation advanced towards the final multicarrier generation validation in small steps. In first place, the correct phase coherency of the dual VSG setup is confirmed in section 6.6.1. Next, the phase drift recorded between two traveling wave tubes high power amplifiers (TWTA) is characterized in section 6.6.2. Then, the signal distortion obtained at the output of the digital signal generators using strategy 4 is shown in section 6.6.3. Finally, section 6.6.4 shows the low power results for the considered strategy.

6.6.1 Phase coherence performance

This section proves that the phase drift between two phase coherent digtal signal generators is negligible in the long term.

For the experimental validation a 11 GHz signal is generated in each VST and recorded in two oscilloscope channels for several hours. The setup used for this measurement is shown in Fig. 6.6.

Once the measurement is completed, the phase for each channel is recovered using a LabView algorithm used to recover the amplitude, frequency and phase of a single tone signal. For a given time instant two phase values are available, being the different between them the phase offset to be measured. For a phase coherent system this offset may not be zero, but must be constant over time.

Results shown in Fig. 6.7 displays the phase difference between the two generators from a cold start. From the graph, it is clear that the system is phase coherent in the long term as a phase drift lower than 0.1 degree per hour has been recorded after 1 hour of warm up.

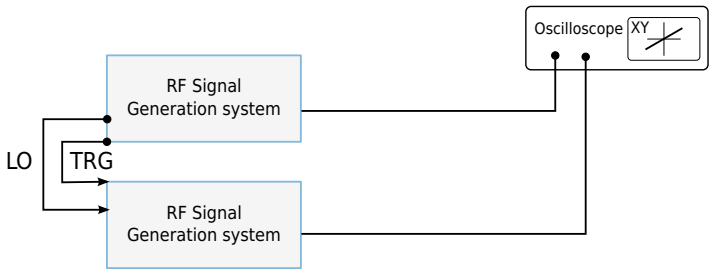

Figure 6.6: Measurement schematic for the phase drift characterization over time for two vector signal generators.

6.6.2 High power amplifier phase drift

The second validation consists in the measurement of the phase drift between two high power amplifiers (TWTs in this case).

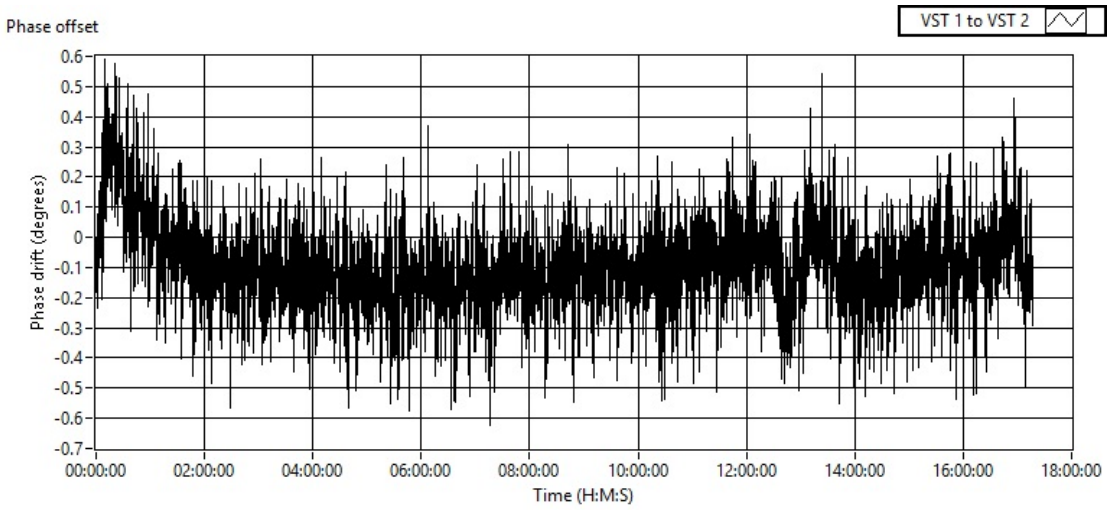

Figure 6.7: Phase drift over time for two NI PXIe-5820 units when generating an 0 dBm tone at 11 GHz.

As the multicarrier generation algorithm does not run in real time, the system drift must be slow (<3 degrees per minute) in order to configure and keep a given phase scheme in the short term.

As a setup comprised of two generators has been confirmed to be phase locked, the only phase drift source are the amplifiers. For the experimental measurement only one signal source is used. This ensures no phase drift at all in the short and long term may occur. This setup ensures that both TWTAs are feed with a phase coherent signal, see Fig. 6.8.

Measurements shown in Fig. 6.9 indicate that over the first 90 minutes of operation there is a noticeable phase drift. However, it is slow enough for the algorithm to compensate it (<3 degrees per minute). Then, once the amplifiers reach temperature stabilization, phase drift is reduced to less than 1 degree per hour.

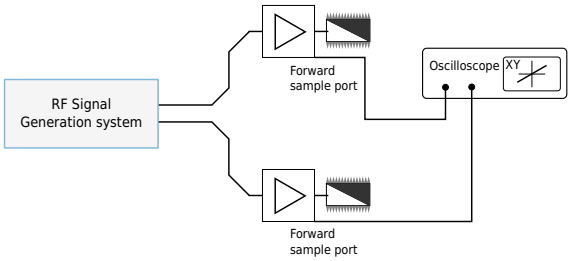

Figure 6.8: Measurement schematic the phase drift characterization of two high power amplifiers (TWTAs) when amplifying an 11 GHz tone.

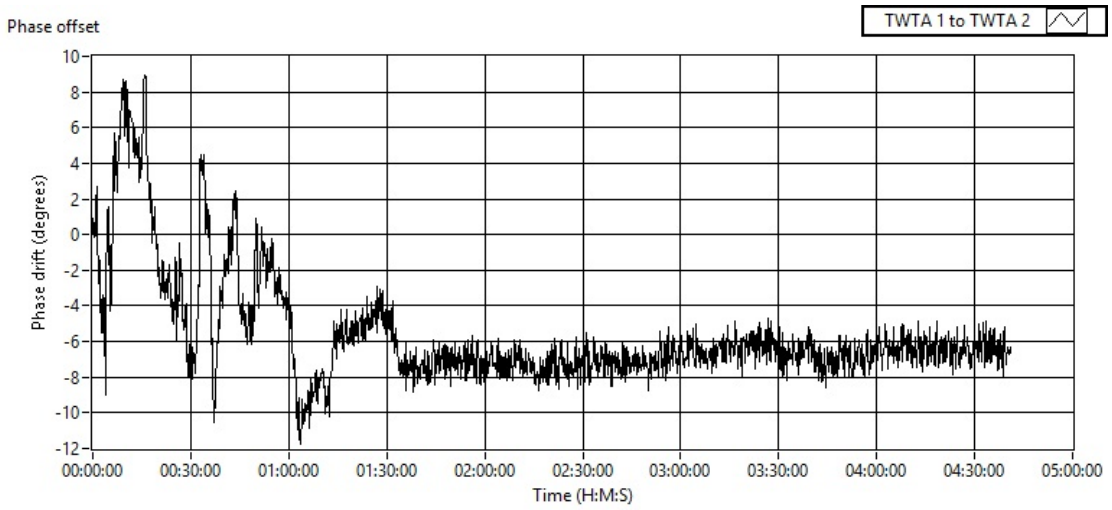

Figure 6.9: Phase drift over time for two ETM 400IJ high power traveling wave tube amplifiers with a 10 W carrier signal at 11 GHz in each amplifier. Driving source is common for both TWTAs.

6.6.3 Undersired spectral content and inter-modulation distortion

Next, the noise characterization when creating a multicarrier signal by means of strategy 4 is considered. When digitally creating any signal, there are several tones which appear alongside the desired ones. These are: harmonics, local oscillator leakage and active inter-modulation tones.

Because of their low amplitude, these tones have an small impact for some types of high power testing. However, it is of major relevance for passive inter-modulation (PIM) testing. Whereas for multipactor, power handling or corona testing these undesired signals, which are further filtered by the IMUX and OMUX networks, do have an small impact.

In PIM testing the active inter-modulation is not acceptable at all, as it overlaps in the same frequencies as the PIM terms, but with larger amplitude. However, when more than one signal generator is used to create the multicarrier signals, there are some PIM tones which do not overlap with the active inter-modulation tones. So, potentially, it could be possible to use this implementation for PIM testing, although with major constrains in the PIM tones to be measured.

In this section the measured spectrum of a multicarrier signal is shown. To obtain the results each VST generates five tones, odd and even carriers, respectively. The signal combination is done using a 3 dB hybrid device.

The setup used for this measurement can be seen in Fig. 6.10. One Rhode & Schwarz FSPU 26.5 GHz spectrum analyzer has been used. A very small resolution bandwidth (500 Hz) has been configured in order to reduce the noise and increment the dynamic range. Sweep time has been larger than 4 hours.

The tone center frequencies (in MHz) are obtained from

$$f_i = 10713 + i \cdot 99 \quad i = 0, \ldots, 9. \tag{6.14}$$

The phase is set to zero and amplitude is the same for all tones.

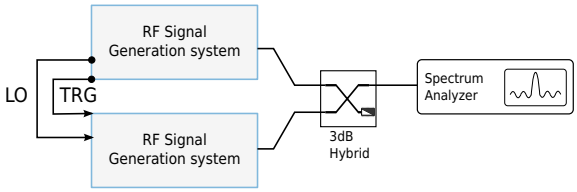

Figure 6.10: Measurement schematic for the wide band inter-modulation noise when creating a multicarrier signal using two phase-coherent vector signal transceivers.

The spectrum displayed in Fig. 6.11 shows the actual tones and the spurious signals. The measurement covers from 20 Hz to 26.5 GHz.

As expected, the acquired data analysis indicates that the spectral contents include many more tones than the desired ones:

- Intermodulation tones close to the carriers.
- Intermodulation tones close to DC.
- Intermodulation tones around the second harmonic frequencies.
- Harmonic components.
- Local oscillator leakage.

In Figure 6.12, the local oscillator can be observed when only the odd carriers are active (6.12a) and when odd an even carriers are active (6.12b). In Figure 6.12a the local oscillator is shown at 11.16 GHz to be about -30 dBc with respect to the carrier. An inter-modulation tone located at the six-th carrier frequency is also observed at -50 dBc. When the odd and even carriers are enabled the local oscillator tone is reduced, most likely due to a partial out-of-phase combination of the local oscillator leakage produced in each generator.

As a remark, from the results shown in Figures 6.12b and 6.12a can be observed that in a dual vector signal generator set-up, it should be possible to reduce the local oscillator noise level by means of an out-of-phase combination of the tone coming from each generator. To further cancel this tone the local oscillator phase in one of the generators should be adjusted. Then, the digital phase of each the carrier in that generator should be corrected by this phase shift.

6.6.4 Multicarrier signal generation

This final verification section shows the performance obtained when creating a low power multicarrier signal. In this example a system composed by two phase coherent vector signal generators have been employed. For the signal acquisition an oscilloscope is used. A schematic of the test bed is shown in Figures 6.13 and 6.14.

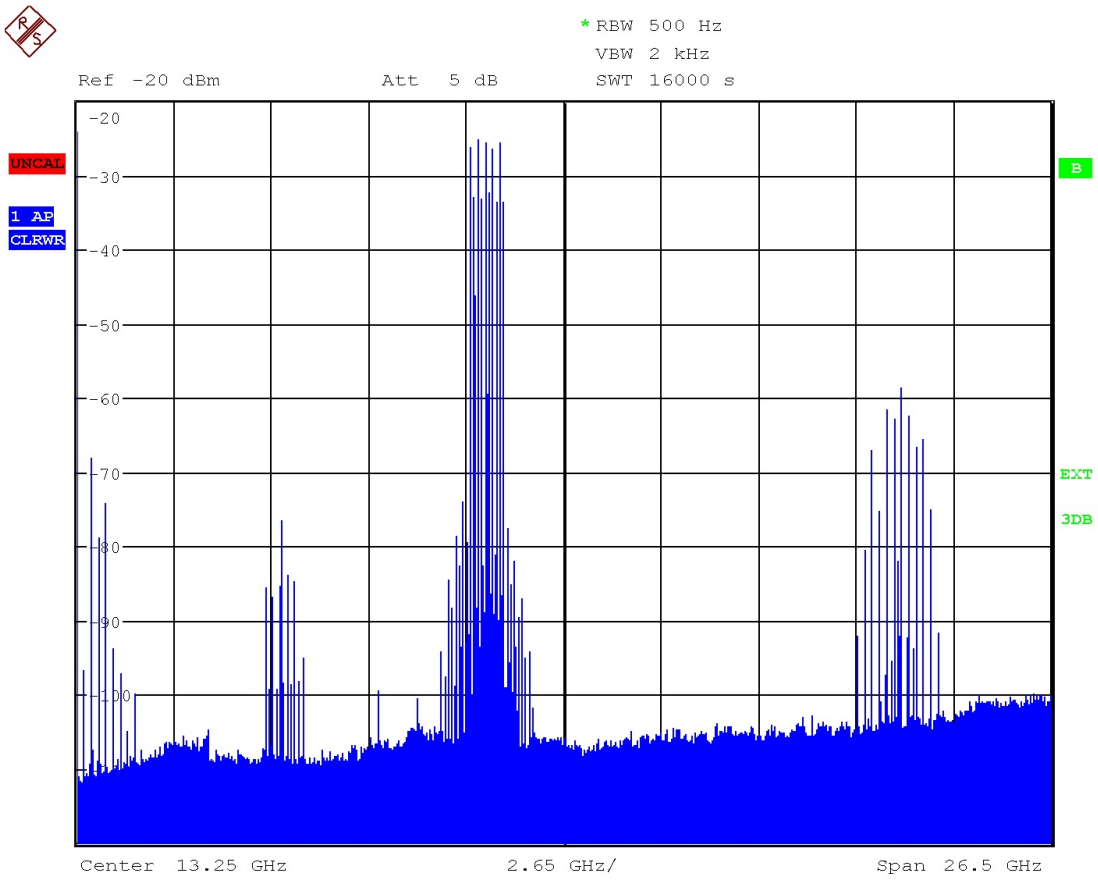

Figure 6.11: Wide band measurement for a ten tone multicarrier signal generated using two vector signal transceivers in a 5+5 approach. Notice the large amount of low energy intermodulation tones.

It is important to remark that although the RF amplitude and phase levels shall be adjusted, it is convenient not to change the phase until the amplitude has been properly recovered. Applying a phase recovery when RF amplitude level is not properly adjusted may lead to incorrect phase results.

The signal to be generated (low power) is a ten carrier signal with a frequency spacing of 100 MHz. The RF power is arbitrarily set to 1 mW per carrier. The phase scheme has been set to in-phase. The tones center frequencies (in MHz) are obtained from,

$$f_i = 10713 + i \cdot 100 \quad i = 0, \ldots, 9. \tag{6.15}$$

Firstly, Figure 6.15 shows the RF power level per carrier value as the algorithm iterates. The RF power level is adjusted in every iteration. It must be noted that phase adjustment produces a change in signal envelope, which has consequences in the RF power level for every carrier (iterations 7 and 10).

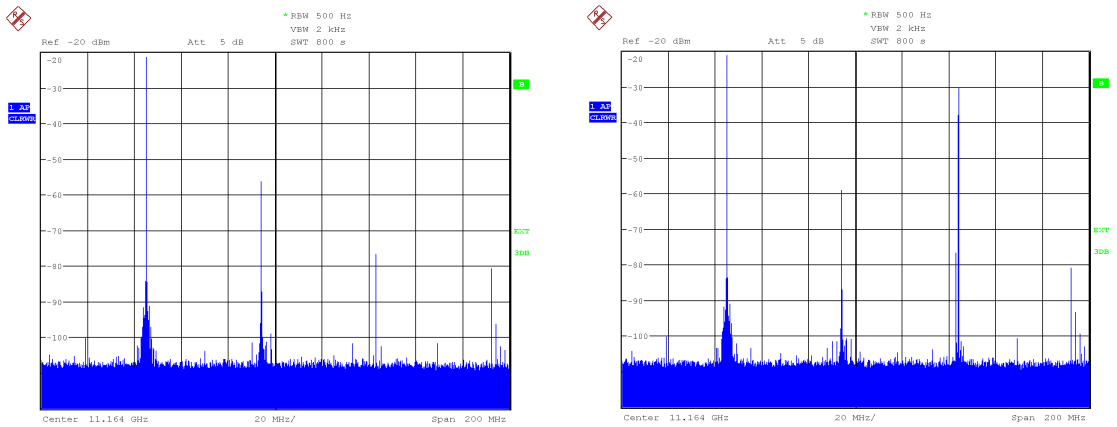

(a) Only odd carriers active

(b) Odd and even carriers active

Figure 6.12: In-band spectrum for the 5^{th} and 6^{th} carriers.

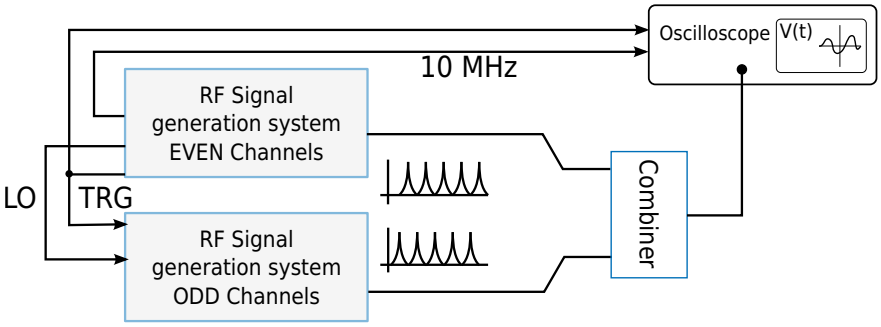

Figure 6.13: Test bed used to validate the dual phase coherent signal generation method to create a ten carrier signal.

Secondly, Figure 6.16 shows the phase error (of each carrier) over time. It is worth mentioning that phase is adjusted only in iterations $6 \rightarrow 7$ and $9 \rightarrow 10$. Final error is very good, i.e. < 0.1 radians per carrier.

With respect to the actual multicarrier envelope shape, Figures 6.17 to 6.19 display the evolution of the generated multicarrier signal. In Figure 6.17 the initial waveform shape is shown. This signal is the one measured in the oscilloscope for iteration 0. Then, in Figure 6.18 the waveform in iteration 7 is shown. Finally, Figure 6.19 shows the final multicarrier waveform after iteration 10.

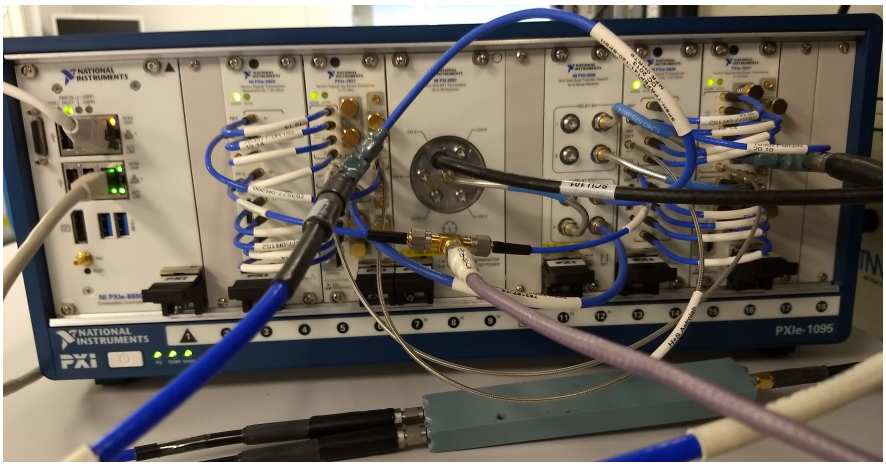

Figure 6.14: Pair of vector signal generator used to obtain the experimental results.

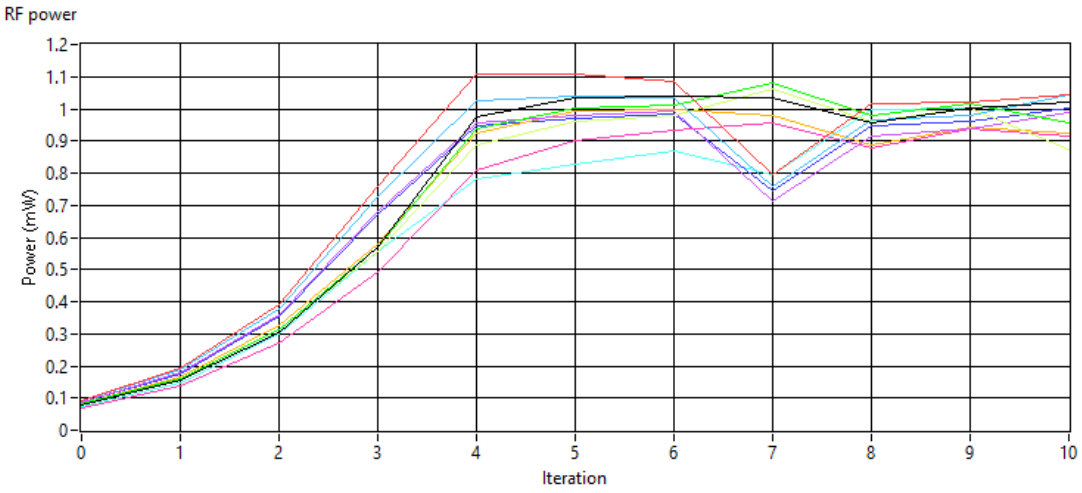

Figure 6.15: RF power recovered in each algorithm iteration. This value is computed from the integral of the spectral density in all the channels bandwidth. After each phase adjustment, a small error in the RF power value is produced and must be corrected.

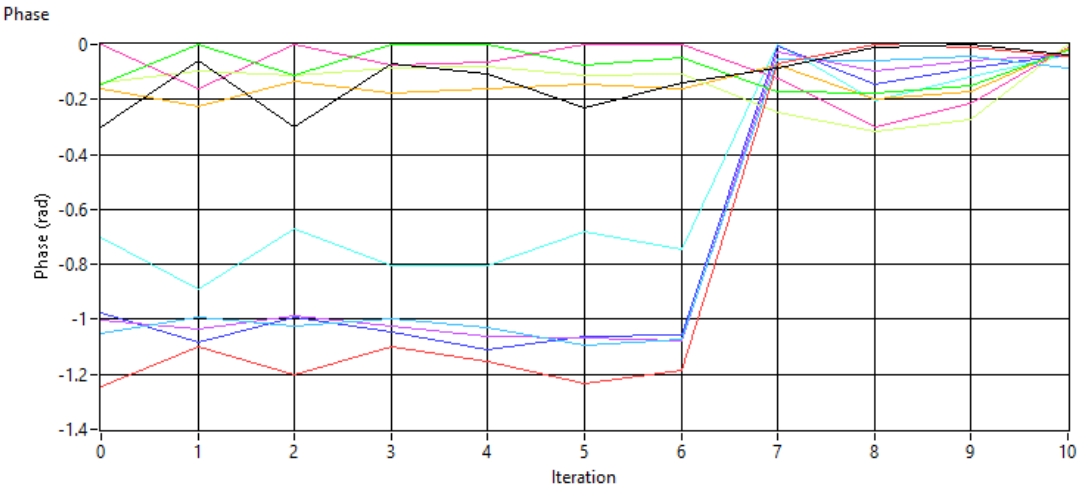

Figure 6.16: Carrier phase recovered in each algoritm iteration. Although this parameter is computed in every iteration, phase adjustment is only applied in $6 \rightarrow 7$ and $9 \rightarrow 10$.

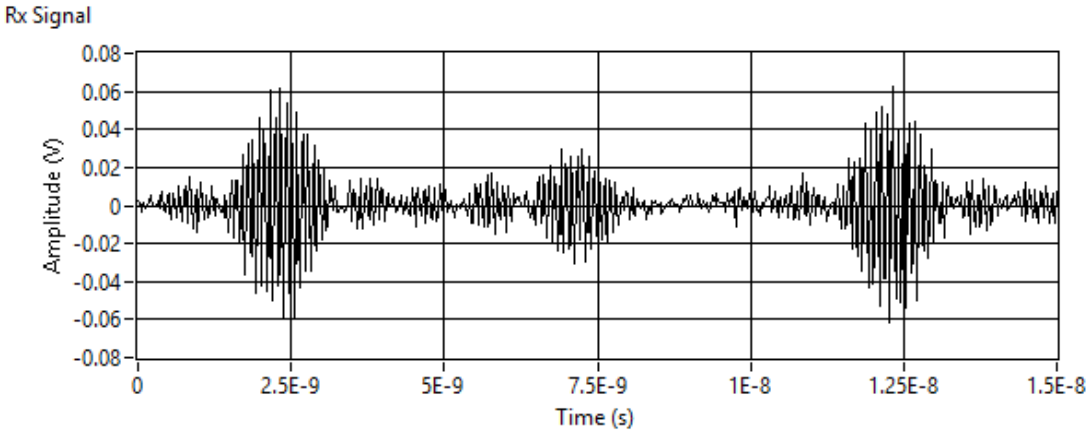

Figure 6.17: Initial multicarrier waveform shape, as recorded in iteration 0.

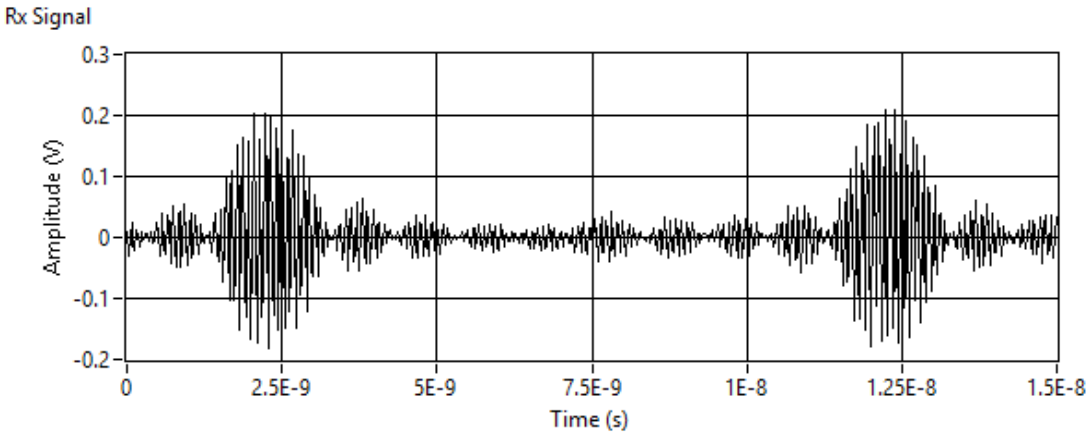

Figure 6.18: Intermediate multicarrier waveform shape, as recorded in iteration 7. Improvements are clearly visible, however there is still a large lobe in the center part.

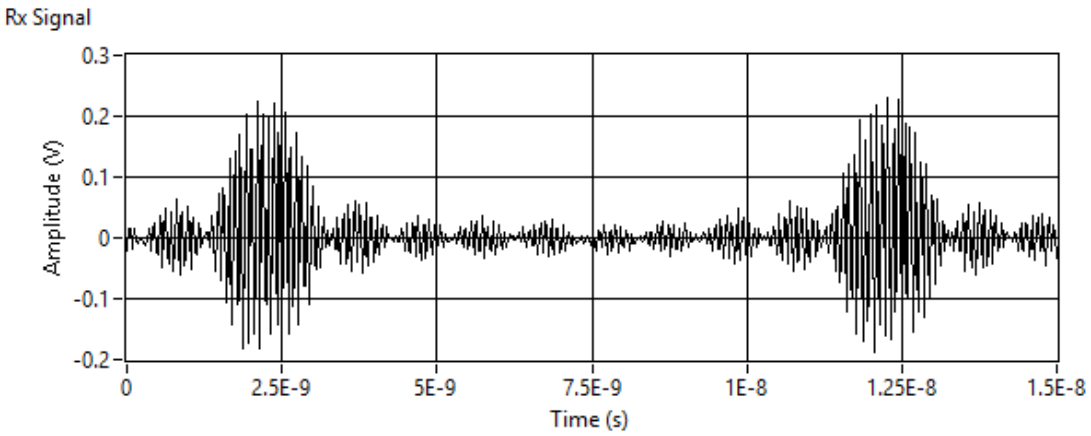

Figure 6.19: Final multicarrier waveform shape, as recorded in iteration 10. Finally, the center lobes follow the expected shape for an in-phase 10 carrier signal.

6.7 Conclusions

Four strategies for the generation of multicarrier signals using digital signal generators have been presented. All the strategies do allow the generation of modulated and/or non-modulated carriers. Among the benefits of this generation method the next ones should be highlighted: enhanced phase stability, reduced number of RF equipment and fast re-configuration.

However, digital generation has several constraints that, in the case of multipactor testing, do not affect in a great extend the typical test procedure. Constraints found in this implementation, such as the limits in setting arbitrary frequencies or about the maximum length of the modulated signals, can be met without modifying the device overall multipactor response (small frequency shifts).

Strictly speaking, multipactor testing using the techniques shown in this chapter or those found in chapter 3 is equivalent. However, digital generation of multicarrier signals is better suited long testing with the same phase scheme, as phase drift is minimum.

Another important benefit of the method presented in this chapter is that the RF equipment for testing digitally modulated signals is the same thus, when modulated and multicarrier tests are to be conducted in the same facility, costs is shared. Furthermore, this RF hardware is also able to perform ultra short pulse testing with arbitrary spacing between pulses, which is also interesting when exploring the transition between short and long-term multipactor discharges. However, testing with modulated or ultra-short pulses is limited to the use of one single amplifier, which drives down the maximum RF power applied to the DUT.

The set of experimental measurements have proved the method validity for one single generator and multiple signal generators. For that reason, phase coherency with more than one signal generator has been achieved and validated. Then, the phase drift between high power amplifiers has been measured, confirming that drift is limited to such a rate which can be corrected by the algorithm along the initial minutes, and negligible after 90 minutes of operation. Finally, a set of results have shown that the amplitude, frequency and phase recovery strategies shown in chapter 5 are applicable to this generation approach, thus leading to excellent results with a minimum amount of RF equipment.

Part III

Advanced testing techniques

Chapter 7

Advanced RF breakdown detection

7.1 Summary

This chapter presents a novel RF breakdown detection system which monitors the same physical magnitude as the microwave nulling: RF at the fundamental frequency. However, instead of canceling two waves to obtain a null, it performs a statistical analysis of the measured in-phase and quadrature (IQ) data. This algorithms computes the residual error for the measured signal, by subtracting an averaged waveform computed from the last N measurements and then fits the residual IQ data into a noise model. By applying an hypothesis test to these residual noise IQ samples, the digital processing algorithm determines if the current measurement fits pass the hypothesis test (no discharge) or does not (discharge).

When this new detection system is compared to the standard ones described in section 2.7, and recommended in [49, 50, 51, 8], the following benefits can be highlighted: *1*) it does not require continuous tuning, *2*) its sampling rate is higher (only limited by the RF equipment and system background noise) and, *3*) its output is not only qualitative but quantitative.

For comparison, the acquisition rate in this method goes beyond 40 MHz (see section 7.2), whereas it is limited to 1 kHz or less in the electron or UV light monitoring detection systems, and to 3 MHz in the microwave nulling or harmonic detection methods, respectively [58]. So, due to its larger analysis bandwidth, this method is better suited to cope with small or short-term discharges (see section 7.2.3), more likely to happen when modulated signals are being transmitted.

Also, this detection method provides the same sensitivity for CW signals, improves the accuracy when dealing with modulated signals –such as the ones used in [86, 62]– because of its wider bandwidth and digital signal processing and requires fewer RF components to set up.

When operating the traditional microwave nulling system, the operator performs the "detection" by observing the signal changes on the analyzer screen. Even for skilled operators, the response time to the RF breakdown is no shorter than 1 second. In contrast, for the IQ detection system [136, 137, 138, 139, 140], the execution time is shorter than 5 ms as the

algorithm is executed in a CPU.

To properly appreciate the relevance of this novel detection system, it is crucial to fully understand the microwave nulling basics, which are found in section 2.7.1, since both detection systems monitor the same physical magnitude, and the nulling is the IQ detection predecessor.

Because of the strong push in digital communications for satellite and terrestrial applications, RF measurement technology has improved dramatically in recent years [86], [141]. Almost all signal analyzer available in the market today are able to capture the amplitude and phase information of an RF signal, known as IQ data. However, the microwave nulling system only considers scalar data and does not benefit from these advances.

7.1.1 Implementation and test bed simplification

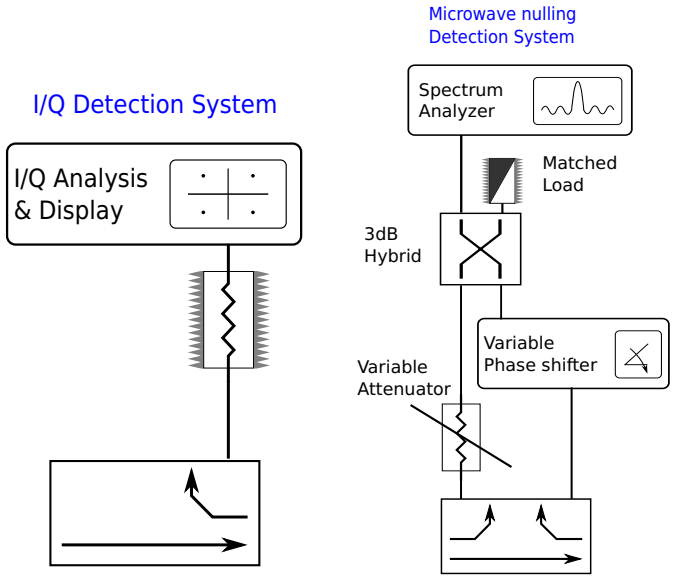

(a) IQ Detection system **(b)** Nulling system

Figure 7.1: Side to side comparison of the IQ detection (a) and the microwave nulling (b) implementations.

In terms of implementation, Fig. 7.1 shows a side-to-side comparison of both methods. From these two implementations, it is clear that less hardware is required in the proposed IQ detection system.

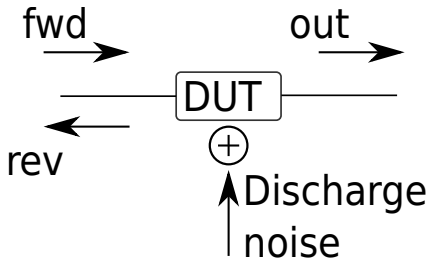

Figure 7.2: Waves involved in a two port device which can be acquired in order to detect the presence of the RF breakdown discharge.

7.2 Hypothesis testing applied to multipactor detection

The IQ detection method is based on the mathematical analysis of the in-phase and quadrature information of the RF high power signal. Its operation principle relies on the RF breakdown generating additional noise that overlaps the already present system background noise. For each new measurement, the algorithm determines if the measured noise matches the expected noise range (system background noise) or not (background noise plus RF breakdown noise).

The first step is to identify the noise sources in the test bed. Given that the propagation of the RF signal in a typical multipactor test bed is conducted (through coaxial or waveguide), the passive elements will not introduce noise with different patterns. The primary noise sources are the signal generator and the high power amplifier (HPA) [142, 143, 78]. For simplicity, the losses in the test bed are considered negligible. The signal to noise ratio (in dB) at the DUT input is defined as:

$$\left(\frac{S}{N}\right)_{\text{fwd}} = \left(\frac{S}{N}\right)_{\text{gen}} - \text{NF}_{\text{HPA}} \tag{7.1}$$

where NF_{HPA} is the noise factor of the high power amplifier HPA. As the algorithm tries to identify the breakdown noise (N_{dsc}) out of the system ground noise (N_{S}), the path in which the system noise is lower is the one in which a larger "breakdown noise" to "system background noise" ratio is found, thus improving the detection accuracy.

Under the scenario of a two port DUT (see Fig. 7.2), there are three signals which can be measured at the DUT ports: forward, output, and reflected (rev).

Following the signal path, the forward signal should not be significantly affected by the extra noise due to the discharge. For the reflected and output signals, the one showing a larger $N_{\text{dsc}}/N_{\text{S}}$ ratio will depend on the DUT scattering parameters. Assuming a scenario in which the DUT is symmetrical, and the discharge happens at its middle point, the following equations define the noise at the reverse (N_{rev}) and output (N_{out}) paths:

$$\begin{aligned} N_{\text{rev}} &= N_{\text{S}}|S_{11}|^2 + 0.25N_{\text{dsc}}|S_{21}|^2 \\ N_{\text{out}} &= N_{\text{S}}|S_{21}|^2 + 0.25N_{\text{dsc}}|S_{21}|^2 \end{aligned} \tag{7.2}$$

From equations in (7.2) it is clear that when $|S_{11}| < |S_{21}|$, the discharge to system noise level will be more significant in the reverse signal than in the output signal.

7.2.1 Noise modeling

Once the location of the detection system with respect to the DUT has been defined, it is time to model the system noise. As the discharge noise has an unknown statistical distribution, it is easier to model the the noise always present, and use hypothesis testing to verify whether the noise being measured fits the expected characteristics or not.

For signals containing the in-phase and quadrature signals, it is assumed that the noise in each component can be modeled as a Normal distribution. If the real and imaginary parts of the noise follow each one a Normal distribution, then the error vector noise (EVN) calculated as the absolute value of the complex error follows a Rayleigh distribution.

A random variable, $R \sim \text{Rayleigh}(\sigma^2)$ follows a Rayleigh distribution if $R = \sqrt{I^2 + Q^2}$, where $I \sim N(0, \sigma^2)$ and $Q \sim N(0, \sigma^2)$ are Normal independent distributions. The Rayleigh probability density function (PDF) is:

$$f_R(r;\sigma) = \frac{r}{\sigma^2} e^{-r^2/(2\sigma^2)} \tag{7.3}$$

$$\sigma \approx \sqrt{\frac{1}{2P}\sum_{i=0}^{P} r_i^2} \tag{7.4}$$

being r a random noise sample, and r_i a random noise sample within the set of P samples used to compute the distribution scale parameter σ.

The hypotheses used to determine if there has been a discharge in a given measurement are (see Fig. 7.3):

- H_0: There is no RF breakdown discharge.
- H_1: There is an RF breakdown discharge.

RF breakdown detection occurs when H_1 is true and, moreover, H_1 is decided ($P_{\text{D}} = P\{H_1|H_1\}$). Nonetheless, false alarm RF breakdown occurs when H_0 is true but H_1 is decided ($P_{\text{FA}} = P\{H_1|H_0\}$). Since the PDF for the RF breakdown noise is not currently known, it is easier to calculate the false alarm probability (P_{FA}) instead of the detection probability. Hence, in that case:

$$P_{\text{FA}} = \int_{\eta}^{+\infty} f_{H_0}(\tau) d\tau \tag{7.5}$$

where f_{H_0} is the Rayleigh PDF defined in (7.4) and τ is the noise power.

In order to define the IQ detection method in a way closer to the microwave nulling system operation, instead of fixing a detection error (probability), a threshold η setting (to achieve a certain false alarm probability) provides a good compromise.

However, knowledge of the optimal η value requires some experience on test bed background noise and signal modulation. On top of that, a relevant standard to be followed is not available yet. Therefore, the procedure used here consists of estimating the EVN distribution using the concatenated EVN traces from the first N measurements. These measurements can be acquired at the same or different RF power level because the acquisition is normalized in order to obtained the EVN. The sample set is presumed not to have suffered from RF breakdown because the power level is low. From that large set of data, the EVN distribution is modeled, and η is determined from the false alarm probability, which is estimated according to (7.6). As the data has discrete values instead of continuous, the false alarm probability is given by:

$$P_{\text{FA}} = \sum_{i=q}^{N \cdot P} \Delta\tau \cdot f_{H_0}(\tau_i) \tag{7.6}$$

where $\Delta\tau$ is the discretization interval, P is the number of points in each measurement and q is the index position where $\tau = \eta$.

7.2.2 Reference signal

Once the current measurement has been normalized, its EVN is obtained. The next question is which reference signal, when used to compute the EVN, gives the best sensitivity for RF breakdown detection. This section discusses why the DUT input signal is not optimal for computing the EVN, and how the previously measured signals are stored to compute the reference signal.

Following how the nulling system is implemented, it would make sense to use the input signal as the reference to compute the EVN. However, in practice, there are several considerations that do not support this approach: *1*) it requires a second analyzer, which is expensive; *2*) due to unequal frequency response in both paths (measurement and reference) the EVN would be larger if equalization is not used; *3*) there is a trigger jitter error between both devices.

For these reasons, the reference signal is defined from the average of the previous N measurements with no RF breakdown. In order to build this reference, a buffer spanning the N previous acquisitions is implemented. The buffer follows a First In First Out (FIFO) scheme, so once it is full, the oldest measurement is replaced by the newest one. This FIFO buffer follows the actual signal and, as the oldest traces are replaced, any possible distortion in the amplifier or the signal generator is taken into account.

The value for N is dependent on the high power amplifier being used, system return

losses, the DUT characteristics, and environmental parameters such as temperature. Therefore, there is no optimal value for N that can be applied in all the possible scenarios.

Finally, once the current and reference signals are available, the EVN is computed as the difference between them.

7.2.3 Handling small discharges

Small discharges are challenging to handle in multipactor testing. Slow sampling rates in the local detection methods (about 1 kHz or less), and relative low sampling rate in the microwave nulling and harmonic detection systems (about 3 MHz), make difficult to detect these small discharges, as they are averaged out.

The small RF breakdown discharges can be classified into three groups: *1*) fast events (in the order of ns) of moderate or even high amplitude; *2*) moderate length events ($< 1\ \mu s$) of weak amplitude; and *3*) fast events of weak amplitude.

Although from the perspective of the proposed algorithm, it always returns a statistically correct pass/fails result, from the actual RF breakdown point of view, reliable results are to be expected mainly in cases 1 and 2. This is due to the larger acquisition bandwidth of this method, only constrained by the RF equipment, which provides more samples per second (> 40 MSps). Nevertheless, small discharges of type 3 may, as it happens with all the other detection systems, be incorrectly detected or even missed.

In the experimental validation, it was observed that fast random values in the EVN were reported as discharges. At that stage, pulsed CW signals were being tested, which inherently could not suffer from extremely short discharges. This was confirmed by independent detection systems running in parallel, which did not record any discharge. For that reason, the algorithm was enhanced to require a minimum discharge length (i.e., a certain amount of consecutive samples M failing the hypothesis test). This requirement ensures that random noise peaks, which do not fit the Rayleigh distribution but are not RF breakdown, do not produce a false detection. However, setting a large M value (i.e., > 20) reduces the method responsiveness for small multipactor discharges.

Finally, the algorithm has the following three tuning parameters, which allow it to be either more responsive to small discharges or more robust against false detection: probability for the hypothesis test (η), number of consecutive samples failing the hypothesis test (M) and FIFO buffer size (N).

7.2.4 Algorithm flowchart

The flowchart of the proposed detection algorithm is shown in Fig. 7.4. The threshold value (but not the false alarm probability) is updated during the test in order to take into account possible changes in the background noise. In case RF breakdown is detected, the algorithm: *1*) notifies the operator; *2*) does not include the corresponding measurement in the buffer, and *3*) reduces the RF power level (optional).

7.2.5 Method limitation and drawbacks

The proposed algorithm, as implemented in this thesis, has several identified limitations. Some of these are related to the way is has been programmed and others are specific to the used RF equipment. Next, the most relevant limitations are highlighted.

- When obtaining the detection system residual noise for a new measurement the following factors play impact the final accuracy

  Trigger error due to jitter Is produced by the delays and propagation time between the signal generator output trigger and the analyzer trigger. Becomes a major error contributor when the signal under test has a large bandwidth (>100 MHz). Technical solutions for this problem exists, although are vendor dependent [144, 145]. Choosing any of these technologies solves the issue, although ties the implementation to a specific manufacturer. None of these specific solutions has been available during this investigation.

  Device under test return loss . A large reflected signal propagates the high power amplifier noise into the signal analyzer being used for this detection method. Noise from high power amplifier does not only follows a Rayleight distribution [143, 142], thus increasing the chances of the hypothesis giving an incorrect result.

  RF equipment reference level . An incorrect setting in the reference level will produced either: an incorrect modeling of the background noise (if the reference level is too high) or an incorrect measurement of the larger amplitude at the analyzer input when a RF multipactor breakdown happens (due to clipping). Either of this will produce am incorrect hypothesis test result.

- Algorithm execution speed is far from real time

  Method configuration parameters Large FIFO size or signal length impact the code execution speed.

  Data transfer Large IQ arrays (> 20000 samples) takes longer to transfer than to analyze with the current implementation.

  Software language the method is implemented in Matlab, although it should be implemented either en C/C++ or Fortran for optimal performance.

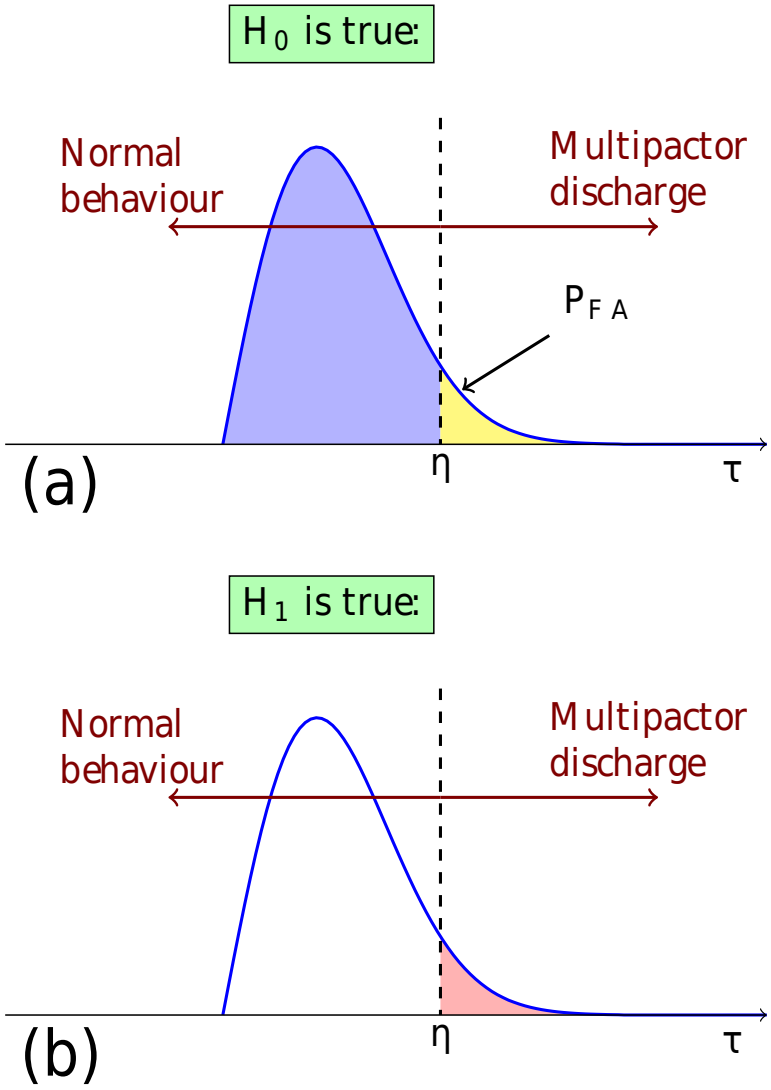

Figure 7.3: Hypotheses tests. Given that the noise PDF is unknown, hypothesis testing is done using H_0 (a), which is assumed to follow a Rayleigh distribution. The probability of false alarm is the degree of freedom that determines the EVN threshold used for the RF breakdown detection. The hypothesis testing using H_1 (b) is not used because the multipactor noise distribution is unknown.

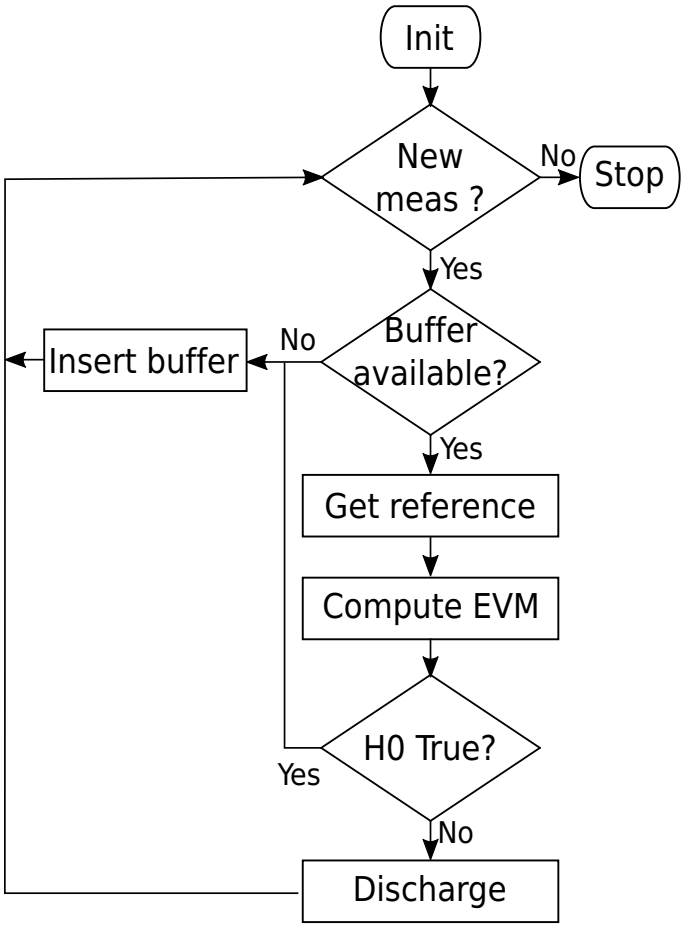

Figure 7.4: Simplified IQ detection method flowchart. The management of the FIFO buffer is not detailed.

7.3 Experimental validation

This section presents the experimental validation of the proposed RF breakdown IQ detection system. Out of all the possible signals to be used in multipactor tests, the following ones have been selected: *1*) pulsed CW; *2*) linear frequency modulated CW (FM chirp), and *3*) QAM digitally modulated signal.

The first signal –pulsed CW– is the standard waveform used in multipactor tests as defined in [8]. The FM chirp has been selected as the most interesting analog modulation for space applications, being widely used in radar systems. Finally, the third signal is a widespread digitally modulated signal.

The test bed was operated at L-band using very high-quality RF equipment so that the background noise is minimized. Thus, a Keysight vector signal generator M9383A and a signal analyzer M9393A have been used, with a sample rate of 200 MHz to cope with 160 MHz of IQ bandwidth. Both RF devices provide an amplitude flatness better than 0.5 dB and a deviation from linear phase $< \pm 1$ degree. The signal amplification was carried out with an R&S BBA150, a 1 kW solid-state power amplifier (SSPA). The actual test bed is shown in Fig. 7.5, while Fig. 7.6 shows its schematic.

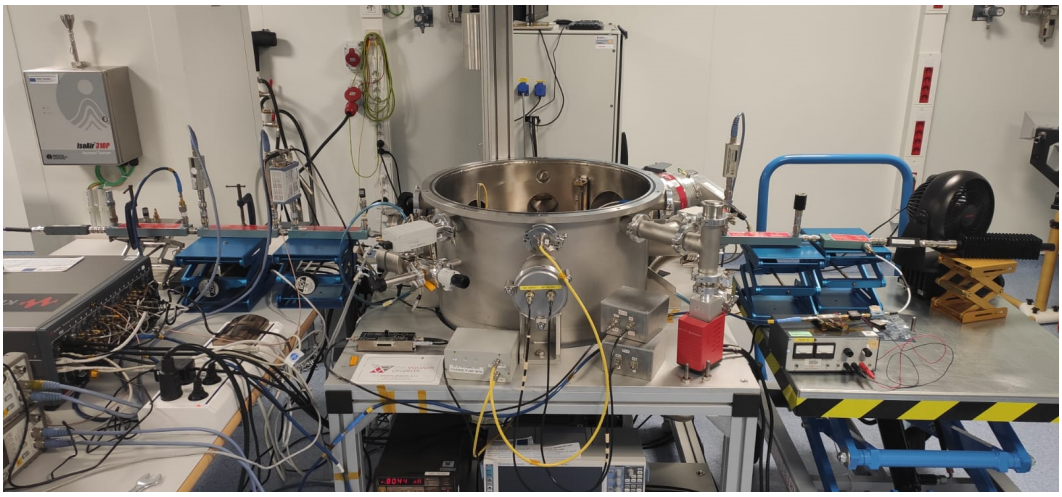

Figure 7.5: Picture of the test bed, with the PXI chassis on the left, the TVAC on the center and the output branch on the right. The test sample was installed in the TVAC.

The multipactor reference sample is a reduced gap coaxial transmission line operating at L-band, with a multipactor threshold of about 60 W peak for a CW signal. The sample threshold was verified with standard detection systems such as electron measurement, harmonic monitoring, and the classic nulling system (for the CW case). Periodic CW measurements were run between tests in order to detect any conditioning in the DUT. Harmonic and electron current monitoring systems were working in parallel with the IQ detection method.

For the following examples, the proposed method runs in about 1-2 ms, measured from the moment the algorithm receives a new trace until a pass/fail decision is made. However,

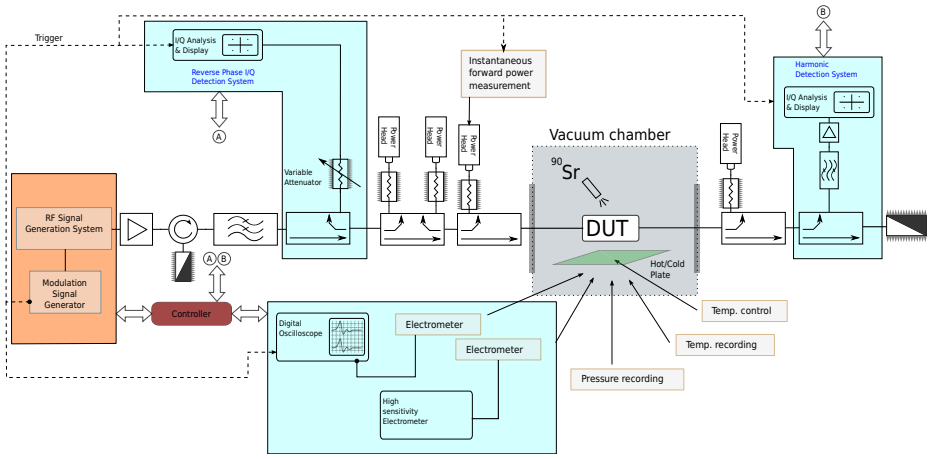

Figure 7.6: Schematic of the test bed used for the IQ validation test campaign. During the initial threshold verification, the IQ detection system was replaced by the well-known microwave nulling system. The following detection methods were also continuously monitored during the validation of the IQ detection system: RF harmonic detection system (1x, global) and electron monitoring (2x, local).

the overall execution time is limited by the acquisition and trace transfer actions. For short signals (< 300 μs), the total execution time (including acquisition) is about 5 ms, although this time increments with the number of samples.

The minimum discharge length should be one, in order tone to obtain the maximum multipactor detection responsivity. However, this requires a very low system noise, as if only one sample does not pass the hypothesis test, then multipactor detection is triggered.

In the validation stage, it was observed that, with the used setup, it was not possible to remove these short random noise events. As a consequence, several false detection were observed. In order to obtain a robust multipactor detection, a minimum discharge length of $M = 10$ was found to be enough for this setup. This value remained the same for all the tested cases.

In terms of sensitivity, for the tested cases, the novel detection system recorded all the discharges simultaneously -i.e., same power step-, or even before the harmonic and electron monitoring systems, which were running in parallel, as shown in Fig. 7.6.

Table 7.1 shows a summary of the experimental results. For each of the test signals the background noise and the noise increment is specified. It is worth mentioning that, although the background noise is a characteristic of the set-up and remains at similar levels all the test long, the noise increment recorded during a multipactor discharge depends on the discharge strength (which has a random nature).

Signal	Background noise (dB)	Noise increment (dB)
Pulsed continuous wave	-40	40
Analog modulation FM chirp	-30	20
Digital modulation QAM	-30	20

Table 7.1: Summary of the RF multipactor breakdown results. The background noise is the detection noise system after substrating the reference signal to a trace in which there is no multipactor. The noise increment represents the noise power increment, with respect to the background noise, computed for a measurement in which there is multipactor.

7.3.1 Pulsed continuous wave

This signal scenario is the standard one in which the microwave nulling system shows its best performance. As defined in [8], the signal under test is a 20 μs CW pulse. As shown in Fig. 7.7, the residual EVN is better than -35 dB, which is a value comparable to the one that can be typically achieved in the nulling system when the operator is constantly tuning it, using a very precise phase shifter and a variable attenuator.

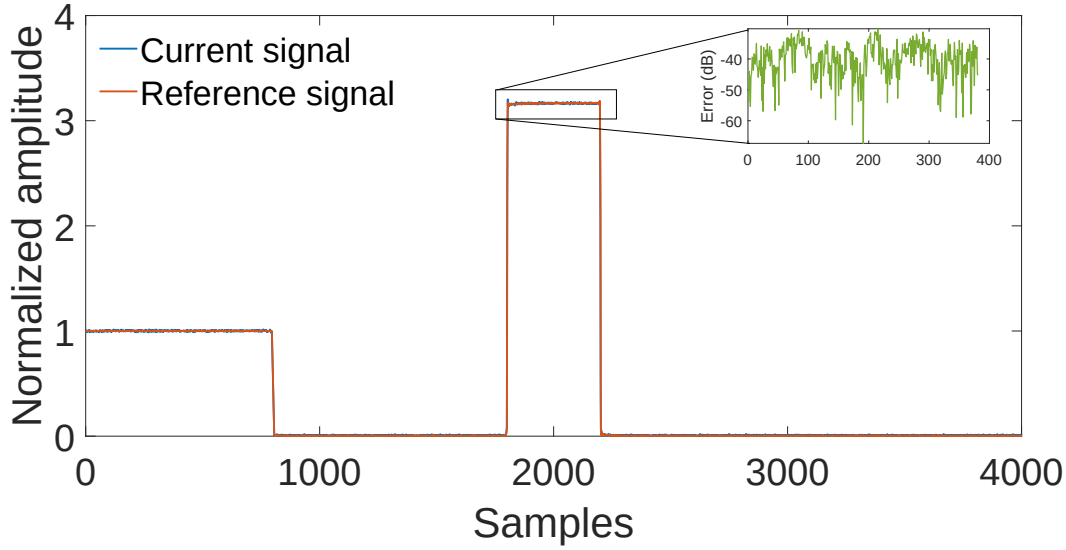

Figure 7.7: Example of a signal sequence for a CW payload with no RF breakdown discharge. The small plot shows that EVN remains lower than -35 dB during the whole sequence.

Fig. 7.8 shows how the response appears when there is an RF breakdown discharge with a clear increment in the EVN. This increment translates into the noise PDF, which is shown in Fig. 7.9, where extra noise due to the RF breakdown discharge can be observed on the

right-hand side of the figure.

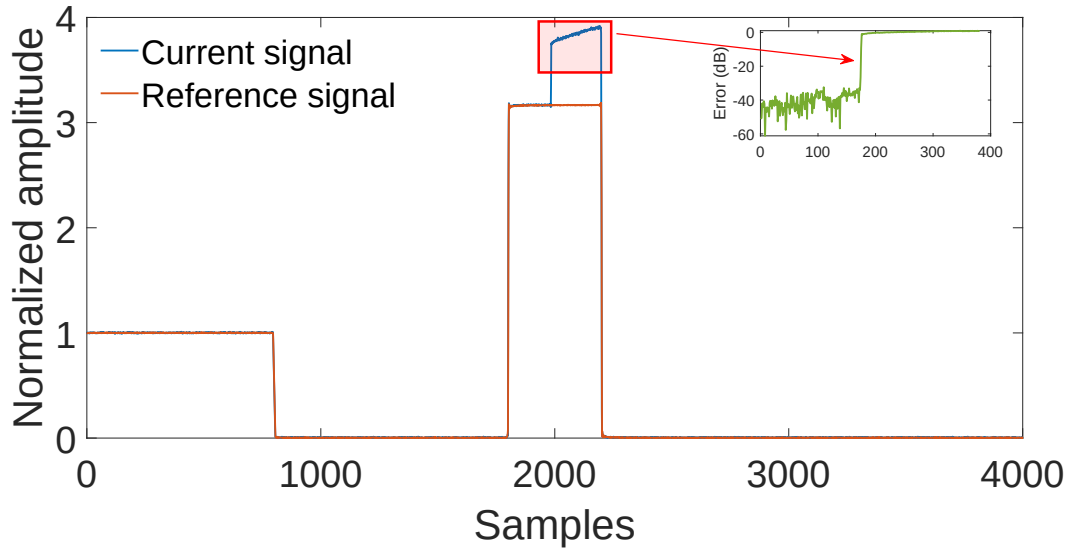

Figure 7.8: Example of a signal sequence for a CW signal with an RF breakdown discharge. The small plot shows that EVN increases by 40 dB when the discharge happens.

7.3.2 Analog modulation FM chirp

The following validation example consists of using an analog modulated signal. In this case, a chirp signal has been selected due to its constant power but linearly varying frequency. The chirp signal is the one shown in Fig. 7.10. The microwave nulling system cannot be used for this modulation type, as the signal only stays at a given frequency for a few time intervals through its complete duration. Consequently, the nulling system would not be tuned at the signal instantaneous frequency most of the time.

As depicted in Fig. 7.11, the response is not flat. This lack of flatness is due to the response of the passive elements and the RF generator (which is not pre-distorted). For this verification, this residual effect is not important and adds value to the experimental results, as they show that the algorithm can cope with this residual amplitude modulation. The EVN level, lower than -30 dB, provides enough margin for reliable detection.

An interesting result in these results can be observed in Fig. 7.12 where the discharge starts when the chirp signals goes through the center frequency while going down in frequency. However, it does not only remains active through the lower chirp frequencies, but also stays active till the end of the chirp signal, where frequencies are higher that the center frequency.

Fig. 7.12 shows how the response appears when the discharge happens, and the corresponding increment in the EVN level. This response translates into the noise PDF, which is

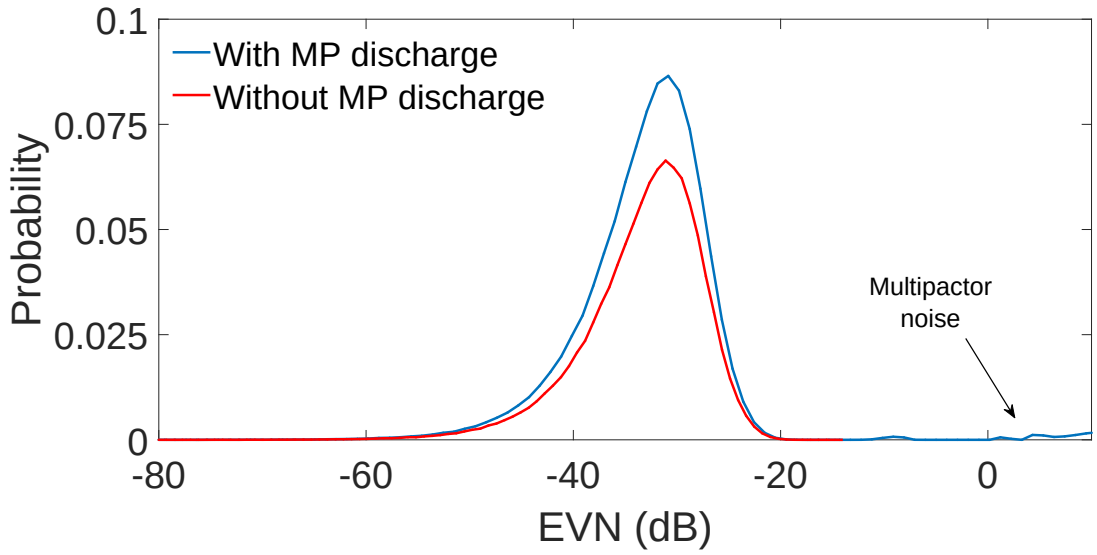

Figure 7.9: PDF for the pulsed CW signal when there is a discharge and when there is not. The extra noise out of the Rayleigh distribution can be clearly identified on the right.

shown in Fig. 7.13, where extra noise due to the RF breakdown discharge can be observed on the right-hand side of the figure.

7.3.3 Digital modulation QAM

The final validation is done with a QAM signal of 500 kHz bandwidth. Due to its constant frequency and amplitude changes, these signals are not properly detected using the nulling system.

The EVN background level stays close to -30 dB, as shown in Fig. 7.14. The effect of the multipactor discharge is shown in Fig. 7.15. This increment translates into the noise PDF, which is shown in Fig. 7.16, where extra noise due to the RF breakdown discharge can be observed on the right-hand side of the figure.

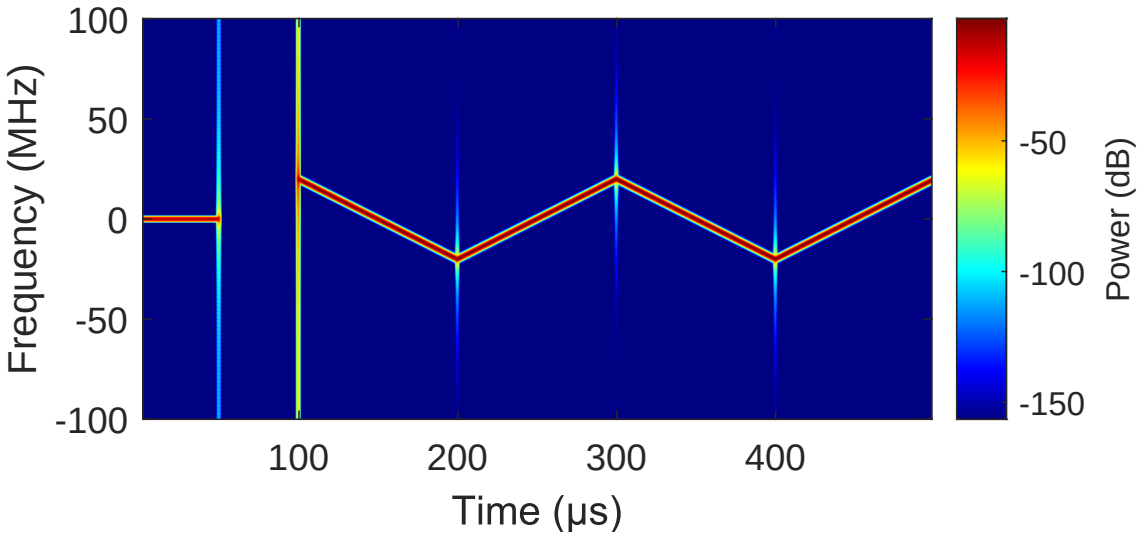

Figure 7.10: Example of the three parts composing the typical signal structure used in this work. The signals starts with an initial 50 μs CW pulse at -10 dBc used for calibration purposes. Next, there is a 50 μs interval with RF OFF for electron relaxation. Finally, the signal of interest is found at 0 dBc peak. In this particular example, the signal is an analog linear-frequency modulated chirp with two up-down intervals of ± 20 MHz each lasting for 100 μs.

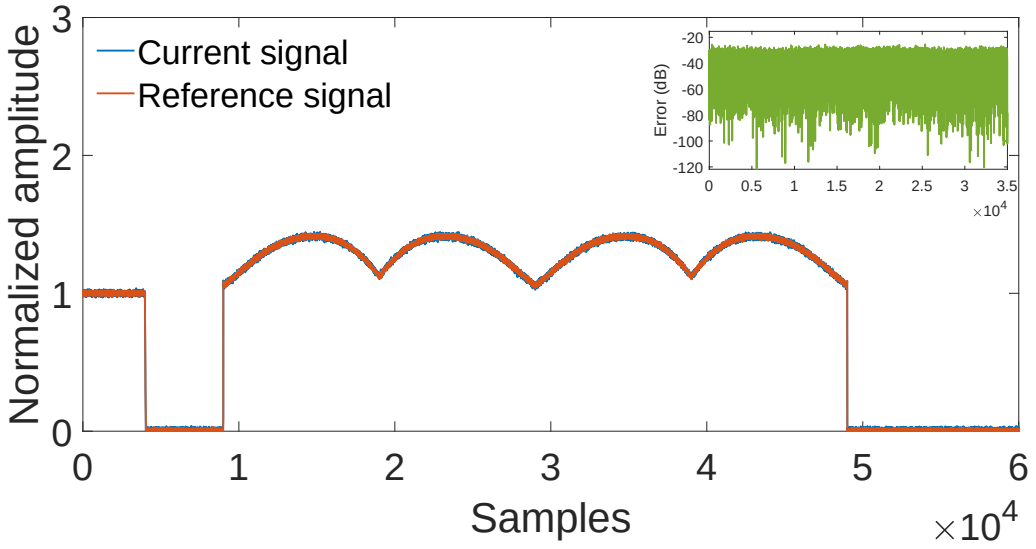

Figure 7.11: Example of a signal sequence for an FM chirp signal with no RF breakdown discharge. The small plot shows that EVN remains lower than -30 dB during the whole sequence.

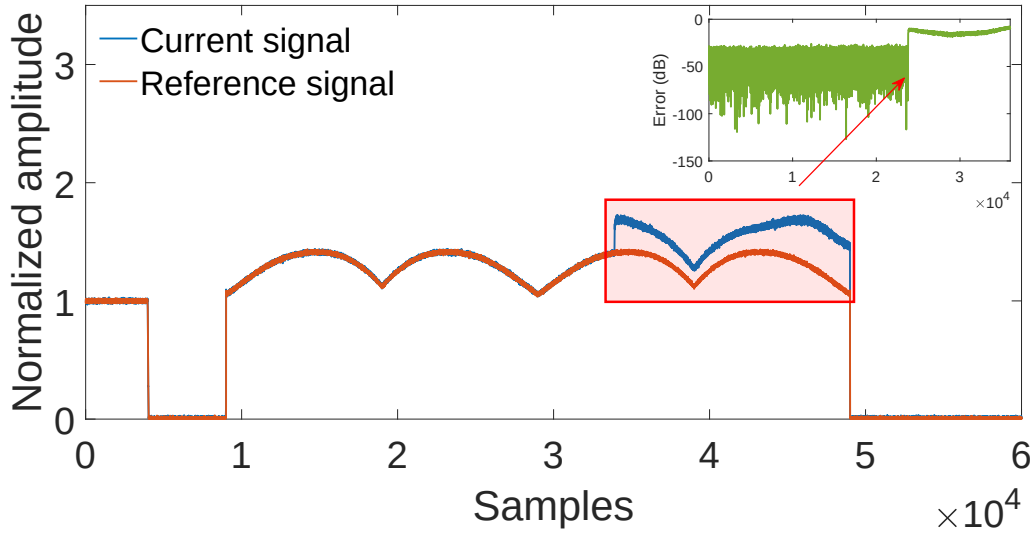

Figure 7.12: Complete signal sequence for an FM chirp signal in which there is an RF breakdown discharge. The small plot shows that EVN increases by 20 dB when the discharge happens.

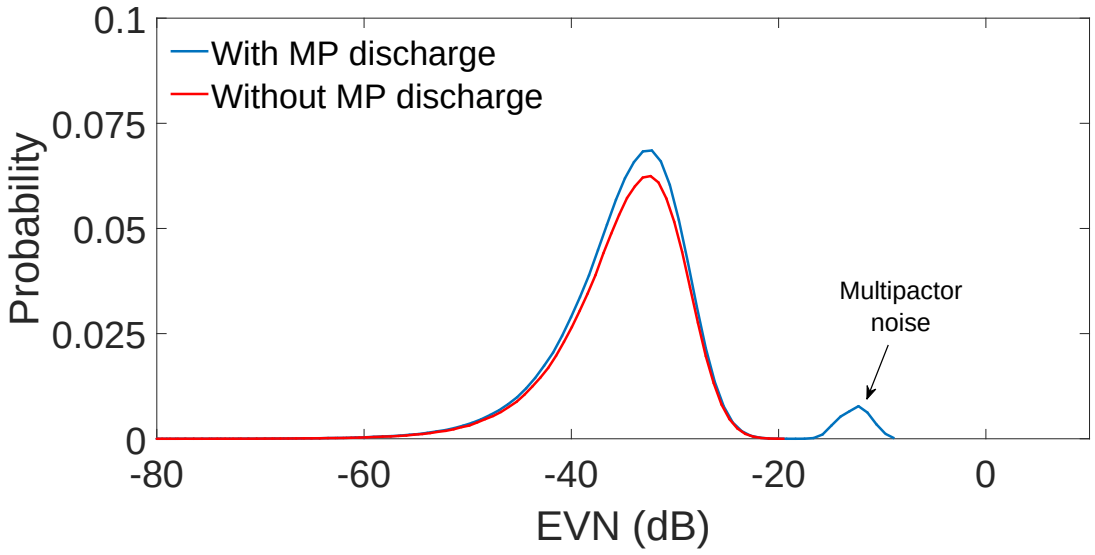

Figure 7.13: PDF for the FM Chirp payload when there is a discharge and when there is not. The extra noise out of the Rayleigh distribution can be clearly identified on the right.

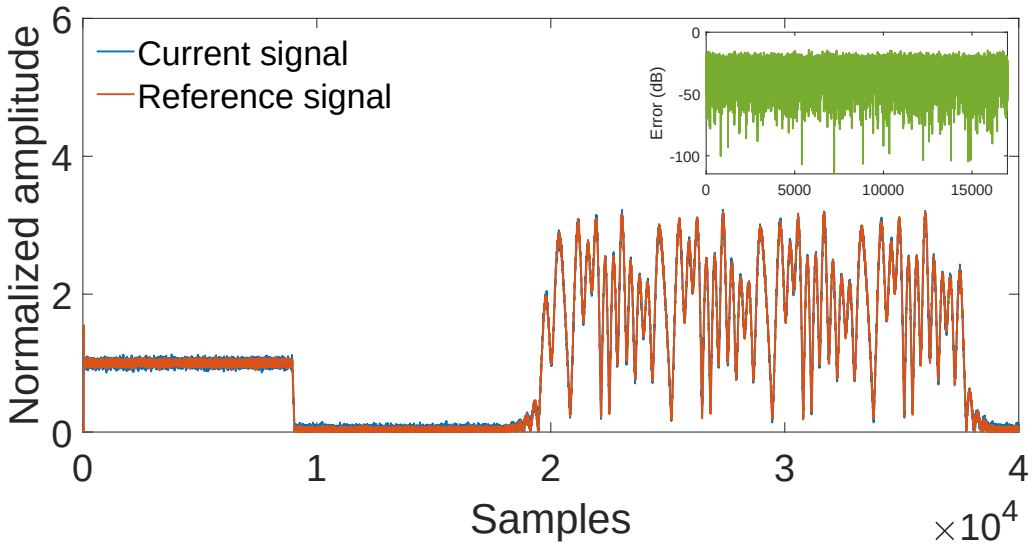

Figure 7.14: Example of a signal sequence for a QAM signal with no RF breakdown discharge. The small plot shows that EVN remains lower than -30 dB during the whole sequence.

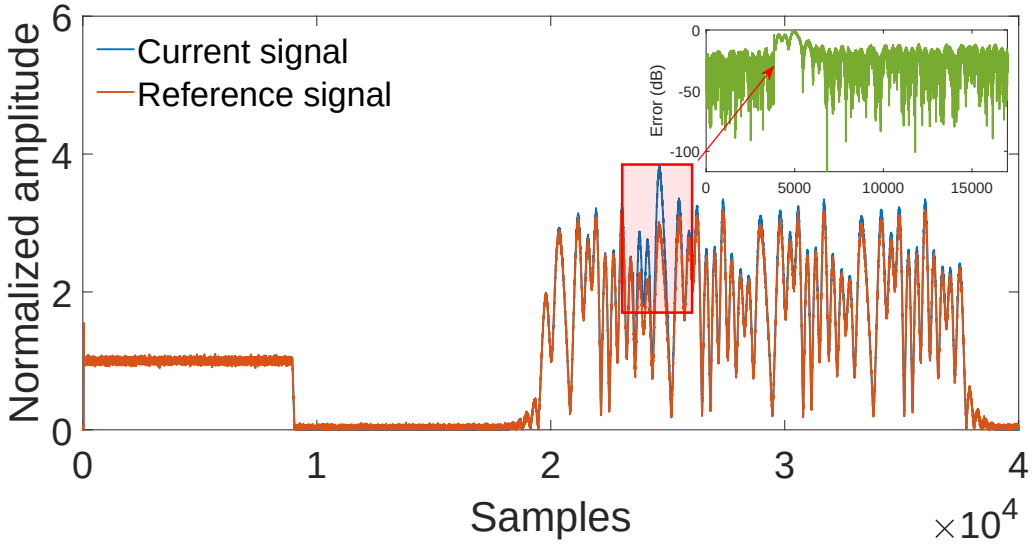

Figure 7.15: Example of a signal sequence for a QAM payload in with an RF breakdown discharge. The small plot shows that EVN increases by 20 dB when the discharge happens.

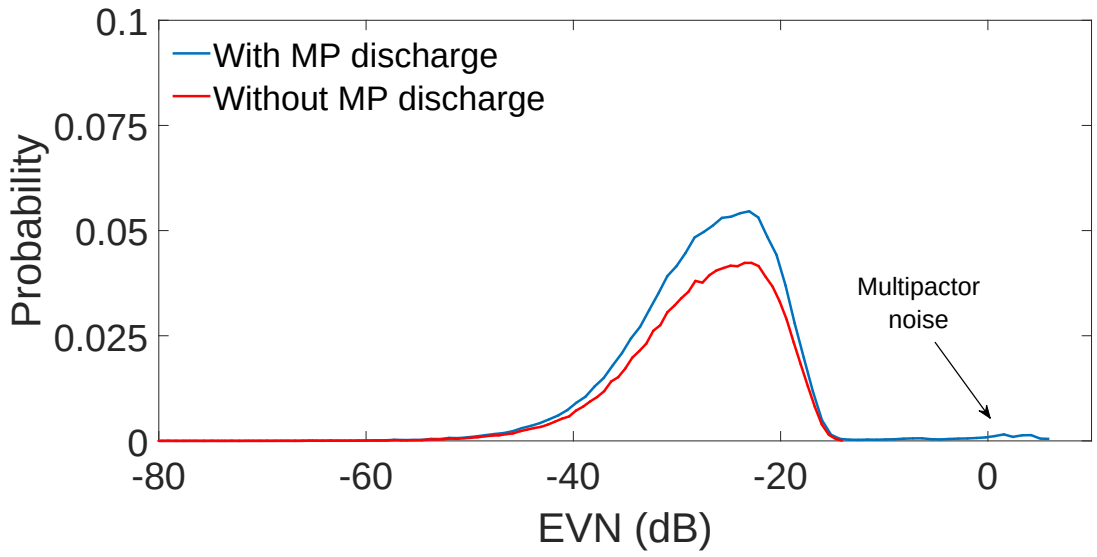

Figure 7.16: PDF for the QAM signal when there is a discharge and when there is not. The extra noise out of the Rayleigh distribution can be clearly identified on the right.

7.4 Conclusions

This chapter has shown a novel RF high power breakdown detection technique, surpassing the microwave nulling system while maintaining its sensitivity and improving its robustness and capabilities. The method simplifies the required RF equipment and increases the signal processing complexity to allow excellent multipactor detection with a high automation.

The detection algorithm is based on the analysis of the signal residual noise using hypothesis testing. The hypothesis test assumes that the in-phase and quadrature components of the residual error follow, each one, a Normal distribution. However, when considering both components combined and squared the result follows a Rayleigh distribution. By fitting the measured error vector noise to a Rayleigh distribution, and fixing a operator determined false alarm probability, a threshold level is obtained.

Finally, each new acquired sample is tested versus the threshold level and a decision is made. Whenever the signals is below the threshold a discharge of no multipactor discharge is made, whereas those cases in which the new sample is above a discharge decision is reported.

To improve the overall detection robustness, as the background noise does not strictly follows a Rayleigh distribution, an additional verification is made. The algorithm requires also that 1 or more consecutive samples fail the hypothesis test. This extra requirement, which is a user-define parameter, is very efficient in preventing false alarms. However, it comes comes at the cost of blinding the algorithm to detect discharges shorter than the user defined number of samples.

When looking at the detection system background noise, several factors play a role in its value. In first place, the actual test bed and the DUT return loss impact the noise power (Rayleigh and of other kinds) being measured in the signal analyzer. In second place the trigger jitter becomes a major error source when large bandwidths are used, unless advanced trigger systems such as the Keysight timming hardware or the National Instruments TClk are used [144, 145]. This trigger error translates does not allows the optimal computation of the system background noise. In third place, the analysis bandwidth also contributes to increment the acquired noise, thus reducing the system sensitivity.

The method has been experimentally validated with CW, analog, and digital modulated signals. The detection limits of the technique are only related to the signal analyzer being used, and the test system residual noise level. These parameters determine the minimum residual EVN level, which must be as low as possible. The execution time of the proposed technique has proved to be about 5 ms or less, although the current bottleneck is the IQ data transfer, which typically takes longer than the detection method execution and becomes the predominant delay for large IQ arrays (> 20000 samples).

When considering the experimental background noise, experiments have shown that levels between 30 dB to 40 dB can be expected. The noise increment produced by the multipactor discharge has been 20 dB for modulated signals and 40 dB for the pulsed CW case.

The method has also proved that it can detect multipactor discharges within the waveform (see Fig. 7.15). As, for the QAM case the multipactor discharge happens within the first half of the signal, being extinguished by the signal amplitude changes and not happening again

in the second half. In the recorded case, the multipactor discharge is several microseconds long, however, the same capability would be used to detect short multipactor discharges.

Another interesting result is found in the chirp signal (see Fig. 7.12). There it can be observed that the multipactor discharge start when the chirp signals goes through the center frequency while going down in frequency. However, it does not only propagates through the lower chirp frequencies, but also stays active till the end of the chirp signal, where frequencies are higher that the center frequency.

Additionally, by not requiring operator tuning, and providing quantitative results, it can be considered a candidate for standardization in the RF breakdown testing field. A future RF breakdown standard could specify the maximum background noise acceptable for a test bed, and the false alarm probability to be used depending on the signal characteristics.

Finally, this testing method, in which the signals are acquired and analyzed one by one, allows the operator to store all the transmitted pulses, thus creating a data base for a later post-processing with other algorithm parameters. The analysis of other trends is also possible once the data is stored, such as the analysis of the number of consecutive sequences in which multipactor happens, as typically multipactor happens in a row of 1 to +60 consecutive sequences with multipactor being happening on them.

7.5 List of own publications and projects

The multipactor detection method presented in this chapter has been subject to peer review, and has been accepted in several international journals and conferences. Next, we list such publications and projects related to this topic.

7.5.1 Journal papers

- **O. Monerris**, R. Cervera, M. Rodríguez, E. Diaz, C. Alcaide, J. Petit, V.E. Boria, B. Gimeno and D. Raboso, "High power RF Discharge detection technique based on the in-phase and quadrature signals", in IEEE Transactions on Microwave Theory and Techniques, vol. 69, no. 12, pp. 5429-5438, Dec. 2021,
  doi: 10.1109/TMTT.2021.3120657.

- P. González, C. Alcaide, R. Cervera, M. Rodríguez, **O. Monerris**, J. Petit, A. Rodríguez, A. Vidal, J. Vague, J.V. Morro and P. Soto, "Multipactor threshold estimation techniques based on circuit models, electromagnetic fields, and particle simulators", in IEEE Journal of Microwaves, vol. 2, no. 1, pp. 57-77, Jan. 2022, doi: 10.1109/JMW.2021.3132284.

7.5.2 Conference papers

- R. Cervera, M. Rodríguez, **O. Monerris**, C. Alcaide, V.E. Boria, P. Soto and D. Raboso, "Diseño e implementación de un sistema de detección automática de descargas de RF de alta potencia", in XXXVII Simposium de la Unión Científica Internacional de Radio (URSI), Malaga, Spain, September 2022.

- R. Cervera, M. Rodríguez, **Ò Monerris**, C. Alcaide Guillén, P. Soto, V.E. Boria, D. Raboso, "Design and implementation of a new automatic system of high-power RF discharge detection based on In-Phase and Quadrature Signals", in International workshop on Multipactor, Corona and Passive Intermodulation (MULCOPIM), Valencia, Spain, October 2022

7.5.3 Projects

- **Title** H2020-ESA-007 Multipactor Prediction Techniques for GNSS Signals

  Reference 4000126048/18/NL/AS

  Holder Val Space Consortium

  Number of members in the research team 8

  Issuer European Space Agency

Chapter 8

Scattering parameters measurement in temperature

8.1 Summary

The scattering parameters (S-parameters) are the most valuable data to perform an electrical characterization of an RF device. These parameters are typically measured using a vector network analyzer (VNA) like the one shown in Fig. 1.3b.

It is common to perform the scattering parameters measurement at room temperature. However, it is relevant for many applications to know the actual device parameters at temperatures other than room temperature. The measurement and calibration method proposed in this chapter, allows to obtain the same accuracy typically achieved at room conditions but at any other temperature. In general terms this calibration method is of high interest in many applications. However, from the RF breakdown point of view, the correct measurement of the group delay and its drift over temperature has a major relevance.

The voltage magnification factor, which happens right in the group delay peaks, has a significant role in the multipactor threshold if the RF signal is located at that frequency. In narrow band applications signals do not typically get close to the group delay peaks (because of increased insertion losses). However, when using wide band modulations, or when re-using the same passive component to handle wider signals, it may happen that a portion of the signals get close to this peaks. If it happens that these group delay maximum drift up or down due to thermal effects, the multipactor threshold may change dramatically.

From the experimental point of view, obtaining correct and accurate measurements is related to the RF equipment being used, and closely linked to the calibration process being performed in the VNA before the actual device under test (DUT) is measured.

A commercially available solution was developed by COMDEV and sold from late 2013 by Agilent Technologies (CalPod) [146]. However, it is constrained to the coaxial transmission line technology and a has narrow temperature operational range (-30 °C to +80 °C).

In general terms, the calibration routine is typically a VNA built-in process in which

different element are measured. The most common microwave components present in a calibration kit (see Fig. 1.3c), individually known as standards, are: *open*, *short*, *line*, *thru*, *load* and *sliding load*.

There are several calibration methods found in literature, being the most commons ones: *transmission*, *line*, *thru* (TRL) [15]; and: *short*, *open*, *load*, *thru* (SOLT). The difference between those methods is the presence of the matched load, which is difficult to implement in some technologies. So the TRL standards are easier to manufacture, however this comes at the expenses of the lower frequency span in which the calibration stands valid for a given *line* length.

For space applications, components must be tested under different temperatures matching, at least, the most extreme operating conditions in the spacecraft. The temperature range differs depending on whether the components are placed outside the spacecraft (antennas or phased arrays) or inside (RF filters, amplifiers, circulators). For missions operating close to the Earth, components outside the spacecraft may operate in a typical range -100°C to 150°C is typical. Whereas for a component placed close to the heat pipes, a temperature range -30°C to 90°C is more common. Special missions, such as the ones getting close to the sun (Solar orbiter) or those traveling far from it (Voyager missions), may have hotter or cooler temperature requirements.

As already mentioned, when measuring scattering parameters at different temperatures, a calibration must be performed at each temperature of interest. By performing separate calibrations, the actual test system conditions can be correctly characterized at that specific temperature. However, this is not feasible using the VNA built-in procedure. Since, for calibrating the instrument at each temperature, it would be necessary to break the temperature profile to connect all the standards.

As handling the standards at the different temperatures is not possible, the traditional way of calibrating a VNA cannot be used. When only a room temperature calibration is carried out –from now on referred as the *traditional calibration*– major errors can be expected when temperature is changed. For instance, a measurement carried out at 100°C would be corrected through the calibration standards acquired at room temperature (25°C) [147] [148]. The best approximation found in the literature is the application of some incomplete correction, which can include, for example, the change in insertion loss levels in the cables due to thermal effects [149].

8.2 Operation principle

The main contribution of this novel method is that, instead of calibrating the measurement using the VNA built-in routine, the calibration is performed after taking all the acquisitions within the temperature profile. Hence the approach is [141]:

- set up the temperature profile and the measuring points,

- run the temperature profile for each calibration standard, measuring at the different temperature points and storing the acquired data,
- run the thermal profile for the DUT, measuring at the different temperature points and storing the acquired data, without performing any calibration with the VNA; and finally,
- perform the calibration at each temperature of interest by using the stored data corresponding to the measurements of the calibration standards and the DUT at that specific temperature.

In order to perform the calibration after the acquisition of all the required measurements, a Matlab routine has been implemented for performing the appropriate corrections at each different temperature. In particular, a TRL calibration [15] has been used since manufacturing its different standards, to properly behave over a wide temperature range, is easier than achieving the same performance when building the SOLT standards.

This is because the standards used in TRL are very robust with temperature, as a short will have a similar response over a wide range of temperatures. The same happens for the line and thru standards, whose dimensions change with temperature will not affect their response. However, the SOLT calibration uses a matched load. This element is difficult, if not impossible, to manufacture in a way in which its frequency response remains constant in a wide temperature range.

The thermal conditions are achieved either using a climatic chamber (ambient pressure) or a high vacuum system (typically at pressures < 1^{-5} mbar). The particularities applicable of vacuum testing are detailed in section 8.2.1.

The proposed method for obtaining calibrated scattering parameters at several temperatures requires from these building blocks:

Thermal system: element in charge of providing the thermal boundary conditions. The VNA signal must be routed to the reference plane, in which the DUT or standards are connected. It can be either a climatic chamber or a thermal vacuum chamber.

- Climatic chamber: consists of one single receptacle device with a with access ports. The heating and cooling system is integrated into the same device. An example of a climatic chamber is shown in Fig. 1.3a
- Thermal vacuum system: There are two independent sub-systems (see their next description).
  - Firstly, the vacuum system, in control of the vacuum pumps and valves.
  - Secondly, the thermal bath providing the hot and cold liquid (silicone), which then circulates through the vacuum chamber base plate and shroud[1].

[1]The silicone oil is the element which actually constrains the system temperature range. Light silicones, required for low temperature (-90 °C), can not be used for hot temperatures (>+140 °C) [150]

The RF system is in charge of performing the measurement and guiding the RF signal.

- VNA: this is the core element in order to perform the scattering parameters measurement. It is the same device used for the ambient temperature measurement.
- RF cables: in this case, there a two types of cables involved. Any test cable capable of operating with the proper frequency range and temperature rating for the ambient pressure measurement is sufficient. For the vacuum measurement, there are three segments. The ambient segment, the RF feedthrough, and the vacuum segment.

The controller It is a personal computer connected to the thermal system and the VNA. It is in charge of:

- control the thermal profile,
- store the temperature measured by the thermocouples,
- save the non-calibrated VNA data (at certain points or periodically) and,
- apply the TRL calibration to the stored data.

An automatic routine has been implemented using Labview to control the climatic chamber and VNA. The test set-up is shown in Fig. 8.1. The additional Data Acquisition (DAQ) unit is used to have more accurate temperature data on the DUT and TRL standards. These additional thermocouples verify the actual temperature of the element being measured. Once all the elements are measured, the same computer can execute the TRL calibration.

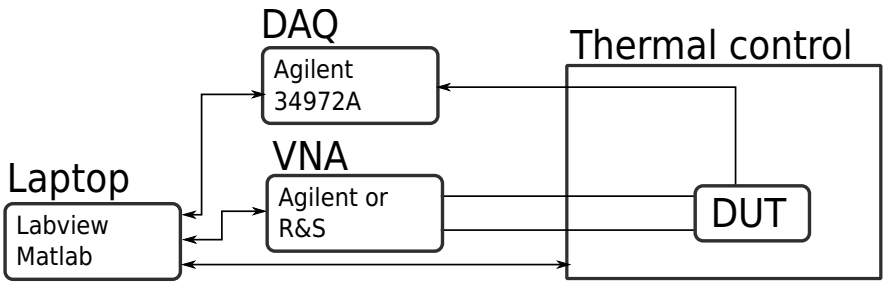

Figure 8.1: Test setup diagram in which the LabView software is in charge of executing the thermal profile, and storing the VNA measurement at the desired points or at a constant time rate.

Applying the same temperature profile to all the calibration standards and the DUT is essential. It is also necessary to include some dwell time before each measurement to ensure thermal stabilization. An example of the applied temperature profile is shown in Fig. 8.2.

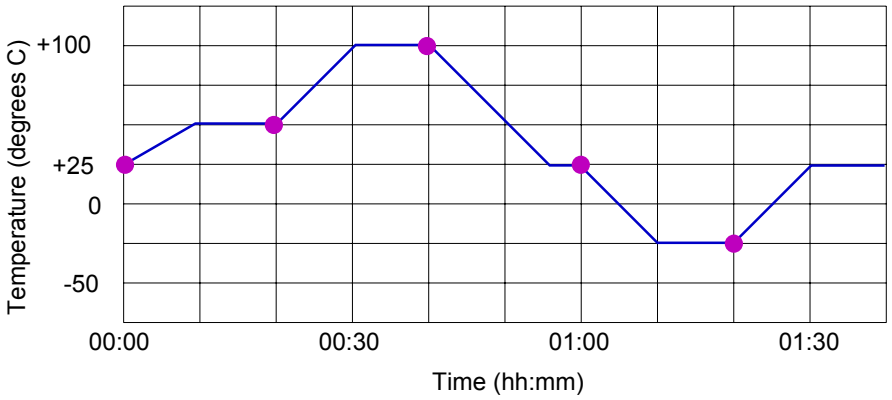

Figure 8.2: Typical temperature profile (blue line) and VNA measurements (pink dots).

8.2.1 Remarks for vacuum operation

The proposed method is, theoretically, independent of the environment pressure conditions. However, performing scattering measurements in a high vacuum environment is, in practice, more complex, time-consuming, and more prone to fail due to improper operator handling.

In particular, we must consider the following remarks:

Thermal transfer: the lack of convective heat exchange due to the high vacuum environment increases, the complexity of achieving and stabilizing temperature at the desired dwell value. This is an important handicap, especially for very cold temperatures. The physical reasons behind this issue are:

- lack of convective heat flux in high vacuum, which homogenizes the DUT temperature;
- reduced contact area between the DUT and the TVAC base plate, which is the main thermal transfer mechanism in this typical temperature range and,
- negligible thermal radiation due to the small temperature difference between the different system bodies.

RF connections: guiding the RF signal from ambient (VNA side) to high vacuum (DUT side) requires additional elements which impact the measurement procedure. These are detailed next:

- vacuum tight feedthrough: which handles the transition from ambient pressure to the vacuum; and,
- low outgassing vacuum RF cables: special RF cables which must be low loss but, at the same time, are required to have low outgassing properties.
  - These cables are very thin and made of special polymers. As a result, their phase and loss stability with handling are not optimal (compared to the standard VNA test cables).

- Their low amplitude and phase stability turns connecting the different TRL standards and DUT at the reference plane into a very delicate operation. Moving the cables will change their response, which might jeopardize the final TRL calibration results.
- Handling errors are not noticeable until all the standards and devices have been measured (a few days later).

8.3 Experimental validation

The following sections show the validation results, which allow to validate the novel proposed technique. The presented data also show that this method is applicable either at ambient or in vacuum conditions. The different RF transmission lines used to implement the DUTs and the standard prove that the method is applicable as long as the RL kit can be implemented.

Firstly, in section 8.3.1, the method is compared to the standard procedure in which the calibration is done before the measurement, under room temperature. Secondly, in section 8.3.2, the method is applied to four substrate integrated filters in ambient and vacuum conditions.

8.3.1 Experimental validation at ambient pressure

The purpose of this section is to demonstrate the improved results given by this new technique. In order to provide practical results, two microwave filters have been characterized at several temperatures. Two completely different rectangular waveguide microwave filters have been used for this purpose, since temperature changes do alter the resonance frequency and the couplings in different ways. The first DUT is a bandpass filter with metallic inserted posts in WR-42 standard waveguide. The second DUT is a smooth profile lowpass filter [32] in WR-75.

The measurements have been made inside a thermal chamber, able to provide a temperature range going from -70°C to 180°C in ambient pressure. Nevertheless, given that the used RF interface cables[2] are only rated from -55°C to 120°C, the temperature profile has been constrained to meet those limits.

In this section, first, the TRL temperature calibration will be validated at room temperature, and then both DUTs –and their respective appropriate TRL standards- will be measured at several temperatures, and the results compared with those obtained after the traditional VNA calibration.

In order to prove the correct performance of the developed TRL temperature calibration, a WR-42 bandpass filter has been used. First, the temperature calibration has been applied after measuring all the standards and the DUT at room temperature (25°C), obtaining the

[2] Gore™ TVAC qualified precision coaxial cable rated up to 50 GHz.

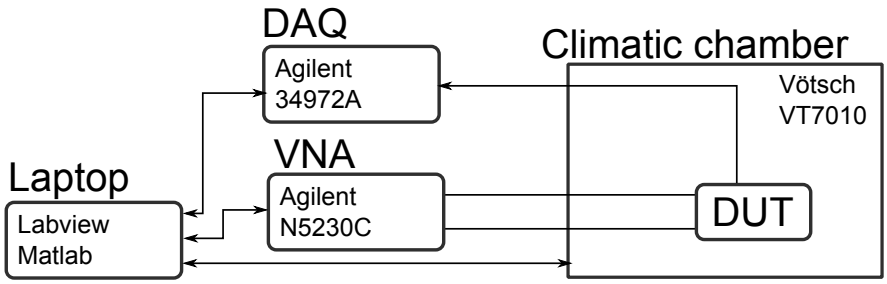

Figure 8.3: Test setup diagram for the ambient pressure measurements.

data in solid lines in Fig. 8.4. Then, the traditional calibration using the VNA routine has been applied for measuring the DUT, obtaining the data in dashed lines in Fig. 8.4. It can be observed that both calibration procedures give the same result, thus validating the new calibration procedure.

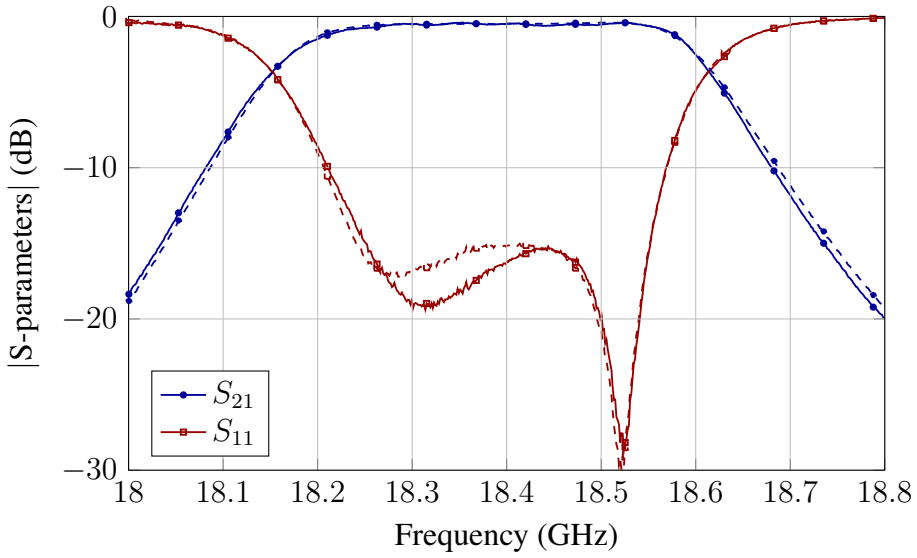

Figure 8.4: Validation of the TRL temperature calibration at room temperature: comparative of the temperature calibration (solid) and the traditional VNA calibration (dashed).

The same WR-42 bandpass filter has been measured at several temperatures, applying a temperature profile shown in Fig. 8.2.

Figure 8.5 shows the comparison between the S-parameters obtained at 25°C and 100°C using the temperature calibration procedure. A frequency shift can be observed in the response at 100°C, which makes sense since the filter dimensions are slightly larger due to the temperature increment, thus shifting the bandpass filter response to lower frequencies.

The second filter is a WR-75 lowpass filter having a continuous profile. It has been chosen since this topology claims to be less sensitive to thermal effects in terms of increased

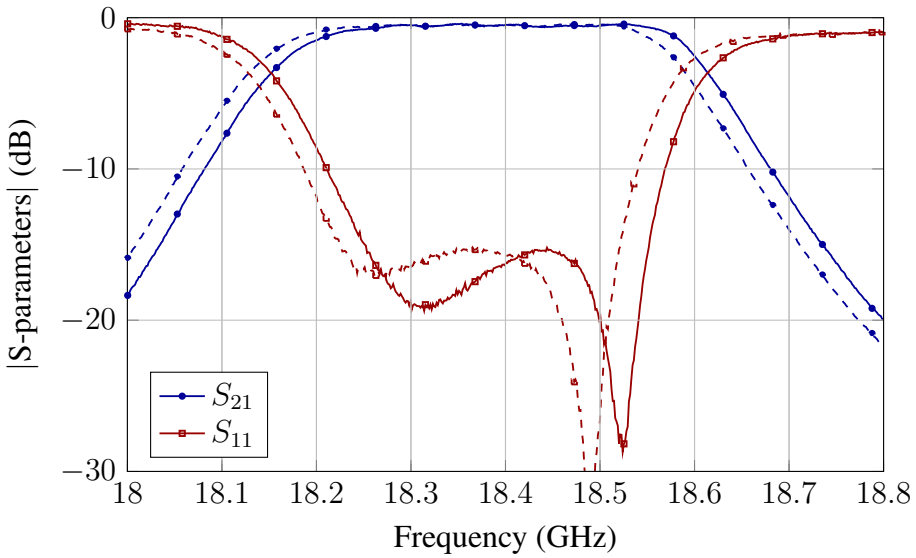

Figure 8.5: S-parameters of the WR-42 bandpass filter at 25°C (solid) and 100°C (dashed). Measurements using the temperature calibration procedure.

losses and bandwidth shrinking [32]. This fact can be noticed in Fig. 8.6, where the temperature increment from measurements in blue (-15°C) to the ones in green (115°C) is almost twice as the increment considered in Fig. 8.5, but the observed frequency shift is smaller.

Some details over the improvements observed in the measurements using the temperature calibration compared to the traditional calibration are shown in Fig. 8.5. From these results, it can be concluded that the traditional calibration, being unable to consider the actual conditions –in cables, connectors, etc.– for each different temperature, can yield errors in the insertion losses of $\Delta \approx +0.5$ dB observed at 100°C,and of $\Delta \approx -0.5$ dB at -15°C, or in the bandwidth, bandwidth shrinking and widening at 100°C and -15°C, respectively. Note that those errors could lead to inconsistent results, such as the observed positive values for S_{21} (dB) in Fig. 8.8, which could be even more positive at even lower temperatures.

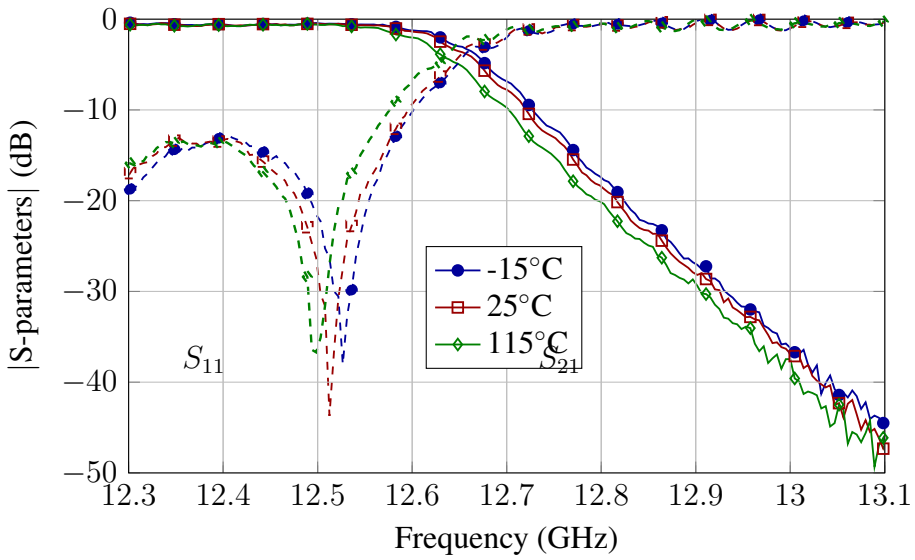

Figure 8.6: S-parameters of the WR-75 lowpass filter at several temperatures. Measurements using the temperature calibration procedure.

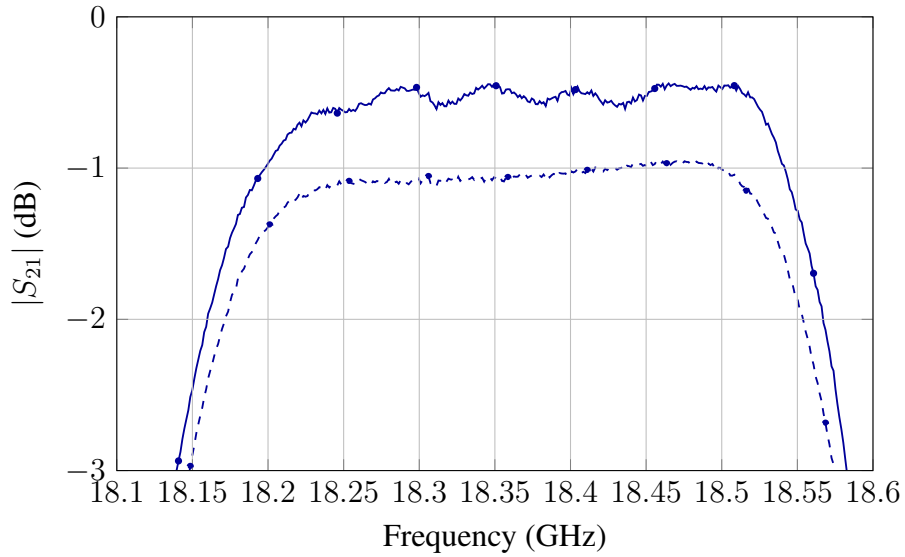

Figure 8.7: WR42 filter at 100°C. Details of the improvements due to the proposed temperature calibration procedure (solid) compared to the traditional calibration method (dashed).

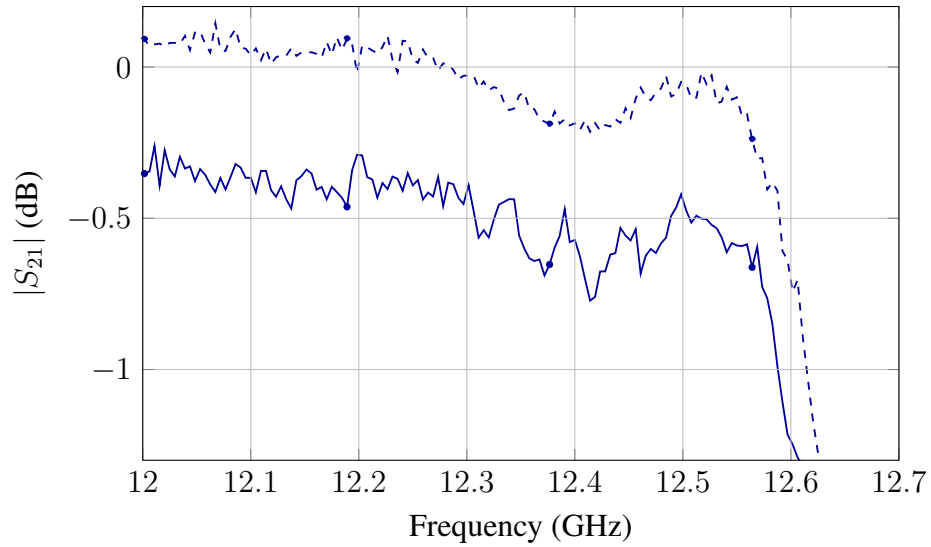

Figure 8.8: WR75 filter at -15°C. Details of the improvements due to the proposed temperature calibration procedure (solid) compared to the traditional calibration method (dashed).

8.3.2 Experimental validation in high vacuum

To conclude the experimental validation, the results shown in this section compare the measurements obtained in a set of devices characterized in ambient pressure and high vacuum.

For this validation, four filtering devices have been used. All of these bandpass filters share the same specifications: five poles, 0.1 dB of ripple Chebyshev response with return loss around 25 dB in the pass-band, center frequency $f_0 = 13$ GHz and 400 MHz of bandwidth. However, their design and physical dimensions are different, as they have been manufactured using different independent substrate integrated (SI) technologies (more details in [151]): substrate integrated waveguide (SIW), empty substrate-integrated waveguide (ESIW), alternating Dielectric Line Sections (ADSL), and empty substrate-integrated coaxial line (ESICL).

For the vacuum test, a set of test jigs were manufactured in order to enhance the thermal transfer between the DUTs and the TVAC chamber. The filters and the TRL standards are shown in Figs. 8.9, 8.10 and 8.11.

In order to provide a good thermal contact between the RF items to be measured and the vacuum chamber base plate, two different test jig structures have been explored:

Aluminum test jig as shown in Figs. 8.9 and 8.10, a metal frame was manufactured for each SI filter in order to hold it in place, and to provide a flat contact area with the TVAC base plate. Note that these devices have soldering and protrusions on both sides, which do not have a flat bottom surface with a large and smooth contact area with the base plate.

Cooper thermal bridge that is a sort of thermal transfer mechanism (see Fig. 8.11), it was implemented for small and low weight elements such as the TRL calibration kit standards.

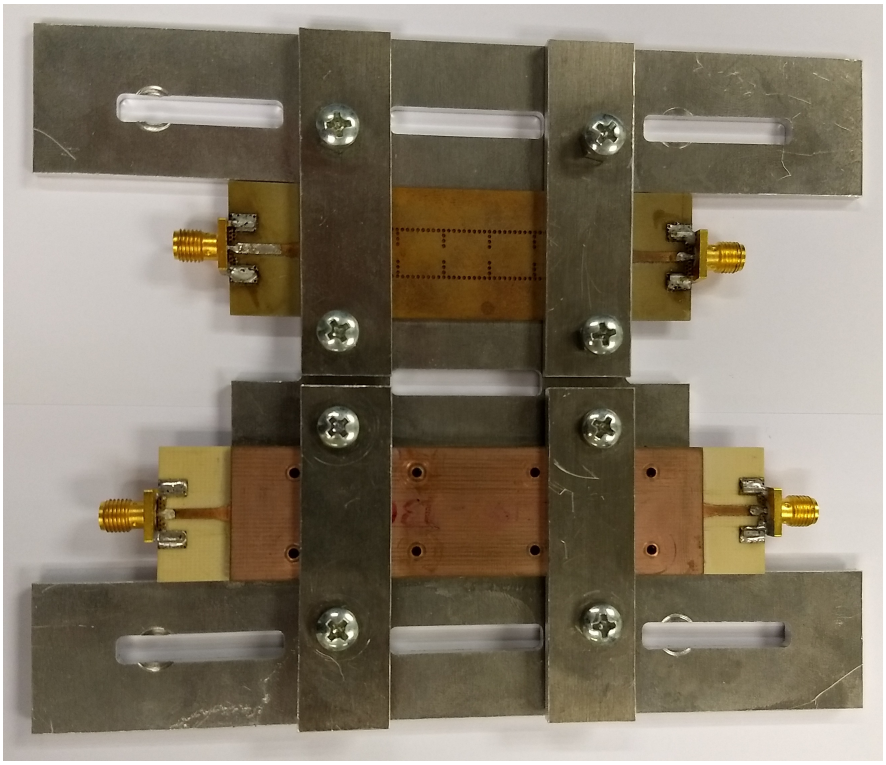

Figure 8.9: View of the substrate integrated filters (SIW and ESIW) used as DUTs for the calibration method validation. The test jig is also shown in this picture, and its thickness is larger than the RF connector protrusion.

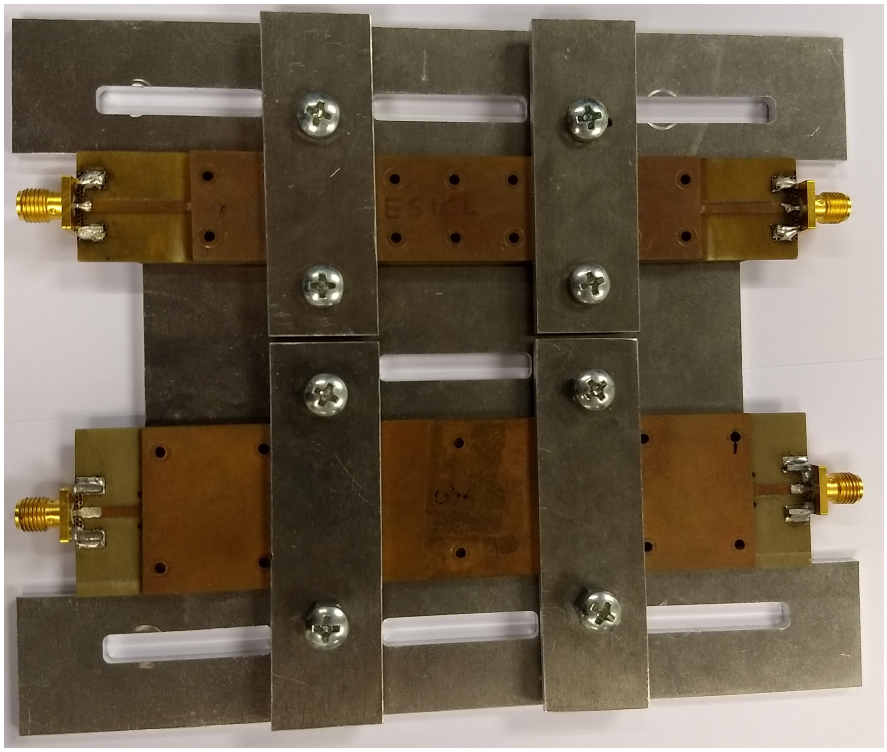

Figure 8.10: View of the substrate integrated filters (ESICL and ESIW) used as DUTs for the calibration method verification. The test jig is also shown in this picture and its thickness is larger than the RF connector protrusion.

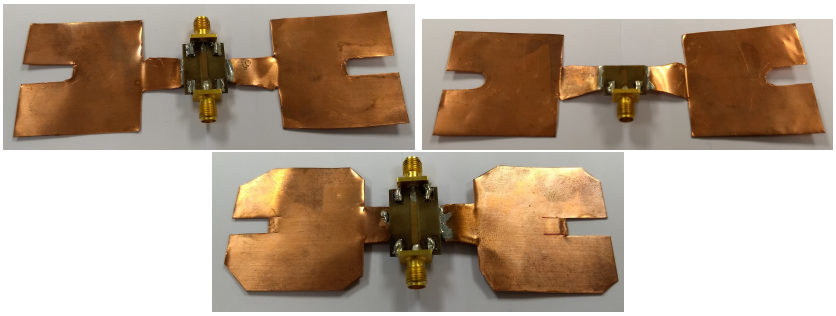

Figure 8.11: TRL standards used to characterize the errors due to the cables and interfaces from the VNA to the device input connectors (ports 1 and 2). In this case, the test jig is a cooper thermal bridge.

The applied thermal profiles are depicted in Figs 8.12 and 8.13.

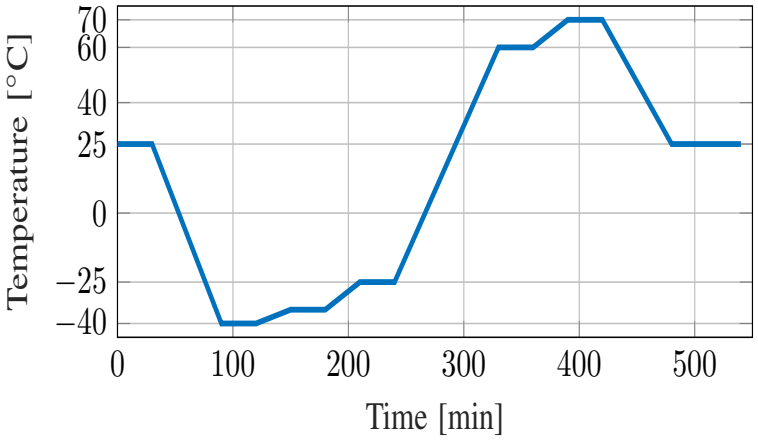

Figure 8.12: Applied thermal profile for the ambient pressure measurements. The dwell intervals have been set to: -40, -35, -25, +0, +60 and +75 °C.

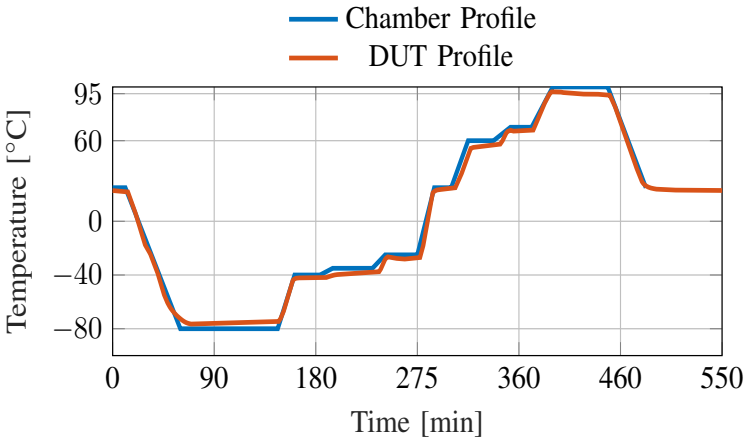

Figure 8.13: Applied thermal profile for the high vacuum measurements. The dwell intervals have been set to: -80, -40, -35, -25, +25, +60, +70 and +100 °C.

Despite using the thermal bridges, the actual temperature excursion measured on the devices has been lower than the desired one. The results for each thermal bridge type are:

- For the aluminum test jig, the devices reached a hot temperature of +95 °C, +5 °C lower than the programmed one (+100 °C). And a cold temperature of - 75 °C, 5 °C higher than the programmed one (-80 °C).
- For the cooper thermal bridge the devices reached a hot temperature of +95 °C, +5 °C lower than the programmed one (+100 °C). And a cold temperature of - 65 °C, 15 °C higher than the programmed one (-80 °C).

These unexpected results, and the lack of resources in order to repeat the measurements, implied that the temperature calibration technique could only be applied to those temperatures in which the scattering parameters for all the elements were available. Thus, in this experiment, the temperature range was from -65 °C to +95 °C. This decision implied that the -65 °C measurement did not meet the expected thermal stabilization time.

Despite the reduction in the temperature range, the measurement is still compliant with the specifications found in the ECSS vacuum test requirements [152, 14].

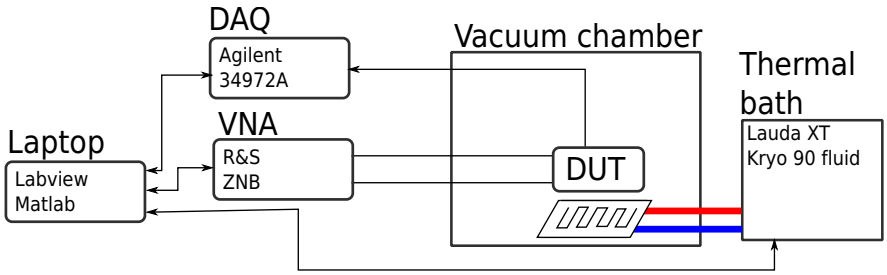

Figure 8.14: Test setup diagram for the high vacuum measurements.

The setups employed in these measurements are shown in Fig. 8.3 for the ambient pressure, and Fig. 8.14 for the high vacuum.

Experimental results are shown in Figs. 8.13 to 8.23. As documented in [153], applying a SOLT calibration in the RF connector of the VNA test cable, compared to applying a TRL calibration using a SIW TRL calibration kit, may result in scattering parameter errors in the order of 0.5 dB or more in the insertion losses, a reduction of the filter passband and errors in the measurement of the return loss of more than 5 dB. This implies that the accuracy obtained in the following results could not be measured unless using this new temperature calibration method.

From the measurement analysis, it is observed that lowering the temperature increases the center frequency, whereas a temperature increment lowers it.

- Ambient pressure: SIW filter presents a drift of +23 MHz at -40 °C and -14 MHz at +70°C.
- Ambient pressure: ESIW filter, a drift of +11 MHz at-40°C and -8 MHz at +70 °C.
- Vacuum: SIW filter presents a drift of +22 MHz at -60 °C and -24 MHz at +95°C.
- Vacuum: ESIW filter, a drift of +15 MHz at-60°C and -21 MHz at +95 °C.

Concerning the insertion losses, a drift coefficient of 0.0125 dB/°C for the SIW filter and 0.0023/°C for the ESIW has been obtained. These results are in coherence with the fact that the SIW filter has a dielectric filling, which is more temperature-dependent than the air-filled ESIW device (see Fig. 8.15).

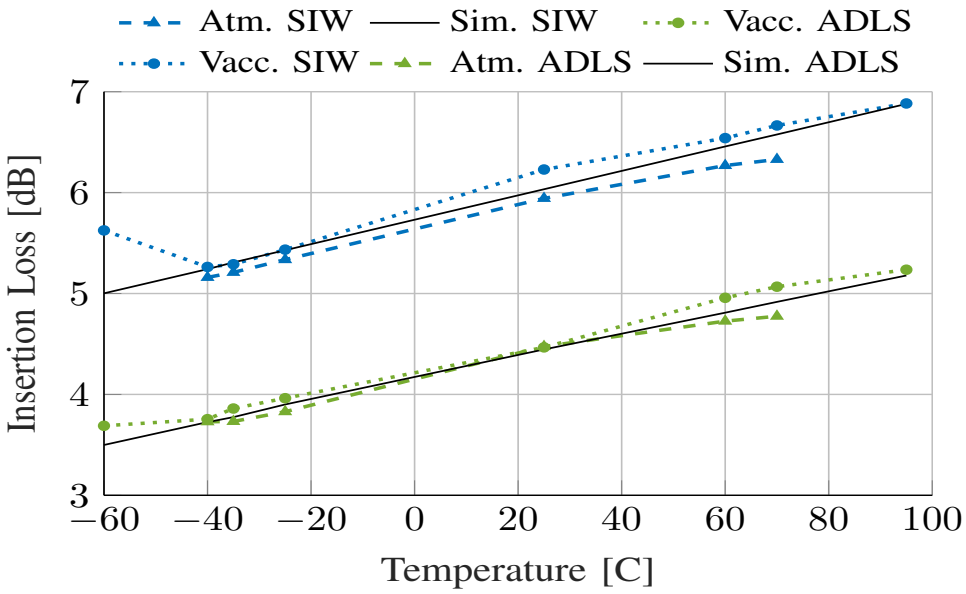

Figure 8.15: Accurate side to side comparison of the measured transmission losses variation for the SIW and ADSL substrate integrated technologies.

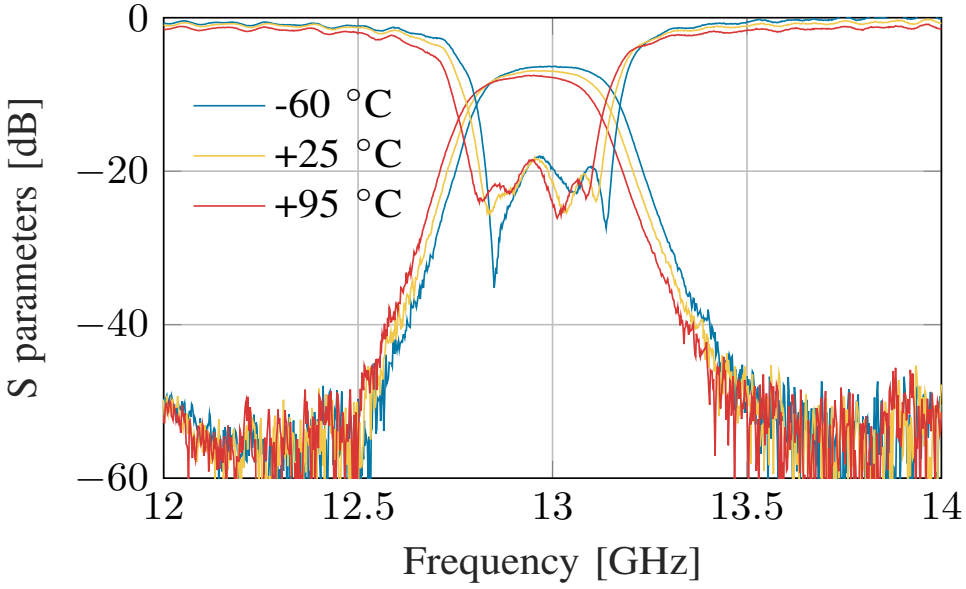

Figure 8.16: Calibrated scattering parameters at several temperatures for the SIW filter (high vacuum).

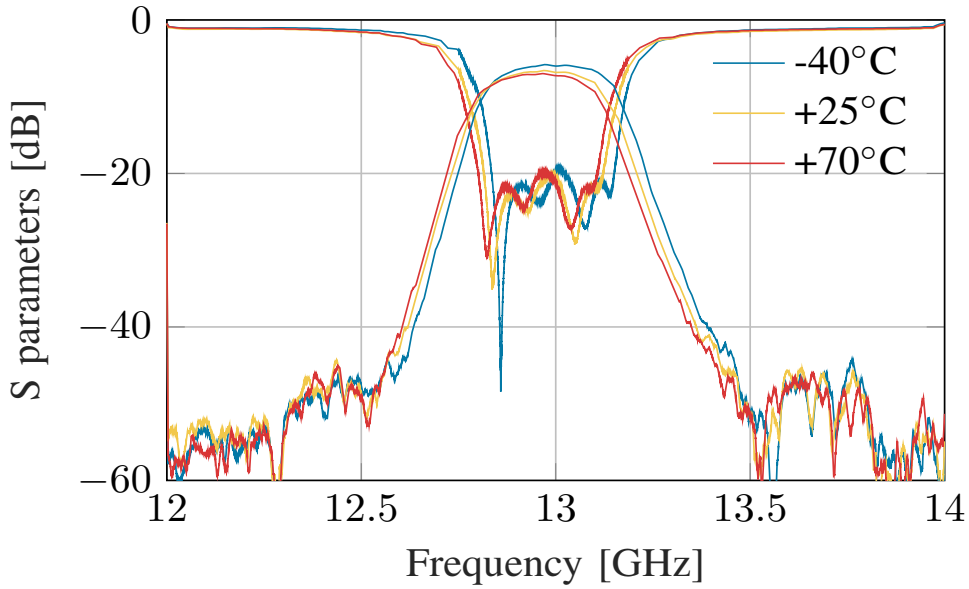

Figure 8.17: Calibrated scattering parameters at several temperatures for the SIW filter (atmospheric pressure).

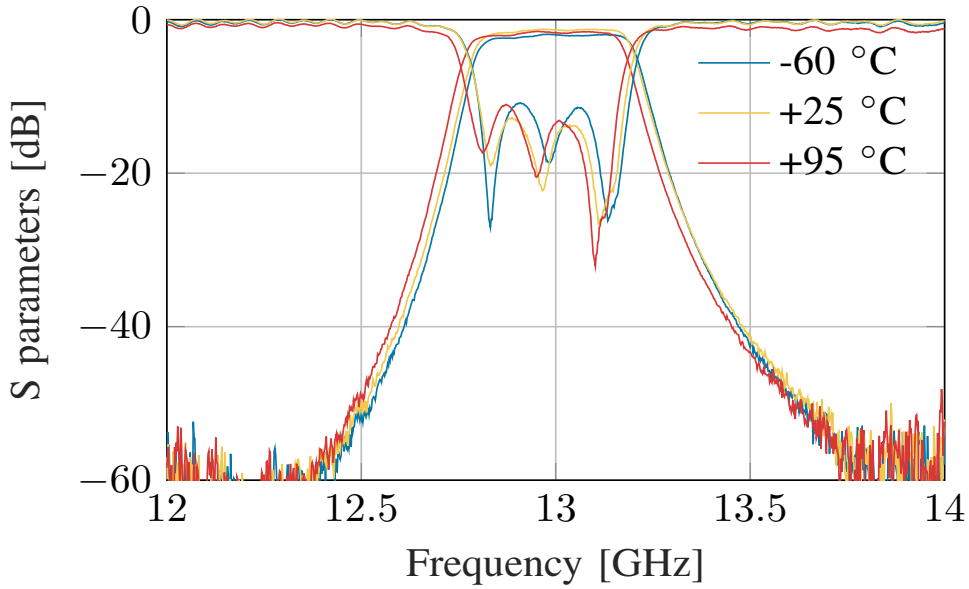

Figure 8.18: Calibrated scattering parameters at several temperatures for the ESIW filter (high vacuum).

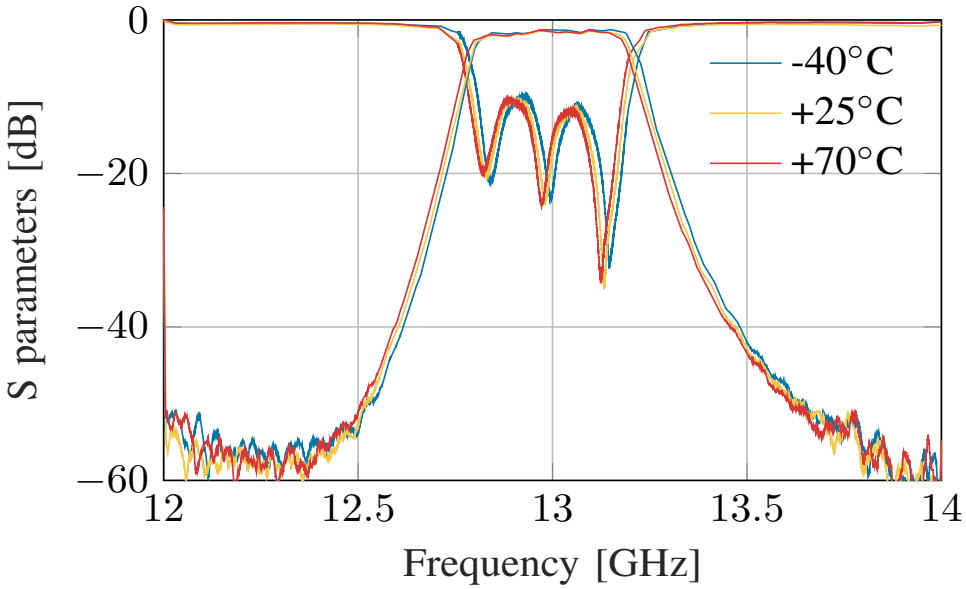

Figure 8.19: Calibrated scattering parameters at several temperatures for the ESIW filter (atmospheric pressure).

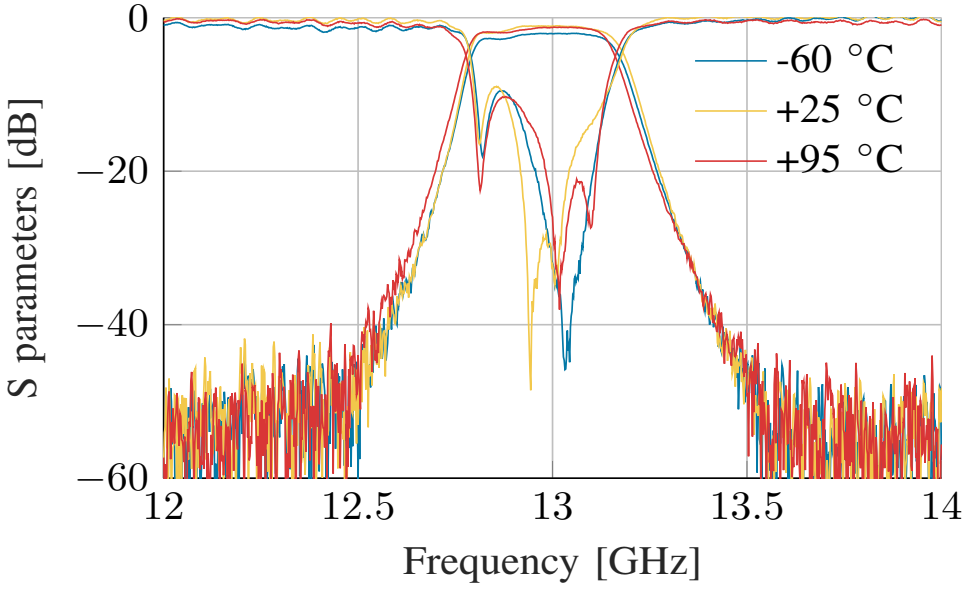

Figure 8.20: Calibrated scattering parameters at several temperatures for the ESICL filter (high vacuum).

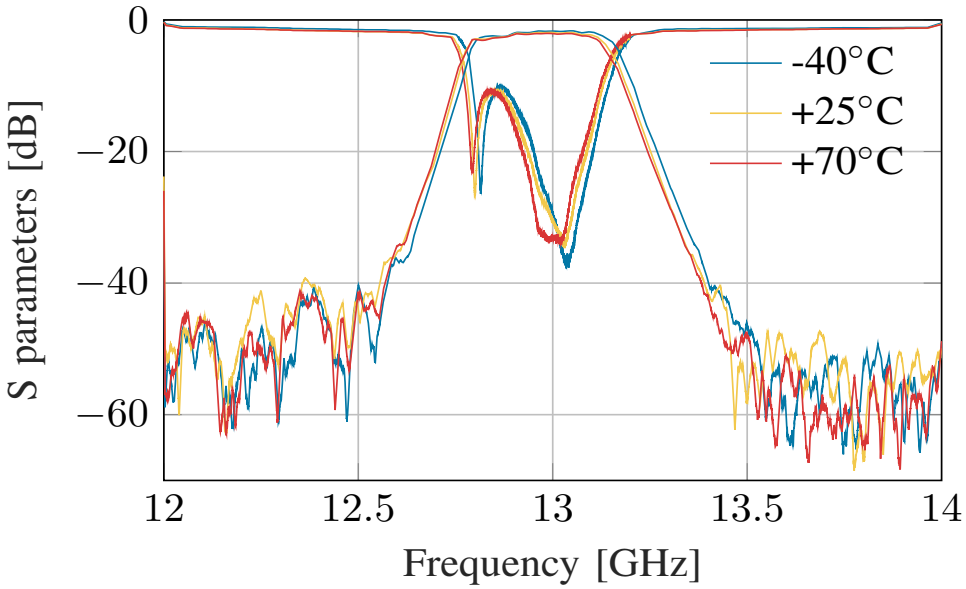

Figure 8.21: Calibrated scattering parameters at several temperatures for the ESICL filter (atmospheric pressure).

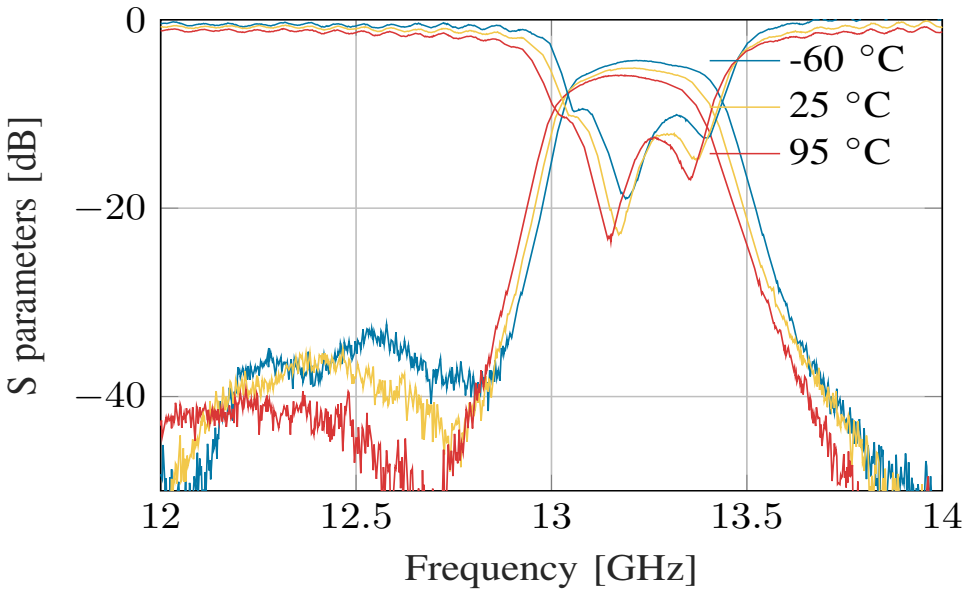

Figure 8.22: Calibrated scattering parameters at several temperatures for the ADSL filter (high vacuum).

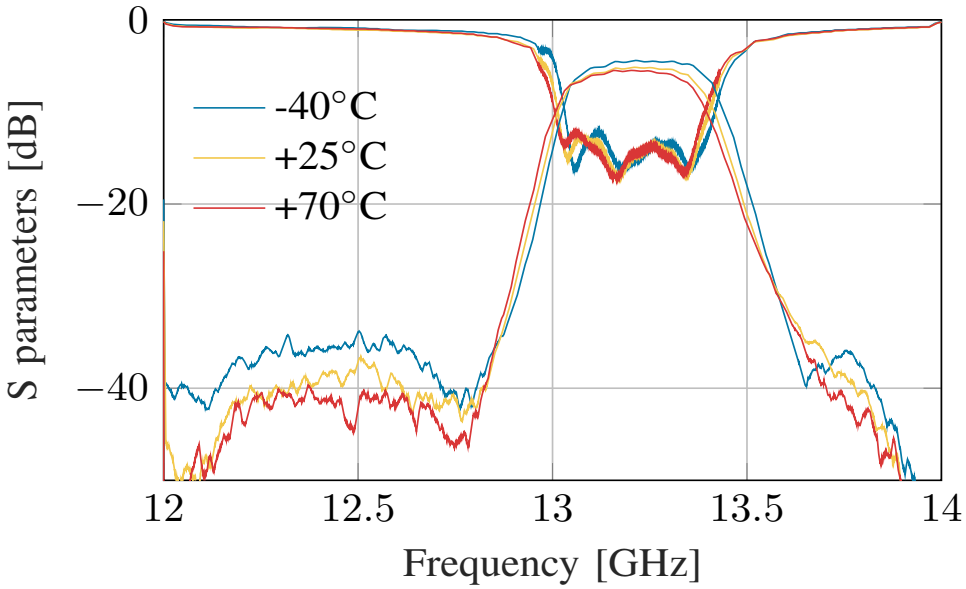

Figure 8.23: Calibrated scattering parameters at several temperatures for the ADSL filter (atmospheric pressure).

8.4 Conclusions

An automatic and accurate procedure has been proposed to measure the S-parameters in microwave components at temperatures other than ambient. The accuracy is guaranteed since, for the first time, the calibration is performed at each temperature of interest. In contrast to previous methods, in which the setup performance was assumed to remain unchanged due to temperature.

Experimental results are provided for microwave components implemented in two totally different technologies (rectangular waveguide and substrate integrated devices). Moreover, the applicability of this method to high vacuum environments has been demonstrated as well. Among the benefits of this method, the following ones should be highlighted:

- This method is applicable to any transmission line technology in which a TRL calibration kit can be manufactured.
- It provides the widest temperature range, only limited by the thermal system capabilities and the temperature limits of the interface transmission line.
- It can be applied either to ambient pressure or vacuum environments.
- Compatible with any thermal system and VNA with minor software changes.
- The TRL calibration method can be run in open source programming languages such as GNU Octave or python.

The most notable drawbacks of this method are also discussed next:

- The measurement process is slow it may take several days.
- Errors due to improper RF connection handling are not detected until the end of the process.
- Temperature convergence in vacuum operation is difficult to achieve in some cases.
- Noise floor after calibration is not typically better than 40 dBc. This is due to VNA circuitry drifts, RF cables handling, and the involved long measurement time.

8.5 List of own publications and projects

The method to obtain accurate scattering parameters measurements in temperature has been subject to peer review, and has been accepted in several international journals and conferences. Next, we offer a list with all these related publications.

8.5.1 Journal papers

- **O. Monerris**, E. Diaz, J. Ruiz and V. E. Boria, "Automatic, calibrated and accurate measurement of S-parameters in climatic chamber", in IEEE Microwave and Wireless Components Letters, vol. 25, no. 6, June 2015, doi: 10.1109/LMWC.2015.2421330.

- V. Nova, C. Bachiller, J.A. Martínez, H. Esteban, J.M. Merello and A. Belenguer, **O. Monerris** and V.E. Boria, "Thermal stability analysis of filters in substrate integrated technologies under atmospheric pressure and vacuum conditions", in IEEE Access, vol. 8, pp. 118072-118082, 2020, doi: 10.1109/ACCESS.2020.3004875.

8.5.2 Conference papers

- E. Diaz, A. Belenguer, H. Esteban, **O. Monerris**, V.E. Boria, "Una nueva transición de microstrip a una guía de onda integrada en sustrato con mayor impedancia característica", in XXVIII Simposium de la Unión Científica Internacional de Radio (URSI). Santiago de Compostela, Spain, September 2013

- E. Diaz, A. Belenguer, H. Esteban, **O. Monerris**, V.E. Boria, "A novel transition from microstrip to a substrate integrated waveguide with higher characteristic impedance", in proceeding of: 2013 IEEE/MTT-S International Microwave Symposium Digest. Seattle, WA, USA, June 2013.

- **O. Monerris**, E. Diaz, V.E. Boria, "Medida automática, calibrada y precisa de parámetros S en temperatura", in XXX Simposium de la Unión Científica Internacional de Radio (URSI). Pamplona, Spain, September 2015.

Chapter 9

Conclusions and future work

9.1 Summary

This final chapter closes the PhD thesis recapping the achieved research goals. The scientific contributions in the field of advance multipactor testing techniques have been validated by the large number of publications in peer reviewed journals (9) and conferences (24).

This thesis has completed its initial research topics. The multipactor testing methods for rapid verification of microwave and RF components used in space applications have seen major results in the previous pages. Current industry requirements typically involve high order digital modulations and multicarrier operation. These signals are both, costly to simulate using commercial tools and difficult to experimentally verify. The three parts in which this thesis is organized have provided excellent results in all these aspects.

In part one, the multipactor effect in the presence of modulated signals and dual carrier has been considered. Numerous results based on simulations show the impact in the multipactor threshold produced by time varying signals, with significant changes recorded in most cases. The short and long-term multipactor has also been considered in some parts of the research.

In part two, the experimental aspects of the multipactor effect for multicarrier signals with different modulations are addressed. Currently, no commercial solution is available to generate flexible high power multicarrier signals with smooth adjustment in terms of phase and amplitude. This thesis dissertation presents different methods to create, amplify and adjust the multicarrier signals required to verify the multipactor performance of the RF designs.

The final and third part of this document presents two new testing methods. The first one is a novel detection system based on digital signal processing capable of identifying the multipactor pattern from the RF information. This method has proved to be as sensitive as the well known microwave nulling when continuous waves signals are used, and much more sensitive when modulated signals are employed. The second one is a new procedure for the accurate measurement of the scattering parameters in temperature. Although commercial solutions exists to fill part of this market requirement, the procedure developed in this thesis

surpasses those commercial solutions in terms of operating temperature range.

9.2 Conclusions

A detailed review of the research finding and achieved goals is carried out next.

Chapter three has shown new multipactor results for analog modulations. In first place, the effect of short pulses in the multipactor threshold has been considered. This thesis has provided not only simulation results, as in previous works found in literature, but also experimental data. By means of special RF equipment the investigation has confirmed that a significant increment in the multipactor threshold is produced. Increments up to +6 dB with respect to the CW threshold have been predicted and measured when pulses lasting for 45 RF periods are applied. Shorter pulses have been experimentally applied, however, the combined effect of the signal generator and the high power amplifier produces pulses with shapes closer to Gaussian than to a square. For that reason this experiment has not considered pulses shorter than 45 RF cycles.

Continuing in chapter three, the dual carrier results have provided an excellent scenario for exploring the so-called long and short-term multipactor regimes. A dual carrier signal, with its periodic pattern, produces a RF envelope in which the time length above the multipactor threshold (ON interval) and the time below the threshold (OFF interval) can be easily set by varying the frequency spacing. Three different RF power ratios have been also considered $P_1 = P_2$, $2 \cdot P_1 = P_2$ and $P_1 = 2 \cdot P_2$, being P_1 and P_2 the RF power in Watts for the first and second carrier, respectively. In this occasion the experiments have not proved the presence of the short-term multipactor regime. This mismatch is assumed to be produced by the lack of enough time resolution in the multipactor detection systems.

In particular, the combline device has given excellent simulations results in order to isolate these two multipactor regimes, with the prediction in the 20-30 W for the short-term and 130-200 W for the long-term. However, experimental results recorded multipactor thresholds in the 140-210 W, with increasing RF power as Δf increases. This can be understood as a limitation in current detection systems, which have not been able to detect such short-term discharges. The author considers that only the long-term ones have been detected. The reason why the simulations for this sample show such large threshold difference is due to the resonators shape. The resonators in this device are not solid cylinders, but their shape is closer to that of a bucket. As a consequence a band gap is created, this band gap implies that there is an initial RF power interval in which multipactor can happen, followed by an interval in which it cannot, and a final one in which multipactor can happen again. This uncommon effect reflects in the computed α (instantaneous electron growth factor) values for this structure, which have a negative interval within two positive intervals.

In contrast, the other devices show a common multipactor behavior with no band gaps. However, simulation this sample also shows that shor-term and long-term multipactor regimes also exist. Perhaps due to the lack of a band gap, both multipactor regimes show a similar threshold value. Experimental results for this sample have shown a significant deviation

when compared to simulations in absolute terms. It is suspected that it comes from the SEY data. As for the combline device, the short and long-term regimes have not been identified by testing either.

With respect to the digital modulations considered in chapter 4, all the ones included in the DVB-S2 standard have been taken into account. Which comprise all the digital modulations being used in current satellite communications. Two different sets of results have been obtained. In the first one periodic sequences have been used, whereas in the seconds one random sequences have been considered.

For the periodic signals it must be highlighted that simulations indicate that the BPSK and the QPSK X-sequence have shown a similar trend. These two cases have zero crossing. In contrast, the Q-signal have shown a more constant threshold. Experiments also confirms such trend, although they do not match simulations with the same accuracy as for the analog modulations experiments. For the random signals, increments between 1.7-3.2 dB from the $\xi = 40$ to the $\xi = 400$ case have been observed. In all cases this margins has been positive, being the largest change recorded for the 16-QAM case.

The final conclusion which arises from chapters 3 and 4 concerns the "20-gap crossing rule". This rules, widely employed in industry because its simplicity, has been proved not to provide reliable predictions. As its output is based in only one variable (time), large errors have been recorded in those cases where the signal changes rapidly (> 4 dB). For that reason, this dissertation proposes to replace this rule by the coarse multipactor simulation method. For the coarse method to provide stand alone multipactor predictions, analytic geometries could be employed to produce the α values. However, as shown in this document, the most reliable results are obtained when accurate PIC simulators and measured SEY data are used to determine α values.

Moving to the multicarrier generation, two novel methods to develop setups for the generation of such signals have been presented. Commercial products currently available do not provide an optimal solution to this specific industry problem. For that reason, the numerous strategies proposed in this thesis are required. As in any complex problem, there is not one single solution to the problem. The proposed strategies adapt to the various situations observed in multipactor testing laboratories.

First, the re-purpose of already existing RF equipment represents an excellent option for high power RF laboratories in which a permanent multicarrier facility is not available. In those cases, the technical solution proposed in this thesis has proved to produce signals with sufficient stability in order to carry out multipactor tests. The method described in chapter 5 focuses on the generation of CW, pulsed CW or modulated signals using independent signal generators. The results have reported a very good convergence to the desired multicarrier signal in four to six iterations. Experimental results have also shown that phase locking or high-frequency sharing among the signal generators are not strictly required. A method to have modulated carriers has also been proposed, but these digital generators handle only one carrier, so they may be narrowband.

The second method presented in chapter 6 requires RF equipment capable of generating

digital signals with as much bandwidth as the complete multicarrier signal. On top of that, phase locking or local oscillator sharing techniques are required if more than one RF equipment is to be used. The benefits from this method are that the phase stability over time is almost perfect (phase shift < 0.2 degree per hour), and the use of a smaller amount of low RF power equipment.

Both method share the same CPU intensive algorithms to retrieve the phase of each carrier from the high power signal. Experimental results have proved that results are convergent in less than 10 iterations in all cases.

In terms of performance, the excellent spectral purity which can be obtained with the implementation shown in chapter 5 might be useful not only for multipactor testing but also for passive intermodulation testing. However, this comes at the expenses of requiring more frequent phase adjustments, even when the system has reached thermal stability, and a larger number of RF equipment. In contrast, the implementations shown in chapter 6 have better long-term phase stability and are more suitable for creating accurate multicarrier signals with digitally or analog modulated carriers, although the spectral purity obtained with this second set of techniques is low. Nevertheless, the spectral purity achieved with this second set of techniques is sufficient for multipactor testing and comes with the additional benefit of using less RF equipment.

The improvement of the multipactor detection methods has been a topic of major concern for the author. The need of rapid verification of the multipactor threshold on the same device when using different signals has forced the constant upgrade of the multipactor test bed and its detection methods. Besides several minor updates on the typical multipactor test bed, this dissertation has provided two major upgrades in the multipactor testing field. The first one has been the novel in-phase and quadrature detection method. And the second one is the novel test procedure in which the signal under test is not repeated at a constant rate, but following an ex-ante multipactor detection in the previously sent signal.

This novel method relies on digital signal processing to model the background noise present in the multipactor test RF signal. This noise is assumed to follow a Rayleigh distribution. By means data obtained from a certain amount of previous samples, an empirical noise distribution is found. Next, from this noise distribution and a false alarm probability, a threshold is determined. Then, each new sample is tested versus this threshold. When the new sample is below the threshold it is considered not to have multipactor, otherwise it does. The noise model is updated once the last acquisition is verified not have multipactor.

The benefits of this novel technique are many. Firstly, its detection sensitivity is comparable to that of the well proven microwave nulling as shown in the experimental results. Secondly, it can cope with wideband signals and its not constrained to continuous wave signals, as the nulling system is. Thirdly, its hardware implementation is simpler an requires no periodic operator tuning. Fourthly, by being based in digital signal processing it can run autonomously. And, fifthly, its output is not only qualitative but also quantitative.

Different experimental results have shown that a dynamic range of 40 dB can be obtained for non modulated signals. And 30 dB for analog and digital modulated signals. The noise

increment measured in the experiments has been 40 dB for the continuous wave signal and 20 dB for the modulated ones.

Nevertheless this methods has some limitations which impacts in a large extent its performance. First of all, the method is prone to suffer from false alarms. This is due to the fact that the noise from the amplifier does not only follow a Rayleigh distribution. To overcome this limitation the extra requirement has been implemented in this thesis. This additional requirement requires a minimum number of the consecutive samples to fail the hypothesis test, turning the algorithm more robust at the expensive or being unable to detect shorter discharges.

The second limitations comes from the trigger errors, which translate into large increment of the background noise. This is caused by the way in which the reference waveform is currently obtained. This waveform is used to obtain the compute acquisition noise by subtracting the reference to the current measurement. In the experiments carried out in this dissertation this error has not be handled, although commercial solutions to overcome this technical problem have been identified for the major RF equipment vendors. This is the reason why signals with very large bandiwdth have not been included in the examples.

The second testing development is detailed in annex A. This novel testing procedure is the one ensuring that surface conditioning is minimal when determining the multipactor threshold. In contrast to the standard multipactor test objective, which typically has the device as central element, this thesis has challenged the need of performing many multipactor tests in the same device.

Performing an ex-ante multipactor detection allows stopping or reducing the RF power before conditioning is produce in the device being employed. By avoiding unnecessary multipactor discharges from being triggered, many different modulated sequences can be tested safely. An standard practice is to add intermediate pulsed CW test within the modulations to be tested. As long as the pulsed CW test provide the initial multipactor threshold, conditioning can be considered not to have occurred.

It is a common practice to break the vacuum conditions to recover the multipactor threshold when conditioning is observed. However, this approach limits the maximum number of tests that can be conducted by day, as time in vacuum prior testing is several hours. By applying the proposed ex-ante multipactor analysis the amount of tests run in one single day can go up to 5 or more without breaking the vacuum.

Still, implementing this new test procedure is not straightforward as typical multipactor detection is manually carried out by the test operator. Automation of all the multipactor detection system is required in order to achieve a sufficiently high repetition rate. Considering as target the 1 kHz pulse repetition rate suggested in the ECSS standard, the implementation achieved in this thesis has reached repetition rates between 250 to 500 ms.

To conclude the results section, this thesis has also developed a new technique for the measurement of scattering parameters over a wide temperature range. The lack of commercial solutions to accurately characterize devices at very low or very high temperatures, has led to the development of a new temperature calibration procedure in this PhD thesis. Compared

to commercial solutions which only operate in the -30°C to +80°C range, this technique is only limited by the interface cables being used (in this work from -80°C to +115°C).

This novel scattering parameter measurement technique is capable of measuring the actual $|S_{21}|$ in a waveguide filter. Whilst the new method provides a value of -0.4 dB at -15°C, the classical calibration procedure at room temperature indicate that there is a $+0.1$ dB gain in the $|S_{21}|$, which is not feasible in a passive filter. Errors up to $+0.5$ dB for hot temperatures (+115°C) and -0.5 dB in a cold (-15°C) environment have been detected while measuring the $|S_{21}|$ in waveguide filter measurements.

Experimental results have also shown that the method is applicable to ambient and vacuum conditions. Sample measurements carried out at ambient pressure for SIW and ESIW technologies have registered changes up to $+22$ MHz in hot temperatures (+100°C) and -24 MHz in cold temperatures (-80°C) for the SIW filter, with smaller drifts being observed in ESIW technology, which has no dielectric material in the RF path.

As a major drawback, calibrated results using this method have shown to be slower to obtain than with the traditional calibration or comparable industry solutions. Whereas a standard TRL calibration typically takes less than 5 minutes to be completed, the measurement of all the different calibration standards required for the new method may take several days.

As a global conclusion, it can be said that the initial objectives of this PhD work have been achieved, being the quality of the results and their scientific interest justified by the numerous journal (9) and conference (24) publications (see Appendix E) that are a consequence of the work described in this doctoral thesis.

It is worth mentioning that the work conducted during this PhD thesis was motivated by the European space market's need of having a cutting-edge multipactor testing capabilities. The work described in the thesis has successfully met this challenge. The compact multipactor test incorporating all the new advances is available to entities from the European Space Agency's (ESA) member states at the European High Power RF Space Laboratory, a joint initiative of ESA and Val Space Consortium (VSC).

9.3 Future work

This thesis is one single step in the path of RF multipactor breakdown research. Although most of the research goals have been covered, they allow further improvement in many ways. From the identified limitations this section presents how the different topics can be enhanced.

As mentioned in the introduction section, multipactor breakdown is an undesired phenomenon in satellite RF components. Multipactor may be fully developed under canonical RF signal excitation, such as CW or pulse CW, which typically lead to long-term multipactor discharge. However, very short pulses or modulated periodic signals may lead to short-term multipactor discharges. Although it is crucial to be capable of simulating and detecting these short-term discharges, which last hundreds of nano-seconds, the next questions to be solved by academia are: *1*) are these discharges sufficient to prevent the communication system from operating nominally? *2*) may they lead to a mission failure in the long-run?

Perhaps the multipactor standard [8, 9] will require further updates, to re-define the multipactor margins. These updates should address the issues about the actual signal to be transmitted, its randomness and the probability of having short or long-term discharges through the satellite operational life. It is evident that the current testing routes, which may represent an over-testing, fully warrant that multipactor will not occur. However, the threshold levels might be relaxed, while not affecting the actual component performance or mission success.

On top of that, it is also true that the presented testing techniques are more precise, accurate and sensitive. Consequently, discharges that could not be noticed in the past can be easily detected with the new techniques proposed in this work. This raises the following question: how many devices have been put into orbit suffering from short-term or even weak long-term discharges, which have been unnoticed in their validation or operational phases?

This field of research will be of significant interest for the industry, since reducing the multipactor margin while keeping the mission success is always beneficial to them.

Another area that requires further research is the multipactor threshold definition. Currently, the margins do not consider the signal modulation being used, but this should be considered in future standards, adding a positive or negative value to the margins when the verification is done using CW or pulsed CW signals. This margin should depend on the modulation type, relative bandwidth, and even the total number of carriers in the system.

In the multcarrier generation methods presented in this dissertation the current bottleneck is the signal acquisition. Currently an oscilloscope has been used to sample the signal, which in high bands can result in a very expensive design. Making the phase recovery algorithm compatible with the phase recovered in a signal analyzer would be convenient for high frequency multicarrier systems. Even more, by using a phase coherent signal analyzer the phase stability would be significantly increased.

The main issue with the new multipactor detection method presented in this work comes from its execution rate. Although the obtained results are consistent with simulations, the execution rate should be able to cope with the standard pulse repetition frequency (PRF) of the multipactor test, which currently is 1 kHz. The next step would be to implement the method in such a way that it is executed in real-time, so it can be used even with CW or pulsed CW signals. Most likely this requires streaming the data directly to an FPGA, where the multipactor detection is carried out with a sufficiently high rate.

Reducing the RF equipment required in a multipactor test bed is another field of research and development. New equipment can perform several tasks simultaneously, and now RF power measurement and multipactor detection can be made with confidence in the same device. A proposal in that direction is shown in Appendix B. Another research in this field may come from using inexpensive software-defined radio (SDR) devices which work up to 6 GHz, and may be a good platform to implement inexpensive multipactor test beds.

Finally, one central point that has not been solved yet is implementing a detection global method capable of determining the discharge location within the DUT from the RF perturbation produced by the multipactor discharge. This is an unexplored research field where no references or attempts can be found in the literature. In addition, some other possibilities

of research related to this topic could be approached, such as using artificial intelligence for multipactor detection.

The number of multipactor related topics that can be further investigated is broad. Industry and academia interests will push the research in any of those directions.

Appendix A

Advanced multipactor testing methodology

A.1 Introduction

This appendix presents a novel multipactor testing approach in which a software controlled waveform rate replaces the standard constant waveform rate. The proposed methodology has been developed in order to meet a requirement frequently observed along this thesis: the maximization of multipactor tests which can be conducted in the same sample without braking the vacuum.

When studying the threshold change with modulated signals, either digital or analog, the devices under test is the same all the campaign long. During the first campaigns, for the short pulses, BPSK or QPSK it was observed that sample conditioning was frequent, and the number of tests carried out each day were not many.

Device conditioning is determined by inserting pulse CW tests within the modulated tests. If the same threshold is observed in the first pulse CW test and the verification pulse CW test, all the modulated tests carried out within these two are considered valid and free of surface conditioning.

In parallel, the improvements in the signal processing for multipactor detection allowed all the standard and new methods to be software driven instead of operator controlled. So decision making has been moved from the operator to the machine, which now is capable of performing an initial guessing of the multipactor presence.

As a consequence, the new testing methodology uses a master software which waits for the different detection methods evaluation before allowing the next waveform transmission. Thus increasing the number of tests executed in a single day by minimizing the device conditioning.

The main advantage of the proposed method are:

1. Minimization of the material conditioning.

2. Exhaustive multipactor detection. 100% probability of successful detection.

3. Full test logging.

In order to meet these requirements, the standard multipactor detection methods must be enhanced in two aspects: to have some sort of digital signal processing which detects multipactor automatically and, to work at faster acquisition rates. Most of the methods described in [8] are implemented in such a way that a continuous stream of RF waveforms is expected. So they are not capable of handling one single pulse or sequence. Because the traditional multipactor detection methods work asynchronously with respect the pulse repetition rate, they rely on this constant and fast waveform rate to detect the discharge.

In the standard implementation, the asynchronous operation turns multipactor detection into a probabilistic issue. In table A.1 the effective acquisition time, defined as the percentage of time in which the signal is being monitored with respect the total acquisition time, are summarized. This table is compiled for the standard acquisitions rates and integration times as described in [8] (1 KHz pulse repetition frequency, 20 μs pulse width).

Detection method	**Effective acquisition time (%)**
Microwave nulling (MN)	2 - 99
Harmonic monitoring (Hm)	2 - 99
Electron monitoring (Em)	0.5
UV ligh monitoring (UV)	0.5
Pressure (Pm)	0.2

Table A.1: Multipactor testing typical effective acquisition time (in percentage) considering that multipactor could within the 20 microseconds with RF ON every 1 millisecond and that the different detection systems operate at their maximum measurement rate [154, 8].

It is worth noting that when asynchronous detection is used and pulsed signals are applied, there is a signal to noise ratio loss due to the RF duty cycle. Which for a 2% duty cycle corresponds to a 17 dB loss. This figure may be relevant or not depending on the discharge strength however, it is a drawback to be considered.

The probability of detection for a set-up with only one detection method of each kind (table A.1) can be computed as

$$P_d = 1 - (1 - P_{dMN}) \cdot (1 - P_{dHm}) \cdot (1 - P_{dEm}) \cdot (1 - P_{dUVm}) \cdot (1 - P_{dPm}) \qquad \text{(A.1)}$$

being P_{dMN}, P_{dHm}, P_{dEm}, P_{dUVm}, P_{dPm}, the probability of intercepting the time interval in which the discharge happens.

This translates into two very different scenarios. For the lowest values, the best case detection probability is $P_d = 5.1$ %, whereas for the high end values $P_d = 99.99$ %. These figures clearly indicates that fast measurement devices are required to have large chances

of detecting an RF breakdown discharge in, at least, one single method. However, in both cases, the detection probability is not 100%.

By following the classic testing approach, the improvements listed at the beginning of this appendix cannot be reached:

1. Very consistent multipactor threshold between several discharges.
   (a) Pulse repetition is not driven by the multipactor detection methods, so RF pulses will be transmitted even if a discharge has been detected before.
   (b) Pulse rate is high for human operation (1 kHz). Many RF pulses will be transmitted after the initial multipactor discharge. Typically, rounds of 20-60 consecutive pulses with multipactor discharge happen in what operators typically call one multipactor discharge.
2. Exhaustive multipactor detection. 100% detection probability.
   (a) Even for the best scenario, a small number of pulses are not even measured.
   (b) In some cases, a large portion of the pulses are not even measured.
3. Full test logging.
   (a) It is only possible to record time aggregated (< 1 kHz sampling rate) results, but not time domain with at least one microsecond resolution trace.
   (b) Recorded data cannot be used later to apply other detection algorithms.

For the previously mentioned reason a novel multipactor testing methods has been implemented and used in multipactor test campaigns for R&D activities carried out by this PhD thesis author.

A.2 Sequence by sequence testing

Sequence by sequence testing is the name of this new multipactor test technique. Its main features are:

1. Synchronous signal generation and acquisition.
2. Wideband signal generation, analysis, and RF power measurement.
3. Software-driven sequence repetition period.
4. Co-existence of novel detection methods with classic methods.
5. Centralized and distributed operation.

6. Full data logging.

Without loss of generalization, an example of the typical schematic is shown in Fig. A.1. In this setup, the new detection methods that drive the test execution rate are used in parallel of some standard local detection methods for electron monitoring. The novelties of the testing approach are:

Transmit, analyze and advance This novel multipactor testing technique uses a sequence by sequence approach. An RF pulse or waveform is not transmitted to the DUT until the multipactor detection algorithms have analyzed the previous one. This is a novelty with respect to the standard testing procedure in which a constant pulse or sequence rate is transmitted [8].

Advanced signal sequencing To enhance the multipactor detection precision, some extra information is transmitted alongside the signal under test. Detailed description of the sequence structure can be found in section A.2.2.

Wide band RF power measurement A novel kind of RF power sensors manufactured by Rohde & Schwarz (NRQ6) are used. These devices are capable of measuring the power envelope of modulated signals with up to 100 MHz bandwidth. These sensors are capable of providing not only the power versus time trace, but the time domain in-phase and quadrature voltage.

Upgraded multipactor detection methods An upgraded set of local multipactor detection methods is implemented by using signal conditioners, and a fast oscilloscope as data acquisition unit. Simple yet fast signal data processing for multipactor detection is implemented in these methods

Full data logging with fine time-domain resolution All the responses from the detection methods are logged.

A.2.1 Transmit, analyze and advance

The testing methodology does not follow a constant sequence repetition rate. In contrast, a dedicated software tool drives the signal generator, and forces a trigger once all the connected multipactor detection methods have confirmed that the discharge was not present in the previous one.

Communication among the different software tools is implemented over TCP/IP. This allows the tools to be allocated in one single computer, or distributed among several computers in the network (local or global/internet).

Having all the tools in the same computer improves the inter-software communication due to network latency, allowing faster signal repetition rates. However, CPU based multipactor detection at high speeds may overload the CPU. In that case distributing the detection

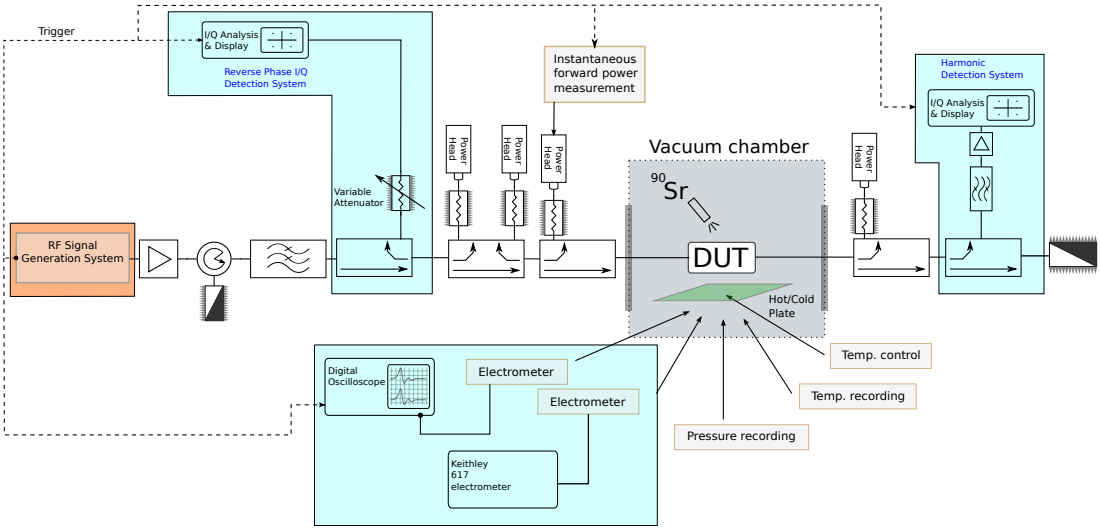

Figure A.1: Test bed schematic in which the novel IQ detection is implemented and one wideband NRQ6 power sensor is employed to accurately measure the forward RF power.

load among several computers might be a more suitable option. The software in charge of controlling the signal generation can also operate at constant pulse repetition rates, without the need of waiting for the detection software feedback.

If a multipactor discharge is recognized in any detection method, the RF power level in the signal generator is reduced by a specific amount defined by the test operator. By reducing the RF power instead of switching it off, two advantages arise:

1. temperature inside the high power amplifier circuitry is kept constant, improving the gain stability and output power level stability,

2. all the multipactor discharge detection system, based on the RF power measurement, do measure RF signal instead of noise. It prevents the algorithm from trying to detect RF breakdown discharges in a measurement in which there is only noise.

Even when synchronous testing is used, there is a maximum reaction time for the detection tool (time-out). If this data processing time is exceeded, the next sequence is sent.

The typical repetition rates are currently bounded in the 250-500 ms range. It must be noted that the slowest detection method constrains the repetition rate. In particular, for the instrumentation devices used in some experiments of this PhD thesis: the data acquisition and logging from the oscilloscope limits the maximum rate in tests using short sequences ($<$ 200 micro-seconds), and the IQ detection methods limit the maximum rate for long sequences ($>$ 2 milliseconds).

A.2.2 Advanced signal sequencing

The RF signal used in this new testing methodology has three parts which include, but are not limited to, the signal of interest. Due to the nature of RF breakdown testing, data throughput is not a critical requirement, so that additional signal sections can be appended for the sake of better detection performance. In particular, all the signals that have been experimentally validated are created by concatenating three segments whose purpose is very specific.

The first segment (training) is used for amplitude normalization and phase alignment between the RF source and analyzers. Additionally, small frequency offsets can be corrected if required. The amplitude of this segment must be set to prevent RF breakdown discharge from occurring.

The second segment is an RF OFF interval, used to relax the electrons inside the RF device to lose kinetic energy and any existing resonance.

The third segment is the actual signal of interest, which means the portion in which the RF breakdown must happen when increasing the RF power.

The time and amplitude characteristics of these three segments are:

Segment 1 RF ON with a CW signal (50 μs long) with 0 degrees phase and -10 dBc,

Segment 2 RF OFF (50 μs long), and

Segment 3 RF ON with the signal of interest (any length) with a peak level of 0 dBc.

An example of this signal configuration is shown in Fig. A.2.

Once a new acquisition is available ($s_{in}(t)$), the complete signal is normalized ($s_{out}(t)$). The scaling factors, computed from the training segment ($s_T(t) = s_{in}(t)$ for $0 \leq t \leq 50\ \mu s$), are obtained as follows:

Amplitude scaling (a_s) computed so that $s_T(t)$ has 1 V_{rms}.

Phase correction factor (θ_s) average phase of $s_T(t)$.

Frequency offset (θ_{fa}, θ_{fb}) obtained from the linear regression to $s_T(t)$ phase.

Then, the normalized signal is computed as:

$$s_{out}(t) = a_s s_{in}(t) \cdot e^{j\theta_s} e^{j(\theta_{fa}+\theta_{fb}t)} \tag{A.2}$$

A.2.3 Detection method

For multipactor detection in this advanced multipactor testing methodology, the measured magnitudes are the same ones as in the classic approach. However, they are sampled at a higher speed, and digital signal processing is done to automatically detect the breakdown.

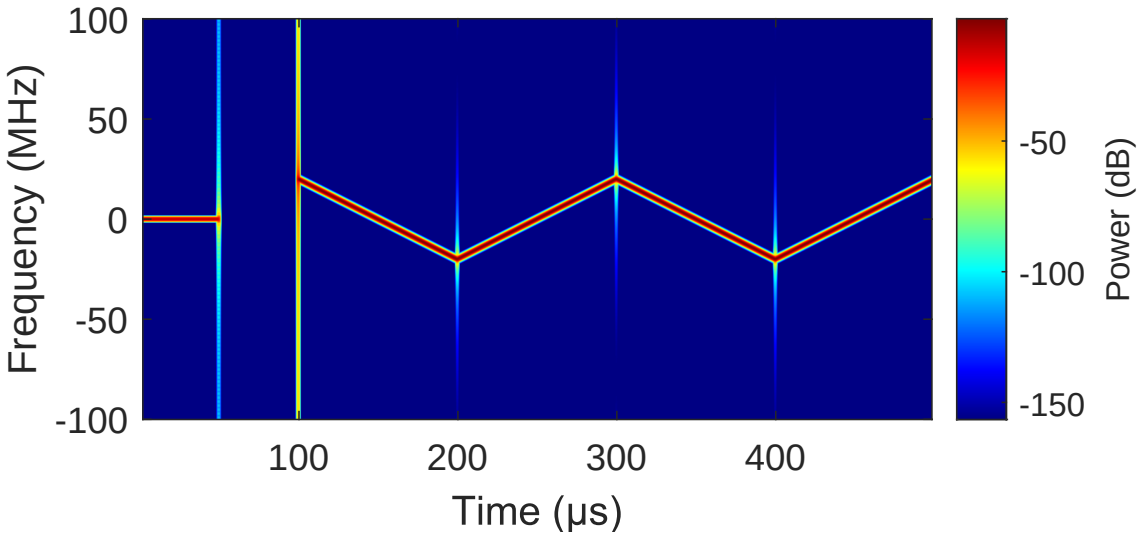

Figure A.2: Example of the three parts composing the typical signal structure used in this work. The signal starts with an initial 50 μs CW pulse at -10 dBc used for calibration purposes. Next, there is a 50 μs interval with RF OFF for electron relaxation. Finally, the signal of interest is found at 0 dBc peak. In this particular example, the signal is an analog linear-frequency modulated chirp with two up-down intervals of ± 20 MHz each lasting for 100 μs.

Two kind of data can be detected: complex data (IQ detection) or scalar data (local detection methods). Depending on the data type several approaches can be used to process the data and recognize a multipactor discharge pattern.

For complex data the method implemented in chapter 7 is recommended. For scalar methods, in which the measurement is background noise except when a discharge happens, a fix used-defined threshold level can be used.

The IQ detection is an RF-based detection method. The algorithm is typically used at the fundamental and harmonic frequencies. Its applicability, as a replacement of the nulling system, is explained in full detail in chapter 7. When this algorithm monitors the harmonic frequencies, the detection parameters must be changed to operate with noisy data.

For the electron and UV light monitoring a time-domain approach is implemented. In contrast to the standard implementations, which have a slow sampling rate that prevents them from sampling the time interval with RF ON, this novel test bed uses an oscilloscope to capture the signals. As the responses have a magnitude that is not sufficient to be directly acquired, a signal conditioning stage is required in both cases. A wideband current amplifier is used for the current monitoring to transform the measured signal into the +2/-2 V range. For UV light monitoring, the photomultiplier tube amplifies the incoming light it into a measurable range (0.1 - 100 V).

A.2.4 Data logging

Complete test data logging is an additional benefit which this testing methodology provides. As all the information when the RF is enabled is sampled in the different detection methods, this raw data is available to be processed and saved for future use.

Storing all the data significantly impacts the maximum sequence rate as long signals (> 1 millisecond) take time to be analyzed ans stored.

Once a test is completely saved, it is possible to verify the presence of multipactor at the detected threshold level with different detection algorithms (or with the same one using different parameters). This also allows to verify if weak signs of discharge were recorded at slightly lower RF power levels.

Appendix B

Compact multipactor test bed

This appendix gives some hints on future multipactor test bed implementations. In particular, for optimizing the RF equipment when implementing a compact multipactor test bed.

As already mentioned in several parts of this PhD thesis, there are several types of devices involved in a multipactor test bed:

RF devices: power sensors, signal analyzers, and signal generators.

AC acquisition: oscilloscopes, digitizers and/or data acquisition units.

Signal conditioning: current amplifiers, low noise amplifiers, and photomultipliers.

These elements are required to generate and measure the RF signals, as well as other physical magnitudes involved in a test.

When focusing on the RF components, there is a new kind of RF power sensors, the NRQ6 peak power sensors manufactured by Rhode and Schwartz (R&S), see Fig. B.1a, from which multipactor testing can benefit in a large extent. These sensors are a new kind of RF power measurement device that fits the following definition: vector signal analyzer with low amplitude error.

The NRQ6 is a breakpoint in the RF power measurement technology in which the NRP-Z8x R&S family comprises the previous state-of-the-art peak power sensor, see Fig. B.1b. Whereas the NRP-Z8x R&S family provides wideband scalar peak power measurement, the new NRQ6 sensors have a larger bandwidth, phase coherency and IQ data measurement.

The NRQ6 is not a complete vector signal analyzer, but it implements a subset of their typical capabilities, which are sufficient for multipactor testing. In Table B.1, the most relevant specifications required to implement multipactor detection are compared for the NRP-Zx family, the NRQ6 and the FSVA3000 family, all of them from R&S.

The core idea for optimizing the test bed is to integrate the RF power measurement and multipactor detection. The start point is the standard multipactor test bed for modulated signal testing. As shown in Fig. B.2, the RF section has a set of powerheads to measure the RF power at different parts of the test bed and vector signal analyzers for multipactor detection using the method described in chapter 7.

(a) R&S NRQ6

(b) R&S NRP Z-8x family

Figure B.1: NRQ6 vector power sensor (up to 6 GHz) and the NRP-Z8x scalar peak power sensor (up to 44 GHz). Source: https://www.rohde-schwarz.com/

Parameter	NRP-Zx	NRQ6	FSVA3000
Frequency max. (GHz)	44	6	44
IQ mode	No	Yes	Yes
Sampling rate (MHz)	30	100	200
Phase coherence	No	Yes	Yes
Measurements and transfert time (ms)	200	10	10

Table B.1: Relevant specifications for multipactor testing

For each IQ detection system, one vector signal analyzer is used. However, new NRQ6 power heads from R&S do not only provide peak power measurement capabilities, but do also measure calibrated IQ data. Consequently, the RF power measurement can be carried out alongside multipactor detection technique, implying a dramatic reduction in terms of test bed complexity. This simplification is shown in Fig. B.3, where the number of RF devices is reduced from 6 to 4.

The advantages of the test bed simplification are:

- One or even two couplers in the input branch are no longer required, thus reducing the losses in the input branch.
- The NRQ6 can measure the envelope peak power $P_e(t)$ in signals with a bandwidth up to 100 MHz.
- Power sensors measuring the input and output RF power may also run the IQ detection algorithm at no extra cost, as the sensors are already present.
- The local oscillator can be shared between them, so that phase-coherent measurement can be made.

However, there are a few disadvantages when using the NRQ6 instead of a vector signal analyzer:

- The acquisition and maintenance cost of one NRQ6 sensors is comparable to those of a vector signal analyzer of the same frequency range.
- The maximum analysis bandwidth is 100 MHz, compared to 160 MHz (or even higher) typically found in vector signal analyzers of similar price.
- The dynamic range is lower.
- Signal analysis features are limited.

Nevertheless, these sensors have several advantages, making them a good alternative for implementing a compact multipactor tests bed or set-ups for R&D entities with budget constraints.

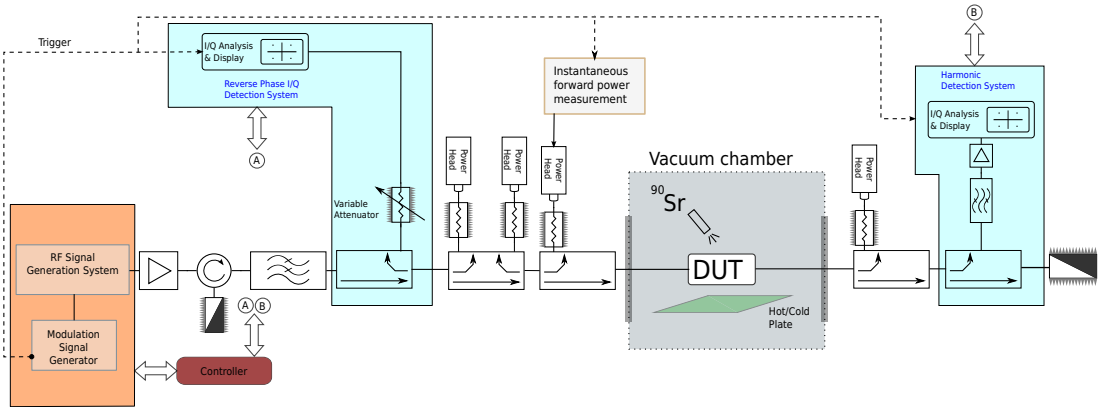

Figure B.2: Schematic for the RF section where the IQ detection system is used to monitor the reflected RF signal at the fundamental frequency, and the harmonic at the DUT output. For that purpose two vector signal analyzers are used.

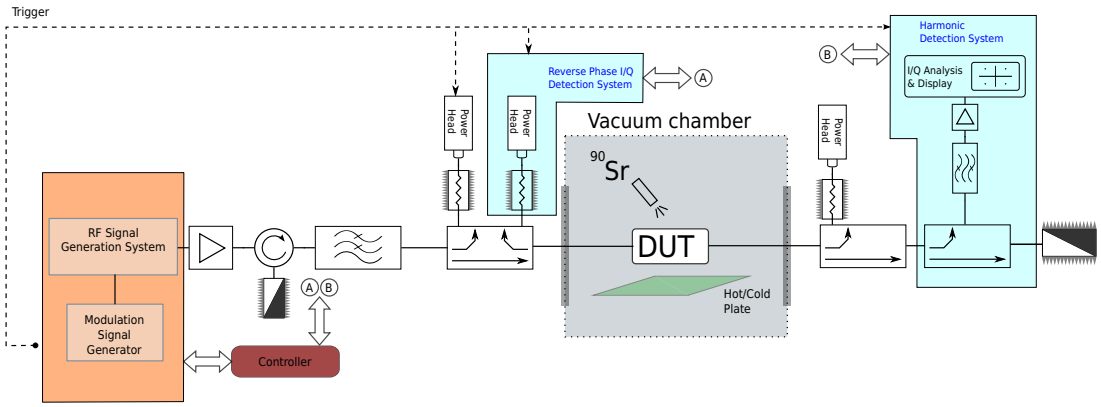

Figure B.3: Schematic for the RF section where the IQ detection system is used to monitor the reflected RF signal at the fundamental frequency, and the harmonic at the DUT output. New NRQ6 power heads, capable of providing not only accurate RF power but IQ data, are used in order to simplify the test bed.

Appendix C

Pulse pre-distortion

C.1 Introduction

Testing with pulsed signal is, has been, and will be an standard test procedure in the field of RF multipactor testing. Because of the need of large power margins, with respect to the RF nominal power level of the device under test (DUT), pulsed testing is required for the next three reasons:

1. the DUT may not be able to withstand a CW test including the requested RF power margin,
2. it may not be possible to reach the required maximum power using CW amplifiers; and
3. the scientific community [8, 58] has proved that pulse testing with a $t_{pulse} = 20\ \mu s$ at a 1 kHz rate, provided that sufficient electron seeding in the critical gap is available, leads to the same multipactor threshold as testing with CW signals.

Even when dealing with modulated signals, the pulse CW is a test case that is repeated several times in the measurement campaign. The reasons why it is so useful are:

1. to asses the matching between test and analysis under a simple signal excitation; and,
2. to verify that the secondary emission yield parameters are not being affected by previous discharges (conditioning), which would lead to a threshold change with the same signal excitation.

In the RF multipactor measurement facilities, it is common to have a large set of amplifiers procured along several years, which typically provide from different vendors. For that reason their performance changes from device to device.

Depending on the vendor, frequency band and RF output level, each amplifiers may produce several types of signal distortion. From the multipactor testing point of view, the following issues are the ones which impact the test results in a larger extent:

Initial overshoot This is the RF power spike recorded at the beginning of the RF pulse. Its length is t_{rise} seconds.

Final overshoot In some units, a spike is also observed before the end of the RF pulse. Its length is t_{fall} seconds.

Flatness deviation from constant RF power level within the pulse length.

The standard method to create pulsed RF signals is based on the use of analog pulse generation circuits. The pulse shape quality of the current signal generators is excellent and pulses, with ON RF intervals of 30 ns and ON/OFF ratios > 90 dB can be achieved. The drawback of analog generation comes from the fact that distortion produced in the amplifier cannot be compensated.

For this reason, the method for producing smooth high power pulses is achieved by means of digital signal generation techniques.

C.2 Pulse smoothing method

The presented smoothing method improves the high power pulse shape by means of an initial and/or final ramps, to prevent the overshoots, and a center slope which handles the lack of flatness. Adjusting these three parts is a simple mechanism to achieve good quality RF pulse for multipactor testing.

Although other implementations are possible, the schematic shown in Fig. C.1 is the most simple one. Alternatively, the same RF power head used for forward signal measurement can be used for this purpose.

The pulse smoothing comprises the following stages:

1. Create a square pulse of the desired length.
2. At ambient pressure, and increases the RF pulsed power to the maximum test level.
3. Measure the time length of the initial and final overshoots
4. Measure the power after the initial overshot ad the power before the final overshoots.
5. Measure the length among the two previously determined power levels.
6. Compute the pre-distorted pulse.
7. Load the pre-distorted pulse in the vector signal generator.
8. Increase the RF power and check that the pulse shape has improved.

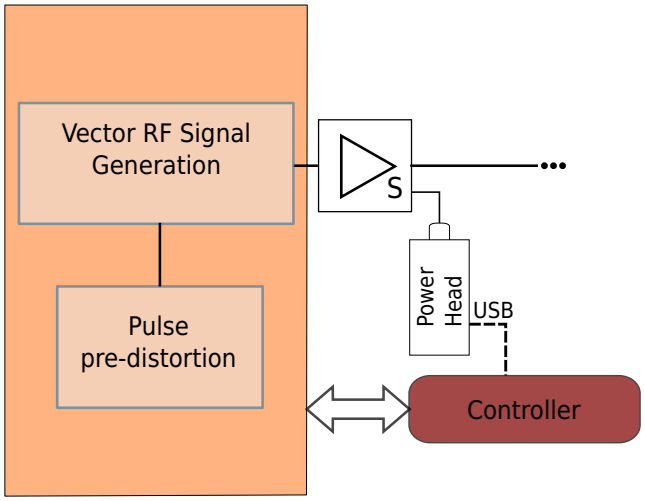

Figure C.1: Schematic for the application of the pulse smoothing technique. The power head is connected to the high power amplifier sample port.

The equation which models the distortion parameters is shown next,

$$p(t) = w(t) \cdot (1 + m \cdot n) \tag{C.1}$$

where m is the pulse slope in V/sample ,and $w(t)$ is the overshoots reduction function.

The overshoot reduction function is the split cosine bell (Tukey window) [155], typically used for the Fourier analysis. This window has a tuning parameter α, which adjusts the proportion of time in which its response is other than unity. For $\alpha = 1$ it becomes a Hann window, and for $\alpha = 0$ it is a rectangular window.

$$w(t) \begin{cases} \frac{1}{2}\left[1 - \cos\left(\frac{2\pi t}{\alpha}\right)\right], & 0 \leq t < \frac{\alpha}{2}, \\ 1, & \frac{\alpha}{2} \leq t < 1 - \frac{\alpha}{2}, \\ \frac{1}{2}\left[1 - \cos\left(\frac{2\pi(1-t)}{\alpha}\right)\right], & 1 - \frac{\alpha}{2} \leq t \leq 1, \end{cases} \tag{C.2}$$

where $\alpha = t_{raise}/t_{pulse}$ is the proportion of the data that is tapered.

An asymmetric Tukey window, not used in the field of Fourier transform, can be defined as

$$w(t) \begin{cases} \frac{1}{2}\left[1 - \cos\left(\frac{2\pi t}{\alpha_r}\right)\right], & 0 \leq t < \frac{\alpha_r}{2}, \\ 1, & \frac{\alpha_r}{2} \leq t < 1 - \frac{\alpha_f}{2}, \\ \frac{1}{2}\left[1 - \cos\left(\frac{2\pi(1-t)}{\alpha_f}\right)\right], & 1 - \frac{\alpha_f}{2} \leq t \leq 1, \end{cases} \tag{C.3}$$

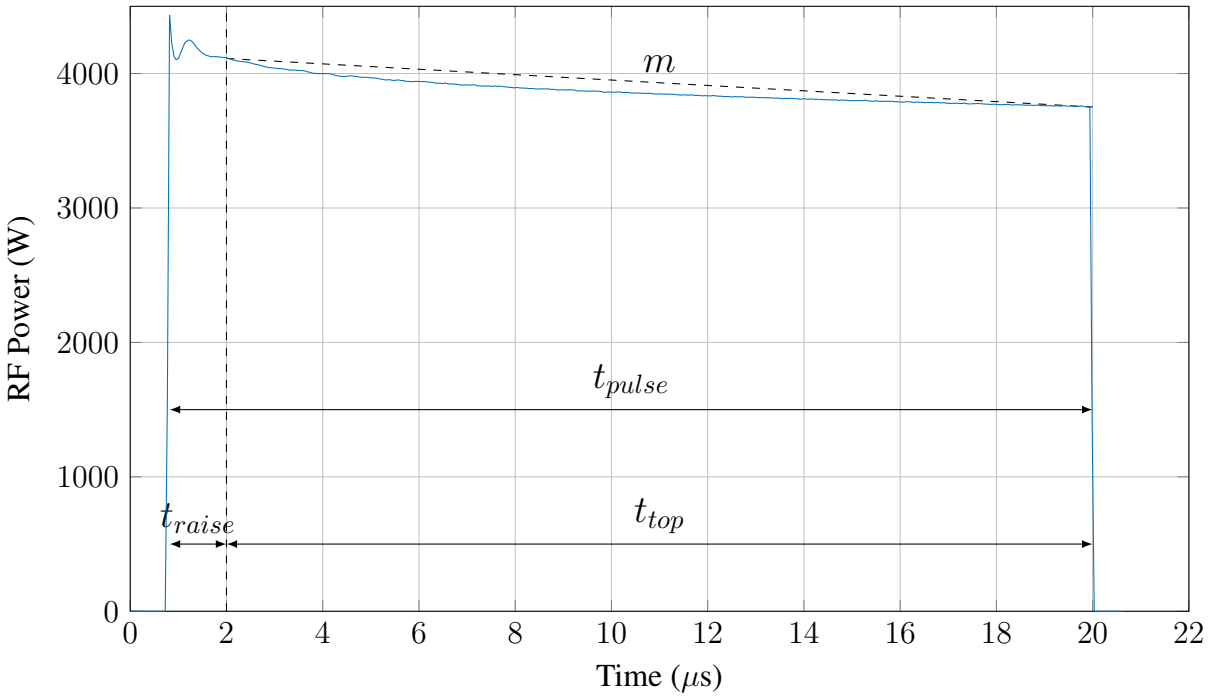

Figure C.2: Pulse distortion parameters.

where $\alpha_r = t_{raise}/t_{pulse}$ and $\alpha_f = t_{fall}/t_{pulse}$ are the proportion of the data that is tapered for the rise and fall intervals, respectively.

The tuning parameters (see Fig. C.2) are obtained during the ambient validation of the set-up, and used in the vacuum operation. Depending on the amplifier, the distortion may drastically change or not as RF power is increased. For the ones showing a constant pulse distortion for all RF powers, the same smoothing pulse can be used. In the other cases, it might be required to store different pulses to be used at specific RF power levels. In both cases, the nature of multipactor test allows to control the timing in which the sequence switch is produced.

C.3 Experimental results

The proposed pulse pre-distortion method has been verified at L-band. The vector signal generator has been a Keysight M9383A unit, with 160 MHz of instantaneous bandwidth. The high power amplifier is a 4 kW pulsed SSPA manufactured by Amplifier Research. The pulse width is set to 20 μs and the pulse repetition frequency to 1 kHz, as defined in [8].

As shown in Fig. C.3, this unit produces pulses without spikes at low RF power levels. At high RF power levels (Fig. C.4), the pulse shape presents a large initial overshoot and a noticeable RF power decay over the pulse length. However, at the end of the pulse there is no overshoot.

By means of the previously described algorithm, the pulse shape can be optimized. In these experimental results the total pulse width has been kept at $20\mu s$. As a symmetric tapering window has been used without increasing the pulse ON time, the total pulse length at maximum power would be shorter. The pulse width reduction, due to the windowing effect, can be compensated by increasing the RF pulse width, so that the total time at maximum power meets the initial value.

The pre-distorted pulse is shown in blue in both plots. In this example the pulse has been tuned at high power, and the same parameters have been also used for the low power RF measurement.

Results prove that over an RF power range of 23 dB, the pulse shaping parameters obtained for the highest output level can recover the pulse shape at all power levels. This prevents the need of switching the pulse pre-distortion parameters along the multipactor test.

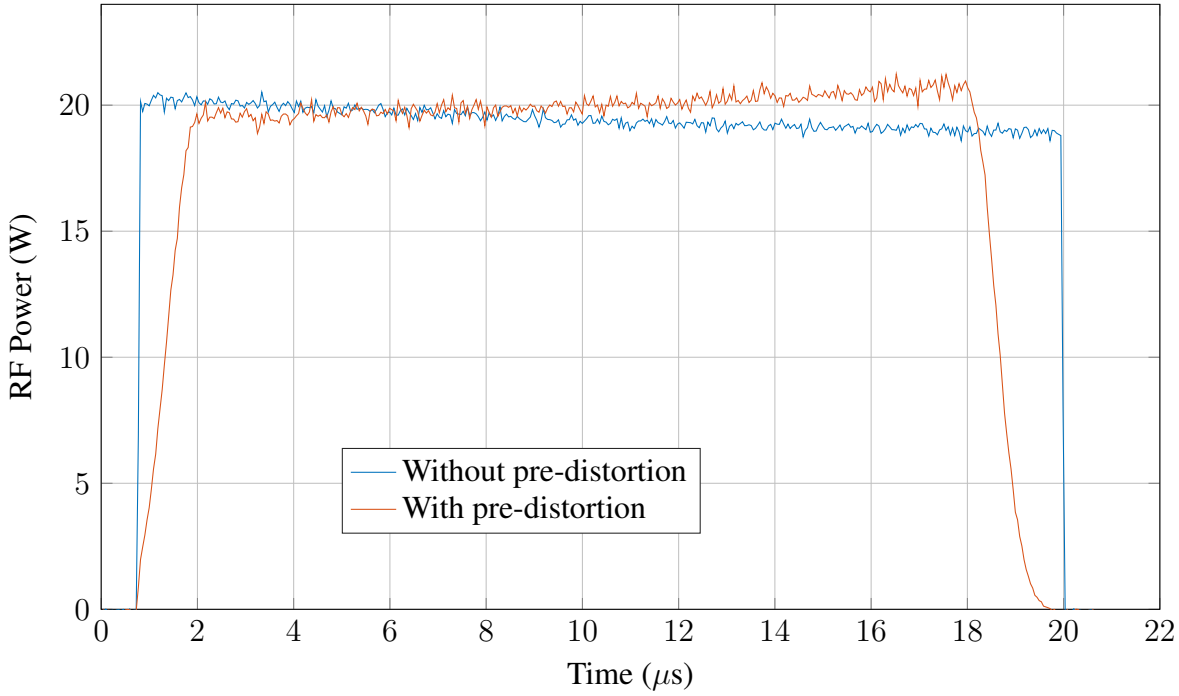

Figure C.3: Performance of the pulse smoothing at an RF output power of 20 W peak with an adjustment made for the HPA saturation RF power. Without smoothing (blue) and with smoothing (red).

C.4 Conclusions

The pulse smoothing technique presented in this appendix provides a simple yet robust method to avoid undesired distortion in the RF pulse. As the pre-distorted pulse is stored in memory, incorrect pulse shapes will not happen during the actual multipactor test.

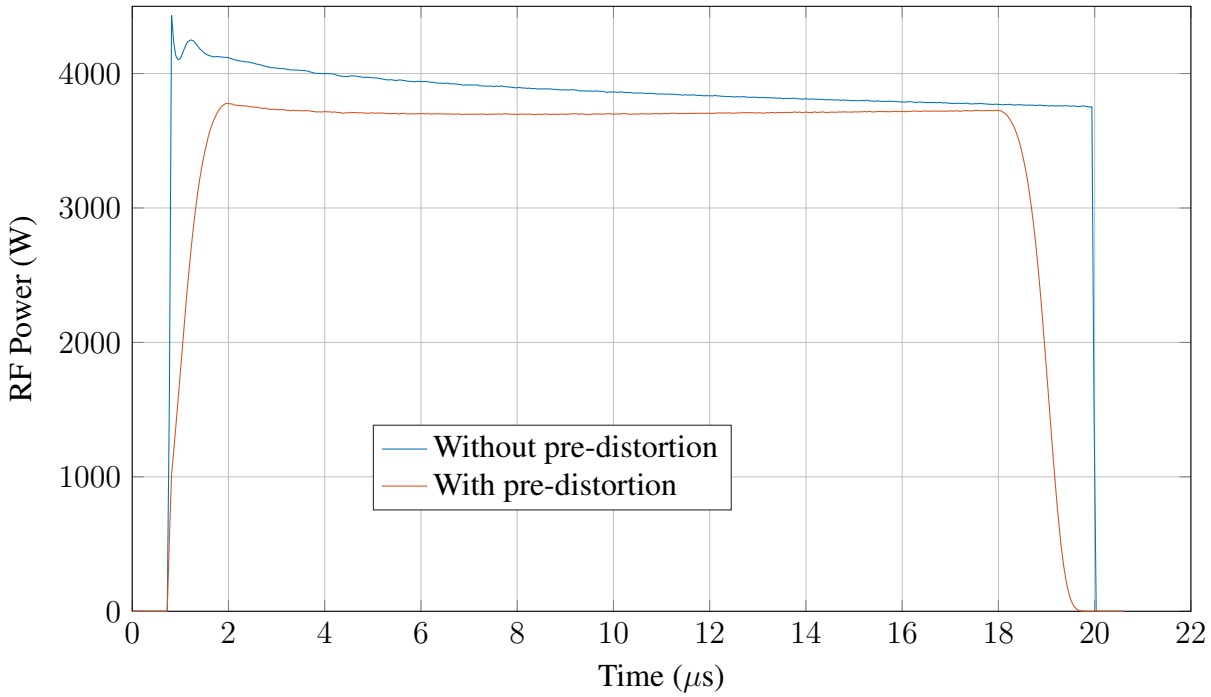

Figure C.4: Pulse smoothing at saturation (3800 W peak) RF output power. Without pulse smoothing (blue) and with pulse smoothing (red).

Experimental results prove that, typically, one single waveform can be used in all the HPA operational range, thus getting rid of the unacceptable initial and final over peaks which may tamper the multipactor test results. During actual testing it has been observed that the proposed shaping function has provided satisfactory results, being the need of more complex functions unnecessary.

Appendix D

Projects related to the development of the PhD thesis

- **Title** Soluciones tecnológicas compactas para dispositivos pasivos de alta frecuencia con respuestas avanzadas y reconfigurables

  Reference TEC2013-47037-C5-1-R

  Holder Technical University of Valencia

  Year 2013

  Number of members in the research team 6

  Issuer Ministerio de Economía y Competitividad. Convocatoria 2013 del Programa Estatal de Investigación, Desarrollo e Innovación Orientada a los Retos de la Sociedad, modalidad 1, "Retos Investifación": Proyectos I+D+I

- **Title** H2020-ESA-007 Multipactor Prediction Techniques for GNSS Signals

  Reference 4000126048/18/NL/AS

  Holder Val Space Consortium

  Number of members in the research team 8

  Issuer European Space Agency

- **Title** Development and validation of an enhanced multipactor prediction method with multicarrier digital modulated signals (Part I)

  Reference VSC2017/ESA/RFQ1300042382

  Holder Val Space Consortium

  Number of members in the research team 3

  Issuer European Space Agency

- **Title** Development and validation of an enhanced multipactor prediction method with multicarrier digital modulated signals (Part II)

  Reference VSC2017/ESA/RFQ1300042381_v2

  Holder Val Space Consortium

  Number of members in the research team 5

  Issuer European Space Agency

- **Title** Method for Controlled Modulated RF Signal Testing in Non- Linear Test Bed Scenarios

  Reference UPV2017/ESA/RFQ1300043567

  Holder Universitat Politècnica de València

  Number of members in the research team 5

  Issuer European Space Agency

Appendix E

List of own scientific publications

E.1 Journal papers

- D. González, M.P. Belloch, **O. Monerris**, B. Gimeno, V.E. Boria and D.Raboso, "Analysis of multipactor effect using a Phase-Shift Keying single-carrier digital modulated signal", in IEEE Transactions on Electron Devices, vol. 60, no. 8, pp. 2664-2670, Aug. 2013, doi: 10.1109/TED.2013.2266275.

- D. González, **O. Monerris**, M.E. Díaz, B. Gimeno, V.E. Boria and D. Raboso, "Experimental analysis of the multipactor effect with rf pulsed signals", in IEEE Electron Device Letters, vol. 36, no. 10, pp. 1085-1087, Oct. 2015, doi: 10.1109/LED.2015.2468068.

- **O. Monerris**, E. Diaz, J. Ruiz and V.E. Boria, "Automatic, calibrated and accurate measurement of S-parameters in climatic chamber", in IEEE Microwave and Wireless Components Letters, vol. 25, no. 6, June 2015, doi: 10.1109/LMWC.2015.2421330.

- D. González, **O. Monerris**, B. Gimeno, M.E. Díaz, V.E. Boria and P.Martín, "Multipactor RF breakdown in coaxial transmission lines with digitally modulated signals", in IEEE Transactions on Electron Devices, vol. 63, no. 10, pp. 4096-4103, Oct. 2016, doi: 10.1109/TED.2016.2596801.

- **O. Monerris**, E. Díaz, V.E. Boria and B. Gimeno, "High-power multicarrier generation for RF breakdown testing", in IEEE Transactions on Electron Devices, vol. 64, no. 2, pp. 556-563, Feb. 2017, doi: 10.1109/TED.2016.2641243.

- V.E. Semenov, E.I. Rakova, E. Sorolla, D. Gonzalez, **O. Monerris**, B. Gimeno, J. Puech, Jerome and J.B. Sombrin, "Enhancement of the multipactor threshold inside nonrectangular iris", in IEEE Transactions on Electron Devices, vol. 65, no. 3, pp. 1164-1171, March 2018, doi: 10.1109/TED.2018.2798538.

- V. Nova, C. Bachiller, J.A. Martínez, H. Esteban, J.M. Merello and A. Belenguer, **O. Monerris** and V.E. Boria, "Thermal stability analysis of filters in substrate integrated technologies under atmospheric pressure and vacuum conditions", in IEEE Access, vol. 8, pp. 118072-118082, 2020, doi: 10.1109/ACCESS.2020.3004875.

- **O. Monerris**, R. Cervera, M. Rodríguez, E. Diaz, C. Alcaide, J. Petit, V.E. Boria, B. Gimeno and D. Raboso, "High power RF discharge detection technique based on the in-phase and quadrature signals", in IEEE Transactions on Microwave Theory and Techniques, vol. 69, no. 12, pp. 5429-5438, Dec. 2021,
doi: 10.1109/TMTT.2021.3120657.

- P. González, C. Alcaide, R. Cervera, M. Rodríguez, **O. Monerris**, J. Petit, A. Rodríguez, A. Vidal, J. Vague, J.V. Morro and P. Soto, "Multipactor threshold estimation techniques based on circuit models, electromagnetic fields, and particle simulators", in IEEE Journal of Microwaves, vol. 2, no. 1, pp. 57-77, Jan. 2022, doi: 10.1109/JMW.2021.3132284.

E.2 Conference papers

- **O. Monerris**, P. Soto, S. Cogollos, V.E. Boria, J. Gil, C. Vicente and B. Gimeno, "Accurate circuit synthesis of low-pass corrugated waveguide filters", in 40th European Microwave Conference, Paris, France, September 2010, pp. 1237-1240, doi: 10.23919/EUMC.2010.5616983.

- E. Diaz, A. Belenguer, H. Esteban, **O. Monerris** and V.E. Boria, "Una nueva transición de microstrip a una guía de onda integrada en sustrato con mayor impedancia característica", in XXVIII Simposium de la Unión Científica Internacional de Radio (URSI). Santiago de Compostela, Spain, September 2013

- E. Diaz, A. Belenguer, H. Esteban, **O. Monerris** and V.E. Boria, "A novel transition from microstrip to a substrate integrated waveguide with higher characteristic impedance", in proceeding of: 2013 IEEE/MTT-S International Microwave Symposium Digest. Seattle, WA, USA, June 2013, doi: 10.1109/MWSYM.2013.6697773

- L. Accatino, M. Diaz Martin, P. Martin Iglesias, N. Sidiropoulos and **O. Monerris**, "A high power Ku-band triplexer", in International workshop on Multipactor, Corona and Passive Intermodulation (MULCOPIM), Valencia, Spain, 2014

- D. González, **O. Monerris**, B. Gimeno, V.E. Boria, D. Raboso and V. Semenov, "Análisis del efecto multipactor en señales moduladas con Phase-Shift Keying", in XIX Simposium de la Unión Científica Internacional de Radio (URSI). Valencia, Spain, September 2014

- **O. Monerris**, E. Diaz and V.E. Boria, "Medida automática, calibrada y precisa de parámetros S en temperatura", in XXX Simposium de la Unión Científica Internacional de Radio (URSI). Pamplona, Spain, September 2015.
- **O. Monerris**, D. Argilés, V.E. Boria, B. Gimeno, D. Raboso and P. Angeletti, "Multipactor testing and emerging qualification protocols", in 46th European Microwave Conference (EuMC), Madrid, Spain, September 2016, pp. 222-225, doi: 10.1109/EuMC.2016.7824318.
- V.E. Boria, L. Nuño, **O. Monerris**, D. Smacchia, D. Argilés and D. Raboso, "Experimental measurements and diagnosis of radio-frequency space high power and electromagnetic compatibility effects", in ESA Workshop on Aerospace EMC (Aerospace EMC), Valencia, Spain, May 2016, pp. 1-6, doi: 10.1109/AeroEMC.2016.7504600.
- D. Gonzalez, A. M. Pérez, **O. Monerris**, S. Anza, J. Vague, B. Gimeno, V.E. Boria, Á. Gomez, A. Vegas, E. Díaz, D. Raboso, and A. Coves, "Recent advances of the multipactor RF breakdown in RF satellite microwave passive devices", Progress In Electromagnetic Research Symposium (PIERS), Shanghai, China, August 2016
- **O. Monerris**, D. Raboso, V.E. Boria, B. Gimeno and D. Argilés, "Nuevos métdos de ensayo del efecto multipactor", in XXXI Simposium de la Unión Científica Internacional de Radio (URSI), Madrid, Spain, September 2016.
- D. González, **O. Monerris**, B. Gimeno, V.E. Boria and D. Raboso "Estudio del efecto multipactor en líneas de transmisión coaxial con señales pulsadas", in XXXI Simposium de la Unión Científica Internacional de Radio (URSI), Madrid, Spain, September 2016.
- D. González, **O. Monerris**, B. Gimeno, M.E. Díaz, V.E. Boria and P. Martín, "Analysis of the multipactor effect in a coaxial transmission line under the excitation of digitally modulated signals", in XI Iberian Meeting on Computations Electromagnetics (EIEC), Oviedo, Spain, November 2016
- D. González, **Ò. Monerris**, B. Gimeno, M.E. Díaz, V.E. Boria, P. Martín, Á. Gómez, Ó. Fernández, Á. Vegas, F. Casas, S. Anza, C. Vicente, J. Gil, R. Mata, I. Montero and D. Raboso, "Novel multipactor studies in RF satellite payloads: single-carrier digital modulated signals and ferrite materials", in IEEE MTT-S International Conference on Numerical Electromagnetic and Multiphysics Modeling and Optimization for RF, Microwave, and Terahertz Applications (NEMO), Bari, Italy, September 2017, pp. 248-250, doi: 10.1109/NEMO.2017.7964249.
- **O. Monerris**, D. Gonzalez, V.E. Boria, B. Gimeno and D. Raboso, "Impact of the multipactor discharge on the digital signal integrity", in International workshop on Multipactor, Corona and Passive Intermodulation (MULCOPIM), ESTEC, The Netherlands, April 2017

- **Ò. Monerris**, E. Díaz, V.E. Boria and B. Gimeno, "Generación de señales multiportadora en la zona crítica del componented de RF", in XXXII Simposium de la Unión Científica Internacional de Radio (URSI). Cartagena, Spain, September 2017.

- D. González, **O. Monerris**, M. E. Díaz, B. Gimeno, V.E. Boria, D. Raboso and Á. Coves, "Analysis of the multipactor effect with RF pulsed signals", in XII Iberian Meeting on Computational Electromagnetics (EIEC), Coimbra, Portugal, May 2018

- C. Alcaide, P. Gonzalez, M. Rodriguez, R. Cervera, J. Petit, **O. Monerris**, P. Soto, V.E. Boria and C. Miquel, "Multipactor analysis by exploiting Kadane's method", in XXI Mediterranean Microwave Symposium, Pizzo, Italy, May 2022.

- R. Cervera, M. Rodríguez, **O. Monerris**, C. Alcaide, V.E. Boria, P. Soto and D. Raboso, "Diseño e implementación de un sistema de detección automática de descargas de RF de alta potencia", in XXXVII Simposium de la Unión Científica Internacional de Radio (URSI), Malaga, Spain, September 2022.

- M. Rodríguez, R. Cervera, C. Alcaide,**Ò Monerris**, P. Soto, Pablo; V.E. Boria, D. Raboso and C. Miquel, "Estudio y mejora de métodos rápidos para la estimación del umbral de descarga multipactor", in XXXVII Simposium de la Unión Científica Internacional de Radio (URSI), Malaga, Spain, September 2022.

- S. Lanfranco, L. Maestro, G. Derkits, H. Rubin and **O. Monerris**, "Multipactor measurements for an ultra-compact LTE network for proximity communications in space", in International workshop on Multipactor, Corona and Passive Intermodulation (MULCOPIM), Valencia, Spain, October 2022

- R. Cervera, M. Rodríguez, **Ò. Monerris**, C. Alcaide, P. Soto, V.E. Boria and D. Raboso, "Design and implementation of a new automatic system of high-power RF discharge detection based on In-Phase and Quadrature Signals", in International workshop on Multipactor, Corona and Passive Intermodulation (MULCOPIM), Valencia, Spain, October 2022

- **O. Monerris**, S. Chazbeck, R. Cervera, M. Rodríguez, V.E. Boria, D. Raboso and R. Fiengo "Real-Time FPGA-based electron monitoring with automatic detection in high power RF testing", in International workshop on Multipactor, Corona and Passive Intermodulation (MULCOPIM), Valencia, Spain, October 2022

- L. Esteve, **O. Monerris**, M. Reglero and D. Raboso, 'Impact of short RF pulses and free electrons in the Corona threshold", in International workshop on Multipactor, Corona and Passive Intermodulation (MULCOPIM), Valencia, Spain, October 2022

E.3 Seminars and Workshops

- **Workshop title** Summer School on "RF High Power Effects: Characterization Techniques for Space Communciation Systems

  Date 5 – 9 July 2021

  Organized by UPV for TESLA — H2020-MSCA-ITN-2018

  Total length 20 h

  Format Online

  Talk title Measurement Techniques of RF High-Power Effects

  Talk speaker **O. Monerris Belda**

  Talk length 2 h

- **Workshop title** Workshop on "Microwave Filters and Multiplexing Networks for Space Communication Systems (FIMU4SPACE)

  Date 25 – 29 November 2019

  Organized by EuMA, ESA and UPV

  Total length 40 h

  Format UPV

  Talk title RF Discharge effects and passive inter-modulation ESA-VSC activities

  Talk speaker **O. Monerris Belda**

  Talk length 1 h

- **Workshop title** WM-02 (EuMC) High Power RF Breakdown and PIM in Space Applications

  Date 8th July 2018

  Organized by David Raboso Garcia-Baquero, **Oscar Monerris**, Petronilo Martín-Iglesias

  Total length 8 h

  Format EUMW 2018

  Talk title Signal Management in High Power Modulated Testing

  Talk speaker **O. Monerris Belda**

  Talk length 1 h

Appendix F

List of Acronyms

.

AC	Alternating Current
ARB	Arbitrary base-band generator
ACM	Adaptative Coding and Modulation
ADSL	Alternating Dielectric Line Sections
AM	Amplitude Modulation
AM-AM	Ampltiude - Amplitude Distortion
AM-PM	Ampltiude - Phase Distortion
APSK	Amplitude Phase Shift Keying
BER	Bit Error Rate
BPSK	Binary Phase Shift Keying
CCDF	Complementary Cumulative Distribution Function
CW	Continuous Wave
dB	decibels
DC	Direct Current
DUT	Device Under Test
DPD	Digital Pre-Distortion
DVB-S2	Digital Video Broadcasting - Satellite version 2
ESA	European Space Agency
ESICL	Empty Substrate Integrated Coaxial Line
ESIW	Empty Substrate Integrated Waveguide
EVN	Error Vector Noise
FM	Frequency Modulation

FFT	Fast Fourier Transform
FIFO	First In First Out
FSK	Frequency Shift Keying
GMP	Generalized Memory Polynomial
GNSS	Global Navigation Satellite System
GSps	Giga samples per second
HPA	High Power Amplifier
IF	Intermediate Frequency
IFFT	Inverse Fast Fourier Transform
IQ	In-phase and Quadrature
ISI	Inter-Symbol Interference
LEO	Low Earth Orbit
LTE	Long Term Evolution
LNA	Low Noise Amplifier
LUT	LookUp Table
MCS	Multicarrier system
MODCON	modulation and coding
MPM	Memory Polynomial Model
NASA	National Aeronautics and Space Administration
PAPR	Peak to Average Power Ratio
PCB	Printed Circuit Board
PDF	Probability Density Function
PM	Phase Mdulation
OCXO	Oven Controlled Crystal Oscillators
OFDM	Orthogonal Frequency-Division Multiplexing
PAPR	Peak to Average Power Ratio
PIC	Particle-in-cell
QAM	Quadrature Amplitude Modulation
QPSK	Quadrature Phase Shift Keying
RAM	Random Access Memory
RF	Radio Frequency

RFSA	RF Signal Acquisition
RFSG	RF Signal Generation
RMS	Root Mean Square
SEY	Secondary Emission Yield
SDR	Software-Defined Radio
S2P	Touchstone File format for 2-port S-parameters
SI	Substrate Integrated
SIW	Substrate Integrated Waveguide
SNR	Signal to Noise Ratio
SOLT	Short-Open-Load-Thru
SRRC	Square Root Raise Cosine
SSPA	Solid State Power Amplifier
TCP/IP	Transmission Control Protocol / Internet Protocol
TDMS	Technical Data Management Streaming
TEM	Transverse Electro-Magnetic
TRL	Thru-Reflect-Line
TVAC	Thermal vacuum chamber
VNA	Vector Nework Analyzer
VSA	Vector Signal Analyzer
VSC	Val Space Consortium
VSG	Vector Signal Generator
VST	Vector Signal Transceiver

List of Figures

List of Tables

Bibliography

[1] P. Farnsworth, "Television by electron image scanning," *Journal of the Franklin Institute*, vol. 218, no. 4, pp. 411–444, 1934.

[2] W. Rann, "Amplification by secondary electron emission," *Journal of Scientific Instruments*, vol. 16, no. 8, p. 241, 1939.

[3] E. Gill and A. von Engel, "Starting potentials of high-frequency gas discharges at low pressure," *Proceedings of the Royal Society of London. Series A. Mathematical and Physical Sciences*, vol. 192, no. 1030, pp. 446–463, 1948.

[4] A. Hatch and H. Williams, "Multipacting modes of high-frequency gaseous breakdown," *Physical Review*, vol. 112, no. 3, p. 681, 1958.

[5] S. Brown, *Basic Data of Plasma Physics: the Fundamental Data on Electric Discharges in Gases*. MIT Press, Cambridge, MA, USA, reprinted 1997, Classics in Vacuum Science, 1959.

[6] H. Aircraft, *The Study of Multipactor Breakdown in Space Electronic Systems*, 1965.

[7] J. Nanevicz, "Radiation and reception of electromagnetic energy from aircraft and guided missiles," Stanford Research Institute Menlo Park, CA, USA, Tech. Rep., 1967.

[8] E. Requirements and S. D. ESTEC, *Space Engineering. Multipaction Design and Test (ECSS-E-ST-20-01C)*. ESA-ESTEC, 15 June 2020.

[9] A. I. of Aeronautics and Astronautics, *Standard/Handbook for Multipactor Breakdown Prevention in Spacecraft Components (ANSI/AIAA S-142-2016)*. American Institute of Aeronautics and Astronautics, Inc., 2016.

[10] G. Varrall, *5G and Satellite Spectrum, Standards, and Scale*, ser. Artech House space technology and applications library. Artech House, 2018. [Online]. Available: https://books.google.es/books?id=pYUsswEACAAJ

[11] R. Cameron, C. Kudsia, and R. Mansour, *Microwave filters for communication systems: fundamentals, design, and applications*. John Wiley & Sons, 2018.

[12] G. Maral, M. Bousquet, and Z. Sun, *Satellite Communications Systems: Systems, Techniques and Technology*. John Wiley & Sons, 2020.

[13] G. van Eden, D. Verheijde, and J. Verhoeven, "Secondary electron emission yield measurements of dielectrics based on a novel collector-only method," *Nuclear Instruments and Methods in Physics Research Section B: Beam Interactions with Materials and Atoms*, vol. 511, pp. 6–11, 2022.

[14] E. Requirements and S. D. ESTEC, *Space Engineering. Thermal Control General Requirements (ECSS-E-ST-31C)*. ESA-ESTEC, 15 November 2008.

[15] G. E. C. Hoer, "Thru-reflect-line: An improved technique for calibrating the dual six-port automatic network analyzer," *IEEE transactions on microwave Theory and Techniques*, vol. 27, no. 12, pp. 987–993, 1979.

[16] J. Vaughan and M. Rodney, "Multipactor," *IEEE Transactions on Electron Devices*, vol. 35, no. 7, pp. 1172–1180, 1988.

[17] R. Woo, *Final Report on RF Voltage Breakdown in Coaxial Transmission Lines*. Jet Propulsion Laboratory, California Institute of Technology, 1970.

[18] W. Tang and C. Kudsia, "Multipactor breakdown and passive intermodulation in microwave equipment for stellite applications," in *IEEE Conference on Military Communications*. IEEE, 1990, pp. 181–187.

[19] N. Rozario, H. Lenzing, K. Reardon, M. Zarro, and C. Baran, "Investigation of telstar 4 spacecraft ku-band and c-band antenna components for multipactor breakdown," *IEEE Transactions on Microwave Theory and Techniques*, vol. 42, no. 4, pp. 558–564, 1994.

[20] C. Kudsia, R. Cameron, and W. Tang, "Innovations in microwave filters and multiplexing networks for communications satellite systems," *IEEE Transactions on Microwave Theory and Techniques*, vol. 40, no. 6, pp. 1133–1149, 1992.

[21] G. Torregrosa, A. Coves, C. Vicente, A. Perez, B. Gimeno, and V. Boria, "Time evolution of an electron discharge in a parallel-plate dielectric-loaded waveguide," *IEEE Electron Device Letters*, vol. 27, no. 7, pp. 619–621, 2006.

[22] A. Coves, G. Torregrosa, C. Vicente, B. Gimeno, and V. Boria, "Multipactor discharges in parallel-plate dielectric-loaded waveguides including space-charge effects," *IEEE Transactions on Electron Devices*, vol. 55, no. 9, pp. 2505–2511, 2008.

[23] J. Vague, J. Melgarejo, M. Guglielmi, V. Boria, S. Anza, C. Vicente, R. Moreno, M. Taroncher, B. Gimeno, and D. Raboso, "Multipactor effect characterization of dielectric materials for space applications," *IEEE Transactions on Microwave Theory and Techniques*, vol. 66, no. 8, pp. 3644–3655, 2018.

[24] G. Torregrosa, A. Coves, B. Gimeno, I. Montero, C. Vicente, and V. Boria, "Multipactor susceptibility charts of a parallel-plate dielectric-loaded waveguide," *IEEE Transactions on Electron Devices*, vol. 57, no. 5, pp. 1160–1166, 2010.

[25] C. Jing, C. Chang, S. Gold, R. Konecny, S. Antipov, P. Schoessow, A. Kanareykin, and W. Gai, "Observation of multipactor suppression in a dielectric-loaded accelerating structure using an applied axial magnetic field," *Applied Physics Letters*, vol. 103, no. 21, p. 213503, 2013.

[26] A. Sounas, "Modeling of long-term multipactor evolution in microwave components including dielectric layers," EPFL, Tech. Rep., 2015.

[27] V. Semenov, E. Rakova, M. Belhaj, J. Puech, M. Lisak, J. Rasch, and E. Laroche, "Preliminary results on the multipactor effect prediction in RF components with ferrites," in *2013 IEEE 14th International Vacuum Electronics Conference (IVEC)*. IEEE, 2013, pp. 1–2.

[28] D. González, A. Pérez, S. Anza, J. Cardona, B. Gimeno, V. Boria, D. Raboso, C. Vicente, J. Gil, and F. Caspers, "Multipactor mitigation in coaxial lines by means of permanent magnets," *IEEE Transactions on Electron Devices*, vol. 61, no. 12, pp. 4224–4231, 2014.

[29] D. González, B. Gimeno, V. Boria, A. Gómez, and A. Vegas, "Multipactor effect in a parallel-plate waveguide partially filled with magnetized ferrite," *IEEE Transactions on Electron Devices*, vol. 61, no. 7, pp. 2552–2557, 2014.

[30] J. Vague, J. Melgarejo, V. Boria, M. Guglielmi, R. Moreno, M. Reglero, R. Mata, I. Montero, D. González, and B. Gimeno, "Experimental validation of multipactor effect for ferrite materials used in L-and S-band nonreciprocal microwave components," *IEEE Transactions on Microwave Theory and Techniques*, vol. 67, no. 6, pp. 2151–2161, 2019.

[31] V. Semenov, E. Rakova, E. Sorolla, D. González, O. Monerris, B. Gimeno, J. Puech, and J. Sombrin, "Enhancement of the multipactor threshold inside nonrectangular iris," *IEEE Transactions on Electron Devices*, vol. 65, no. 3, pp. 1164–1171, 2018.

[32] I. Arregui, I. Arnedo, A. Lujambio, M. Chudzik, D. Benito, R. Jost, F. Gortz, T. Lopetegi, and M. Laso, "A compact design of high-power spurious-free low-pass waveguide filter," *IEEE Microwave and Wireless Components Letters*, vol. 20, no. 11, pp. 595–597, 2010.

[33] A. Panariello, M. Yu, and C. Ernst, "Ku-band high power dielectric resonator filters," *IEEE Transactions on Microwave Theory and Techniques*, vol. 61, no. 1, pp. 382–392, 2012.

[34] V. Nistor, L. González, L. Aguilera, I. Montero, L. L. Galán, U. Wochner, and D. Raboso, "Multipactor suppression by micro-structured gold/silver coatings for space applications," *Applied Surface Science*, vol. 315, pp. 445–453, 2014.

[35] M. Sánchez, S. Marini, J. Vague, C. Gómez, F. Quesada, A. Álvarez, V. Boria, and M. Guglielmi, "Study on multipactor breakdown in coaxial to microstrip transitions," in *2018 IEEE MTT-S International Conference on Numerical Electromagnetic and Multiphysics Modeling and Optimization (NEMO)*. IEEE, 2018, pp. 1–4.

[36] S. L. N. Jordan, Y. Lau, and R. Gilgenbach, "CST particle studio simulations of coaxial multipactor and comparison with experiments," *IEEE Transactions on Plasma Science*, vol. 48, no. 6, pp. 1942–1949, 2020.

[37] D. Wolk, C. Vicente, H. Hartnagel, M. Mattes, J. Mosig, and D. Raboso, "An investigation of the effect of fringing fields on multipactor breakdown," in *Workshop on Multipactor, RF and DC Corona and Passive Intermodulation in Space RF Hardware*. Citeseer, 2005, pp. 93–99.

[38] D. Gonzalez, P. Soto, S. Anza, B. Gimeno, V. Boria, C. Vicente, and J. Gil, "Multipactor susceptibility charts for ridge and multiridge waveguides," *IEEE Transactions on Electron Devices*, vol. 59, no. 12, pp. 3601–3607, 2012.

[39] D. Gonzalez, A. Perez, S. Anza, J. Vague, B. Gimeno, V. Boria, D. Raboso, C. V. J. Gil, and F. Caspers, "Multipactor in a coaxial line under the presence of an axial DC magnetic field," *IEEE Electron Device Letters*, vol. 33, no. 5, pp. 727–729, 2012.

[40] D. Wen, A. Iqbal, P. Zhang, and J. Verboncoeur, "Suppression of single-surface multipactor discharges due to non-sinusoidal transverse electric field," *Physics of Plasmas*, vol. 26, no. 9, p. 093503, 2019.

[41] D. Wu, J. Ma, Y. Bao, W. Cui, T. Hu, J. Yang, and Y. Bai, "Fabrication of porous Ag/TiO_2/Au coatings with excellent multipactor suppression," *Scientific Reports*, vol. 7, no. 1, pp. 1–10, 2017.

[42] I. Montero, L. Olano, L. Aguilera, M. Dávila, U. Wochner, D. Raboso, and P. Martín, "Low-secondary electron emission yield under electron bombardment of microstructured surfaces, looking for multipactor effect suppression," *Journal of Electron Spectroscopy and Related Phenomena*, vol. 241, p. 146822, 2020.

[43] S. Anza, C. Vicente, B. Gimeno, V. Boria, and J. Armendáriz, "Long-term multipactor discharge in multicarrier systems," *Physics of Plasmas*, vol. 14, no. 8, p. 082112, 2007.

[44] S. Anza, M. Mattes, C. Vicente, J. Gil, D. Raboso, V. Boria, and B. Gimeno, "Multipactor theory for multicarrier signals," *Physics of Plasmas*, vol. 18, no. 3, p. 032105, 2011.

[45] J. Angevain, L. Salghetti, P. Sarasa, and C. Mangenot, "A boundary function for multicarrier multipaction analysis," in *2009 3rd European Conference on Antennas and Propagation*. IEEE, 2009, pp. 2158–2161.

[46] P. Martin, F. Teberio, and M. Laso, "Analysis of the multipactor effect with linear frequency modulated signals," in *2018 IEEE MTT-S International Conference on Numerical Electromagnetic and Multiphysics Modeling and Optimization (NEMO)*. IEEE, 2018, pp. 1–4.

[47] A. Sounas, J. Mosig, and M. Mattes, "Effect of digitally modulated signals on multipactor breakdown," in *2013 7th European Conference on Antennas and Propagation (EuCAP)*. Ieee, 2013, pp. 33–36.

[48] D. Raboso and A. Woode, "A new method of electron seeding used for accurate testing of multipactor transients," in *1995 25th European Microwave Conference*, vol. 1. IEEE, 1995, pp. 190–193.

[49] J. Farrell, T. Musselman, and A. Hubble, "Innovations in radio frequency breakdown detection methods," in *2016 IEEE International Conference on Plasma Science (ICOPS)*. IEEE, 2016, pp. 1–1.

[50] R. Udiljak, D. Anderson, P. Ingvarson, U. Jordan, U. Jostell, L. Lapierre, G. Li, M. Lisak, J. Puech, and J. Sombrin, "New method for detection of multipaction," *IEEE Transactions on Plasma Science*, vol. 31, no. 3, pp. 396–404, 2003.

[51] H. Wei, X. Wang, W. Cui, Y. He, T. Hu, and Q. Sun, "Progress of multipactor detection in the space high-power microwave components," in *2019 International Conference on Microwave and Millimeter Wave Technology (ICMMT)*. IEEE, 2019, pp. 1–3.

[52] d. L. J, F. Pérez, M. Alfonseca, L. Galán, I. Montero, E. Román, and D. Raboso, "Multipactor prediction for on-board spacecraft RF equipment with the MEST software tool," *IEEE Transactions on Plasma Science*, vol. 34, no. 2, pp. 476–484, 2006.

[53] D. Wooldridge, "Theory of secondary emission," *Physical Review*, vol. 56, no. 6, p. 562, 1939.

[54] R. Lye and A. Dekker, "Theory of secondary emission," *Physical Review*, vol. 107, no. 4, p. 977, 1957.

[55] E. Bronchalo, A. Coves, R. Mata, B. Gimeno, I. Montero, L. Galán, V. Boria, and L. M. E. Sanchís, "Secondary electron emission of pt: Experimental study and comparison with models in the multipactor energy range," *IEEE Transactions on Electron Devices*, vol. 63, no. 8, pp. 3270–3277, 2016.

[56] L. Aguilera, I. Montero, M. Dávila, J. Sacedón, V. Nistor, L. Galán, D. Raboso, S. Anza, C. Vicente, and J. Gil, "ESA survey on secondary emission yield of industry materials and their impact on multipactor threshold multipactor," *Corona and Passive Intermodulation, ESA MULCOPIM*, vol. 11, 2011.

[57] A. Shih and C. Hor, "Secondary emission properties as a function of the electron incidence angle," *IEEE Transactions on Electron Devices*, vol. 40, no. 4, pp. 824–829, 1993.

[58] A. Woode and J. Petit, "Diagnostic investigations into the multipactor effect, susceptibility zone measurements and parameters affecting a discharge," *Eur. Spacy Agency, Noordwijk, The Netherlands, ESTEC Working Paper*, vol. 1556, 1989.

[59] L. Esteve, *Influencia de la Técnicas de Siembra de Electrones en la Determinación del Umbral de Descarga del Efecto Multipactor*. Val Space Consortium - Universitat Politècnica de València, 2018.

[60] F. Pérez, J. Lara, L. Conde, M. Alfonseca, L. Galán, and D. Raboso, "CEST and MEST: Tools for the simulation of radio frequency electric discharges in waveguides," *Simulation Modelling Practice and Theory*, vol. 16, no. 9, pp. 1438–1452, 2008.

[61] A. Frotanpour, G. Dadashzadeh, M. Shahabadi, and B. Gimeno, "Analysis of multipactor RF breakdown thresholds in elliptical waveguides," *IEEE Transactions on Electron Devices*, vol. 58, no. 3, pp. 876–881, 2010.

[62] D. González, M. Rodríguez, O. Monerris, B. Gimeno, V. Boria, D. Raboso, and V. Semenov, "Analysis of multipactor effect using a phase-shift keying single-carrier digital modulated signal," *IEEE Transactions on Electron Devices*, vol. 60, no. 8, pp. 2664–2670, 2013.

[63] CST, *CST-Particle Studio User Manual*, CST - Computer Simulation Technology AG, Darmstadt, Germany, 2020.

[64] ——, *SPARK3D User Manual*, CST - Computer Simulation Technology AG, Darmstadt, Germany, 2020.

[65] F. Zimmermann, "A simulation study of electron-cloud instability and beam-induced multipacting in the lhc," CERN, Tech. Rep. LHC-Project-Report-95, 1997.

[66] S. Riyopoulos, "Multipactor saturation due to space-charge-induced debunching," *Physics of Plasmas*, vol. 4, no. 5, pp. 1448–1462, 1997.

[67] D. Gonzalez, O. Monerris, B. Gimeno, M. Díaz, V. Boria, and P. Martin, "Multipactor RF breakdown in coaxial transmission lines with digitally modulated signals," *IEEE Transactions on Electron Devices*, vol. 63, no. 10, pp. 4096–4103, 2016.

[68] E. Sorolla and M. Mattes, "Multipactor saturation in parallel-plate waveguides," *Physics of Plasmas*, vol. 19, no. 7, p. 072304, 2012.

[69] E. Sorolla, A. Sounas, and M. Mattes, "Space charge effects for multipactor in coaxial lines," *Physics of Plasmas*, vol. 22, no. 3, p. 033512, 2015.

[70] G. Iadarola, H. Bartosik, G. Rumolo, G. Arduini, V. Baglin, D. Banfi, S. Claudet, O. Domınguez, J. Esteban, and T. Pieloni, "Analysis of the electron cloud observations with 25 ns bunch spacing at the LHC," *Proceedings of IPAC2014*, 2014.

[71] V. Gopinath, J. Verboncoeur, and C. Birdsall, "Multipactor electron discharge physics using an improved secondary emission model," *Physics of Plasmas*, vol. 5, no. 5, pp. 1535–1540, 1998.

[72] R. Kishek and Y. Lau, "Interaction of multipactor discharge and RF circuit," *Physical Review Letters*, vol. 75, no. 6, p. 1218, 1995.

[73] V. Semenov, E. Rakova, N. Zharova, J. Rasch, D. Anderson, and J. Puech, "Simple model of the RF noise generated by multipacting electrons," *Journal of Physics D: Applied Physics*, vol. 47, no. 5, p. 055206, 2014.

[74] J. You, H. Wang, J. Zhang, S. Tan, and T. Cui, "Accurate numerical analysis of nonlinearities caused by multipactor in microwave devices," *IEEE Microwave and Wireless Components Letters*, vol. 24, no. 11, pp. 730–732, 2014.

[75] S. Anza, C. Vicente, J. Gil, M. Mattes, D. Wolk, U. Wochner, V. Boria, B. Gimeno, and D. Raboso, "Multipactor prediction with multi-carrier signals: Experimental results and discussions on the 20-gap-crossing rule," in *The 8th European Conference on Antennas and Propagation (EuCAP 2014)*, 2014, pp. 1638–1642.

[76] S. Heinz, "Voltage and power measurements: Fundamentals, definitions, products," *Germany*, 1999.

[77] V. Chaplin, A. Hubble, K., and T. Graves, "Center conductor diagnostic for multipactor detection in inaccessible geometries," *Review of Scientific Instruments*, vol. 88, no. 1, p. 014706, 2017.

[78] O. Shimbo, "Effects of intermodulation, AM-PM conversion, and additive noise in multicarrier TWT systems," *Proceedings of the IEEE*, vol. 59, no. 2, pp. 230–238, 1971.

[79] J. Chang, P. Lawless, and T. Yamamoto, "Corona discharge processes," *IEEE Transactions on Plasma Science*, vol. 19, no. 6, pp. 1152–1166, 1991.

[80] A. Rustako, "An earth-space propagation measurement at Crawford Hill using the 12-GHz CTS satellite beacon," *Bell System Technical Journal*, vol. 57, no. 5, pp. 1431–1448, 1978.

[81] J. Rasch, D. Anderson, and V. Semenov, "Multipactor breakdown in microwave pulses," *Journal of Physics D: Applied Physics*, vol. 46, no. 50, p. 505201, 2013.

[82] A. Marrison, R. May, J. Sanders, A. Dyne, A. Rawlins, and J. Petit, "A study of multipaction in multicarrier RF components," *rep. AEA/TYKB/31761/01/RP/05*, no. 1, 1997.

[83] V. Baglin, I. Collins, B. Henrist, N. Hilleret, and G. Vorlaufer, *A Summary of Main experimental Results Concerning the Secondary Electron Emission of Copper (Report LHC Project Report-472)*. CERN, 2001.

[84] M. Furman and M. Pivi, "Probabilistic model for the simulation of secondary electron emission," *Physical Review Special Topics-Accelerators and Beams*, vol. 5, no. 12, p. 124404, 2002.

[85] M. Furman and M. T. Pivi, "Simulation of secondary electron emission based on a phenomenological probabilistic model," Lawrence Berkeley National Lab.(LBNL), Berkeley, CA (United States), Tech. Rep., 2003.

[86] D. González, O. Monerris, M. Diaz, B. Gimeno, V. Boria, and D. Raboso, "Experimental analysis of the multipactor effect with RF pulsed signals," *IEEE Electron Device Letters*, vol. 36, no. 10, pp. 1085–1087, 2015.

[87] L. Verlet, "Computer "experiments" on classical fluids. I. Thermodynamical properties of Lennard-Jones molecules," *Physical review*, vol. 159, no. 1, p. 98, 1967.

[88] H. Bruining, *Physics and Applications of Secondary Electron Emission: Pergamon Science Series: Electronics and Waves*. Elsevier, 2016.

[89] V. Semenov, N. Zharova, R. Udiljak, D. Anderson, M. Lisak, and J. Puech, "Multipactor in a coaxial transmission line. II. Particle-in-cell simulations," *Physics of Plasmas*, vol. 14, no. 3, p. 033509, 2007.

[90] J. Greenwood, "The correct and incorrect generation of a cosine distribution of scattered particles for Monte-Carlo modelling of vacuum systems," *Vacuum*, vol. 67, no. 2, pp. 217–222, 2002.

[91] R. Udiljak, D. Anderson, M. Lisak, V. Semenov, and J. Puech, "Multipactor in a coaxial transmission line. i. analytical study," *Physics of Plasmas*, vol. 14, no. 3, p. 033508, 2007.

[92] B. Boashash, "Estimating and interpreting the instantaneous frequency of a signal. I. fundamentals," *Proceedings of the IEEE*, vol. 80, no. 4, pp. 520–538, 1992.

[93] V. Semenov, M. Buyanova, D. Anderson, M. Lisak, R. Udiljak, and J. Puech, "Multipactor in microwave transmission systems using quadrature phase-shift keying," *IEEE Transactions on Plasma Science*, vol. 38, no. 4, pp. 915–922, 2010.

[94] N. L. Gallou, C. Miquel-Espanya, S. Matinfar, C. Ernst, and F. D. Paolis, "Multipactor threshold and margins using realistic modulated signals," in *Proc. MULCOPIM*, 2011, pp. 21–23.

[95] A. Morello and V. Mignone, "DVB-S2: The second generation standard for satellite broad-band services," *Proceedings of the IEEE*, vol. 94, no. 1, pp. 210–227, 2006.

[96] T. Braun and W. Braun, *Digital Communications Theory*. Wiley-IEEE Press, 2021.

[97] R. van Nee and R. Prasad, *OFDM for Wireless Multimedia Communications*. Artech House, 2000.

[98] C. Thomas, M. Weidner, and S. Durrani, "Digital amplitude-phase keying with M-ary alphabets," *IEEE Transactions on Communications*, vol. 22, no. 2, pp. 168–180, 1974.

[99] D. Lefevre, "A power-efficient BPSK communications system for small satellites," *Small Satellites Conference*, 1989.

[100] R. Ludwig and J. Taylor, "Descanso design and performance summary series article 4: Voyager telecommunications," *Washington: NASA*, pp. 1–6, 2002.

[101] J. Statman and C. Edwards, "Coding, modulation, and relays for deep space communication Mars rovers case study," in *IEEE 23rd Convention of Electrical Engineers in Israel, Herzlia, Israel, September 6-7*. Pasadena, CA: Jet Propulsion Laboratory, National Aeronautics and Space Administration, 2004.

[102] D. Roddy, *Satellite Communications*. McGraw-Hill Education, 2006.

[103] G. Proakis and M. Salehi, *Digital Communications*. McGraw-Hill., 2008.

[104] S. Anza, C. Vicente, J. Gil, V. Boria, and D. Raboso, "Experimental verification of multipactor prediction methods in multicarrier systems," in *2016 46th European Microwave Conference (EuMC)*. IEEE, 2016, pp. 226–229.

[105] E. S. Agency, "ECSS Multipactor Tool," Mar. 2022, [Online; accessed 8. Jan. 2023]. [Online]. Available: http://multipactor.esa.int

[106] D. Lim, S. Heo, J. No, and H. Chung, "On the phase sequence set of SLM OFDM scheme for a crest factor reduction," *IEEE Transactions on Signal Processing*, vol. 54, no. 5, pp. 1931–1935, 2006.

[107] R. Sperlich, Y. Park, G. Copeland, and J. Kenney, "Power amplifier linearization with digital pre-distortion and crest factor reduction," in *2004 IEEE MTT-S International Microwave Symposium Digest (IEEE Cat. No. 04CH37535)*, vol. 2. IEEE, 2004, pp. 669–672.

[108] R. Mansour, S. Ye, J. Dokas, W. Tang, and C. Kudsia, "Feasibility and commercial viability issues for high-power output multiplexers for space applications," *IEEE Transactions on Microwave Theory and Techniques*, vol. 48, no. 7, pp. 1199–1208, 2000.

[109] S. Cogollos, P. Soto, V. Boria, M. Guglielmi, M. Brumos, B. Gimeno, and D. Raboso, "Efficient design of waveguide manifold multiplexers based on low-order em distributed models," *IEEE Transactions on Microwave Theory and Techniques*, vol. 63, no. 8, pp. 2540–2549, 2015.

[110] C. Carceller, P. Soto, V. Boria, M. Guglielmi, and J. Gil, "Design of compact wideband manifold-coupled multiplexers," *IEEE Transactions on Microwave Theory and Techniques*, vol. 63, no. 10, pp. 3398–3407, 2015.

[111] J. Uher, Y. Demers, and S. Richard, "Complex feed chains for satellite antenna applications at Ku-and Ka-band," in *2010 IEEE Antennas and Propagation Society International Symposium*. IEEE, 2010, pp. 1–4.

[112] E. Nicol, J. Robison, R. Ortland, A. Ayala, and G. Saechao, "TWTA on-orbit reliability for space systems loral satellite fleet," in *2016 IEEE International Vacuum Electronics Conference (IVEC)*. IEEE, 2016, pp. 1–2.

[113] U. Reimers, "DVB-T: the COFDM-based system for terrestrial television," *Electronics & Communication Engineering Journal*, vol. 9, no. 1, pp. 28–32, 1997.

[114] S. Sesia, I. Toufik, and M. Baker, *LTE - the UMTS Long Term Evolution: from Theory to Practice*. John Wiley & Sons, 2011.

[115] K. Technologies, *Fundamentals of Arbitrary Waveform Generation. M8190-91050, Reference Guide Edition 4.0*, USA, 2015.

[116] ——, *M8196A 92 GSa/s Arbitrary Waveform Generator Data Sheet*, USA, 2015.

[117] C. Tröster and T. Bednorz, "Generating multiple phase coherent signals–aligned in phase and time," *Rohde & Schwarz GmbH & Co. KG, München*, 2016.

[118] K. Remley, D. Williams, D. Schreurs, G. Loglio, and A. Cidronali, "Phase detrending for measured multisine signals," in *61st ARFTG Conference Digest, Spring 2003.* IEEE, 2003, pp. 73–83.

[119] E. Armstrong, "A new system of short wave amplification," *Proceedings of the Institute of Radio Engineers*, vol. 9, no. 1, pp. 3–11, 1921.

[120] Y. Anand and W. Moroney, "Microwave mixer and detector diodes," *Proceedings of the IEEE*, vol. 59, no. 8, pp. 1182–1190, 1971.

[121] O. Tang and C. Aitchison, "A very wide-band microwave MESFET mixer using the distributed mixing principle," *IEEE Transactions on Microwave Theory and Techniques*, vol. 33, no. 12, pp. 1470–1478, 1985.

[122] G. Picchi and G. Prati, "Blind equalization and carrier recovery using a "stop-and-go" decision-directed algorithm," *IEEE Transactions on Communications*, vol. 35, no. 9, pp. 877–887, 1987.

[123] N. Jablon, "Joint blind equalization, carrier recovery and timing recovery for high-order QAM signal constellations," *IEEE Transactions on Signal Processing*, vol. 40, no. 6, pp. 1383–1398, 1992.

[124] J. Eaton, *GNU Octave A High-Level Interactive Language for Numerical Computations Edition 6 for Octave Version 6.3.0*, Free Software Foundation, Boston, USA, July 2021.

[125] D. Pilz and P. Feldle, "RF-payload of TerraSAR-X," in *Proc. German Microw. Conf.(GeMiC)*, 2005, pp. 140–143.

[126] J. Dugundji, "Envelopes and pre-envelopes of real waveforms," *IRE Transactions on Information Theory*, vol. 4, no. 1, pp. 53–57, 1958.

[127] A. Papoulis, *The Fourier Integral and its Applications*. Polytechnic Institute of Brooklyn, McCraw-Hill Book Company Inc., USA, ISBN: 67-048447-3, 1962.

[128] K. Schneider and W. Tranter, "Efficient simulation of multicarrier digital communication systems in nonlinear channel environments," *IEEE Journal on Selected Areas in Communications*, vol. 11, no. 3, pp. 328–339, 1993.

[129] A. T. Inc., *Two-tone and Multitone Personalities for the E8267C PSG Vector Signal Generator. Technical note 1410.*, USA, 2003.

[130] F. Teberio, I. Arregui, P. Soto, M. Laso, V. Boria, and M. Guglielmi, "High-performance compact diplexers for Ku/K-band satellite applications," *IEEE Transactions on Microwave Theory and Techniques*, vol. 65, no. 10, pp. 3866–3876, 2017.

[131] E. S. Agency, "High-power multicarrier facility inaugurated in spain," Oct 2021, [Online; accessed 17. Oct. 2021]. [Online]. Available: https://www-acc.esa.int/Enabling_Support/Space_Engineering_Technology/High-power_multicarrier_facility_inaugurated_in_Spain

[132] K. Technologies, *M8196A 92 GSa/s Arbitrary Waveform Generator Data Sheet*, USA, 2017.

[133] R. . Schwarz, *R&S SMW200A Vector Signal Generator Specifications*, Germany, 2022.

[134] B. Lee, H. Lee, G. Kang, H. Lee, J. Kim, J. Lee, and N. Kim, "Local oscillator leakage reduction," *Microwave and Optical Technology Letters*, vol. 32, no. 5, pp. 379–381, 2002.

[135] C. Arnold, J. Parlebas, R. Meiser, and T. Zwick, "Fully reconfigurable manifold multiplexer," *IEEE Transactions on Microwave Theory and Techniques*, vol. 65, no. 10, pp. 3885–3891, 2017.

[136] L. Anttila, M. Valkama, and M. Renfors, "Frequency-selective I/Q mismatch calibration of wideband direct-conversion transmitters," *IEEE Transactions on Circuits and Systems II: Express Briefs*, vol. 55, no. 4, pp. 359–363, 2008.

[137] R. Hassun, M. Flaherty, R. Matreci, and M. Taylor, "Effective evaluation of link quality using error vector magnitude techniques," in *Proceedings of 1997 Wireless Communications Conference*. IEEE, 1997, pp. 89–94.

[138] T. Jensen and T. Larsen, "Robust computation of error vector magnitude for wireless standards," *IEEE Transactions on Communications*, vol. 61, no. 2, pp. 648–657, 2013.

[139] K. Freiberger, H. Enzinger, and C. Vogel, "A noise power ratio measurement method for accurate estimation of the error vector magnitude," *IEEE Transactions on Microwave theory and techniques*, vol. 65, no. 5, pp. 1632–1645, 2017.

[140] R. A. Shafik, M. S. Rahman, and A. Razibul, "On the extended relationships among EVM, BER and SNR as performance metrics," in *2006 International Conference on Electrical and Computer Engineering*. IEEE, 2006, pp. 408–411.

[141] O. Monerris, E. Diaz, J. Ruiz, and V. Boria, "Automatic, calibrated and accurate measurement of S-parameters in climatic chamber," *IEEE Microwave and Wireless Components Letters*, vol. 25, no. 6, pp. 412–414, 2015.

[142] J. Walker, *Handbook of RF and microwave power amplifiers*. Cambridge university press, 2011.

[143] J. Huijsing, R. V. de Plassche, R. V. de Plassche, and W. Sansen, *Analog Circuit Design: Volt Electronics; Mixed-Mode Systems; Low-Noise and RF Power Amplifiers for Telecommunication*. Springer Science & Business Media, 1998.

[144] Keysight, "PXI System Synchronization Modules," Tech. Rep., Sep. 2018. [Online]. Available: https://www.keysight.com/es/en/products/modular/pxi-products/pxi-system-synchronization-modules.html

[145] NI, "National Instruments NI-TClk Technology for Timing and Synchronization of Modular Instruments," Tech. Rep., Oct. 2020. [Online]. Available: https://www.ni.com/es-es/innovations/white-papers/20/national-instruments-ni-tclk-technology-for-timing-and-synchroni.html

[146] *CalPod Service Information*, Jun. 2022, [Online; accessed 6. Jun. 2022]. [Online]. Available: https://na.support.keysight.com/calpod

[147] W. Hu, O. Hamza, A. Prasetiadi, M. Jost, and R. Jakoby, "Temperature controlled artificial coaxial line for microwave characterization of liquid crystal," in *GeMiC 2014; German Microwave Conference*. VDE, 2014, pp. 1–4.

[148] G. Guo, E. Li, Z. Li, Q. Zhang, and F. He, "A test system for complex permittivity measurements of low-loss materials at high temperatures up to 2000° C," *Measurement Science and Technology*, vol. 22, no. 4, p. 045707, 2011.

[149] Z. Schwartz, A. Downey, S. Alterovitz, and G. Ponchak, "High-temperature RF probe station for device characterization through 500/spl deg/C and 50 GHz," *IEEE Transactions on Instrumentation and Measurement*, vol. 54, no. 1, pp. 369–376, 2005.

[150] L. GmbH, "Heat transfer liquid for thermostat, circulation chiller, water bath," Sep 2021, [Online; accessed 21. Sept. 2021]. [Online]. Available: https://www.lauda.de/en/constant-temperature-equipment/heat-transfer-liquids

[151] V. Nova, C. Bachiller, J. Martínez, H. González, J. Merello, A. Belenguer, O. Monerris, and V. Boria, "Thermal stability analysis of filters in substrate integrated technologies under atmospheric pressure and vacuum conditions," *IEEE Access*, vol. 8, pp. 118 072–118 082, 2020.

[152] E. Requirements and S. D. ESTEC, *Space Engineering. Testing (ECSS-E-ST-10-03C)*. ESA-ESTEC, 1 June 2012.

[153] E. Diaz, A. Belenguer, H. Esteban, and V. Boria, "Thru-reflect-line calibration for substrate integrated waveguide devices with tapered microstrip transitions," *Electronics Letters*, vol. 49, no. 2, pp. 132–133, 2013.

[154] F. Ramian, *Implementation of Real-Time Spectrum Analysis*, 2011.

[155] P. Bloomfield, *Fourier Analysis of Time Series: an Introduction*. John Wiley & Sons, 2004.